UNIVERSITIES OF GLASGOW AND STRATHCLYDE

DEPARTMENT OF NAVAL ARCHITECTURE & MARINE ENGINEERING

SIMULATION OF PROGESSIVE FLOODING OF DAMAGED SHIPS BY CFD

LOOKING BACK TO GO FURTHER

By

Clemens Strasser

A THESIS SUBMITTED IN PARTIAL FULFILMENT OF THE
REQUIREMENTS FOR THE DEGREE OF
DOCTOR OF PHILOSOPHY

GLASGOW, UK
FEBRUARY 2010

This thesis is the result of the author's original research. It has been composed by the author and has not been previously submitted for examination which has lead to the award of a degree.

Signed: _____ Date: 23/02/2010

“The best way to predict the future is to invent it.”

[Alan Curtis Kay]

Acknowledgments

The research of this thesis has been carried out at the Ship Stability Research Centre, Department of Naval Architecture & Marine Engineering, Universities of Glasgow and Strathclyde, during the years 2005 and 2008. The Research was funded by Safety @ Sea Ltd. and the Universities of Glasgow and Strathclyde. Financial support is gratefully acknowledged.

Professor Dracos Vassalos was the supervisor of the study. I want to express sincere gratitude to Professor Dracos Vassalos for his guidance throughout the period of my work. He inspired me and introduced me to the subject of damage stability and computational fluid dynamics.

I also owe Professor Papanikolaou and Professor Huang a debt of gratitude for giving valuable hints and support on present research work.

Particular thanks to Dr. Andrzej Jasionowski, the project manager of the project "Research Study of Sinking Sequence of M/V Estonia", for interesting discussions and encouragement throughout my research.

I want to thank Dr. Jan Blok from MARIN and Dr. Pekka Rupponen from NAPA Ltd. who provided valuable validation data for the case studies.

I would also like to thank my colleagues at the Ship Stability Research Centre, Safety @ Sea Ltd. and the Department of Naval Architecture & Marine Engineering for providing a stimulating work environment.

Special thanks to Vienna Model Basin Ltd. for giving me the possibility to take a time out and spend some fruitful years on research.

Lastly, I would like to thank my parents and my sister for their support during my studies.

Summary

This thesis addresses the assessment of the damage survivability of passenger and Ro-Ro vessels from a fundamental point of view. Ultimate aim was to develop a tool that is capable of collecting detailed physical information and flow characteristics at any location inside a flooded ship hull. Floodwater dynamics and water ingress through various openings and opening shapes in the ship hull structure are accounted. Walls of compartments and rooms are considered to be watertight and non-permeable. In void areas of flooded compartments the flooding can also result in air compression since the ventilation of these rooms is restricted either due to the relatively small air pipes or no ventilation at all.

A commercial numerical Computational Fluid Dynamics (CFD) code is used to create a flooding scenario with simplified boundary conditions which speeds up the calculations compared to CFD calculations using standard practice boundary conditions. The method avoids the creation of large water domains surrounding the involved damaged ship hull which in return saves CPU load and calculation time. A side effect of one method is the nonexistence of reflecting waves in the water domain outside of the damaged ship hull caused by quasi-static ship motions which is always a problematic issue in numerical models where the floating geometry is surrounded by large water/air domains. In some cases, depending on the geometry of the model, compressible air is used in simulations where trapped air is expected or the influence of trapped air could be crucial.

Moreover, a k-ε turbulence model is adopted in cases of flooding scenarios with high velocity in- or egress of water or air in order to simulate scenarios as true-to-life as possible. Additionally, a six degrees-of-freedom solver has been integrated which simulates quasi-static ship motions in calm water excited by flood water motion inside the compartment. The ship hull domain is then moved by the method of grid remeshing.

Aiming to find out about the time-to-flood, the results of the simulation are compared to an alternative numerical method based on strip theory and lump mass concept. Furthermore, the influence of scale effects is investigated by performing CFD calculations with models of different model scale. Final evaluation of the derived data is carried out with a comparison to various model tests.

Starting point of this research is a review of the available literature striking models and methods, which assess damage stability and survivability of passenger ships, aiming to identify strength and weaknesses of existing theories. Based on this knowledge it is decided to utilise CFD which gives to date more information and details of the physics of progressive flooding than any other numerical method but in contrary is more expensive in calculation time compared to other numerical simulation methods. For the validation of the simulation basic and simplified geometry of ships and ship decks are taken as basis. These cases contain all relevant elements that are of significance for a “successful” flooding scenario.

The numerical model described in this thesis represents an advanced treatment of modelling the process of progressive flooding with the use of CFD. The effectiveness of the tool has been demonstrated by undertaking strict analysis of the M/V Estonia disaster, a fictitious model of a box-shaped barge which has been used as ITTC validation model and damaged compartment of an ITTC Ro-Ro passenger ship. It can be concluded that the applied method agrees very well with all validation cases and that accuracy is sufficient though simulations with simplified models are carried out. A drawback of the method is its high consumption of computing power and its relatively long computation time compared to other numerical methods. However, compared to other RANSE calculations of similar flooding scenarios presented method is 8 – 24 times faster. Inferential, the prediction of time-to-flood is mainly derived in a period where the ship remains in quasi-hydrostatic conditions.

Room for future development is given by carrying out calculations considering the influence of the sea state in flooding scenarios and taking into account collapsing structures or cargo shifting.

Keywords: boundary conditions, compressible air, Computational Fluid Dynamics (CFD), damage stability, flooding dynamics, M/V Estonia, box-shaped barge, ITTC Ro-Ro passenger ship, progressive flooding, sloshing, time-to-flood, turbulence models, water ingress, dynamic mesh, six degrees-of-freedom, scale effects.

Table of Contents

List of Figures

List of Tables

Nomenclature

Abbreviations

a	linearised coefficient
A	wetted area
$\vec{A}$	surface area vector
$\vec{A}_f$	face area vector in 3D
AFRA	Average Freight Rate Assessment
ALARP	As Low As Reasonably Practicable
ALE	Arbitrary Lagrangian Eulerian
α_q	volume fraction in cell
AMG	Algebraic Multigrid
β	coefficient of thermal expansion
B	centre of buoyancy, damping constant
Γ_ϕ	diffusion coefficient for ϕ
$C_{1\varepsilon}$, $C_{2\varepsilon}$, $C_{3\varepsilon}$	constants
C_μ	constant
Ca	capillary number
CFD	Computational Fluid Dynamics
CFL	Courant-Friedrich-Lewy number

CICSAM	Compressive Interface Capturing Scheme for Arbitrary Meshes
CPU	Central Processing Unit
CSF	Continuum Surface Force
CWL	Construction WaterLine
$\vec{d}$	vector connecting cell centres adjacent to the face *f*
DOF	Degree-Of-Freedom
ε	rate of dissipation
E	energy
f	face
F	flow coefficient, factor of subdivision, force
$\vec{f}_E$	external forces and
$\vec{f}_G$	forces due to gravity
$\vec{f}_H$	hydrodynamic forces
ϕ	scalar quantity
FDM	Finite Difference Method
FEM	Finite Element Method
FVM	Finite Volume Method
FMPS	Free-Mass-on-Potential-Surface
G	centre of gravity
G_b, G_k	turbulence kinetic energy

GM	metacentric height
GZ	righting arm
HARDER	Harmonization of Rules and Design Rationale
H_S	significant wave height
HRIC	High Resolution Interface Capturing scheme
I	moment of inertia
IMO	International Maritime Organization
[*J*]	coefficient matrix
J_f	mass flux through face *f*
φ	roll angle
κ	doubly curved surface curvature
k	kinetic energy
k_{eff}	effective thermal
KB	height of centre of buoyancy above keel
KG	height of centre of gravity above keel
L	length, inertia tensor
L_{OA}	Length Over All
L_{PP}	Length between PerPendiculars
LES	Large Eddy Simulation
LNG	Liquefied Natural Gas
LOWI	Loss Of Watertight Integrity

MAC	marker and cell
MARIN	Maritime Research Institute Netherlands
$\overrightarrow{M_B}$	moment vector of the body
MFS	Multi-Free Surface
MTcm	moment to trim per cm
MUSCL	Monotone Upstream-Centred Schemes for Conservation Laws
μ	permeability
μ_t	turbulent or eddy viscosity
n	index for time step
N_f	number of nodes on the face
N_{faces}	number of faces enclosing the cell
nb	neighbour cell
∇	displacement, differential operator
NAME	Department of Naval Architecture & Marine Engineering
p	pressure
p'	cell pressure correction
Pe	Peclet number
PISO	Pressure Implicit with Splitting of Operators
PIV	Particle Image Velocimetry
PRESTO!	PREssure STaggering Option
q	number of phase

QUICK	Quadratic Upwind Interpolation
ρ	density
R	radius
RANSE	Reynolds Averaged Navier-Stokes Equations
Re	Reynolds number
Ro-Ro	Roll in - Roll out
RSM	Rankine Source Method
σ	surface or interfacial tension between the two fluid phases
σ_k , σ_ε	turbulent Prandtl number
S	modulus of the mean rate-of-strain tensor, surface area
S@S	Safety at Sea Ltd.
S_h	contributions from radiation and other volumetric heat sources
S_k , S_ε	user-defined source terms
S_ϕ	source of ϕ per unit volume
SIMPLE	Semi-Implicit Method for Pressure-Linked Equations
SIMPLEC	Semi-Implicit Method for Pressure-Linked Equations Consistent
SOLAS	Conference of Safety Of Life At Sea
SPH	Smoothed Particle Hydrodynamics
t	time
T	heeling arm, period, temperature
TCG	Transversally shifted Centre of Gravity

TPcm	tons per cm
tpcm	lost tons per cm
TSTE	Taylor Series Truncation Error
TTF	Time-To-Flood
U	the free-stream velocity
U_f	volume flux through the face, based on normal velocity
V, v	volume, volume of floodwater, flow velocity
$\vec{v}$	velocity vector
$\dot{\vec{v}}_G$	translational acceleration of the centre of gravity
VMB	Vienna Model Basin
VOF	Volume Of Fluid
$\overrightarrow{\omega_B}$	rigid body angular velocity vector
$\dot{\vec{\omega}}_B$	angular acceleration
W	weight of floodwater
We	Weber number
WT	WaterTight
x	distance
Y_M	contribution of the fluctuating dilatation in compressible turbulence to the overall dissipation rate
Z_w	water level height

1 Introduction

1.1 General Remarks

Damage stability of passenger ships or Ro-Ro ferries is still a topic of great research interest to the maritime industry and scientific community. The trend in naval industry is to build bigger and faster ships and superlatives are more important than ever to attract and carry more people. For example: currently, Genesis (Figure 1), the world largest cruise ship - which hull weighs 220.000 tons, length over all (L_{OA}) is 360m, beam (B) is 47m, height (H) above waterline is 65m, draft (D) is 9m and she carries 8.400 people - is built in Finland, STX Europe AS former Aker Yards, and she was expected to be delivered to Royal Caribbean Cruises in 2009.

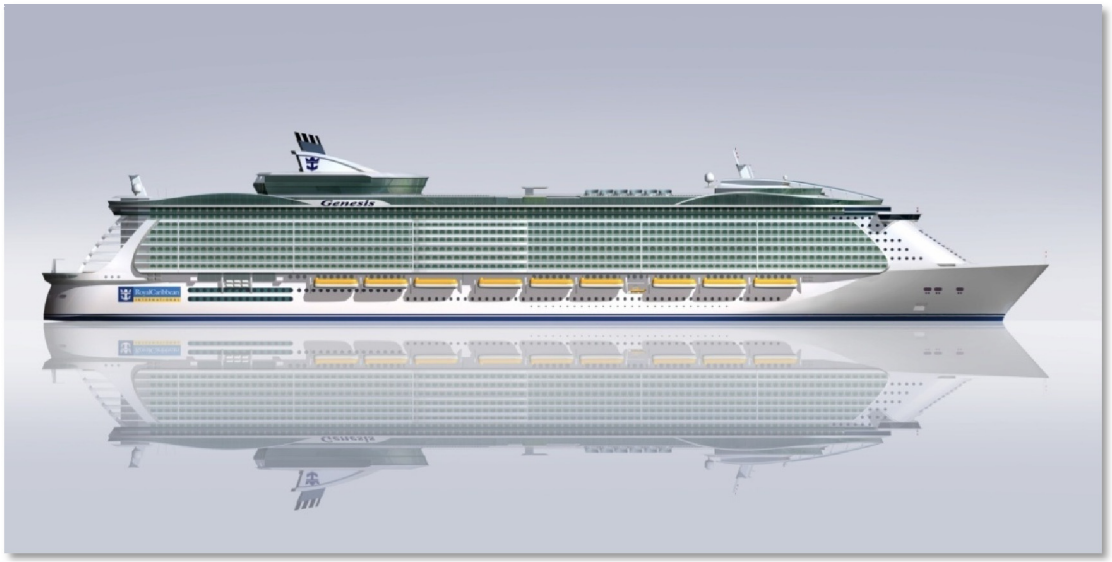

Figure 1: Cruise ship Royal Caribbean Genesis

The main features of the ship are impressive though there are some inherent problems: bigger ships are more difficult to manoeuvre due to their heavy inertial mass; if the worse comes to the worst and flooding is inevitable the bigger compartments in the ship hull structure of such ocean liners provide larger free surface area that can cause a quick loss of static stability and floatability. ROPAX vessels on the other side are affected by the possible flooding of a large free surface

area (car deck) and have a high risk to capsize when involved in an accident. Furthermore, in case of an accident it is not so easy to control and evacuate thousands of people – some of which in panic - during a probably short time in which the ship remains viable for evacuation and abandonment. Hence, attention has to be turned to safety and survivability; on board but especially to the design phase of a ship where important precautions can be arranged to prevent or limit dangerous situations. For instance, for the flooding of a vessel this could mean to put all engineering effort to extend the time-to-flood to such an extent that the ship can be safely evacuated or remains in a stable and safe position. This can be a challenging task for an engineer as many different worst case scenarios have to be considered in order to minimise the risk.

Foregoing mentioned paragraph raises a philosophical question: what is safety and how safe must a ship be? As is generally defined by various dictionaries, the term safety is the state of being safe and to be free of danger which neither includes a far-reaching compass of the expression nor specifies a precise condition in absolute terms. It is important to realise that safety is relative and nothing is 100% safe under all conditions. Eliminating all risks, if even possible, would be extremely difficult and very expensive. A safe situation is one where risks of injury or property damage are low and predictable. In mathematical probability terms there is no absolute safety. This uncertainty about safety led to the evolution of a new scientific field aiming to prevent accidents by unveiling their causes and consequences through new scientific findings and collection of fundamental knowledge. The Science of Safety is still in the beginning of its development but is a necessary and inevitable area of expertise for improving the safety rules especially in the field of ship design and ship operating technique.

The unpredictability of potential incidents allows room for only one possible answer to the question above: a ship has to be as safe as possible and risk has to be reduced to a minimum. In the end it comes down to engineers and designers who are in charge to fulfil these requirements. In doing so, they can scoop from a bunch of different methods and tools for safety improvement on sea. A very effective and

reasonable tool is using computer simulations which can help the designer to find crucial factors in the ship design that finally bring ship safety to an acceptable level, such as explained with the ALARP principle.

In the milieu of safety critical and high-integrity systems the term of ALARP (As Low As Reasonably Practicable) principle is used very often. In other words, the ALARP principle is that the residual risk shall be as low as reasonably practicable. The ALARP principle arises from the fact that it would be possible to spend infinite time, effort and money attempting to reduce a risk to zero. It means that a risk is low enough that attempting to make it lower would be more costly than any cost likely to come from the risk itself which is generally called tolerable risk. It should not be understood as simply a quantitative measure of benefit against detriment. It is more a best common practice of judgement of the balance of risk and societal benefit. So called carrot diagrams (Figure 2) are often used to display risks.

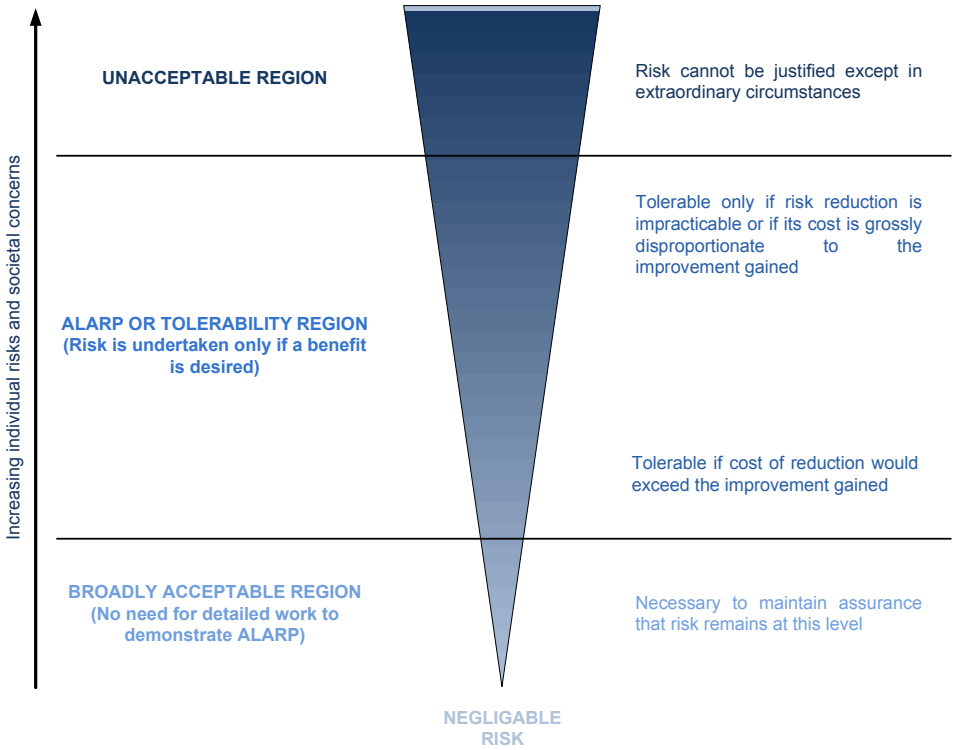

Figure 2: Levels of risk and ALARP *(HazardsForum (1995))*

In order to understand the diagram above the term risk has to be defined. *Chicken and Posner (1998)* provide their interpretation of what risk constitutes:

Risk = Hazard x Exposure

They define hazard as ".. *the way in which a thing or situation can cause harm,* " and exposure as *".. the extent to which the likely recipient of the harm can be influenced by the hazard*". Harm is taken to imply injury, damage, loss of performance, etc., whilst exposure imbues the notation of frequency and probability. It can be argued that hazard is not the "*.. way in which ..*" rather it is the "*thing*" itself.

Beck (1986) considered risk as a "*systematic way of dealing with hazards*". If it is assumed that there is uncertainty associated with any prediction of a hazard occurring, then there is only uncertainty because there is only ever a prediction of the likely occurrence.

Therefore for a risk to exist there must be a hazard. The perception of hazards is entirely subjective. What one person finds hazardous, his neighbour may not. It is the way in which we feel threatened by circumstance and in turn the opinion we develop by association with the threat or hazard.

This perception of hazard is centred around previous experience, cultural values and to some extent the aspect of specialist training in an area or field of expertise to which the hazard relates, *Greene (2000)*.

Methods of risk and reliability analysis in various engineering disciplines , developed during the last decades, are becoming more and more important as decision support tools in engineering applications. Integration of risk and reliability analysis methods into the design process leads to "risk-based design", *Papanikolaou (2009)*. Marin industry is progressively catching up in the fields of risk-based ship design. Risk-based design is a formalised methodology that integrates systematically risk assessment in the design process with prevention/reduction of risk (to life, property and the environment) embedded as a design objective, alongside "conventional" design objectives (such as speed, capacity, etc)., *Vassalos et al. (2006)*.

Recapitulatory, the minimisation of risk is always a very complex process and the designer has to aim to find a balance of cost, efficiency, time, reliability and other constraints concerning safety issues. Therefore it is necessary that traditional design philosophies have to be reconsidered which can be accomplished by a generation of designers with a very broad knowledge that is not only focused on the principles of naval architecture. The future of naval architecture and especially development of safety tools will strongly feature an interdisciplinary character.

1.2 Damage Stability

In the past damage stability of ships was treated stepmotherly and safety was only improved after the event of a disastrous accident. After the loss of Titanic wing bulkheads were not allowed to use anymore; after the accident of Andrea Doria crosslinks between tanks were introduced. Whenever an accident happened IMO rules were adopted. In fact these accidents should have provoked to focus on the optimisation of safety in general and to look for different aspects in safety improvement and risk minimisation. Instead, scientists and engineers continued to optimise the ship's performance, speed, manoeuvrability, capacity, etc. Whenever tragic accidents happened resulting in human live loss public was shocked and pressure was on the maritime community. It was discussed about taking action regarding safety issues but it seemed there was neither a scientific nor a commercial interest.

The development of Ro-Ro vessels turned the view about safety of ships to the better as commercial transportation of passengers and cars seemed to be highly profitable. Moreover, the pressure of competition between shipping owners became more and more active and nobody could afford to make major mistakes especially when it comes to safety. But, why - all of a sudden - has the view about safety been changed? The modern roll-on/roll-off ship can trace its origins back more than one hundred years to the early days of the steam train. Ships were specially designed to take trains across rivers which were too wide for bridges: the

ships were equipped with rails, and the trains simply rolled straight on to the ship, which sailed across the river to another rail berth where the train would roll off again. An example is the Firth of Forth ferry in Scotland which began operations in 1851. It was not until the Second World War, however, that the idea of applying the Ro-Ro principle of road transport became practicable - and was used in constructing the tank landing craft used at D-Day and in other battles. It must be mentioned that the first Ro-Ro ferry for military transport was Comet (USA 1953), *Papanikolaou (2003)*. The principle was applied to merchant ships in the late 1940s and early 1950s. It proved to be extremely popular, especially on short-sea ferry routes, encouraged by technical developments on land as well as sea, notably the increase in road transport.

Obviously, the design of a new ship type with large loading openings at the bow and rather big cargo decks without any subdivisions required the introduction of development in safety regulations and design. Due to the fact that large open space inside ships with a large free surface can increase the damage displacement or cause loss of stability – both of which resulting in capsize or sink – such spaces were located above the waterline in calm water. Seafaring is unfortunately subject to very dynamic actions and most of the accidents happen in very rough sea and weather conditions which can let floodwater on the vehicle deck through a damage opening causing three different cases:

- Floodwater enters the deck but the ship provides sufficient stability to keep the vehicle deck above the waterline. Water would flow out again
- The ship is stable but the elevation of the vehicle deck allows continuous flooding. This condition can cause capsize or sink following progressive flooding.
- The ship loses stability and already capsizes during the stage of transient flooding.

The last scenario is the worst case but has been observed in most of the lethal disasters where Ro-Ro vessels were involved.

The numerical reflection of damage cases of such highly non-linear systems is very complex. Even small changes in some parameters, like the change of the centre of gravity due to additional mass onboard, can have major influence on the final result of the calculation. In this regard it has to be ensured that all important parameters are carefully considered and included in the numerical model. Hence, it requires severe discipline to build up a well structured methodology in order to “illuminate” the subject matter of damage stability.

1.3 Structure of the Thesis

The thesis can be subdivided into six main parts consisting of 10 chapters. Focus of the present work is given in chapter 2 which deals with the aim and specific objectives. A critical review of literature, relevant to the topic of damage stability and especially progressive flooding, is presented in chapter 3 followed by chapter 4 giving information about the adopted approach. The first technical chapter 5 explains the physical background while chapter 6 concentrates on the principles of the numerical calculations. The implementation of the previously exercised two technical chapters is described in chapter 7. Finally chapter 8 presents various case studies illustrating the applicability of the used tool. Developments, findings, aims and main contributions are discussed in chapter 9 and chapter 10 completes this thesis with a summary of the main conclusions. Below Figure 3 is presenting a visual impression of the structure.

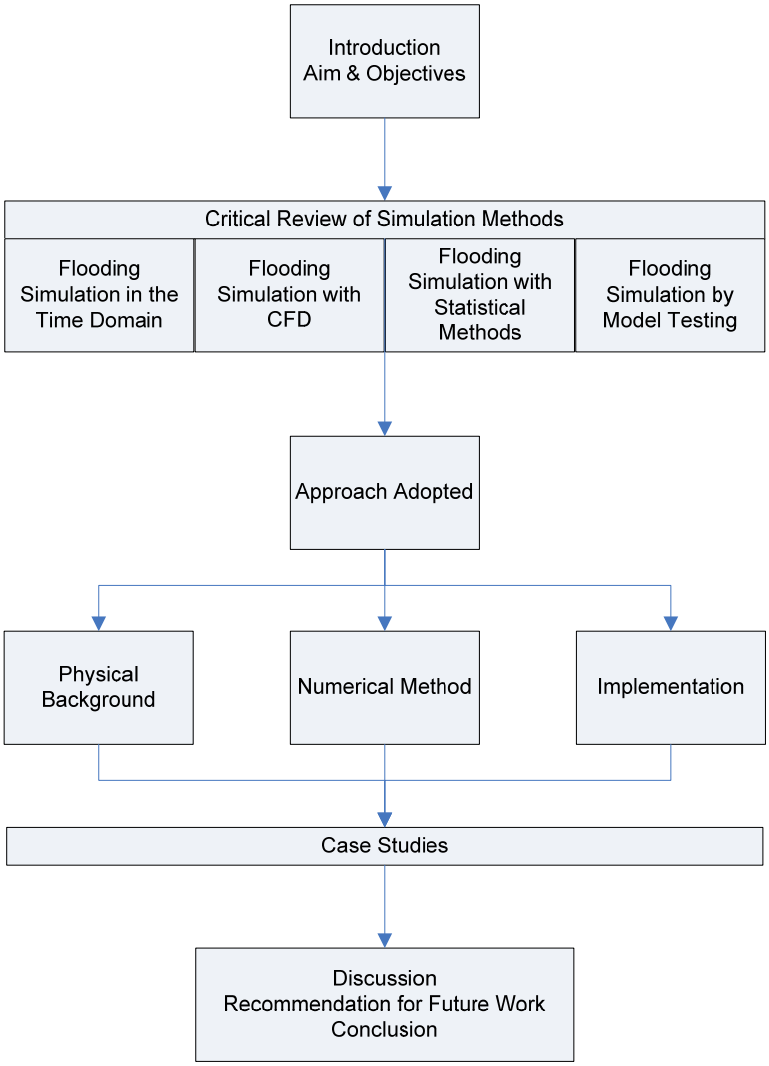

Figure 3: Structure of the thesis

1.4 Concluding Remarks

Providing a tool which makes it possible to improve the design of a ship regarding its stability in a damage case is only one goal that has to be established. Another goal is to account for any influential physical factors involved in a flooding scenario by using different methods and approaches adopted from various scientific areas. The full potential of current available technology should be tapped in order to get reliable results in a detailed way which is difficult to achieve with model tests or traditional hydraulic simulation methods.

Keywords in this technology dominated era are optimisation and true-to-life simulations; thus one should make use of by thoughtful application especially of tools for the minimisation of risk onboard. Present thesis is driven by this categorical philosophy and treats various aspects of progressive flooding by adopting different approaches and finally by integrating them into a numerical model.

2 Aims and Objectives

When a ship is damaged and flooded, the behaviour of the ship is significantly influenced by the flooding water dynamics. In several cases, depending on the magnitude of the floodwater mass and the internal water depth, internal resonances and interactions with the overall ship dynamics will produce additional dynamic effects, which might significantly affect the ship's motion and the vessel's survivability. Therefore it is necessary to analyse the coupled dynamics of flooding water in order to calculate the motion of the damaged ship and finally to evaluate the survivability of the vessel. For a more systematic investigation aiming to gain insight into the floodwater propagation through complex geometries, Computational Fluid Dynamics (CFD) studies using RANSE codes have been undertaken. A six degrees-of-freedom solver promises to be an accurate industry standard prediction of the quasi-static motions of the damaged ship in calm water and an estimation of the time-to-flood (TTF). TTF characterises the period between the start of the flooding until a steady- state condition is reached. Depending upon the final flooding state of the ship the term time-to-capsize or time-to-sink could also be introduced. Moreover, the simulation will give an estimation of the available time for orderly evacuation and abandonment, where there is a risk that the ship will capsize or sink.

The main focus of the simulation is progressive flooding which means that floodwater in a ship can progress in compartments through internal openings such as windows, doors, staircases and pipes. Usually the structure of ship decks is very complex and can involve many rooms and compartments that are connected through various openings. In this study the walls of compartments and rooms are considered to be watertight and non-permeable which has no influence on the feasibility and accuracy of the calculations as real incidents showed.

The CFD studies mostly concentrate on the time it needed to fill a compartment with floodwater with subject to various boundary conditions. Further investigations show the impact of floodwater on the ship motion by deriving forces on walls,

water pressure and velocities on damage openings, windows, doors and air vents. Additionally, the influence of trapped air which can delay the equalised flooding to the undamaged side is taken into account by considering air as a compressible ideal gas.

The IMO Resolution A.266 (VIII) *(1973)* describes a simplified approach for addressing the equalisation time in typical cross-flooding arrangements which cannot be applied to complex flooding cases and cases with trapped air causing counter pressure.

Traditional CFD set-ups can only be used for simplified geometries with limited size. As a result a different approach has been applied, which reduces the amount of cells and computing time drastically. With the regained resources it is possible to get more accurate simulation results for large and complex geometries. The method is expandable with user defined functions that can include a pre-described motion or manipulate physical properties as pressure, density, etc. Another advantage is the use of different kind of turbulence models dependent on the expected floodwater flow speed. Moreover, ship motion in CFD models is usually not regarded because of limited computation power. For that reason an optimised six degree-of-freedom solver is integrated which simulates the quasi-static ship motion in calm water by remeshing the grid every few time steps.

In additional case studies the water inflow through various opening shapes is observed. As numerical studies are usually calculated in full scale and then validated by model tests it is of interest if different scales of the numerical model could influence the calculated results. Therefore scale effects will be evaluated in a few simple case studies.

Present method has to be understood as a tool for the analysis of the flooding process. It is capable of giving local flow characteristics and detailed information of any physical data as pressure, flow velocity, forces induced by flood water, etc. in complex systems at any location in the damaged ship hull which is the main advantage compared to other numerical simulation methods. Due to its still long

computation time this tool is not applicable for decision support systems, where results have to be available in a very short time. A possible field of application for present tool is to be an alternative for model tests which are only capable of collecting a limited number of data in certain ideal metrological locations. Furthermore, this CFD simulation method could be used as validation tool for other numerical simulation methods.

Deriving from the above stated the review of the relevant literature available is carried out in the following section.

3 A Review of Simulation Methods – Looking Back

3.1 General Remarks

The sinking of the ferry "M/V Estonia" in 1994 with 852 human live losses has been again inspiration for putting effort into research of water on vehicle decks and flooding of ships in general. Computer simulations as research tool should provide a variety of data and results which should give deeper insights into the process of flooding and ship behaviour due to flooding that cannot be captured by doing model tests or full scale experiments. In the following paragraphs a critical review of the relevant research and developed work in the subject of intact and damage stability and survivability with a special focus on water in-/egress and its impact on a progressively flooded vessel is presented spanning approximately the last twenty five years, significantly the last five to ten years where more stable and accurate solutions for the calculation of flows around a ship hull could be achieved. Moreover, advantages and drawbacks of the following approaches are epitomised which in succession will smooth the way to further research in the fields of damage stability respectively water in-/egress and progressive flooding.

It is very essential to model the interaction between the fluid and the submerged rigid hull as there are high forces and moments acting upon the ship which influence the ship's manoeuvrability both intact and damaged. In recently found scientific literature plenty of applications and approaches are dealing with the subject sea keeping theory which is making the choice of the method difficult because prediction accuracy and modelling complexity differ in a wide variability.

Söding (2002) believes that nearly all flow problems of interest in ship safety considerations can be solved with existing fluid dynamical methods. For that reason special interest is addressed to widely used state-of-the-art technologies as time domain simulations and especially CFD methods in the following sections (chapters 3.2 and 3.3). Additionally, model tests (chapter 3.4) are mentioned that reflect full scale incidents in the most realistic and immediately observable way as possible

direction for validation of the simulation results. A short excursus about technologies used in CFD with a focus on dynamic meshes can be found in chapter 3.5.

3.2 Numerical Flooding Simulation

Recently more effort is taken in using explicit time domain simulations as they promise a wide field of application regarding the mathematical description of fluid motions interacting with intact or damaged ship hulls. Some recent approaches are going to be described on the following pages. Hereby it is noticeable that consistently a research scheme (Figure 4) is used in order to ensure the feasibility and accuracy of the adopted method.

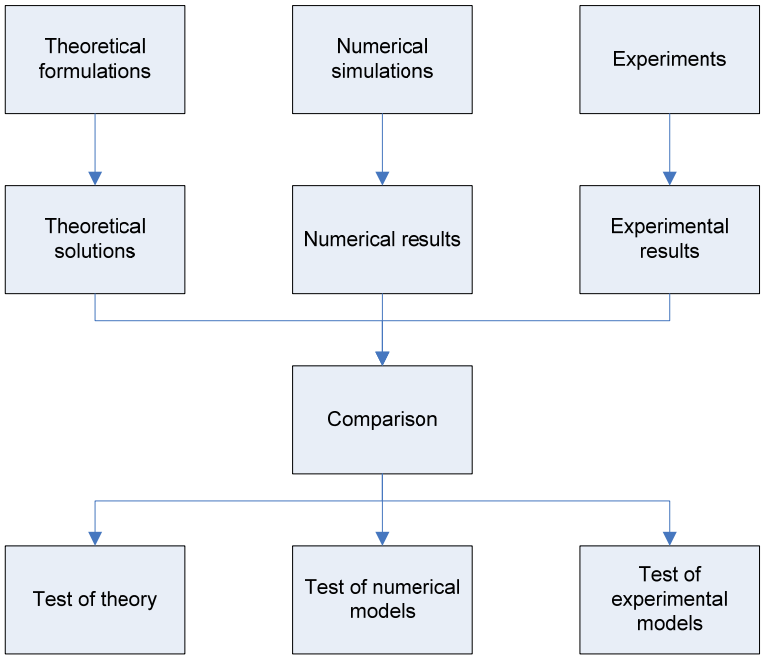

Figure 4: Connection between the numerical simulations, theories and experiments

Letizia (1996) tried to find a totally comprehensive approach by combining and considering every possible terms that could characterise the behaviour of a damaged passenger ship hull. The model introduced was the first known attempt to take into account all 6-DOF ship motions, whilst in damage state. The flooding

mechanism was simulated using a semi-empirical approach. Floodwater was treated as rigid body assuming that the floodwater free surface is flat while the motion was represented as a free mass moving on a prescribed trajectory. The innovation of this research was to account for non-linearities due to hull asymmetries arising from progressive flooding and asymmetric floodwater distribution. This has been solved by a database approach, whereby a set of hydrodynamic forces and coefficients are pre-calculated from linear potential flow theory and the corresponding values are instantaneously interpolated from the storage.

Based on *Letizia's* achievements *Jasionowski (2001)* presented some research work on ship stability of damaged ships and the means for assessing dynamic ship performance in this state. A numerical simulation tool PROTEUS3 has been developed which includes the ensuing effects of floodwater and progressive flooding on the ship. The linear concepts regarding the ship hydrodynamics are based on the strip theory and Rankine source method (RSM).

Non-linear excitation/restoring forces were calculated from pressure integration up to the instantaneous undisturbed wave profile. Non-linearities in hydrodynamic properties arising from variation of mean underwater geometry due to occurrence of non-stationary asymmetries in mass distribution are taken into account by a database approach. Thought has been given to forward speed in arbitrary heading as well as progressive flooding through a ship with any internal subdivision and floodwater motion simulations based on free-mass-on-potential-surface (FMPS) model is considered. Non-linear treatment of the effects of cargo shift or floodwater motions on the overall ship dynamic behaviour could be implemented to the software PROTEUS3. The validity of this model has been tested through comparison with available physical model tests data.

Papanikolaou et al. (2000) presented a non-linear 3D six degrees-of-freedom time domain simulation code, called CAPSIM, on the basis of linear potential theory considering non-linear effects like excitation by large amplitude regular or irregular waves, non-linear body effects, like the effects of the above calm waterline body

shape and its impact on the ship's restoring, as well as possible sloshing effects due to internal to the vessel or trapped on deck moving fluids.

A very recent method was presented by *Ruponen (2007)* who introduced a pressure-correction technique in a time-domain simulation which calculates the flow velocities using Bernoulli's equations as widely applied in hydraulic models. The method is modified in order to handle free surfaces in case of progressive flooding. Ideal gas is assumed to model air compression due to progressive flooding. Though satisfying results could be gained for some cases the model is simplified in the way that it does not take the inertia of floodwater into account and though generally the numerical model accounts for air compressibility it is ignored in compartments where it is not practical to model the whole ventilation system accurately enough. That might influence the reliability of the results when data is entered inconsiderately.

In *Papanikolaou (2007)* and relevant reports of the ITTC Specialists Committee in Stability in Waves a thorough review of methods and concentrated benchmark is presented.

3.3 Flooding Simulation with CFD

Computational Fluid Dynamics (CFD) can be counted to the group of time domain simulations; nevertheless, the author took the liberty to dedicate a self-contained chapter to CFD in order to explain the interrelations between the different methods and technologies used.

Numerical domains in flooding simulations usually consist of a minimum of two fluid phases: water and air. In very rare situations also three or more phases can be taken into account e.g. for flooding incidents with oil tankers or LNG carriers. However, it is always challenging to deal with multi-phase fluid systems because the free surface flow is highly non-linear and neither the shape nor the position of the interface between two phases is known a priori. Basically, there are two approaches

to compute flows with free surface: interface-tracking and interface-capturing methods. The interface-tracking method represents the free surface and tracks it by either marking it with special marker points, or by attaching it to a mesh surface. For that reason a numerical grid has to be used that adapts itself to the shape and position of the free surface. On the contrary, the interface-capturing method both phases are treated as single effective fluid with variable properties. The interface is captured as a region of sudden change in the fluid properties. One of the widely used interface-capturing methods in CFD is the volume of fluid (VOF) method introduced by *Hirt and Nichols (1981)* which will be referred to in the following paragraphs.

Ship motion is considered in some of the following simulation methods. A practical way and state-of-the-art method is the use of six degrees-of-freedom solvers which are coupled with or integrated in the CFD solvers. Only a few of the methods are touched in this chapter and will be explained in detail in chapter 6.5.

van't Veer and de Kat (2000) applied the volume of fluid method (VOF) for the simulation of progressive flooding in an engine room. Results were compared to model tests and the results of calculations based on Bernoulli's equations. Though the correlation between the calculated and measured water heights was good it was agreed that the grid generation and the calculation were too slow for efficient simulations.

A VOF function *F* is introduced with values between zero and one, indicating the fractional volume of a cell that is filled with a certain fluid. The evolution of the VOF function is given by $DF/Dt = 0$. In the original VOF method with a constant piecewise stair-wise reconstruction of the interface the problem of "flotsam" and "jetsam" (small droplets disconnecting from the surface) can occur. These droplets and small air-pockets (wisps) are more likely to be present in lower order methods and originate in the calculation of the fluxes. Mostly it results in the loss or gain of liquid due to rounding the VOF function when $F<0$ or $F>1$ where *F* is the volume fraction function, see chapter 6.2.2 for details. As a result *Kleefsman et al. (2005)* adapted

the VOF method with a local height function to overcome the problems described above.

Also *Löhner et al. (2006)* created a VOF technique considering only the liquid phase in a two phase (liquid-gas) system. The VOF technique is coupled it with an incompressible Euler/Navier-Stokes solver and operated on unstructured grids to simulate the interactions of extreme waves and three-dimensional structures. Extrapolation algorithms have been implemented which obtain velocities and pressures in the gas region of the two phase system. At present – by best knowledge of the author – the method lacks the proper treatment of free surface wall boundary conditions for RANSE cases. Another important point is that incoming and outgoing waves for 3D VOF-based free surface flows cannot be handled and that free surface tension is neglected.

In the past the effect of floodwater was either based on empirical data from model test or the free surfaces of the floodwater was assumed horizontal. Therefore *Woodburn et al. (2002)* coupled a six degrees-of-freedom (6-DOF) solver with a moving grid CFD model in order to predict motions of a damaged Ro-Ro vessel due to flooding in a fundamental way. The ship dynamics program calculates the position of the vessel under the action of forces of the waves on the outside of the hull and the floodwater inside the hull, and also calculates the height of the water surface at the damage, see Figure 6. The position of the vessel and the height of the water surface at the damage are passed to the CFD program. The computational grid used in the CFD program adapts to the vessel motions, see Figure 5. The dynamics of the floodwater and the loads on the vessel due to floodwater are calculated and passed back to the ship dynamics model. Both programs run alternately, waiting between run periods for the other program to complete its calculation at each time step.

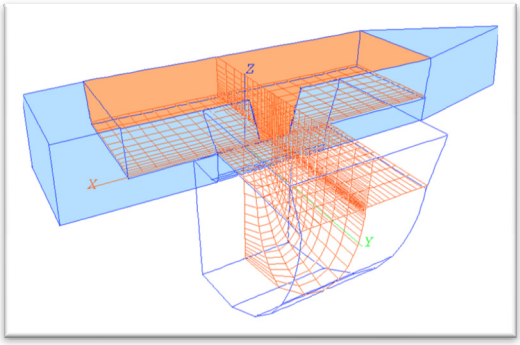

Figure 5: Domain and grid used in CFD calculation, *Woodburn et al. (2002)*

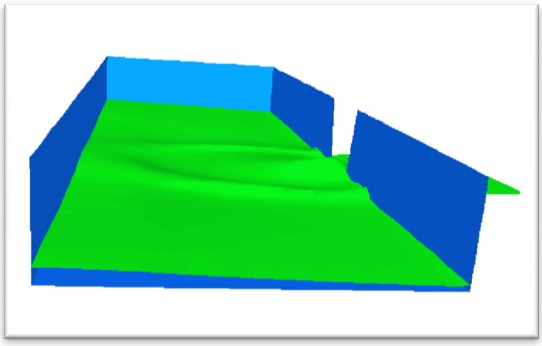

Figure 6: Floodwater in compartment and external water surface, *Woodburn et al. (2002)*

Cho et al. (2005) investigated the dynamic characteristics of flooding water of a damaged compartment of an ITTC RORO passenger vessel. In this work it was tried to show the coupled dynamics of flooding water by the means of CFD (FLOW3D, commercial code which is based on FDM (Finite Difference Method), FVM (Finite Volume Method) and VOF (Volume of Fluid)). Experimental model tests were the basis to fortify the results of the numerical results of the CFD calculations. Two different kinds of simple models (Figure 7 and Figure 8) which were already used for the 24th ITTC Benchmark Study (Figure 9) *(ITTC (2005))* were equipped with various geometrically shaped damage openings in order to investigate the effect of the inner compartments. The CFD simulation (Figure 10) agreed well with the model test especially the computation of the flow rate and the forces where compressibility of air and viscosity has to be taken into consideration. The moments which are influenced by the flooding water distribution and determined by the area of inlet under free surface as well as the internal structures of damaged parts and the inlet conditions only showed a trend towards the experiments.

Figure 7: Simple model of a compartment, *Cho et al. (2005)*

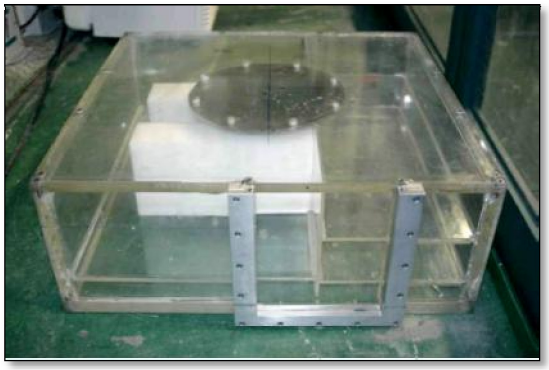

Figure 8: Engine room of 24th ITTC benchmark model, *Cho et al. (2005)*

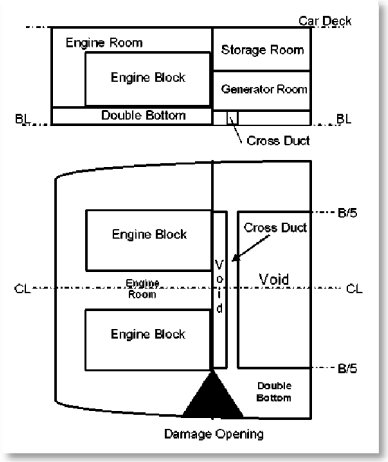

Figure 9: Engine room of 24th ITTC benchmark model with damage opening, *Cho et al. (2005)*

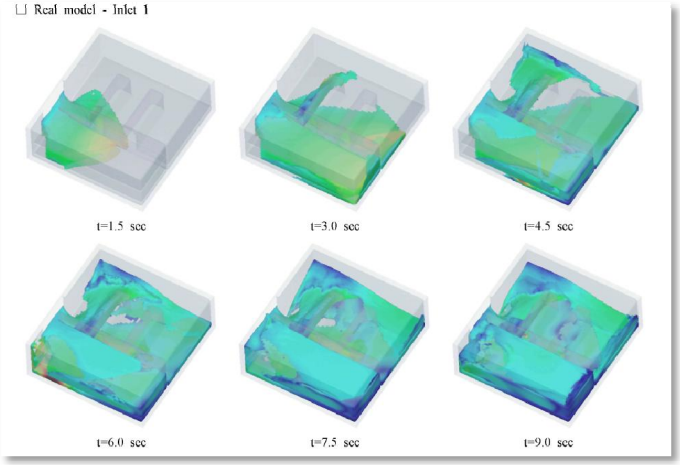

Figure 10: Simulation results of the real case, *Cho et al. (2005)*

Gao et al. (2005) distinguished between two phases during the flooding process: in the first phase water flows very fast into the empty compartment as there is obtained a large hydrostatic pressure gradient; in the second phase a quasi-stationary state predominates when the water in the compartment reaches the same level as the external water. Since the first phase cannot be prevented and lasts till the compartment is filled up to the edge of the damage opening the second phase is even more important because there is enough time to do something corresponding to limitation of damage. This second phase allows the water to flow in and out of the compartment which finally interacts with the ship motion and the motion of the external water. But not only ship motions affect the water motion in

the compartment also the motion of water – sloshing - in the compartment affects the ship motion especially when resonance occurs. A detailed description of the flooding mechanism is also given in chapter 5.1. The damaged ship hydrodynamic was calculated with a RANSE CFD code coupled with time-domain motion software. It was discovered that in case of low frequent heaving the force from CFD calculation in the compartment was 80 % of total force and 20 % from external potential results while at high frequent heaving the potential external force was about 83 % and the force from CFD calculation was about 27 %.

Pittaluga and Giannini (2006) computed pressure losses in cross-flooding tunnels with CFD and derived regression equations for the estimate effective discharge coefficients. This study gives valuable information about pressure losses in various openings but unfortunately, there exists no validation which could give indication about the accuracy.

Nabavi et al. (2006) investigated the effect of specific geometric parameters on the discharge rate of various ship openings with the commercial CFD solver FLUENT. Moreover, the influence on the discharge rate due to the vessel's beam and the depth of the water collected on deck has been studied. The effect of each parameter was analysed by varying the parameter of interest while the other parameters were kept constant. Froude number and non-dimensional discharge time were calculated using the instantaneous water depth, the water discharge rate, and the opening area as a part of the non-dimensional simulation. The results were compared to the experimental results that were obtained previously at UBC.

The sloshing behaviour inside tanks with and without baffles was investigated by *AkyildIz and Erdem Ünal (2006)*. When the frequency of the tank motion is close to the natural frequencies of the tank fluid, large sloshing amplitudes can be expected. In order to avoid moving boundary conditions at the fluid tank interface and to include non-linear motion of the free surface a moving coordinate system is used in addition to the Navier-Stokes equation with free boundary according to the SOLAS scheme. As a result two types of dynamic pressure can be identified for sloshing

liquids: impulsive and non-impulsive pressures. Impulsive pressures are rapid pressure pulses due to the impact between the liquid and the solid surface while non-impulsive pressures are the pressures in an oscillating fluid. The existence of baffles could significantly reduce the fluid motion and the pressure response. Increased amplitude of excitation entails in violently responding liquids like the occurrence of turbulence, wave breaking, hydraulic jump and three-dimensional effects.

Another sway-induced sloshing study comparing homogeneous and inhomogeneous multiphase approach for fluid density and viscosity in a commercial CFD code was done by *Godderidge et al. (2008)*. The computationally cheaper homogeneous and inhomogeneous multiphase models are put side by side for a dimensional analysis of the relative motion between the phases. The homogeneous model tends to underestimate the experimental peak pressure by up to 50% whilst the inhomogeneous model shows a good agreement and seems to be most appropriate to use for violent sloshing over a longer period. For initial CFD analysis of sloshing the use of the homogeneous approach is still recommended.

Chen and Yu (2008) solve the Navier-Stokes equations for multiphase flows in a moving curvilinear coordinate system and discretised with the finite-analytic method on a non-staggered multi-block grid system. To account for the effects of turbulence the large eddy simulations (LES) approach is used together with the Smagorinsky model. The interface was captured by the level-set method. This method can be applied to various fields like dam-breaking, greenwater on deck or wet deck slamming. In all the tested cases a good resolution of the phase interactions could be observed.

Another possibility to simulate the water flow around and in a damaged ship hull could be Smoothed Particle Hydrodynamics (SPH) which is based on a representation of the fluid body by large parcels of water that are subject to Newton's Second Law. This technique was originally developed by *Gingold and Monaghan (1977)*. An advantage is that the geometry as a basis is mesh-free and

not dependent on complicated fixed computational grids and instead of that estimates of derivates are provided by analytical expressions. Further benefit addresses SPH as a future technique to model flows with its capability to deal with free surface problems, moving interfaces and large deformations. A drawback of SPH is its inherent difficulty when modelling boundaries which is important for the ability to account correctly the interaction between a boundary and the flow of nearby particles in order to predict the thin boundary layer around a ship.

Sueyoshi and Naito (2002) are regarded as pioneers in using SPH, particularly MPS (Moving Particle Semi-implicit) for flooding calculations on floating bodies. The MPS method recommended by *Koshizuka and Oka (1996)* is one of the particle methods for incompressible flow. In the research of *Sueyoshi and Naito (2002)* viscous effects are neglected. Advantage of their method is that the diffusion model only requires the relative position of the particles so that a numerical break down does not happen in the spatial discrete model. Moreover, all materials can be expressed by particles meaning that any boundary, free surface, moving wall and floating body are described by fixed or moving particles. The velocity-pressure coupling is solved by the MAC (marker and cell) method. The equations of the ship motions are solved explicitly and forces acting on surface points of the body are integrated directly. Several validation studies of the code were performed: on one hand the roll motion of an intact vessel on the other hand the roll motions of a damaged vessel with floodwater in the hull and water on deck have been investigated.

The dynamic behaviour of a damaged Ro-Ro vessel with a flooded vehicle deck and forced sinusoidal roll motion were carried out by *González et al. (2003).*

Souto Iglesias et al. (2004) have applied the SPH method for sloshing in rectangular tanks with baffles and improved the results later, *Souto-Iglesias et al. (2006)*, by obtaining accurate values for the moment amplitudes. Apparently this sloshing case could also be treated as progressive flooding through compartments with large free surface. The numerical results agreed quite well with the experimental results though work has to be done on obtaining the right pressure on the wall boundaries.

Skaar and Vassalos (2006) used the SPH method for progressive flooding of a Ro-Ro vessel under forced heave and roll motions. A large number of particles are used and the modelling of solid walls and boundaries of the computational domain with seaway is still considered to be problematic.

Incompressible flows with free surface are investigated by *Ataie-Ashtiani et al. (2007)* with a modified formulation of an I-SPH method. The governing equations of mass and momentum conservation are solved in a Langrangian form using a two-step fractional method. Firstly the velocity field is computed without enforcing incompressibility and secondly a Poisson equation of pressure is used to satisfy the incompressibility condition. The introduction of a new source term for the Poisson equation is proposed and also an innovative modified Poisson equation of pressure is developed which improves the stability and accuracy of the SPH method considerably.

3.4 Flooding Simulation by Model Testing

Model tests are used for the validation of numerical simulations and should always been carried out in parallel for verification of the results of a method. A major advantage of model tests is that they are quickly repeatable and that models can be adapted to a great extent to the requirements of a numerical simulation. Ship models underlie the same physical principals, which have been used for testing for the last two centuries, as full-scale ships and are therefore highly reliable and accurate especially with regard to propulsion whereas the modelling of flooding processes is a little less accurate. On the other hand the manufacture of a model can be very expensive and cost a few man-hours. The next paragraphs cover some examples of past and recently carried out model tests and explain which problems are met when modelling in small scale.

The modelling of the flooding process remains a critical issue, as pointed out by *Vassalos and Turan (1994)* and *Vassalos et al. (1997).* Among other issues to be

reconsidered both experimentally and theoretically are the possible shapes of the damage opening. The values of semi-empirical coefficients *K* used in mathematical models were reconfirmed to be about 1.1 for unidirectional and 0.7 for bidirectional flows, respectively.

In the recent past a large number of model tests have been performed worldwide. *Safety at Sea* carried out some model tests with a passenger cruise vessel which was meant to represent most of the large modern vessels nowadays. The tests implied both intact and damaged conditions of the ship and were completed in regular and irregular sea state at different angles of attack. The fibreglass model was completely arranged with an acryl glass deck structure and equipped with water elevation probes and permeability blocks. Furthermore three different sizes of damaged openings could be attached. The reason to carry out the test was on one hand the validation of the probabilistic assessment to the newly introduced regulations of IMO (SOLAS 2009) and on the other hand the survivability assessment based on numerical simulations (PROTEUS3). IMO specifies the value *s* as parameter for the survivability of a ship.

$$s_{final,i} = K \cdot \left[\frac{GZ_{\max}}{0.12} \cdot \frac{Range}{16} \right]^{\frac{1}{4}} \tag{3.5.1}$$

As demonstrated in this study the *s* factor has to be evaluated more accurately and the above does not express the average resistance of such a ship to capsize/survive. This inadequacy is based on a phenomenon called multi-free surface (MFS) effect, which makes quantifying ship stability and survivability in waves by traditional methods extremely inaccurate. A future task should be to possibly better correlate the s factor with ship design parameters which allow more reliable predictions of the survivability of a ship.

This phenomenon was also discovered by *Vassalos et al. (2005)* who distinguished between a prescriptive and a more desirable goal-based approach.

Ro-Ro models have been tested by *Korkut et al. (2004)* in regular waves in intact and damaged conditions. The stationary model was exposed to different wave heights and frequencies for head, beam and stern quartering seas. The motion responses of the ship model have been observed by varying the wave heights and the damage mode. Similar tests have also been carried out by *Korkut et al. (2005)* for the investigation of the global load. In both cases the analysis of the results showed that the damage has a disadvantageous effect on the structural loading responses of the model depending on the direction of attack of the waves and the frequency range applied.

Katayama and Ikeda (2005) analysed the characteristics of inflow velocity from damaged openings by carrying out simple model tests with two geometric similar models only different in scale. It was found that:

- the discharge from the opening is constant if the inside water surface is lower than the lower edge of the opening
- the coefficient of discharge is of higher constant value if the inside water surface is over the lower edge of the opening
- the coefficient of discharge is affected by air compression in the water tight compartment

As part of the European project "The Research Study of the Sinking Sequence of M/V Estonia" MARIN*, Blok and Luisman (2008),* carried out flooding model tests with an acryl model of deck 4 in model scale λ=20. Every bulkhead and opening on deck is modelled and each compartment is equipped with an air duct in order to avoid trapped air and be able to fully fill the deck with floodwater. In some large compartments the water height is measured by wave probes and forces produced by incoming floodwater are recorded with a six-component force transducer which is attached to the bottom of the deck. The flow force is measured behind the damage opening and some doors of the bulkheads and should give an indication

about the flow velocity. Though the measurements were done with great care some of the values, especially the flow velocities, have to be treated with prudence.

The prediction of motion of a damaged ship in waves is necessary to prevent from foundering and structural failure. A theoretical and experimental study on the behaviour of damaged ships in waves has been carried out by *Lee et al. (2007)*. Achievements were the implementation of a time domain model that can be applied to any type of ship and arrangement. In addition to the prediction of the damaged ship motion the effects of flooding of the compartments were taken into consideration. For the validation model tests were carried out for three different damaged conditions: engine room bottom damage, side shell damage and bow visor damage of a Ro-Ro ship in regular and irregular waves with different wave heights and directions. A qualitative agreement between theoretical and experimental results could be found, however, the quantitative agreement was not corresponding due to experimental inaccuracies such as scaling of the water ingress and the associated viscous effects. Moreover, the theoretical model was limited by the incomplete calibration of the water ingress phenomenon.

3.5 CFD Related Methods

As previously mentioned in chapter 1.1, the development of complex simulation tools features an interdisciplinary character. For that reason also other areas connected to CFD and flooding have to be investigated.

When ship motion is considered in a holistic CFD approach attention has to be directed to moving and deforming meshes and mesh adaption in general. In the past the computational effort could not be satisfied but the methods became mature and computing power increased which makes it an alternative to conventionally used coupled methods.

A novel dynamic mesh approach was adopted capable of dealing even with large deformation of the flow fields. In the described study *Zhao and Forhad (2003)*

developed a high-order finite volume Navier-Stokes solver on unstructured dynamic grids to calculate unsteady incompressible flows with moving boundaries using an implicit dual time stepping scheme and the arbitrary Lagrangian Eulerian (ALE) approach. This method has been used to study fluid-structure interaction in a channel with a membrane and could possibly be used for wave generation in a numerical tank.

Liao and Xue (2006) describe a method for the generation of moving meshes and its application in CFD. It is based on controlling the Jacobian determinant directly and precisely. The Jacobian determinant of the transformation generated by the deformation method is equal to any normalised positive function *f(x,y,z,t)* prescribed by the user. To prevent element inversion which is a fundamental problem in moving mesh methods the elements have to be of sufficiently small size and the continuum transformation has to be injective.

A very complex geometry sometimes results in a poor mesh quality which can lead to convergence problems due to highly skewed cells. *McBride et al. (2008)* developed a flow solver strategy which is much more tolerant dealing with poor mesh quality. A combined vertex-based-cell-centre technique solves the flow field at the cell or vertex element and all other variables are solved at the cell centre as in conventional CFD tools. The computational requirements are four times higher than for conventional methods in 3D CFD which makes this method only worth to use in cases where it is hard to achieve a good mesh quality.

Deformable surfaces through dynamic meshes become more and more popular in CFD. A good quality dynamic mesh requires an adaptation process to be consistent during the deformation. *de Goes et al. (2008)* combine normal and tangential geometric corrections with refinement and simplification resolution control. It is about a two step adaption scheme defined by structural and geometrical operations. The geometric error is measured by a stochastic sampling approach.

In a similar manner *Acikgoz and Bottasso (2007)* presented a unified formulation of simplicial and non-simplicial, structured and unstructured for two and three

dimensional meshes. The generation of invalid elements which are created by the same collapse mechanism is avoided by connecting with a spring each vertex in the grid with its normal projection on the ball boundaries. It must be pointed out that present ball-vertex method can also deal with very large amplitude deformations which are usually a problem for the conventional edge-spring method.

3.6 Key Findings

Following areas have been identified as the main focus of research in mathematical modelling of the behaviour of a damaged vessel:

Damaged Vessel Dynamics: A non-linear six degrees-of-freedom model that allows the vessel to drift as well as allows for changes with time in its mass, centre of mass, mean attitude, environmental excitation and hydrodynamic reaction forces.

Water ingress/egress: An adequately accurate water ingress/egress model that allows for multiple-compartment flooding in the presence of oscillatory flows and at times of shear flows in extreme wave conditions is a prerequisite to undertaking any investigations on damage survivability.

Floodwater/Vessel Interaction: A study of damage survivability involves two distinct but intrinsically interrelated and highly interacting processes, namely ship motion and flooding. The vessel motion influences considerably the flooding process and conversely, flooding affects both the vessel's motion and its attitude. The non-stationarity in the vessel motion introduced by the water accumulation coupled with the intermittence of the flooding process itself and the severe non-linearities in the ensuing dynamic system demand great care in dealing with the many issues of this complex problem.

As investigated by reviewing recent literature the flooding mechanism was treated with reserve because of its complexity while the characterisation of the ship motion and wave excitation already reached a high level of simulation. In the last few years scientists and researchers concentrated more on floodwater simulation, especially

in the field of CFD calculation which is the state-of-the-art tool for this kind of calculations. However, so far there is no holistic approach which takes all facets of damage stability into consideration. Especially six degrees-of-freedom approaches to take the ship motion into account were treated stepmotherly and no references could be found about the use of dynamic mesh applications in relation with flooding simulations. So far all methods compromise in the coupling of different kind of approaches and sometimes introduce very simplifying assumptions. It is the author's believe that only very detailed numerical solutions for damage stability problems will make it possible to simplify simulations for specific fields of applications by the use of the right assumptions. Unfortunately these simplifications strongly rely on the actual computational power which will possibly increase in future and render improvement in the accuracy and feasibility of calculations.

4 Approach Adopted – Going Further

4.1 General Remarks

Current ship dynamics with regard to flooding still make two assumptions. Firstly, the rate of inflow has a simple relationship to the hydraulic head driving the flow, and the transient dynamics on the flood are ignored. Secondly, there are a few different approaches how to deal with the floodwater and its distribution on deck. The floodwater within the vessel is either assumed to be hydrostatic, so that any free surface is always plane and horizontal. A more advanced approach considers the relative motion between the floodwater and the ship and the resulting dynamic interaction by the lumped mass concept. The floodwater, oscillating as a separate dynamic system, keeps its free surface plane but it can obtain any inclination as the result of dynamic interaction between floodwater and ship, *Papanikolaou and Spanos (2002b)*. Another approach also considers the wavy character of the floodwater by implementing a shallow water wave modelling, *Papanikolaou (2007)*. According to Glimm, the application of a random choice or fractional step method could solve the shallow water wave equations and couple their solution with a time domain solution for the ship motion, *Santos and Soares (2006)*. Especially, when the vessel undergoes large amplitudes of motion a way to include the dynamics of floodwater on a ship's deck explicitly is to model it in a full 3D flooding simulation which should involve both, transient and progressive flooding. The justification for coupling a CFD of the floodwater dynamics to a ship dynamics model is to provide a tool capable of answering this question. Further, since the floodwater is modelled on a more fundamental level than the empirically based hydraulic flooding models, the underlying dynamics of the transient and, especially, progressive flooding process could also be examined. These results in turn could be fed back to simpler methods which would then better reflect the underlying physics. The level at which CFD could be used to investigate this problem is determined by the available computing power which precludes the simulation of the whole vessel and surrounding sea in a CFD simulation with a 6-DOF solver handling the ship motion.

However, an intermediate step would be to simulate the deck and compartments open to the water together with an area of sea outside the damage using CFD, and to feed the forces generated by the floodwater into a ship dynamics model. This approach definitely is a step back and might give results for the moment but is – in the author's opinion – not sustainable. There are many different technologies available like dynamic meshing which can be used for an adoption of a 6-DOF solver. The advantage is that it is a totally integrated solution, only one single geometry is used which cancels out possible design discrepancies or mistakes, and that data exchange is eliminated which reduce the read/write operations usually considered as being the bottle neck for such calculations.

4.2 Framework of Approach

The framework of the approach is subdivided into four main phases.

- Grid development for stationary and dynamic cases with the grid generator GAMBIT.
- Performing CFD simulations with the commercial CFD solver FLUENT which include numerical methods like discretization methods, pressure-velocity coupling, VOF, turbulence models, 6-DOF solver
- Data processing and analysis
- Validation of the tool with experimental data

In the initial phase a mesh of the investigated geometry is created according to the requirements of the physics and selected methods of the numerical simulation. An appropriate balance between sufficiently high calculation accuracy and computational effort that is spent in terms of time has to be found to estimate the number of cells used for the geometry.

In the second phase the CFD solver will be set up and the boundary conditions will be defined. Main effort will be put into the research of progressive flooding and finally into the influence of trapped air and airflow in damaged Ro-Ro vessels.

Different turbulence models will be used depending on the expected floodwater velocity. A 6-DOF solver will take care of the time-dependent damage ship position in calm water caused by the moving floodwater in the ship; anyway, simplifications will be presumed like disregard of dynamic ship motion excited by seaway because there are many suitable model tests available for validation in calm water. For ship motions in waves there is hardly any validation data available. Due to a lack of computation power only by floodwater affected areas of the ship will be modelled and in cases where ship motion is regarded the fully submerged ship hull will be modelled whilst the mesh density is kept to a medium level.

The third phase will be dominated by data extraction and processing. Firstly data has to be extracted from the various different files. In the next step the same data has to be smoothed and filtered with regression analysis and the use of the Epanechnikov kernel which - simply speaking – is a numerical form of a low pass filter.

In the final fourth phase previously prepared data will be compared with experimental data from model tests, *2007 Blok and Luisman (2008)*. A detailed model of a deck of a Ro-Ro ship will be used in order to get true-to-life parameters for a suitable comparison. This newly developed approach will also be compared in a case study with results from a research study from *Ruponen (2006)*. Especially *Ruponen's* method together with the results of the model tests carried out in the model tank of HUT Ship Laboratory should give a good indication as a benchmark for the CFD simulation. In case the data do not agree well modifications have to be done either in phase one or in phase two or in both.

5 Physical Background

5.1 Flooding Mechanism

5.1.1 General Remarks

This section explains the basics and physics of the complex process of flooding and discusses its importance and modelling possibilities.

Generally the flooding process can be divided into three main phases, *IMO SLF46/INF.3 (2003)*. After a damage incident there is a phase of transient flooding (Figure 11) where water rushes through the damage opening. A phase of progressive flooding follows as the water floods to undamaged compartments through internal openings. In case the ship does not capsize or sink during these phases, a final steady state is eventually achieved. This thesis mainly concentrates on both the phase of transient flooding and the phase of progressive flooding.

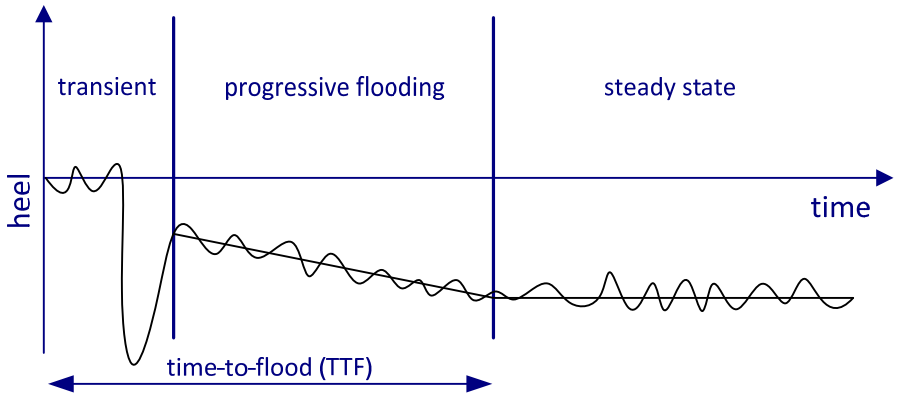

Figure 11: Phases of the flooding process

5.1.2 Transient Flooding

Transient flooding can be defined as a phenomenon occurring in the time period required for the damage compartment to become fully flooded in case of a damage opening, starting from the intact condition, *Papanikolaou and Spanos (2002b)*. After

water has flushed into the ship through the damage opening, depending on the size and location of the damage opening, the floodwater can cause a large intermediate transient heeling angle which forces the ship to heel rapidly to the damaged side. Due to a very sudden loading and free water surface on multiple decks it is possible that the ship capsizes before it reaches a static equilibrium which results in very short time-to-capsize. In case of small damage openings or bottom damage the transient phase plays a minor part as the heeling angle will increase slowly. Also, the flooding of symmetrical compartments can be a transient phenomenon when the distribution of the floodwater is delayed due to the geometrical structure of the compartments. Dynamic phenomena as waves of floodwater increase the moments acting on the damaged ship. The magnitude of the ship's heel motion depends on the amount of floodwater, the ship's inertia and hydrostatics characteristics. Energy dissipation components can act as damping forces on the ship like bilge keels, stabilizers, rudders, or cross-flooding ducts routing the floodwater to the undamaged side of the ship. On one hand the maximum heeling angle depends on the strong non-linear character of the ship hydrostatics at the intermediate stages of flooding on the other hand heeling angles resulting from a hydrostatic analysis are generally amplified which as fact should be considered.

In numerical studies several unknown factors as time of the creation of the damage, forces from the ship and penetration of the damage are usually ignored.

5.1.3 Progressive Flooding

The phase of transient flooding fades to progressive flooding, when the process becomes more quasi-stationary, and can take from a couple of minutes up to several hours depending on the damage case, the internal structure and other possible influences.

The water level in the flooded compartments rises steadily and progressive flooding to other compartments may take place if there are open connections to the flooded compartments. Furthermore, the pressure of the floodwater may cause leaking

through closed doors or permeable non-watertight walls and can even lead to collapsing of internal structures. Especially collapsing structures can have a significant influence on the roll motion of the ship and can lead to a reduction of the time-to-flood or even cause capsizes.

As additional free surfaces always have a negative effect on the ship stability, down-flooding is allowed in order to lower the centre of gravity which increases the stability of the damaged ship. Similarly, asymmetric flooding is compensated by allowing flooding through cross-ducts and other passive counter flooding routes to decrease the heeling angle.

A steady state is reached when the ship does not capsize or sink. The total elapsed time for the phases of transient flooding and progressive flooding is often referred to as time-to-flood (TTF). It is practical to define further criteria since very large heeling angles can be encountered during the intermediate stages of flooding. SOLAS gives the limit of a maximum heeling angle of 20° for evacuation and abandonment. Thus, time for evacuation is often referred to as TTF.

5.1.4 Air Compression

When a compartment is flooded and air cannot escape the air will be compressed as a result of incoming water until the pressure in the air pocket is equal to the effective total pressure on the other side of the opening. This can have significant effects on the flooding process. Such trapped air can delay the flooding process sustainably. Usually trapped air can be found when the water level in a compartment has raised above all openings and pipe inlets. The pressure in the air pocket can still rise as the external hydrostatic pressure increases due to an increasing draft. A flow is likely to be impossible when following condition is fulfilled:

$$p_i \geq p_j + \rho_w g\left(H_{w,j} - H_{o,k}\right) \tag{5.1.1}$$

where the indices *i* and *j* indicate the compartments, *p* is the air pressure, ρ_w is the density of water, *H* is the water height and *k* indicates the opening.

As a result the air pocket will prevent further flooding (Figure 12). In reality a quasi-stationary status can never be reached as also model tests showed, *Ruponen (2006)*. Air escapes from the air pockets in the form of a bubble flow. Compared to full scale incidents air pockets are larger in model scale due to scaling effects and so is the error. For a better comparison CFD calculations with the box-shaped barge were carried out in model scale.

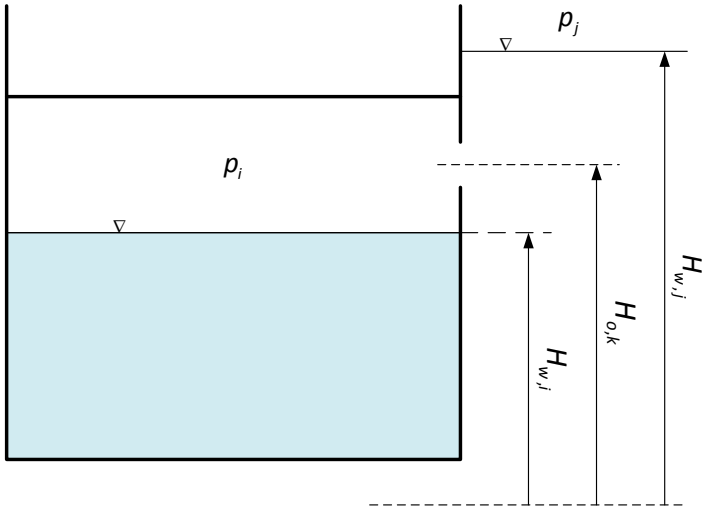

Figure 12: Quasi-stationary status – air pocket

When the compartment is open and air is free to escape (fully vented) the water behaves as a spring mass system (Figure 13), *Palazzi and de Kat (2004)*. The mass is assigned as the mass of the water inside the compartment and the spring is proportional to the water plane area inside the compartment. Such a spring mass system can yield to resonance when damping effects (friction, vortex, and energy dissipation) are too small or neglected. In case the air is enclosed and cannot escape it acts as an additional spring. The spring is non-linear because it must obey the gas law: $PV = const$. For an infinitesimal small volume the equation can be written as $PV = \left(P + dP\right) \cdot \left(V + dV\right)$ which yields the spring formulation:

$$\frac{dP}{dV} = -\frac{1}{V}(P + dP) \tag{5.1.2}$$

The above expression shows that the spring is proportional to the inverse of the volume air. As in the fully vented case, the spring mass system can yield to resonance when damping effects are neglected.

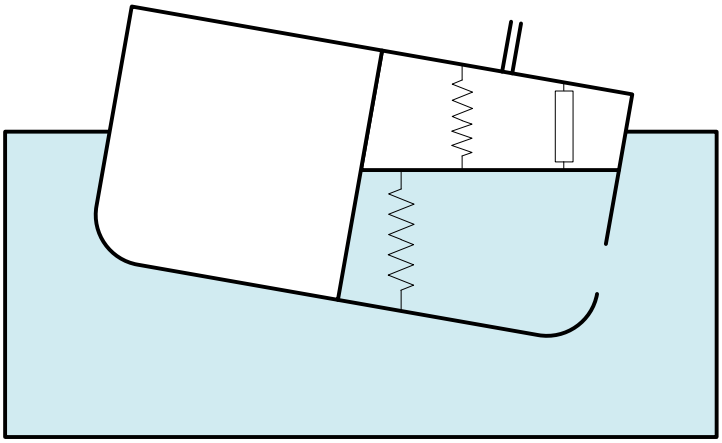

Figure 13: Internal spring mass system

When air can escape, the relation $PV = const$ is still valid, but the volume to consider must account for the volume of air that escaped. In this situation, air compression can occur, but the escape of air also results in energy dissipation. Therefore, air flow provides a damping effect, which limits resonance and can significantly reduce water motion inside the compartment.

Hence, when air flow is not fully taken into account in order to reproduce water motion inside a compartment equipped with vents, the simulation has to be carried out in fully vented conditions for a correct calculation of the static heel equilibrium, which means that air compression is neglected.

However, numerical methods should consider air as compressible fluid which brings up some important questions: how to model a compartment as realistic as possible and where to set airflow routes and ventilation ducts? However, simplifications and

assumptions are always needed as it is not practical to model every single ventilation duct.

5.2 Damage Stability – Ship-Floodwater Interaction

5.2.1 General Remarks

All types of ships and boats underlie the risk of sinkage when a damage caused by collision, launching or explosion leads to the loss of buoyancy. Only ships exclusively made from floatable material and carrying floatable cargo may be excluded from that risk. The probability of having an accident that ends up in the sinkage of a ship is very possible; hence, thought has to be put on damage stability during the design phase of a vessel. The most effective mechanisms to avoid sinkage are the use of longitudinal, transversal and a few horizontal (e.g. double bottom) watertight bulkheads. In fact, this idea is not a new one: by end of the 13th century, Marco Polo mentioned about the use of watertight compartmentation on Chinese junks.

As a matter of principal, flooding of a part of a ship can have two consequences. Firstly, a loss of buoyancy consequently changes the trim of a ship which can lead to an uncontrollable sinkage of the ship. A second consequence can be loss of transversal stability causing a ship to capsize. There are many uncertainties regarding an adequate subdivision in a ship hull, starting from a lack of knowledge about the expected size of the damage opening, the type of cargo to the point of unexpected behaviour of the crew in case of an accident. The construction of bulkheads is expensive and an unsinkable ship may be uneconomical to the ship owner. Therefore, it is desirable to compromise about safety and economic efficiency. Mandatory international regulations could partially solve this dilemma for passenger ships and settle competitive advantage between ship owners.

As already mentioned in chapter 1.2, most ship accidents that result in flooding, take place in different sea states. Statistical research by *Tagg and Tuzcu (2002)*, who took part in the HARDER (Harmonization of Rules and Design Rationale) project,

shows that over 97% of the collision accidents take place in a sea state with a significant wave height of less than 4.0m.

Papanikolaou et al. (2003) calculated the flooding of the vessel *Express Samina* in calm water and waves with a significant wave height of 2.0m. In both cases the heeling angle is very similar.

In the *IMO SLF47/INF.6 (2004)* a final study on time-to-flood for large passenger ships compared *van't Veer (2004)* simulations in calm sea and irregular waves with a significant wave height of 2.0m. A three-compartment damage case of a large passenger ship with two different *GM* values is presented. The heel angle (Figure 14) and the floodwater accumulation (Figure 15) in the three damaged compartments were compared resulting in similar values for calm water and irregular waves. Based on the results it can be assumed that the waves do not have a significant effect on the motions of a large passenger ship if the significant wave height is lower than 2.0m. In the phase of transient flooding wind and waves may have a more significant effect on the transient heeling (see chapter 5.1.2).

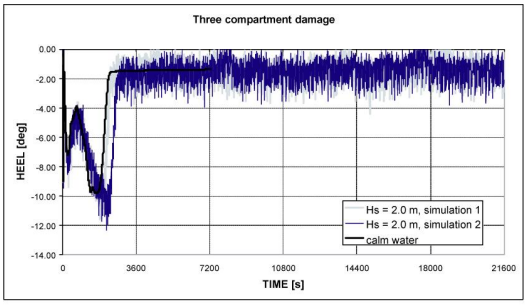

Figure 14: Roll response in waves of H_S = 2.0m

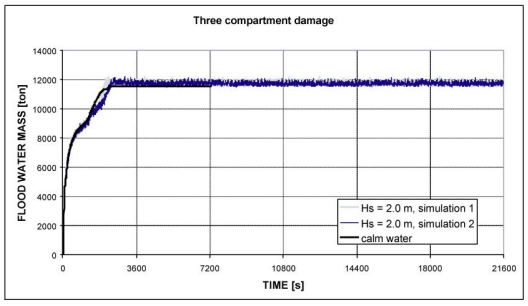

Figure 15: Floodwater accumulation in waves of H_S = 2.0m

However, in higher waves a comparison to calm sea can lead to different results which have been proven by *van't Veer and Serra (2003)* by testing damaged large passenger ships in waves. Large ship motions caused very slow progressive flooding and the results could not be directly compared to cases with calm water though a variation of the results could only be observed after a longer time period.

For that reason a simplified approach on the ship motions is justified and calm sea is assumed, however, further explanation in the following paragraphs will back up this assumption.

5.2.2 Ship Motions

As discussed in previous chapter 5.2.1 calm sea is assumed which gives reason for further assumption of slow ship motions. Therefore it is possible to apply a quasi-hydrostatic force/moment balance solver for determining the time-dependent damage ship position. The time derivates of trim and heave motions in calm water are relatively small which justifies this assumption. In contrary it is well known that during the short phase of transient flooding right after the creation of the damage opening rapid heeling takes place. For progressive flooding in calm water the dynamic roll motion is not very significant in the CFD simulations. This has also been observed by *Svensen and Vassalos (1998)* through numerous model tests with flooded Ro-Ro vessels where it was shown that the ship motions significantly reduce as the amount of water on deck increases. There are two reasons that justify this statement:

- due to the added weight of the floodwater the restoring moment increases
- due to the flooding the roll damping increases (this conclusion can partly be extended to other ship types)

Model tests in Vienna Model Basin (VMB) with Genesis confirmed that there are no heavy roll motions and some heaving in side seas. Based on these facts, it was decided to adopt a fully quasi-hydrostatic approach to the motions of the ship. For progressive flooding inside a damaged ship this simplification is a good approach which is expected to give solid simulation results. For transient flooding *Mustonen (1998)* stated that the transient heeling in case of a large asymmetric side damage due to a collision can be up to two times as large as predicted by the quasi-stationary method. In presented CFD simulation collision forces are not included

though they can significantly affect the transient motions of the ship in early stages of flooding. *Ruponen (2007)* quotes that in some cases exclusion of the collision force can decrease the error that is caused by the assumption of quasi-stationary motions.

5.2.3 Ship-Floodwater Interaction

In previous chapter 3.2 a few methods for the determination of the floodwater distribution on deck of a damaged ship and the floodwater's free surface have been described.

Among them was the simple approach where free surfaces are assumed to remain horizontal independent from any ship motion. This simplification has been used in previous studies, e.g. *Journée et al. (1997)*, *Santos et al. (2002)*, *Lee et al. (2007)* and *Ruponen (2007)* as well as in the MARIN study of time-to-flood simulations, *IMO (2003)* and *van't Veer (2004)*.

In a more sophisticated approach floodwater motion can be approximated with the lump mass concept, where the mass of the floodwater is concentrated in its centre and the free surface is kept plane but is allowed to incline as a result of dynamic interaction between floodwater and ship, *Papanikolaou et al. (2000)*, *Jasionowski and Vassalos (2001)* and *Papanikolaou and Spanos (2002a)*.

It should also be mentioned other approached that also consider the wavy character of the floodwater flow by implementation of a shallow water wave modelling, see chapter 4.1. Researchers who concentrated on this method were *Santos and Soares (2006)* and *Belenky et al. (2003)* who combined this method with a novel finite volume numerical technique reducing the 3D problem of the flow into a 2D problem, which substantially decreased the computational requirements, *Papanikolaou (2007)*.

More sophisticated approaches of CFD solvers have been employed to describe the internal flow in a very detailed way in order to track the free surface of the

floodwater as precise as possible. CFD approaches have been used in previous studies by *Woodburn et al. (2002)*, *Cho et al. (2005)*, *Gao et al. (2005)*, *Nabavi et al. (2006)*, *AkyildIz and Erdem Ünal (2006)* and *Strasser et al. (2009)*.

Other approaches of CFD solvers use meshless particle methods known as SPH method. This method can even capture complicated sloshing phenomena like wave breaking inside a flooded compartment and other violent sloshing behaviour. Applications can be found in *Sueyoshi and Naito (2002)*, *Skaar and Vassalos (2006)* and *Souto-Iglesias et al. (2006)*.

Based on former CFD approach above this should provide good, satisfying and detailed results for both, compartments with a large area such as vehicle decks and smaller compartmentation as can be found on passenger ships. The numerical CFD method seems to be ideal for demonstrating the sloshing phenomena on deck of a damaged ship during the transient flooding phase where the effects on the ship motion are significant which in the end also affects the slower progressive phase of flooding.

5.2.4 SOLAS 2009 Requirements

The survivability and damage stability of a ship can be assessed by two main categories of regulatory concepts and methodologies: the deterministic and the probabilistic one. They both have advantages and weaknesses when the survivability of a ship is assessed. However, the survivability of a ship can be only reliably assessed by performing physical model experiments or numerical simulations which might be a basis for future “performance-based” survivability standards. The deterministic approaches to damage stability of ships rely on semi-empirical rules and criteria gained from statistical analysis of damage history data and practical experience. The probabilistic approach to damage stability of ships is based on a combination of rational statistical assessment of historical accidental data and semi-empirical criteria in order to assess the ship’s survivability for different possible damage scenarios.

As from 2009, IMO will introduce new international standards and regulations aiming for conformance of calculation methods for all ship types. This new harmonised set of regulations of ship's damage stability is based on a probabilistic approach; in this connection p_i is the probability that only compartments under consideration are flooded and s_i is the probability of survival of a ship. It has to be noted that the probability of an incident is not considered. The probabilistic approach to damage stability of a ship underlies the assessment of the probability of a ship surviving a collision incident and is expressed by the attained index, *A*. The attained index is obtained by assessing the ship's stability for a series of different damage scenarios in predefined loading conditions. The attained index, *A*, which expresses the overall survivability should be larger than the required subdivision index, *R*. The detailed procedure for the calculation of the attained and required indices was developed in the HARDER project, *Papanikolaou and Rusaas (2002)*. The harmonization process included the following steps, *Papanikolaou (2007)*:

1. Critical GM values were identified from representative samples of ships of the world fleet. These critical GM values give an indication of the marginal survival capability of the ship in damaged condition.
2. Based on the indentified critical GM values for each sample ship data the Attained Index A was calculated according to the developed HARDER probabilistic procedure.
3. A regression analysis of the obtained Attained Index A data with respect to ship type and size led to the formulation of the new Required Index R. It should be noted that for some ship types and sizes such as passenger ships the scatter of the obtained data was considerable. Such scattered data had to be post processed before they were included in the regression set of data for the determination of R, *Papanikolaou and Eliopoulou (2004)*.

$$R = 1 - \frac{C_1}{L_S + C_2 \cdot N + C_3} \qquad (5.2.1)$$

where L_S is the subdivision length in metres, C_2 expresses the relative importance of ship's length and a proportional number of persons on board in risk, C_1 and C_3 are coefficients resulting from the regression analysis of calculated Attained Indices of sample ships and N is related to the persons on board and the extent of life saving equipment ($N=N_1+2N_2$ where N_1 is the number of persons for whom lifeboats are provided and N_2 the number of persons the ship is permitted in excess of N_1)

For any longitudinal damage the probability of occurrence is calculated. This probability is influenced by following factors:

- Length of damage
- Location of damage in relation to bulkhead spacing
- Limited damage length of 60m ($p_i = 0$ for damage lengths larger than 60m).
- L_{max}/L_S (maximum absolute damage length / subdivision length) must not exceed 10/33, see Figure 16
- The damage must not be higher than 12.5m above the waterline and lower than 2m above keel

However, also several nonadjacent damage zones are taken into consideration. In this condition required heeling angles – different for passenger ships and bulk carriers - must not be exceeded.

In some cases, like compartments in front of the collision bulkhead the probability of survival has to be 1 for passenger ships.

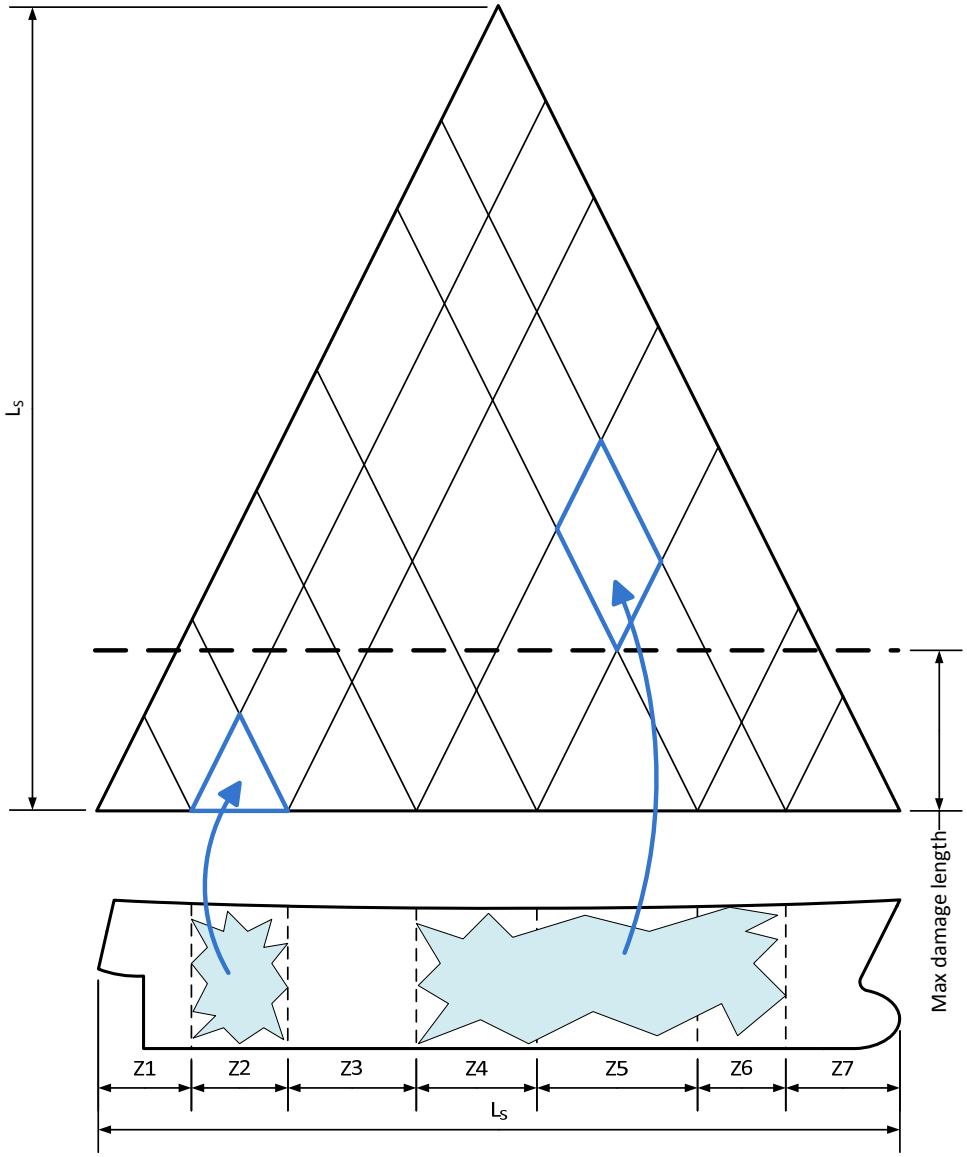

Figure 16: SOLAS 2009, maximum damage length

5.3 Concluding Remarks

The physical background of flooding and its influence upon the resulting ship motions and upon the behaviour of the damaged ship in general has been discussed in this chapter. On the face of it the physics previously described seems to be trivial and easy to employ but this appearance can be deceiving. Integration into numerical models requires solving non-linear terms for the calculus of motion equations and the delineation of the generated wave profile of the free surface in

the damaged ship and outside of the ship. Therefore, it was preferred to use simplified models in previous research studies which could avoid these mathematical difficulties.

A relatively simple way to model floodwater on deck is to assume that free surfaces always remain horizontal, irrespective of ship motions. Sloshing of floodwater is considered to be insignificant and only free surface effects on the stability of the damaged ship are taken into account. This popular approach has been applied in previous but even in recent research studies for instance *Vermeer et al. (1994)*, *Lee et al. (2007)* and *Ruponen (2007)*. It is very suitable for cases with dense subdivisions within the flooded compartment, where sloshing is likely to have a small impact on the ship motions and therefore considered to be neglected. In calm sea sloshing becomes totally unimportant.

For cases with large unobstructed areas, such as vehicle decks on Ro-Ro ferries, sloshing cannot be neglected anymore. Numerically, sloshing effects due to floodwater motion are usually simplified by the use of the lump mass concept which assumes that the mass of the floodwater is concentrated at its centre and moving in space under constraints imposed by the surrounding boundaries, *Papanikolaou et al. (2000)* and *Jasionowski and Vassalos (2001)*.

A more accurate approach is the use of RANSE calculations with the VOF method. Above mentioned methods mainly give an indication about the water volume in the flooded compartments while RANSE computations with VOF go a step further: it is possible to track the free surface in a flooded compartment which hereby allows determining all acting forces in detail for an analysis of the influence of sloshing effects on the ship motion. *van't Veer and de Kat (2000)* compared calculations with a simplified approach and RANSE models to model tests. The calculations were carried out for a captive model with the simplified approach and for a roll enforced model with a RANSE simulation using the VOF scheme. Also *Papanikolaou and Spanos (2002a)* and *Cho et al. (2005)* focused on using RANSE codes for the simulation of progressive flooding.

6 Numerical Method

6.1 General Remarks

Computational Fluid Dynamics (CFD) is applied in a wide variety of industrial settings, for example computation of water flow around ship hulls or air flow around airplane wings.

CFD's founding father, John von Neumann, indulging him in speculations about the possibilities of the emerging digital computer, stated in 1946 that numerical models would eventually completely replace analytic solutions of fluid dynamics equations and even experimental fluid dynamics, *Nieland (1998)*. As usual, the child did not exactly become what the father hoped for, analytic and experimental methods are still used, but by now CFD methods have become a prominent tool in many industrial settings and still form an active research field.

Finite volume methods (FVM) have been used extensively in recent years and can be formulated from the basic tools in the solution of partial differential equations either finite element methods (FEM) or finite difference methods (FDM). The numerical algorithm exists of three main parts, *Versteeg and Malalasekera (2007)*:

- Formal integration of the governing equations of fluid flow over all the (finite) control volumes of the solution domain.
- Discretization involves the substitution of a variety of finite-difference-type approximations for the terms in the integrated equation representing flow processes such as convection, diffusion and sources. This converts the integral equations into a system of algebraic equations.
- Solution of the algebraic equations by an iterative method.

The objective of this chapter is to present the numerical models which are used to carry out CFD calculations with flooded deck arrangements. Following paragraphs will cover the subject areas fluid dynamics (governing equations of viscous fluid flows, boundary conditions, turbulence modelling) and the finite volume method

(FVM) (finite volume discretization, coupling between the flow variables, multiphase flows and dynamic mesh calculations). Governing equations of fluid flow can be found in Appendix C.1. It is impossible to discuss all facets of computational fluid dynamics and it is also not the author's intention but it was tried to include all numerical methods and algorithms that were applied to the case studies.

6.2 Free Surface Flows - Multiphase Flows

6.2.1 General Remarks

In nature and engineering fields a large number of flows are object to a mixture of phases. A phase is a region in the parameter space of thermodynamic variables in which the free energy is analytic. Between such regions there are abrupt changes in the properties of the system, which correspond to discontinuities in the derivatives of the free energy function. Such physical phase as gas, liquid or solid, can be defined as an identifiable class of material which has inertial response to and interaction with the flow and the potential field in which it is immersed. Surface tension plays an important role in these interfaces. Multiphase flows can be grouped into three categories: gas-liquid or liquid-liquid flows; and three-phase flows. In flooding simulations only gas-liquid flows are taken into consideration. Following regime can be identified:

- Bubbly flow (Figure 18): This is the flow of discrete gaseous or fluid bubbles in a continuous fluid.
- Droplet flow (Figure 18): This is the flow of discrete fluid droplets in a continuous gas.
- Slug flow (Figure 17): This is the flow of large bubbles in a continuous fluid.
- Stratified/free-surface flow (Figure 19): This is the flow of immiscible fluids separated by a clearly-defined interface.

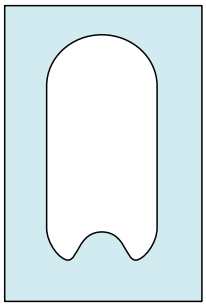

Figure 17: Slug flow

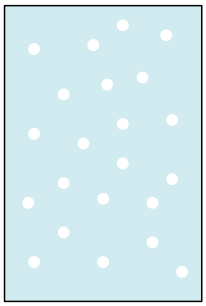

Figure 18: Bubbly, droplet, or particle-laden flow

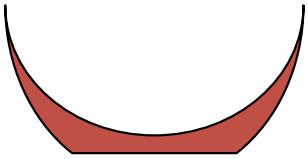

Figure 19: Stratified/free-surface flow

There are two basic ways to model free surface flows: the *Lagrangian method* where the mesh follows the interface shape and the *Eulerian method* which treats different phases mathematically as interpenetrating continua. The concept of phasic volume fraction is a term describing that the volume of a phase cannot be occupied by other phases. The sum of the volume fraction is equal to one and it is assumed that the volume fraction is a continuous function of space and time. A suitable Euler-Euler multiphase model for free-surface problems is the volume of fluid (VOF) model which will be explained in the following chapter.

6.2.2 Volume of Fluid (VOF) Model

The VOF method was originated by *Nichols and Hirt (1975)* and *Noh and Woodward (1976)* and later on further developed by *Hirt and Nichols (1981)*. Over the years the VOF method has been significantly improved pointing out the research work of *Rudman (1997)* and *Rider and Kothe (1998)*.

The VOF model is a surface-capturing technique applied to a fixed Eulerian mesh. It is designed for two or more immiscible fluids or phases that are not interpenetrating and gives the position of the interface between the fluids. For each additional phase added to the model, a variable is introduced; a single set of momentum equations is shared by the fluids and the volume fraction of the phase in the computational cell is tracked throughout the domain. In each control volume, the volume fractions of all phases sum to unity. As long as the volume fraction of each of the phases is known at each location all variables and properties are shared by the phases and represent volume-averaged values. Hence, the variables and properties in any given cell are either representing one of the phases, or represent a mixture of the phases, depending upon the volume fraction values. That means that if the q^{th} fluid's volume fraction in the cell is denoted as α_q, then the following three conditions are possible:

- α_q=0: The cell is empty (of the q^{th} fluid).
- α_q=1: The cell is full (of the q^{th} fluid).
- $0<\alpha_q<1$: The cell contains the interface between the q^{th} fluid and one or more other fluids.

Based on the local value of α_q, the appropriate properties and variables will be assigned to each control volume within the domain.

The tracking of the interface between the phases is accomplished by the solution of a continuity equation for the volume fraction of one or more of the phases where α_q evolves from the transport equation:

$$\frac{\partial \alpha}{\partial t} + div(\alpha v) = 0 \tag{6.2.1}$$

For the q^{th} phase, the equation has the following form:

$$\frac{1}{\rho_q}\left[\frac{\partial}{\partial t}\left(\alpha_q \rho_q\right) + \nabla \cdot \left(\alpha_q \rho_q \vec{v}_q\right)\right] = S_{\alpha_q} + \sum_{p=1}^{n}\left(\dot{m}_{pq} - \dot{m}_{qp}\right) \tag{6.2.2}$$

where $\dot{m}_{pq}$ is the mass transfer from phase *p* to phase *q* and $\dot{m}_{qp}$ is the mass transfer from phase *q* to phase *p*.

The volume fraction equation will not be solved for the primary phase; the primary-phase volume fraction will be computed based on the following constraint:

$$\sum_{q=1}^{n} \alpha_q = 1 \tag{6.2.3}$$

Furthermore, the volume fraction equation may be solved either through implicit or explicit discretization.

Implicit Scheme

When the implicit scheme is used for time discretization, standard finite-difference interpolation schemes, QUICK, Second Order Upwind and First Order Upwind, and the Modified HRIC schemes, are used to obtain the face fluxes for all cells, including those near the interface.

$$\frac{\alpha_q^{n+1}\rho_q^{n+1} - \alpha_q^n \rho_q^n}{\Delta t} V + \sum_f \left(\rho_q^{n+1} U_f^{n+1} \alpha_{q,f}^{n+1} \right) = \left[S_{\alpha_q} + \sum_{p=1}^{n} \left(\dot{m}_{pq} - \dot{m}_{qp} \right) \right] V \tag{6.2.4}$$

Since this equation requires the volume fraction values at the current time step (rather than at the previous step, as for the explicit scheme), a standard scalar transport equation is solved iteratively for each of the secondary-phase volume fractions at each time step.

Explicit Scheme

In the explicit approach, standard finite-difference interpolation schemes are applied to the volume fraction values that were computed at the previous time step.

$$\frac{\alpha_q^{n+1}\rho_q^{n+1} - \alpha_q^n \rho_q^n}{\Delta t} V + \sum_f \left(\rho_q U_f^n \alpha_{q,f}^n \right) = \left[\sum_{p=1}^{n} \left(\dot{m}_{pq} - \dot{m}_{qp} \right) + S_{\alpha_q} \right] V \tag{6.2.5}$$

where $n+1$ = index for current time step

n = index for previous time step

$\alpha_{q,f}$ = face value of the q^{th} volume fraction, computed from the first- or second-order upwind, QUICK, modified HRIC, or CICSAM scheme

V = volume of cell

U_f = volume flux through the face, based on normal velocity

This formulation does not require iterative solution of the transport equation during each time step, as is needed for the implicit scheme. When the explicit scheme is used for time discretization, the face fluxes can be interpolated either using interface reconstruction or using a finite volume discretization scheme.

6.2.3 Interpolation Near the Interface

A special interpolation treatment to the cells that lie near the interface between two phases is applied in order to be able to calculate the convection and diffusion fluxes through the control volume faces and to balance them with the control volume itself. Figure 20 shows an actual interface shape (Figure 20) along with the interfaces assumed during computation by the geometric reconstruction scheme (Figure 21) and the donor-acceptor scheme (Figure 22).

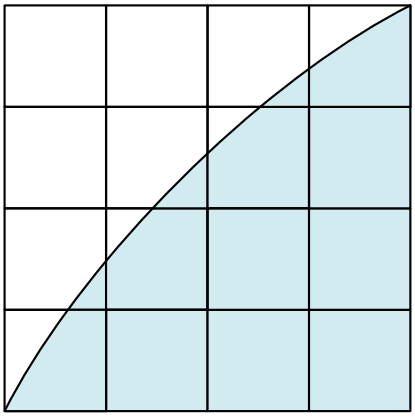

Figure 20: Actual interface shape

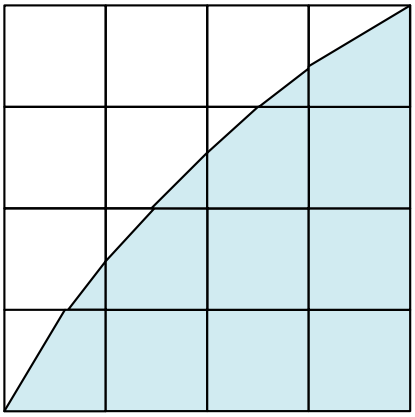

Figure 21: The geometric reconstruction scheme

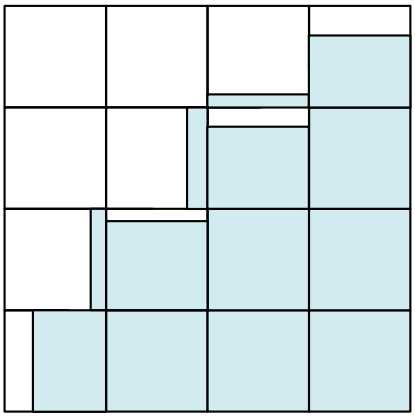

Figure 22: The donor-acceptor scheme

These interface cells are numerically treated in the same way as the cells that are completely filled with one of the phases; the same discretization schemes (chapter 6.2.2) either implicitly or explicitly can be applied to these cells.

The Geometric Reconstruction Scheme

Whenever a cell is completely filled with one phase or another, the standard interpolation schemes are used in order to obtain the face fluxes. The geometric construction scheme is applied when two or more phases split a cell with its interface.

The geometric reconstruction scheme is also known as the piecewise-linear approach which represents the interface between fluids. This scheme is the most accurate and is applicable for general unstructured meshes which was a main

achievement in the work of *Young (1982)*. It is assumed that the interface between two fluids has a linear slope within each cell; therefore, the advection of fluid through the cell faces can be computed by making use of this linear shape, see Figure 21.

The interpolation procedure is carried out in three steps: firstly, the position of the linear interface relative to the centre of each partially-filled cell is derived on the basis of information about the volume fraction and its derivatives in the cell. The second step is calculating the advecting amount of fluid through each face using the computed linear interface representation and information about the normal and tangential velocity distribution on the face. The third step is calculating the volume fraction in each cell using the balance of fluxes calculated during the previous step.

The Donor-Acceptor Scheme

In almost the same manner as in the geometric reconstruction scheme the standard interpolation schemes are used in order to obtain the face fluxes whenever a cell is completely filled with one phase or another. A *donor-acceptor scheme* is used, when the cell is near the interface between two phases, in order to determine the amount of fluid advected through the face, *Hirt and Nichols (1981)*. This scheme identifies one cell as a donor of an amount of fluid from one phase and another neighbour cell as the acceptor of that same amount of fluid, and is used to prevent numerical diffusion at the interface. The amount of fluid from one phase that can be convected across a cell boundary is limited by the minimum of two values: the filled volume in the donor cell or the free volume in the acceptor cell.

The orientation of the interface is also used in determining the face fluxes. The interface orientation is either horizontal or vertical, depending on the direction of the volume fraction gradient of the q^{th} phase within the cell, and that of the neighbour cell that shares the face in question. Depending on the interface's orientation as well as its motion, flux values are obtained by pure upwinding, pure downwinding, or some combination of the two.

Numerical Diffusion

In Eulerian simulations, time and space are divided into a discrete grid and the continuous differential equations of motion (such as the Navier-Stokes equation) are discretised into finite-difference equations. The discrete equations are in general more diffusive than the original differential equations, so that the simulated system behaves differently than the intended physical system. The amount and character of the difference depends on the system being simulated and the type of discretization that is used.

As an example of numerical diffusion, consider an Eulerian simulation of a drop of green dye diffusing through water. If the water is flowing diagonally through the simulation grid, then it is impossible to move the dye in the exact direction of the flow: at each time step the simulation can at best transfer some dye in each of the vertical and horizontal directions. After a few time steps, the dye will have spread out through the grid due to this sideways transfer. This numerical effect takes the form of an extra high diffusion rate.

All CFD codes, whether finite-difference, finite-volume, or finite-element, suffer from the problem of numerical undershoots and overshoots in the flow variables caused by discretization of the convection terms in the flow conservation equations. These problems typically occur when sharp gradients in the flow variables are encountered on the computational grid. The common solution to this problem is to add varying amounts of artificial numerical diffusion to the solution algorithm to stabilise the overall convection scheme. The diffusion has the effect of weighting the convection towards the upwind regions of the flow, hence the algorithms are referred to generically as “upwinding schemes”, *Jones and Clarke (2003)*.

6.2.4 Material Properties

The material properties for interface cells between two phases can be determined by summing up the properties of the volume fraction. These averaged properties

can then be used in the transport equations. In a two-phase system, for example, if the phases are represented by the subscripts 1 and 2, and if the volume fraction of the second of these is being tracked, the density in each cell is given by

$$\rho = \alpha_2 \rho_2 + (1 - \alpha_2)\rho_1 \tag{6.2.6}$$

Generally, the volume-fraction-averaged density for an n-phase system can be written as follows:

$$\rho = \sum \alpha_q \rho_q \tag{6.2.7}$$

All other properties (e.g., viscosity) are computed in this manner.

6.2.5 Momentum Equation

With previously computed volume-fraction-averaged properties a single momentum equation is solved throughout the domain. The momentum equation (6.2.8) is dependent upon the volume fractions of all phases through the properties ρ and μ.

$$\frac{\partial}{\partial t}(\rho \vec{v}) + \nabla \cdot (\rho \vec{v}\vec{v}) = -\nabla p + \nabla \cdot \left[\mu\left(\nabla \vec{v} + \nabla \vec{v}^T\right)\right] + \rho \vec{g} + \vec{F} \tag{6.2.8}$$

The resulting velocity field is shared among the phases though in cases where large velocity differences exist between the phases, the accuracy of the velocities computed near the interface can be adversely affected.

6.2.6 Energy Equation

The energy equation (6.2.9) is also shared among the phases:

$$\frac{\partial}{\partial t}(\rho E) + \nabla \cdot \left(\vec{v}\left(\rho E + p\right)\right) = \nabla \cdot \left(k_{eff} \nabla T\right) + S_h \tag{6.2.9}$$

The VOF model treats energy, E, and temperature, T, as mass-averaged variables:

$$E = \frac{\sum_{q=1}^{n} \alpha_q \rho_q E_q}{\sum_{q=1}^{n} \alpha_q \rho_q} \tag{6.2.10}$$

where E_q for each phase is based on the specific heat of that phase and the shared temperature.

The properties ρ and k_{eff} (effective thermal conductivity) are shared by the phases and the source term, S_h, contains contributions from radiation and other volumetric heat sources.

As with the velocity field, the accuracy of the temperature near the interface is limited in cases where large temperature differences exist between the phases. Such problems also arise in cases where the properties vary by several orders of magnitude. For example, if a model includes liquid metal in combination with air, the conductivities of the materials can differ by as much as four orders of magnitude. Such large discrepancies in properties lead to equation sets with anisotropic coefficients, which in turn can lead to convergence and precision limitations.

Additional Scalar Equations

Depending upon the problem definition, additional scalar equations may be involved in the solution. In the case of turbulence quantities, a single set of transport equations is solved, and the turbulence variables (e.g., k and ε or the Reynolds stresses) are shared by the phases throughout the field.

6.2.7 Surface Tension

The VOF model is capable of treating the effects of surface tension along the interface between each pair of phases by including the contact angles between the

phases and the walls as shown in Figure 23. Because of continuous variation of the surface tension coefficients, tangential stress terms will be considered additional to the normal stress terms. This variation of the surface tension coefficient depends upon the temperature distribution and is called thermo-capillary convection or Marangoni effect. In zero or near-zero gravity conditions variable surface tension coefficient effects can have a significant influence upon the calculation of the wall adhesion.

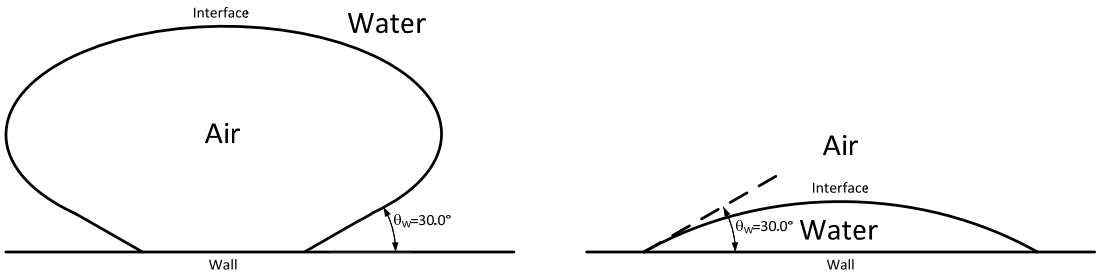

Figure 23: Contact angle between the phases

Surface tension, stored energy on the surface of a liquid, arises because atoms on the surface are missing bonds. The net force on a molecule within an air bubble, for example, is zero due to its neighbours. However, at the surface the net force is radially inward, and the combined effect of the radial components of force across the entire spherical surface is to make the surface contract, thereby increasing the pressure on the concave side of the surface. The surface tension is a force, acting only at the surface, which is required to maintain equilibrium in such instances. It acts to balance the radially inward inter-molecular attractive force with the radially outward pressure gradient force across the surface. In regions where two fluids are separated, but one of them is not in the form of spherical bubbles, the surface tension acts to minimize free energy by decreasing the area of the interface.

The continuum surface force (CSF) model mentioned by *Brackbill et al. (1992)* is widely used for the calculation of the surface tension. Surface tension in the VOF model is considered by an additional source term in the momentum equation.

Assuming the case that the surface tension is constant along the surface and that the forces act normal to the interface it can be revealed that the pressure drop across the surface depends upon the surface tension coefficient, σ, and the doubly curved surface curvature κ as measured by two radii in orthogonal directions, R_1 and R_2:

$$p_2 - p_1 = \sigma\kappa \tag{6.2.11}$$

$$\kappa = \frac{1}{R_1} + \frac{1}{R_2} \tag{6.2.12}$$

where p_1 and p_2 are the pressures in the two fluids on either side of the interface.

In numerical simulations the surface curvature is computed from local gradients in the surface normal at the interface. The surface normal, n, is defined as the gradient of α_q, the volume fraction of the q^{th} phase.

$$n = \nabla \alpha_q \tag{6.2.13}$$

The curvature, κ, is defined in terms of the divergence of the unit normal, $\hat{n}$, *Brackbill et al. (1992)*:

$$\kappa = \nabla \cdot \hat{n} \tag{6.2.14}$$

where

$$\hat{n} = \frac{n}{|n|} \tag{6.2.15}$$

The surface tension can be written in terms of the pressure jump across the surface. The force at the surface can be expressed as a volume force using the divergence theorem. It is this volume force that is the source term which is added to the momentum equation. It has the following form:

$$F_{vol} = \sum_{pairs\ ij,\ i<j} \sigma_{ij} \frac{\alpha_i \rho_i \kappa_j \nabla \alpha_j + \alpha_j \rho_j \kappa_i \nabla \alpha_i}{\frac{1}{2}\left(\rho_i + \rho_j\right)} \tag{6.2.16}$$

This expression allows for a smooth superposition of forces near cells where more than two phases are present. If only two phases are present in a cell, then $\kappa_i = -\kappa_j$ and $\nabla \alpha_i = -\nabla \alpha_j$, and Equation (6.2.16) simplifies to

$$F_{vol} = \sigma_{ij} \frac{\rho \kappa_i \nabla \alpha_i}{\frac{1}{2}\left(\rho_i + \rho_j\right)} \tag{6.2.17}$$

where ρ is the volume-averaged density computed using Equation (6.2.7). Equation (6.2.17) shows that the surface tension source term for a cell is proportional to the average density in the cell.

Based on the value of the dimensionless quantities the Reynolds number, *Re*, and the capillary number, *Ca* or the Reynolds number, *Re*, and the Weber number, *We*, the importance of surface tension effects is determined. For $Re \ll 1$, the quantity of interest is the capillary number:

$$Ca = \frac{\mu U}{\sigma} \tag{6.2.18}$$

and for $Re \gg 1$, the quantity of interest is the Weber number:

$$We = \frac{\rho L U^2}{\sigma} \tag{6.2.19}$$

where *U* is the free-stream velocity. Surface tension effects can be neglected if $Ca \gg 1$ or $We \gg 1$.

6.3 Solver Algorithms

6.3.1 General Remarks

Generally, there can be distinguished between two numerical algorithms:

- pressure-based solver
- density-based solver

In the past, the pressure-based algorithm was developed for low-speed incompressible flows in contrast to the density-based algorithm which was used for high-speed compressible flows. As time went on both methods were adapted and reformulated to operate on a wide range of flow conditions.

In the pressure-based algorithm the pressure field is obtained from the equation of state by solving a pressure or pressure correction equation while in the density-based algorithm the density field is determined from the continuity equation. Both methods obtain the velocity fields from the momentum equations. Equations for the conservation of mass, momentum, energy and other scalars such as turbulence will be solved using a control-volume-based technique. Also the discretization process is similar for the two methods but the linearization and solution approach is a different one.

6.3.2 The Scalar Transport Equation

General scalar transport equations are converted to algebraic equations which can be solved numerically. Therefore, the transport equation (6.3.1) is integrated on each control volume:

$$\int_V \frac{\partial \rho \phi}{\partial t} dV + \oint \rho \phi \vec{v} \cdot d\vec{A} = \oint \Gamma_\phi \nabla \phi \cdot d\vec{A} + \int_V S_\phi dV \tag{6.3.1}$$

where

ρ = density

$\vec{v}$ = velocity vector (=$u\hat{i}+v\hat{j}$ in 2D)

$\vec{A}$ = surface area vector

Γ_ϕ = diffusion coefficient for ϕ

$\nabla\phi$ = gradient of ϕ (=$(\partial\phi/\partial x)\hat{i}+(\partial\phi/\partial y)\hat{j}$ in 2D)

S_ϕ = source of ϕ per unit volume

Then, equation (6.3.1) is discretised, see Figure 24, and gives following equation on a given cell:

$$\frac{\partial\rho\phi}{\partial t}V+\sum_{f}^{N_{faces}}\rho_f\vec{v}_f\phi_f\cdot\vec{A}_f=\sum_{f}^{N_{faces}}\Gamma_\phi\nabla\phi_f\cdot\vec{A}_f+S_\phi V \tag{6.3.2}$$

where

N_{faces} = number of faces enclosing the cell

ϕ_f = value of ϕ convected through face f

$\rho_f\vec{v}_f$ = mass flux through the face

$\vec{A}_f$ = face area vector in 3D

$\nabla\phi_f$ = gradient of ϕ at face f

V = cell volume

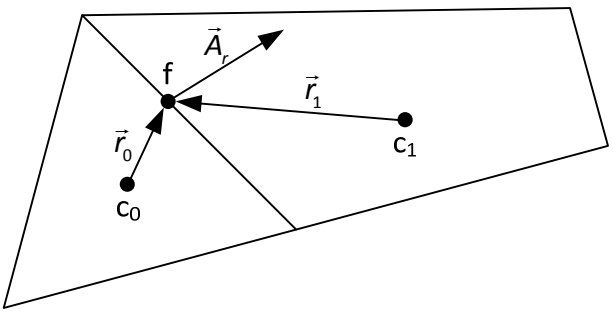

Figure 24: Discretization of a scalar transport equation

The diffusion term in previous equation (6.3.2) are central-differenced and second-order accurate.

The discretised scalar transport equation contains the unknown scalar variable *f* at the cell centre as well as the unknown values in surrounding neighbour cells. A linearised version of equation (6.3.2) has following form:

$$a_p\phi = \sum_{nb} a_{nb}\phi_{nb} + b \tag{6.3.3}$$

Where the subscript *nb* refers to the neighbour cells and a_p and a_{nb} are the linearised coefficients for ϕ and ϕ_{nb}.

6.3.3 Discretization Methods

Discrete values of the scalar ϕ are usually stored at the cell centres. Face values ϕ_f are required for the convection terms in equation (6.3.2) and must be interpolated from the cell centre values. This is accomplished by an upwind scheme.

Upwinding means that the face value ϕ_f is derived from quantities in the cell upstream, or "upwind", relative to the direction of the normal velocity v_n in equation (6.3.2).

Several important upwind schemes will be described in the following sections.

First-Order Upwind Scheme

It is assumed that the cell centres values of any field represent a cell-average value. In other words, when the first-order upwind scheme is used the face value ϕ_f is equal to the cell centre value ϕ in the upstream cell. Figure 25 shows the nodal values used to calculate cell face values when the flow is in the positive direction (west/east) and Figure 26 shows those in the negative direction.

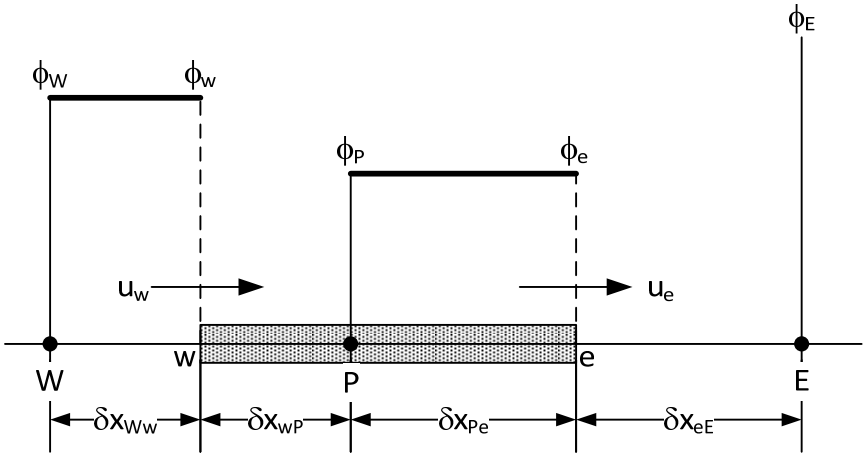

Figure 25: First-order upwind scheme with flow in positive direction

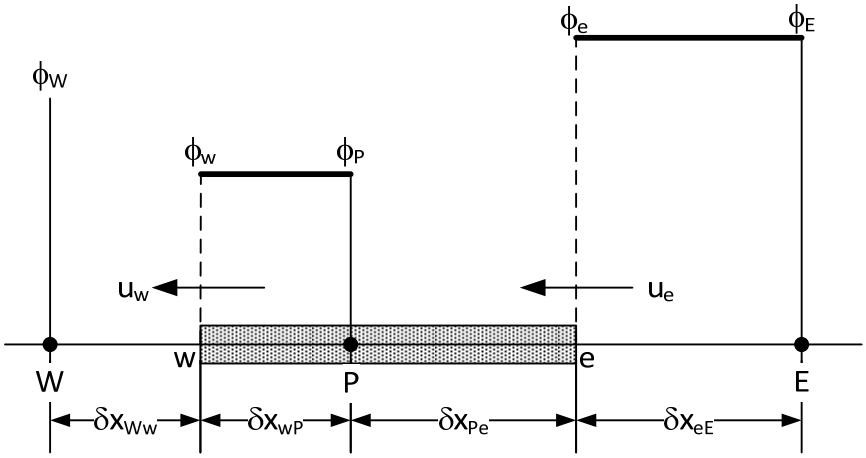

Figure 26: First-order upwind scheme with flow in negative direction

Power-Law Scheme

The power-law discretization scheme interpolates the face value of a variable f using the exact solution to a one-dimensional convection-diffusion equation

$$\frac{\partial}{\partial x}(\rho u \phi) = \frac{\partial}{\partial x}\Gamma\frac{\partial \phi}{\partial x} \tag{6.3.4}$$

where Γ and ρu are constant across the interval ∂x. Equation (6.3.4) can be integrated in order to describe how ϕ varies with x:

$$\frac{\phi(x)-\phi_0}{\phi_L-\phi_0}=\frac{\exp\left(Pe\frac{x}{L}\right)-1}{\exp(Pe)-1} \tag{6.3.5}$$

where

$$\phi_0=\phi\big|_{x=0}$$

$$\phi_L=\phi\big|_{x=L}$$

And *Pe* is the Peclet number:

$$Pe=\frac{\rho u L}{\Gamma} \tag{6.3.6}$$

The variation of $\phi(x)$ between x=0 and x=L is illustrated in Figure 27 for a range of values of the Peclet number. It shows that the value of ϕ at x=L/2 is approximately equal to the upstream value. When there is no flow or pure diffusion, *Pe*=0 and ϕ may be interpolated using the linear average between the values at x=0 and x=L.

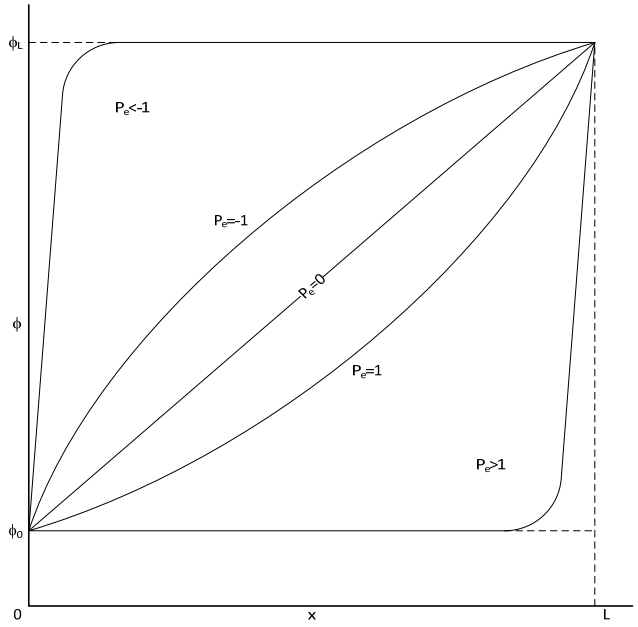

Figure 27: Variable ϕ between x=0 and x=L

The power-law differencing scheme is more accurate for one-dimensional problems because it attempts to represent the exact solution more closely.

Second–Order Upwind Scheme

The accuracy of hybrid and upwind schemes is only first-order in terms of Taylor series truncation error (TSTE). Though the first-order schemes are very stable, they tend to become prone to numerical diffusion errors, see chapter 6.2.3. Hence, such errors can be avoided by introducing higher order discretization which involve more neighbour points and bring in a wider influence.

The second-order upwind scheme, a higher order differencing scheme, is based on the multidimensional linear reconstruction approach proposed by *Barth and Jespersen (1989)*. The cell-centred solution about the cell centroid is interpolated to the cell face ϕ_f through a Taylor series expansion:

$$\phi_{f,SOU} = \phi + \nabla\phi \cdot \vec{r} \tag{6.3.7}$$

where ϕ is the cell-centred value, $\nabla\phi$ is the gradient in the upstream cell and $\vec{r}$ is the displacement vector from the upstream cell centroid to the face centroid.

Quick Scheme

Leonard (1979) developed a quadratic upstream interpolation for convective kinetics (QUICK) scheme which is based on a weight average of second-order–upwind and central interpolations of the variable. For face *e* in Figure 28 following value can be determined if the flow is from left to right:

$$\phi_e = \theta\left[\frac{S_d}{S_c + S_d}\phi_P + \frac{S_c}{S_c + S_d}\phi_E\right] + (1-\theta)\left[\frac{S_u + 2S_c}{S_u + S_c}\phi_P - \frac{S_c}{S_u + S_c}\phi_W\right] \tag{6.3.8}$$

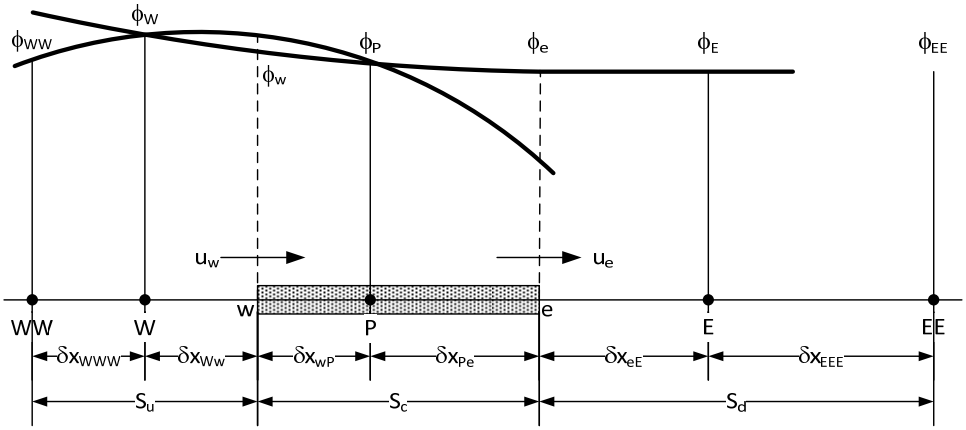

Figure 28: QUICK scheme

When θ = 0 equation (6.3.8) results in a second-order upwind value while when θ = 1 a central second-order interpolation is provided. Usually θ is set to 1/8 in the QUICK scheme.

HRIC Scheme

Generally, upwind schemes are unsuitable to track the free surface in VOF models because of their highly diffusive nature. Central differencing schemes, on the other hand, are unbounded and often give unphysical results though they can track interfaces accurately. The scheme is based on the NVD-diagram, Figure 29, which is a non-linear blend of upwind and downwind differencing. The subscript *U* represents the upwind cell, *D* the donor cell and *A* the acceptor cell.

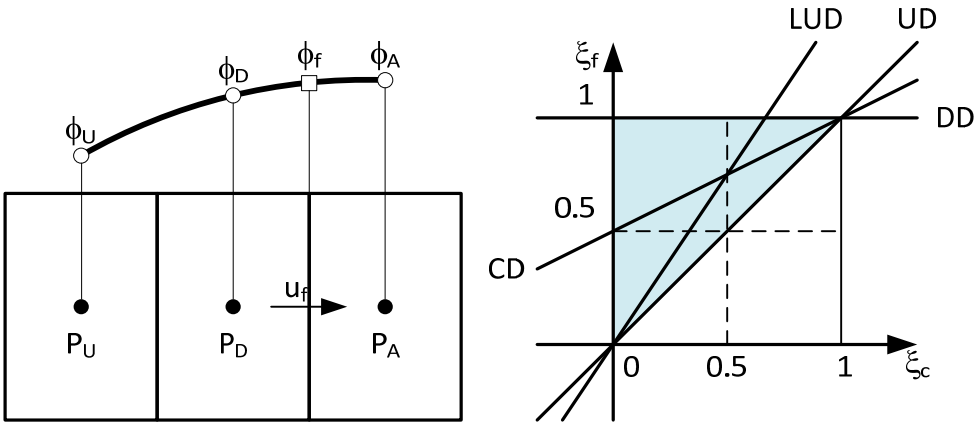

Figure 29: Cell representation and NVD diagram

The normalised cell value of volume fraction $\tilde{\phi}_c$ is derived in order to find the normalised face value $\tilde{\phi}_f$:

$$\tilde{\phi}_c = \frac{\phi_D - \phi_U}{\phi_A - \phi_U} \tag{6.3.9}$$

$$\tilde{\phi}_f = \begin{cases} \tilde{\phi}_c & \tilde{\phi}_c < 0 \text{ or } \tilde{\phi}_c > 1 \\ 2\tilde{\phi}_c & 0 \le \tilde{\phi}_c \le 0.5 \\ 1 & 0.5 \le \tilde{\phi}_c \le 1 \end{cases} \tag{6.3.10}$$

In case an upwind cell is not available, such as unstructured meshes, an extrapolated value is used for ϕ_U. When the flow is parallel to the interface wrinkles can be caused in the interface by the direct use of $\tilde{\phi}_f$. To avoid this phenomenon a one-dimensional bounded version of the QUICK scheme, *Leonard (1991)*, is applied:

$$\phi_f^{\tilde{U}Q} = \begin{cases} \tilde{\phi}_c & \tilde{\phi}_c < 0 \text{ or } \tilde{\phi}_c > 1 \\ MIN\left(\tilde{\phi}_f, \frac{6\tilde{\phi}_c + 3}{8}\right) & 0 \le \tilde{\phi}_c \le 1 \end{cases} \tag{6.3.11}$$

Equation (6.3.11) yields a corrected version of the face volume fraction $\tilde{\phi}_f^*$:

$$\tilde{\phi}_f^* = \tilde{\phi}_f \sqrt{\cos\theta} + \left(1 - \sqrt{\cos\theta}\right)\phi_f^{\tilde{U}Q} \tag{6.3.12}$$

where

$$\cos\theta = \frac{\nabla\phi \cdot \vec{d}}{\left|\nabla\phi\right|\left|\vec{d}\right|} \tag{6.3.13}$$

and $\vec{d}$ is a vector connecting cell centres adjacent to the face *f*.

The face volume fraction evolves from equations above:

$$\phi_f = \tilde{\phi}_f^* \left(\phi_A - \phi_U\right) + \phi_U \tag{6.3.14}$$

The HRIC scheme is less computationally expensive than the Geo-Reconstruct scheme and is more accurate for VOF calculations compared to second-order schemes or QUICK.

Temporal Discretization

For unsteady calculations the governing equations must be discretised in space and time. Every term in the differential equations must be integrated over a time step Δt.

A generic expression for the time evolution of a variable ϕ is given:

$$\frac{\partial\phi}{\partial t} = F\left(\phi\right) \tag{6.3.15}$$

where the function *F* includes any spatial discretization. The first-order accurate temporal discretization is given by

$$\frac{\phi^{n+1} - \phi^n}{\Delta t} = F\left(\phi\right) \tag{6.3.16}$$

and the second-order discretization is

$$\frac{3\phi^{n+1} - 4\phi^{n} + \phi^{n-1}}{2\Delta t} = F(\phi) \tag{6.3.17}$$

where

ϕ = scalar quantity

n+1 = value at the next time level, $t+\Delta t$

n = value at the current time level, t

n-1 = value at the previous time level, $t-\Delta t$

When the time derivative has been discretised, $F(\phi)$ can be evaluated by using a future time level with implicit time integration (equation (6.3.18)), or by using the current time level with explicit time integration (equation (6.3.19)).

- Implicit Time Integration

$$\frac{\phi^{n+1} - \phi^{n}}{\Delta t} = F\left(\phi^{n+1}\right) \tag{6.3.18}$$

This stable approach can be solved iteratively at each time level before moving to the next time step.

- Explicit Time Integration

$$\frac{\phi^{n+1} - \phi^{n}}{\Delta t} = F\left(\phi^{n}\right) \tag{6.3.19}$$

All cells in the domain must use the same time step which is limited by the Courant-Friedrich-Lewy condition.

The Courant-Friedrich-Lewy condition (CFL condition) can be written as follows:

$$\frac{\Delta t}{\Delta x_{cell} / v_{fluid}} < C \tag{6.3.20}$$

where Δt is the time step, Δx_{cell} is the length interval of the cell and v_{fluid} is the velocity of the fluid. The constant C depends on the particular equation to be solved and not on Δt and Δx_{cell} .

The CFL number can be defined as a necessary condition for convergence while solving partial differential equations numerically. It arises when explicit time-marching schemes are used for the numerical solution. As a consequence, the time step must be less than a certain time in explicit time-marching calculations; otherwise the simulation will produce widely incorrect results. For example, if a wave is crossing a discrete grid, then the time step must be less than the time for the wave to travel adjacent grid points. As a corollary, when the grid point separation is reduced, the upper limit for the time step also decreases. In essence, the numerical domain of dependence must include the analytical domain of dependence in order to assure that the scheme can access the information required to form the solution, *Courant et al. (1928)*.

6.3.4 Gradients and Derivatives

In previous sections gradients were used to compute values of a scalar at the cell faces. Additionally, gradients, such as $\nabla\phi$, can also be used for the calculation of secondary diffusion terms and velocity derivatives. Following methods can be distinguished:

- Green-Gauss Cell-Based
- Green-Gauss Node-Based
- Least Squares Cell-Based

Green-Gauss Theorem

Using the Green-Gauss theorem the gradient of the scalar ϕ at the cell centre *c0* can be written as follows:

$$\left(\nabla\phi\right)_{c0} = \frac{1}{\nu}\sum_{f}\bar{\phi}_f\vec{A}_f \tag{6.3.21}$$

where ϕ_f is the value of ϕ at the cell face centroid.

- Green-Gauss Cell-Based

  The face value $\bar{\phi}_f$ in equation (6.3.21) is taken from the arithmetic average of the values at the neighbouring cell centres:

$$\bar{\phi}_f = \frac{\phi_{c0} + \phi_{c1}}{2} \tag{6.3.22}$$

- Green-Gauss Node-Based

  $\bar{\phi}_f$ can also be calculated by the arithmetic average of the nodal values on the face:

$$\bar{\phi}_f = \frac{1}{N_f}\sum_{n}^{N_f}\bar{\phi}_n \tag{6.3.23}$$

  where N_f is the number of nodes on the face

- Least Squares Cell-Based

  The change in cell values between cell *c0* and *ci* along the vector δr_i can be shown in Figure 30 and equation (6.3.24):

$$\left(\nabla\phi\right)_{c0}\cdot\Delta r_i = \left(\phi_{ci} - \phi_{c0}\right) \tag{6.3.24}$$

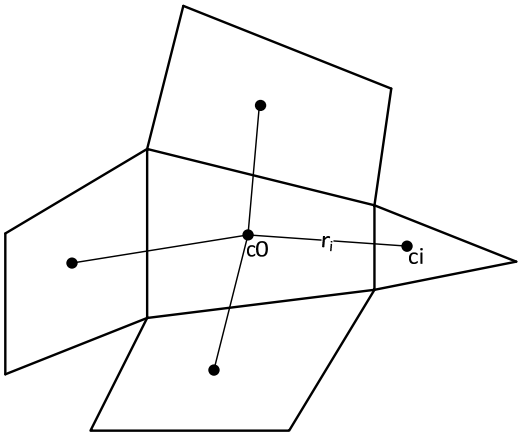

Figure 30: Cell centroid evaluation

For each cell surrounding cell *c0* following equation can be written:

$$[J](\nabla\phi)_{c0} = \Delta\phi \tag{6.3.25}$$

where [*J*] is the coefficient matrix. The cell gradient $\left(\nabla\phi_0 = \phi_x\hat{i} + \phi_y\hat{j} + \phi_z\hat{k}\right)$ is determined by solving the minimization problem for the system of the non-square coefficient matrix in a least-square approach. The coefficient matrix is solved by using Gram-Schmidt process, which gives a matrix of weights (W^x_{i0}, W^y_{i0}, W^z_{i0}) for each cell, *Anderson and Bonhus (1994)*.

Hence, the gradient at the cell centre can be calculated by multiplying the weight factors with the difference vector $\Delta\phi = (\phi_{c1} - \phi_{c0})$.

$$(\phi_x)_{c0} = \sum_{i=1}^{n} W^x{}_{i0} \cdot (\phi_{ci} - \phi_{c0}) \tag{6.3.26}$$

$$(\phi_y)_{c0} = \sum_{i=1}^{n} W^y{}_{i0} \cdot (\phi_{ci} - \phi_{c0}) \tag{6.3.27}$$

$$(\phi_z)_{c0} = \sum_{i=1}^{n} W^z{}_{i0} \cdot (\phi_{ci} - \phi_{c0}) \tag{6.3.28}$$

6.3.5 Pressure-Based Algorithm

The pressure-based algorithm evolved from a method called projection method proposed by *Chorin (1968)*. In this method the mass conservation of the velocity field is defined by the solution of a pressure or pressure correction equation which is derived from the continuity and momentum equations. The velocity field must satisfy the continuity.

Furthermore, it can be distinguished between two different pressure-based algorithms: the segregated and the coupled algorithm.

The governing equations in the pressure-based segregated algorithm are solved sequentially, all solution variables one after another, because they are non-linear and coupled and therefore carried out iteratively. This makes the solution convergence relatively slow.

Compared to the pressure-based segregated algorithm the pressure-based coupled algorithm is solved in a different manner. It solves a coupled system of equations implying the momentum equations and the pressure-based continuity equation. All the other equations are solved in a decoupled fashion like done in the segregated algorithm. The solution convergence is improved and the convergence process is sped up. The sequence of the calculation scheme for both is given in Figure 31.

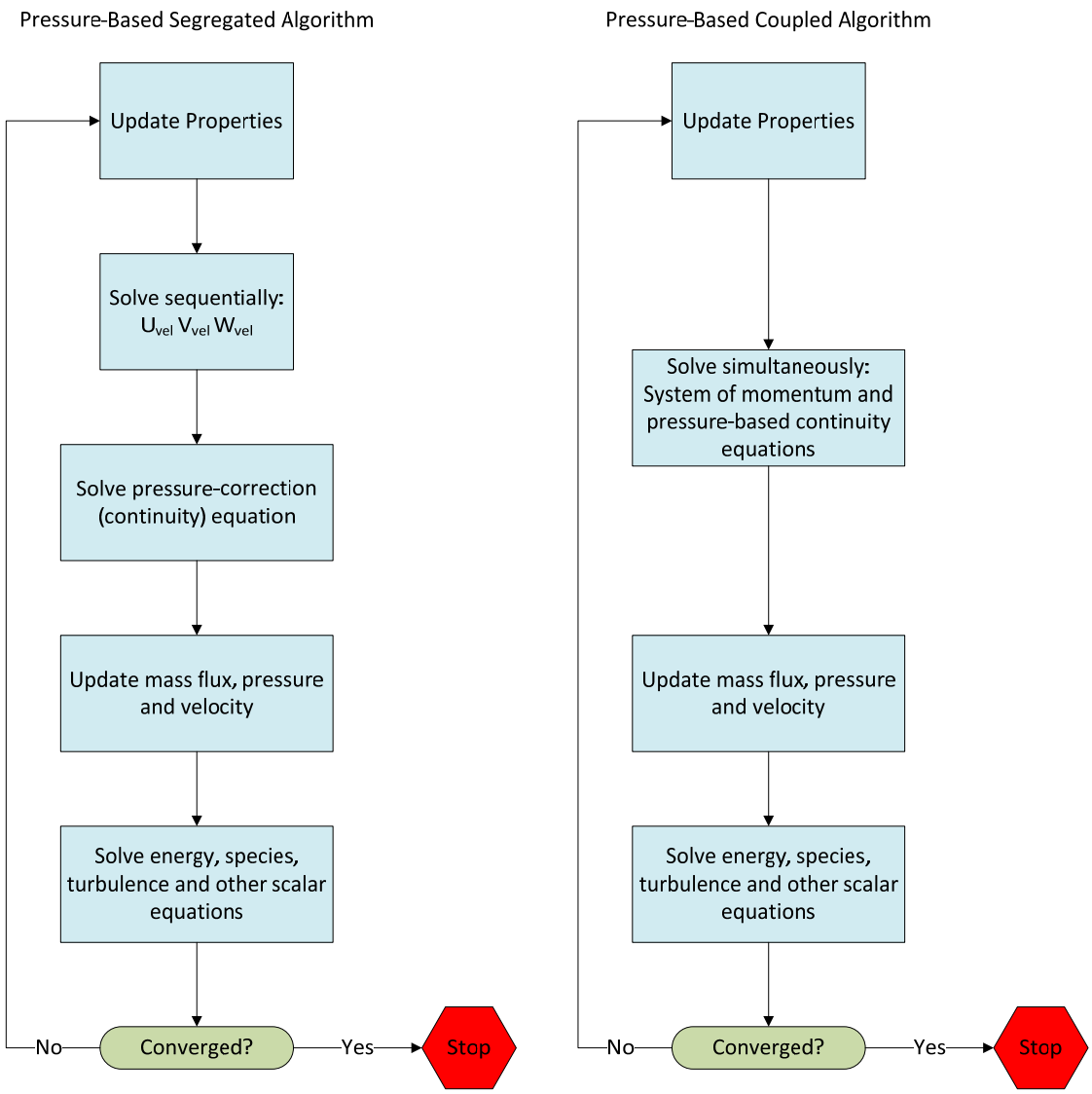

Figure 31: Pressure-based solution methods

Discretization of the Momentum Equation

The discretization of the momentum equation can be obtained by using the discretization schemes discussed in chapter 6.3.3. The equation can be written in its general form:

$$a_p\phi = \sum_{nb} a_{nb}\phi_{nb} + \sum p_f A \cdot \hat{i} + S \tag{6.3.29}$$

Since the pressure field and face mass fluxes are unknowns the pressure field can be obtained by a pressure interpolation scheme. It interpolates the values at the faces using momentum equation coefficients outlined by *Rhie and Chow (1983)*:

$$P_f = \frac{\frac{P_{c0}}{a_{p,c0}} + \frac{P_{c1}}{a_{p,c1}}}{\frac{1}{a_{p,c0}} + \frac{1}{a_{p,c1}}} \tag{6.3.30}$$

This method only works with a consistent pressure variation between cell centres and cannot be used on momentum terms with jumps or large gradients which would cause high pressure gradients at the cell faces.

Discretization of the Continuity Equation

Integration of the steady-state continuity equation over a control volume will give:

$$\sum_{f}^{N_{faces}} J_f A_f = 0 \tag{6.3.31}$$

where J_f is the mass flux through face f. The mass flux trough the face may be written:

$$J_f = \rho_f \frac{a_{p,c0} v_{n,c0} + a_{p,c1} v_{n,c1}}{a_{p,c0} + a_{p,c1}} + d_f \left(\left(p_{c0} + (\nabla p)_{c0} \cdot \vec{r}_0 \right) - \left(p_{c1} + (\nabla p)_{c1} \cdot \vec{r}_1 \right) \right) = \hat{J}_f + d_f \left(p_{c0} - p_{c1} \right) \tag{6.3.32}$$

where p_{c0} and p_{c1} are the pressures, $v_{n,c0}$ and $v_{n,c1}$ are the normal velocities and d_f is a function of $\overline{a}_P$ which is the average of the momentum equation a_P coefficient for the cell on either side of the face f.

Equation (6.3.32) is obtained by linear interpolation of the cell-centre velocities to the face centroids by using a momentum-weighted averaging algorithm introducing weighting factors based on the a_P coefficient from equation (6.3.29).

Pressure Velocity-Coupling

Pressure-velocity coupling is achieved by using equation (6.3.32) to derive an additional condition for pressure by reformatting the continuity equation (6.3.31). The flow problem can be solved in a segregated and a coupled way using different pressure-velocity coupling algorithms. In the following sections segregated and coupled algorithms will be addressed. The SIMPLE, SIMPLEC and PISO algorithm can be counted to the segregated algorithms.

The Simple Algorithm

The SIMPLE algorithm by *Caretto et al. (1972)* uses pressure corrections to update the velocities and to obtain the pressure field.

The resulting face flux $\hat{J}_f^*$ from equation (6.3.32) does not satisfy the continuity equation if the momentum equation is solved with a presumed pressure field *p**:

$$J_f^* = \hat{J}_f^* + d_f \left(p_{c0}^* - p_{c1}^* \right) \tag{6.3.33}$$

Therefore the correction term J_f' is added to the face flux J_f^* which gives the face flux:

$$J_f = J_f^* + J_f' \tag{6.3.34}$$

The SIMPLE algorithm implies that J' is:

$$J_f' = d_f \left(p_{c0}' - p_{c1}' \right) \tag{6.3.35}$$

where *p'* is the cell pressure correction.

When substituting equations (6.3.34) and (6.3.35) into the continuity equation (6.3.31) the equation for the pressure correction *p'* can be written as:

$$a_P p' = \sum_{nb} a_{nb} p_{nb}' + b \tag{6.3.36}$$

where *b* is the net flow rate into the cell:

$$b = \sum_{f}^{N_{faces}} J_f^* A_f \tag{6.3.37}$$

Equation (6.3.36) can be solved by using the algebraic multigrid (AMG) method, so that the cell pressure and the face flux are corrected using

$$p = p^* + \alpha_p p' \tag{6.3.38}$$

$$J_f = J_f^* + d_f \left(p'_{c0} - p'_{c1} \right) \tag{6.3.39}$$

where α_p is the under-relaxation factor for pressure. During each iteration the corrected face flux J_f satisfies the continuity equation.

The SIMPLEC Algorithm

There are various different SIMPLE algorithms in literature. One of them is the SIMPLEC (SIMPLE-Consistent) algorithm described by *Vandoormaal and Raithby (1984)*. The SIMPLEC procedure is very similar to the SIMPLE algorithm, but the flux correction J'_f is expressed differently. The equation (6.3.39) is the same as for the SIMPLE algorithm but the coefficient d_f is refined as a function of $\left(\overline{a_p - \sum_{nb} a_{nb}} \right)$. This method considerably accelerates convergence problems where pressure-velocity coupling causes troubles to obtain a solution.

The PISO Algorithm

The PISO algorithm of *Issa (1986)* stands for Pressure Implicit with Splitting of Operators. It is an extension of the SIMPLE algorithm and involves a predictor step for the solution of the pressure-velocity correction and two corrector steps, neighbour correction and skewness correction.

The Coupled Algorithm

The Coupled algorithm offer some advantages over the segregated or non-coupled algorithms. When the mesh is of poor quality or large time steps are used the Coupled algorithm still gives robust and stable results for transient flows.

As previously mentioned, the Coupled algorithm solves the momentum and pressure-based continuity equations together. A coupling is achieved by an implicit discretization of both, the pressure gradient terms in the momentum equations and the mass face flux.

The pressure gradient for the component *k* in the momentum equation can be written as:

$$\sum_f p_f A_k = -\sum_j a^{u_k p} p_j \tag{6.3.40}$$

where $a^{u_k p}$ is the coefficient computed from the Gauss divergence theorem and coefficients of the pressure interpolation schemes, see equation (6.3.30). The discretised momentum equation for component u_k can then be defined as:

$$\sum_j a_{ij}^{u_k u_k} u_{kj} + \sum_j a_{ij}^{u_k p} p_j = b_i^{u_k} \tag{6.3.41}$$

By expressing the balance of fluxes in equation (6.3.31) with the flux in equation (6.3.32) results in the following:

$$\sum_k \sum_j a_{ij}^{p u_k} u_{kj} + \sum a_{ij}^{pp} p_j = b_i^p \tag{6.3.42}$$

After δ-transformation the system of equations (6.3.41) and (6.3.42) has this form:

$$\sum_j \left[A \right]_{ij} \vec{X}_j = \vec{B}_i \tag{6.3.43}$$

where the influence of a cell *i* on a cell *j* has the form of the matrix:

$$A_{ij} = \begin{pmatrix} a_{ij}^{pp} & a_{ij}^{pu} & a_{ij}^{pv} & a_{ij}^{pw} \\ a_{ij}^{up} & a_{ij}^{uu} & a_{ij}^{uv} & a_{ij}^{uw} \\ a_{ij}^{vp} & a_{ij}^{vu} & a_{ij}^{vv} & a_{ij}^{vw} \\ a_{ij}^{wp} & a_{ij}^{wu} & a_{ij}^{wv} & a_{ij}^{ww} \end{pmatrix} \tag{6.3.44}$$

and the unknown and residual vectors have the form

$$\vec{X}_j = \begin{bmatrix} p_i' \\ u_i' \\ v_i' \\ w_i' \end{bmatrix} \tag{6.3.45}$$

$$\vec{B}_i = \begin{bmatrix} -r_i^p \\ -r_i^u \\ -r_i^v \\ -r_i^w \end{bmatrix} \tag{6.3.46}$$

Under-Relaxation of Variables and Equations

Under-relaxation of variables is used to control the change of ϕ during each iteration. The new value of the variable ϕ within a cell depends upon the old value ϕ_{old} and the change in ϕ and the under-relaxation factor α.

$$\phi = \phi_{old} + \alpha \Delta \phi \tag{6.3.47}$$

The under-relaxation of equations is used to stabilise the convergence behaviour of the non-linear iterations by introducing selective amounts of ϕ in the system of discretised equations.

$$\frac{a_p \phi}{\alpha} = \sum_{nb} a_{nb} \phi_{nb} + b + \frac{1-\alpha}{\alpha} a_p \phi_{old} \tag{6.3.48}$$

The Courant-Friedrich-Lewy (CFL) number is a solution parameter in the pressure-based coupled algorithm and can be written in terms of α, see details in chapter 6.3.3:

$$\frac{1-\alpha}{\alpha}=\frac{1}{CFL} \tag{6.3.49}$$

6.3.6 Density-Based Algorithm

The density-based algorithm solves the governing equations of continuity, momentum, energy and species transport in a coupled way. All other equations are solved segregated from one another. Because of the non-linearity of the governing equations, several iteration of the solution loop must be performed before a converged solution is obtained, see Figure 32.

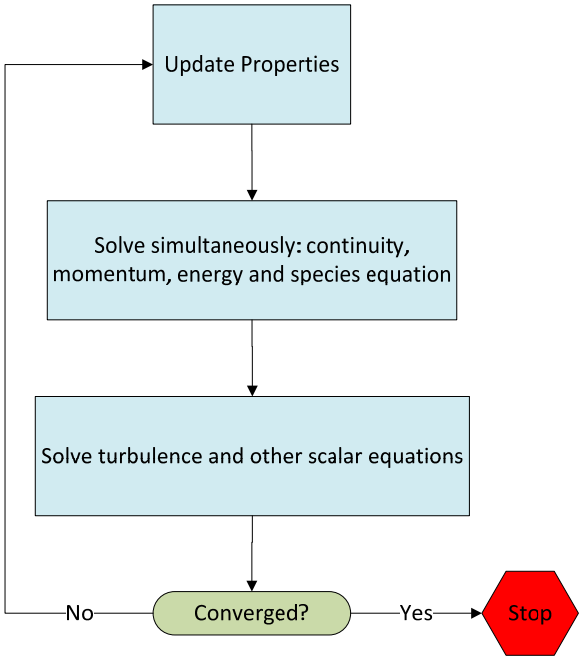

Figure 32: Density-based solution method

The coupled system of equations can be solved either explicitly or implicitly, *Fluent (2006)*.

- explicit: for a given variable, the unknown value in each cell is computed using a relation that includes only existing values. Therefore each unknown will appear in only one equation in the system and the equations for the

unknown value in each cell can be solved one at a time to give the unknown quantities.

- implicit: For a given variable, the unknown value in each cell is computed using a relation that includes both existing and unknown values from neighbouring cells. Therefore each unknown will appear in more than one equation in the system, and these equations must be solved simultaneously to give the unknown quantities.

6.4 Turbulence Model: Standard *k*-ε Model

6.4.1 General Remarks

Most flows encountered in engineering practice are turbulent and become unstable above a certain Reynolds number. Flows at a low Reynolds number are laminar whereas flows at a high Reynolds number are turbulent. These turbulent flows characterised by fluctuations which create additional unknown variables in the modified governing equations in the velocity fields can be calculated with various methods. One of the simplest of turbulence models are two-equation models in which the solution of two separate transport equations allows the turbulent velocity and length scales to be independently determined. The standard *k*-ε model is such a turbulence model and has been used frequently in practical engineering for flow calculations in the time since it was proposed by *Launder and Spalding (1972)*. Excellent performance for many industrially relevant flows and being the most widely validated turbulence model make the *k*-ε turbulence model very popular in engineering and numerical solutions in general. It is a semi-empirical model based on model transport equations for the turbulence kinetic energy *k* and its dissipation rate ε. The model transport *k*-equation is derived from the exact production term, whilst some terms in the model transport ε–equation are obtained empirically. Moreover, the flow must be fully turbulent and the effects of molecular viscosity negligible in order to be applied as a turbulence model.

6.4.2 Transport Equations for the *k*-ε Model

The turbulence kinetic energy *k* and its rate of dissipation ε are obtained from the transport equations shown below:

$$\frac{\partial}{\partial t}(\rho k)+\frac{\partial}{\partial x_i}(\rho k u_i)=\frac{\partial}{\partial x_i}\left[\left(\mu+\frac{\mu_t}{\sigma_k}\right)\frac{\partial k}{\partial x_j}\right]+G_k+G_b-\rho\varepsilon-Y_M+S_k \tag{6.4.1}$$

and

$$\frac{\partial}{\partial t}(\rho\varepsilon)+\frac{\partial}{\partial x_i}(\rho\varepsilon u_i)=\frac{\partial}{\partial x_j}\left[\left(\mu+\frac{\mu_t}{\sigma_\varepsilon}\right)\frac{\partial\varepsilon}{\partial x_j}\right]+C_{1\varepsilon}\frac{\varepsilon}{k}(G_k+C_{3\varepsilon}G_b)-C_{2\varepsilon}\rho+S_\varepsilon \tag{6.4.2}$$

In words the equations are:

Rate of change of *k* or ε + **Transport of *k* or ε by convection** = **Transport of *k* or ε by diffusion** + **Rate of production of *k* or ε** - **Rate of destruction of *k* or ε** + **User-defined source terms**

In these equations, σ_k and σ_ε are the turbulent Prandtl numbers for k and ε, respectively G_k represents the generation of turbulence kinetic energy due to the mean velocity gradients. G_b is the generation of turbulence kinetic energy due to buoyancy. Y_M represents the contribution of the fluctuating dilatation in compressible turbulence to the overall dissipation rate. $C_{1\varepsilon}$, $C_{2\varepsilon}$, and $C_{3\varepsilon}$ are constants and S_k and S_ε are user-defined source terms.

The turbulent (or eddy) viscosity , μ_t, is computed by combining k and ε as follows:

$$\mu_t=\rho C_\mu\frac{k^2}{\varepsilon} \tag{6.4.3}$$

where C_μ is a constant.

The model constants $C_{1\varepsilon}$, $C_{2\varepsilon}$, C_{μ}, σ_k and σ_{ε} have the following default values:

$$C_{1\varepsilon}=1.44,\ C_{2\varepsilon}=1.92,\ C_{\mu}=0.09,\ \sigma_k=1.0,\ \sigma_{\varepsilon}=1.3$$

These five adjustable constants have been obtained from experiments with air and water for fundamental turbulent shear flows, *Holmes and Connell (1989)*. They have been found to work a wide range of turbulent flows such as wall-bounded and free shear flows.

6.4.3 Turbulent Kinetic Energy Due to Mean Velocity Gradients in the *k-ε* Models

The production of turbulence kinetic energy represented by G_k from the exact equation for the transport of *k*, this term may be defined as:

$$G_k=-\rho\overline{u_i'u_j'}\frac{\partial u_j}{\partial x_i} \tag{6.4.4}$$

Another way to evaluate G_k is to make use of an extended Boussinesq relationship,

$$G_k=\mu_t S^2 \tag{6.4.5}$$

where S is the modulus of the mean rate-of-strain tensor, defined as

$$S\equiv\sqrt{2S_{ij}S_{ij}} \tag{6.4.6}$$

6.4.4 Turbulent Kinetic Energy Due to Buoyancy in the *k-ε* Models

In the *k-ε* turbulence models the *k*-term is generated in equation (6.4.1) due to buoyancy (G_b) as well as the *ε*-term in equation (6.4.2) when a non-zero gravity field and temperature gradient are present simultaneously. The generation of turbulence due to buoyancy is given by

$$G_b = \beta g_i \frac{\mu_t}{\mathrm{Pr}_t} \frac{\partial T}{\partial x_i} \tag{6.4.7}$$

where g_i is the component of the gravitational vector in the ith direction and Pr_t with a default value of 0.85 is the turbulent Prandtl number for energy. The coefficient of thermal expansion β is defined as

$$\beta = -\frac{1}{\rho}\left(\frac{\partial \rho}{\partial T}\right)_p \tag{6.4.8}$$

For ideal gases, equation (6.4.7) modulates to

$$G_b = -g_i \frac{\mu_t}{\rho \mathrm{Pr}_t} \frac{\partial \rho}{\partial x_i} \tag{6.4.9}$$

For unstable thermal stratification the turbulence kinetic energy tends to increase ($G_b > 0$) in contrary to the stable case where buoyancy tends to suppress the turbulence ($G_b < 0$). Though the buoyancy effects on the generation of *k* are known very well, the effect on ε is not as obvious. For that reason the buoyancy effects on ε are neglected by setting G_b to zero in the transport equation (6.4.2).

However, the value of G_b given by equation (6.4.9) is used in the transport equation (6.4.2) when the buoyancy effects on ε are included.

The constant $C_{3\varepsilon}$ determines the degree to which ε is affected by the buoyancy according to the following relation *Henkes et al. (1991)*:

$$C_{3\varepsilon} = \tanh\left|\frac{v}{u}\right| \tag{6.4.10}$$

where *v* is the component of the flow velocity parallel to the gravitational vector and *u* is the component of the flow velocity perpendicular to the gravitational vector. If the main flow is aligned with the direction of gravity $C_{3\varepsilon}$ will become 1 for

buoyant shear layers; if the main flow is perpendicular to the gravitational vector $C_{3\varepsilon}$ will become zero for buoyant shear layers.

6.5 Dynamic Mesh

6.5.1 General Remarks

The dynamic mesh model can be used in flow cases where the shape of the domain, respectively the boundaries, is changing with time. These changes can either be prescribed motions with specified changes in linear and/or angular velocities about the centre of gravity or unspecified motions where the linear and angular velocities of the centre of gravity of a solid body are calculated based on the force balance on the body. This body can then move in six-degrees-of-freedom. Each time step the volume mesh is updated with the new position of the boundaries. The volume mesh can be updated with one of the following methods or a combination of them:

- smoothing methods
    - Laplacian smoothing
    - spring-based method
- dynamic layering
- local remeshing

These smoothing methods and local remeshing will be explained in detail in chapter 6.5.3. Beforehand some important equations will be discussed in chapter 6.5.2.

6.5.2 Conservation Equations

The integral form of the conservation equation for a general scalar ϕ on randomly chosen control volume *V* with a moving boundary can be written as

$$\frac{d}{dt}\int_V \rho\phi dV + \int_{\partial V} \rho\phi\left(\vec{u}-\vec{u}_g\right)\cdot d\vec{A} = \int_{\partial V} \Gamma\nabla\phi\cdot d\vec{A} + \int_V S_\phi dV \qquad (6.5.1)$$

where

ρ is the fluid density

$\vec{u}$ is the flow velocity vector

$\vec{u}_g$ is the grid velocity of the moving mesh

Γ is the diffusion coefficient

S_ϕ is the source term of ϕ

Here ∂V is used to represent the boundary of the control volume V.

The time derivative term in equation (6.5.1) can be written, using a first-order backward difference formula, as

$$\frac{d}{dt}\int_V \rho\phi dV = \frac{(\rho\phi V)^{n+1} - (\rho\phi V)^n}{\Delta t} \tag{6.5.2}$$

where n denotes the respective quantity at the current time level and n+1 at the next time level. The (n+1)th time level volume V^{n+1} is computed from

$$V^{n+1} = V^n + \frac{dV}{dt}\Delta t \tag{6.5.3}$$

where dV/dt is the volume time derivative of the control volume. In order to satisfy the grid conservation law, the volume time derivative of the control volume is computed from

$$\frac{dV}{dt} = \int_{\partial V} \vec{u}_g \cdot d\vec{A} = \sum_j^{n_f} \vec{u}_{g,j} \cdot \vec{A}_j \tag{6.5.4}$$

where n_f is the number of faces on the control volume and $\vec{A}_j$ is the j face area vector. The dot product $\vec{u}_{g,j} \cdot \vec{A}_j$ on each control volume face is calculated from

$$\vec{u}_{g,j} \cdot \vec{A}_j = \frac{\delta V_j}{\Delta t} \tag{6.5.5}$$

where δV_j is the volume swept out by the control volume face j over the time step Δt.

6.5.3 Dynamic Mesh Update Methods

Laplacian Smoothing Method

The Laplacian smoothing method is the simplest among the dynamic mesh update methods. It repositions each internal fluid node equidistant to the nodes connected to it, see Figure 33.

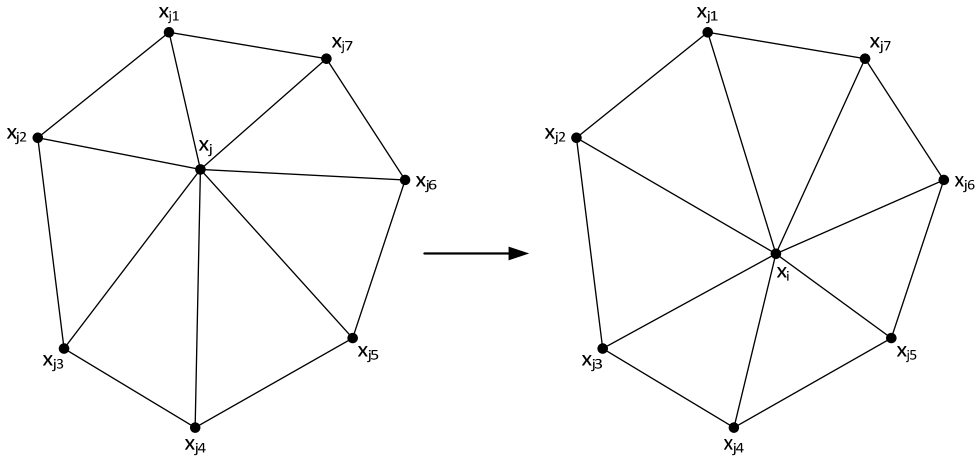

Figure 33: Laplacian algorithm

Unfortunately this method does not guarantee an improvement on the mesh quality but it is fairly computationally inexpensive. The node position at the current time step is:

$$\overline{\vec{x}_i^m} = \frac{\sum_j^{n_i} \vec{x}_j^m}{n_i} \tag{6.5.6}$$

where $\overline{\vec{x}_i^m}$ is the average node position of node *i* at iteration *m*, $\vec{x}_j^m$ is the node position of neighbour node $\vec{x}_i^m$ at iteration *m*, and n_i is the number of nodes neighbouring node *i*. The computation of the node position $\vec{x}_i^{m+1}$ at the next iteration works as follows:

$$\vec{x}_i^{m+1} = \vec{x}_i^m \left(1-\beta\right) + \overline{\vec{x}_i^m}\beta \tag{6.5.7}$$

where β is the boundary node relaxation factor.

Spring-Based Smoothing Method

The spring-based smoothing method is a physics-based mesh updating procedure where the edges of the mesh are replaced with fictitious linear springs. It is assumed that the springs in the initial mesh are in equilibrium. A displacement at a given boundary node will generate a force proportional to the displacement along all the springs connected to the node. The displacement of the nodes can be computed using the generalised Hook's Law and the force on a mesh node can be written as

$$\vec{F}_i = \sum_j^{n_i} k_{ij}\left(\Delta\vec{x}_j - \Delta\vec{x}_i\right) \tag{6.5.8}$$

where $\vec{F}$ is the force vector, n_i, is the number of neighbouring nodes connected to node *i*, k_{ij} is the stiffness between node *i* and its neighbour *j* and $\Delta\vec{x}_i$ and $\Delta\vec{x}_j$ are the displacements of node *i* and its neighbour *j*,. The stiffness k_{ij} of the spring connecting nodes *i* and *j* is chosen to be inversely proportional to the length of the edge and is defined as

$$k_{ij} = \frac{1}{\sqrt{\left|\vec{x}_i - \vec{x}_j\right|}} \tag{6.5.9}$$

The net force on a node due to all the springs connected to the node must be zero when it is assumed that the springs which connect the vertices in the undeformed mesh are in tension. The new nodal positions of the internal nodal points can be computed using:

$$[k]\{x\} = 0 \qquad \text{for } x = \bar{x} \text{ on } \Gamma_b \tag{6.5.10}$$

where x is the position vector and $\bar{x}$ is the known position vector of the moving boundary Γ_b.

This condition results in an equation solved by the Jacobi sweep on all interior nodes:

$$\Delta\vec{x}_i^{m+1} = \frac{\sum_j^{n_i} k_{ij}\Delta\vec{x}_j^m}{\sum_j^{n_i} kij} \tag{6.5.11}$$

At convergence, the positions are updated such that

$$\vec{x}_i^{n+1} = \vec{x}_i^n + \Delta\vec{x}_i^{m,converged} \tag{6.5.12}$$

where n defines the position at the current time step and $n+1$ defines the position at the next time step. The spring-based smoothing is shown in Figure 34 and Figure 35 for a cylindrical cell zone where one end of the cylinder is moving, *Fluent (2006)*.

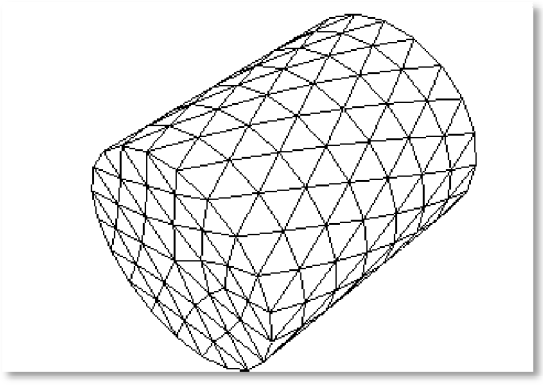

Figure 34: Spring-based smoothing on interior nodes: start

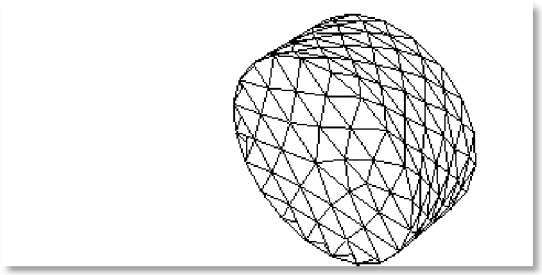

Figure 35: Spring-based smoothing on interior nodes: end

Local Remeshing Method

The cell quality can be strongly influenced by large boundary displacements compared to the local cell size which can lead to negative cell volumes and in the end cause convergence problems. Therefore, areas with faces or cells that do not comply with size or skewness criteria will be locally updated with new cells. The skewness and size criteria that have to be met in order to be updated are:

- It has a skewness that is greater than a specified maximum skewness.
- It is smaller than a specified minimum length scale.
- It is larger than a specified maximum length scale.
- Its height does not meet the specified length scale

Face Region Remeshing Method: Also linear and triangular faces on a deforming boundary can be remeshed according to the minimum and maximum length scale. A region of deforming boundary faces is marked for remeshing; the remeshing algorithm replaces marked faces and adjacent cells with a regular mesh on the deforming boundary at the moving boundary, see Figure 36. This method makes it possible to remesh domains with symmetric boundary conditions and across multiple face zones preserving all features within a face zone and between different face zones.

As an example: A simple tetrahedral mesh of a cylinder having a moving bottom wall is given, (see Figure 36). On the moving boundary, a single loop is generated at the bottom end of the cylinder because the nodes are moving. Thereafter the height of the faces connected to the nodes on the loop is analysed and the faces are split or merged depending on the specified maximum or minimum length scale.

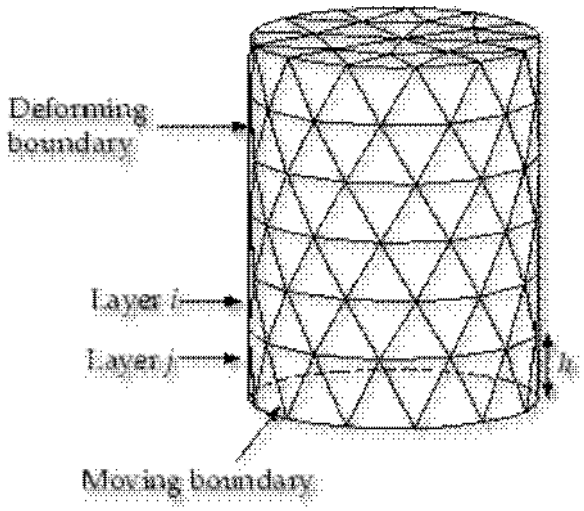

Figure 36: Remeshing at a deforming boundary, *Fluent (2006)*

If the faces in layer *j* are expanding, they are allowed to expand until the maximum length scale is reached; vice versa, if the layer *j* is contracting, faces are allowed to contract until the minimum length scale is reached.

When either of this condition is met, the compressed layer *j* of faces is merged into the layer *i* of faces above it, see Figure 37 and Figure 38.

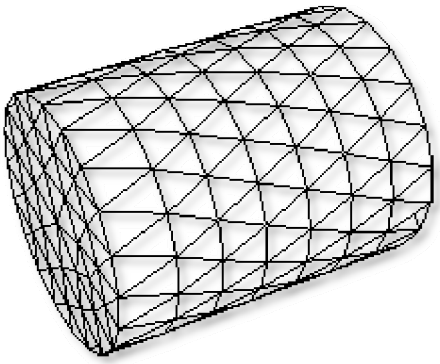

Figure 37: Expanding cylinder before region face remeshing, *Fluent (2006)*

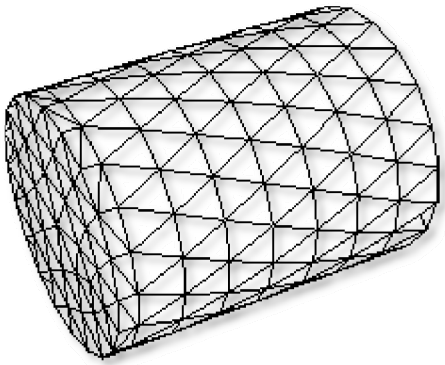

Figure 38: Expanding cylinder after region face remeshing, *Fluent (2006)*

Local Face Remeshing Method: In contrary to the local region remeshing method the local face remeshing method only applies to 3D geometries. Based on the face

skewness on the deforming boundary the faces and adjacent cells are remeshed. Remeshing across multiple face zones is not allowed.

6.5.4 Six DOF Solver

The six DOF solver computes the translational and angular motion of the centre of gravity of a rigid body by taking its forces and moments into account. The mass centre translation is governed by Newton's law of motion, equation (6.5.13), which are written in the inertial coordinate system.

$$\dot{\vec{v}}_G = \frac{1}{m}\sum \vec{f} \tag{6.5.13}$$

where $\dot{\vec{v}}_G$ is the translational acceleration of the centre of gravity, m is the mass, and $\vec{f}$ is the applied force vector through the centre of mass which has been broken into three components, namely $\vec{f} = \vec{f}_H + \vec{f}_E + \vec{f}_G$ where $\vec{f}_H$ are the hydrodynamic forces, $\vec{f}_E$ are the external forces and $\vec{f}_G$ are the forces due to gravity. Basically, these forces are determined by the gravitational force of the ship hull, the hydrostatic force of the floodwater, the hydrodynamic force of the floodwater in the hull as well as the hydrodynamic force of the water surrounding the ship acting on the shell of the hull.

Newton's law can be integrated directly to give the position of the mass centre as a function of time. Holding $\vec{f}$ constant over the discrete physical time step $\left(t^n, t^{n+1}\right)$ gives equation (6.5.14)

$$\vec{r}\left(t^{n+1}\right) = \frac{1}{2}\frac{\vec{f}}{m}\Delta t^2 + \vec{v}_G\left(t^n\right)\Delta t + \vec{r}\left(t^n\right) \tag{6.5.14}$$

It is easier to compute the angular acceleration of the object $\dot{\vec{\omega}}_B$, equation (6.5.15), by using body coordinates.

$$\dot{\vec{\omega}}_B = L^{-1}\left(\sum \vec{M}_B - \vec{\omega}_B \times L\vec{\omega}_B\right) \tag{6.5.15}$$

where L is the inertia tensor, $\vec{M}_B$ is the moment vector of the body, and $\vec{\omega}_B$ is the rigid body angular velocity vector.

The moments are transformed from inertial to body coordinates using

$$\vec{M}_B = R\vec{M}_G \tag{6.5.16}$$

where R is the following transformation matrix:

$$\begin{pmatrix} C_\theta C_\psi & C_\theta S_\psi & S_\theta \\ S_\phi S_\theta C_\psi - C_\phi S_\psi & S_\phi S_\theta S_\psi + C_\phi C_\psi & S_\phi C_\theta \\ C_\phi S_\theta C_\psi + S_\phi S_\psi & C_\phi S_\theta S_\psi - S_\phi C_\psi & C_\phi C_\theta \end{pmatrix}$$

where $C_\chi = \cos(\chi)$ and $S_\chi = \sin(\chi)$. The angles ϕ, rotation about the x-axis (e.g., roll), θ, rotation about the y-axis (e.g., pitch) and ψ, rotation about the z-axis (e.g., yaw), represent the Euler angles.

After having derived the angular and the translational accelerations from equation (6.5.13) and equation (6.5.15), the rates are calculated by numerical integration, *Snyder et al. (2003)* and the rigid body position will be updated.

6.6 Concluding Remarks

The numerical methods to simulate the flooding of a ship with CFD have been presented in this chapter. First, the basic fluid flow equations were discussed briefly in order to make understand the principles used in later chapters. Then, the author went into details for free surface flows - which is the case in flooding scenarios - where special emphasis was put on the VOF model by *Hirt and Nichols (1981)* and surface tracking and interpolation techniques. Next, two solver algorithms were reviewed: the pressure-based and the density-based algorithm whereas the

importance of the pressure-based algorithm was stressed out by examination of the discretization schemes and, in particular, the pressure-velocity coupling algorithms. As high flow velocities at the damage opening are expected in the beginning of the flooding process it was decided to include a turbulence model in the simulation. From all of the available turbulence models the k-ε turbulence model by *Launder and Spalding (1972)* was chosen for its stability and its excellent performance. The mathematical theory for this model is presented in chapter 6.4. The implementation of ship motions due to flooding is a more complex one. It succeeds in adding the dynamic mesh method with a six DOF solver. An overview of mesh update methods is given in chapter 6.5 which also includes a description of the six DOF motion solver and the changes which have to be made in the governing conservation equations.

The next chapter will adumbrate the implementation of the numerical methods into the CFD model and discuss about the advantages, disadvantages and limitations of the previously mentioned methods.

7 Implementation

7.1 General Remarks

The physical and numerical background to carry out flooding simulations was presented in the previous chapters 5 and 6. Current chapter will describe the implementation of the numerical methods and techniques and will give important information about the procedure of the simulation set-up.

In general, a CFD analysis or any other numerical analysis should always pass through following basic steps:

- Problem identification and pre-processing
    - Definition of the modelling goals
    - Identification of the domain
- Solver execution
    - Set-up of the numerical model
    - Computation and monitoring of the solution
- Post-processing
    - Examination of the results
    - Consideration of revisions to the model

The basic structure of the CFD modelling routine can also be presented in a flow chart which shows the dependencies of the steps from each other, see Figure 39. It also shows that every process that is linked to the solver can influence the numerical result that is visualised and analysed in the post-processor.

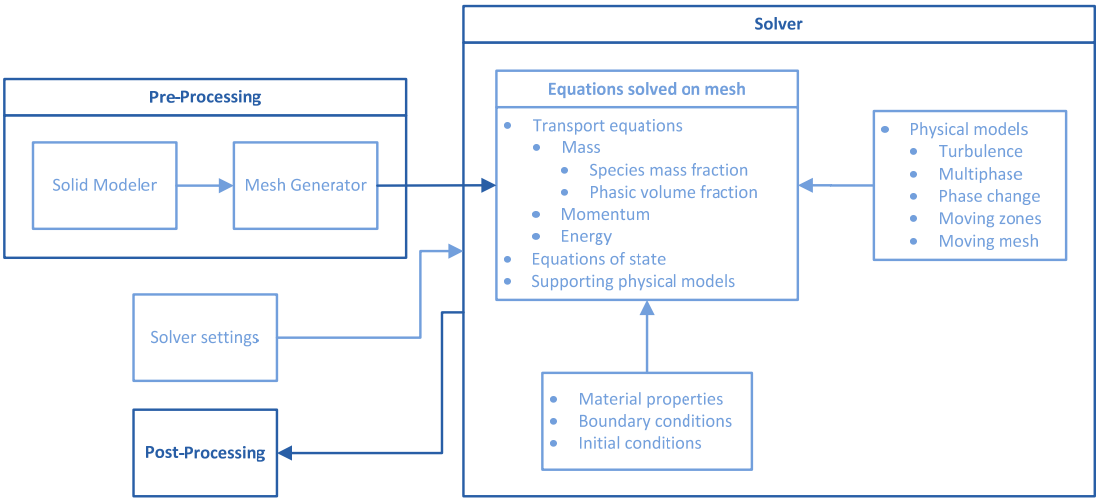

Figure 39: Structure of the CFD modelling

The basic steps and the structure of CFD modelling will be discussed in following sections of this chapter.

7.2 Problem Identification and Pre-Processing

7.2.1 Definition of Modelling Goals

When the modelling goals are defined following questions need to be risen:

What are the desired results and how will they be used? What physical models need to be included to the analysis? What simplifying assumptions have to be made or can be made? What degree of accuracy is required? How quickly are results needed? Answers to above questions regarding flooding can be found below.

Hence, for flooding simulations it has to be distinguished between two cases:

- the static case where the flooded structure is not influenced by ship motion and the sea state
- the dynamic case which includes ship motions.

Based on this determination a decision about the modelling goals can be taken.

The main reason for doing CFD calculations is to find an estimate TTF (time-to-flood) and ship motions if available in an integrated approach. The TTF is characterised by floodwater volume or floodwater height over time for the flooded area. In some cases when the ship is flooded in quasi-static conditions the TTF can also be obtained by disregarding ship motions which simplifies the CFD model extremely. When the flooding motions are taken into account the desired dynamic data are ship motions such as heave, roll and pitch. These values should give a sufficiently accurate picture of the safety of a ship.

For both, the static and the dynamic flooding case some physical models are identical and can be generalised. However, a common physical model that appears in both models is the presence of a free surface with at least two phases, air and water. It is the goal to track the interface between the phases as accurately as possible.

Depending upon the head pressure on the damage opening and the internal openings and depending upon the size of the openings high flow velocities with high Reynolds numbers can occur which may cause turbulent flows.

In chapter 5.1.4 the occurrence of trapped air was discussed and this physical model should be accounted for as it can have a major influence on the TTF.

When the damaged model can float freely, ship motions need to be regarded such as is in the dynamic case.

Another criterion that can influence the goal definition is the availability of eligible validation data. Validation data is usually obtained either by model tests or by other already validated numerical methods. The available validation data has a main influence upon the design process of the CFD model because as a result the computed CFD data has to be comparable. For that reason it is the user's primary goal to design the CFD model in a way to obtain adequate data for comparison which does not mean that the CFD model has to be an exact replication of the validation model. In fact the CFD model must be an appropriately adapted and

possibly simplified model according to the limitation of the numerical and physical models that are used.

A high degree of accuracy is required to make the CFD method more valuable compared to other numerical methods with less computational expenses. This accuracy can be achieved by the design of a sophisticated numerical domain and by integration of above listed physical models as well as a well chosen time step size and discretization method. Taking all this into account quick results cannot be expected and should not be prioritised for the time being.

7.2.2 Identification of the Modelled Domain

In previous section two different flooding cases were distinguished: the principle of the domain set-up for both cases is similar but slightly differs in some details. These details are discussed below for each case, the static case and the dynamic case.

Static case:

For this case two domains with an optional third domain are used, see Figure 40. The required domains are the actual geometry of the superstructure and the water reservoirs for the damage openings. The optional third domain is used for air ventilation ducts necessary for cases which do not consider trapped or compressible air. The damage openings are connected to water reservoirs that are permanently refilled with water through pressure inlet boundary conditions on the bottom of the reservoirs. The pressure inlet boundary conditions provide a constant head pressure to the damage openings; therefore it is applied horizontally. The total pressure for an incompressible fluid is defined as

$$p_0 = p_s + \frac{1}{2}\rho|\vec{v}|^2 \tag{7.2.1}$$

where p_0 is the total pressure, p_s is the static pressure and v is the flow velocity. The pressure field on the pressure inlet boundary condition will also include the

hydrostatic head. The hydrostatic head, denoted *p'*, is obtained by redefining the pressure in terms of a modified pressure.

$$p' = p + \rho_0 \vec{g} \cdot \vec{r} \tag{7.2.2}$$

where ρ_0 is a constant reference density, $\vec{g}$ is the gravity vector, and

$$\vec{r} = x\hat{i} + y\hat{j} + z\hat{k} \tag{7.2.3}$$

is the position vector. Allowing for

$$\nabla\left(\rho_0 \vec{g} \cdot \vec{r}\right) = \rho_0 \vec{g} \tag{7.2.4}$$

it follows

$$\nabla p' = \nabla\left(p + \rho_0 \vec{g} \cdot \vec{r}\right) = \nabla p - \rho_0 \vec{g} \tag{7.2.5}$$

The substitution of this relation in the momentum equation gives pressure gradient and gravitational body force terms of the form

$$\nabla p' + \left(\rho - \rho_0\right)\vec{g} \tag{7.2.6}$$

where ρ is the fluid density. As the fluid density is constant, the reference density ρ_0 can be set equal to the fluid density, thereby eliminating the body force term.

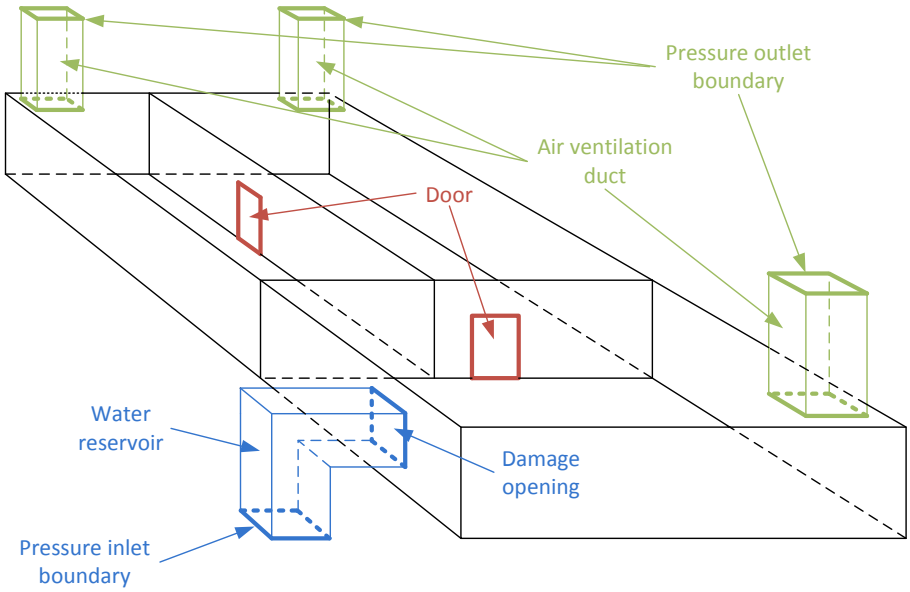

Figure 40: Schematic view of static flooding domain

It is essential to make sure that the boundary conditions are not influencing each other by keeping an ample distance between them. Nevertheless it should be paid attention to keep the water reservoir domain as small as possible to save computational resources. If the model makes use of the optional third domain pressure outlet boundary conditions have to be applied on top of the air ventilation ducts in order to allow air to escape. The pressure outlet boundary condition allows for a backflow of the air which means that air can enter and exit through the pressure outlet boundary. This backflow is controlled by the constant operating pressure and the relative static pressure. The static pressure at the pressure outlet is relative to the operating pressure of the whole domain which is obviously defined as the atmospheric pressure. At the pressure outlet the static pressure p_s is used for calculations and all other conditions are extrapolated from the interior domain.

Dynamic case:

Ideally, five domains, see Figure 41, are used for the dynamic case: the flooded structure of the ship, the water tank, room for air above the water tank, a moving air and water domain around the ship. The moving domains are rigid and follow the

motion of the ship during the dynamic mesh update. The mesh of the water tank and the room for air around the moving domain are deformed according to the data obtained by the six degrees-of-freedom algorithm. The space on the ship which will not be affected by flooding is not modelled and therefore assigned as void space.

When water flows into the ship the water level of the water tank can vary slightly. By introduction of a pressure inlet on the bottom of the water tank and a pressure outlet on top of the air domain above the water tank, the water level can be controlled and occurring waves in the tank are damped; water can exit and enter the pressure inlet boundary on the bottom of the tank and air can enter and exit the domain through the pressure outlet on top of the air domain. This is achieved by defining a predefined backflow condition on the pressure boundaries. The pressure inlet and outlet boundary conditions are working on the same principle as described above in the static case.

The damage openings can be placed on the bottom of the hull for bottom damage or on the side of the hull for side damage and are assigned as interior boundary condition. Optionally, openings for air ventilation, which are as well assigned as interior boundary condition, can be placed on top of the superstructure of the ship.

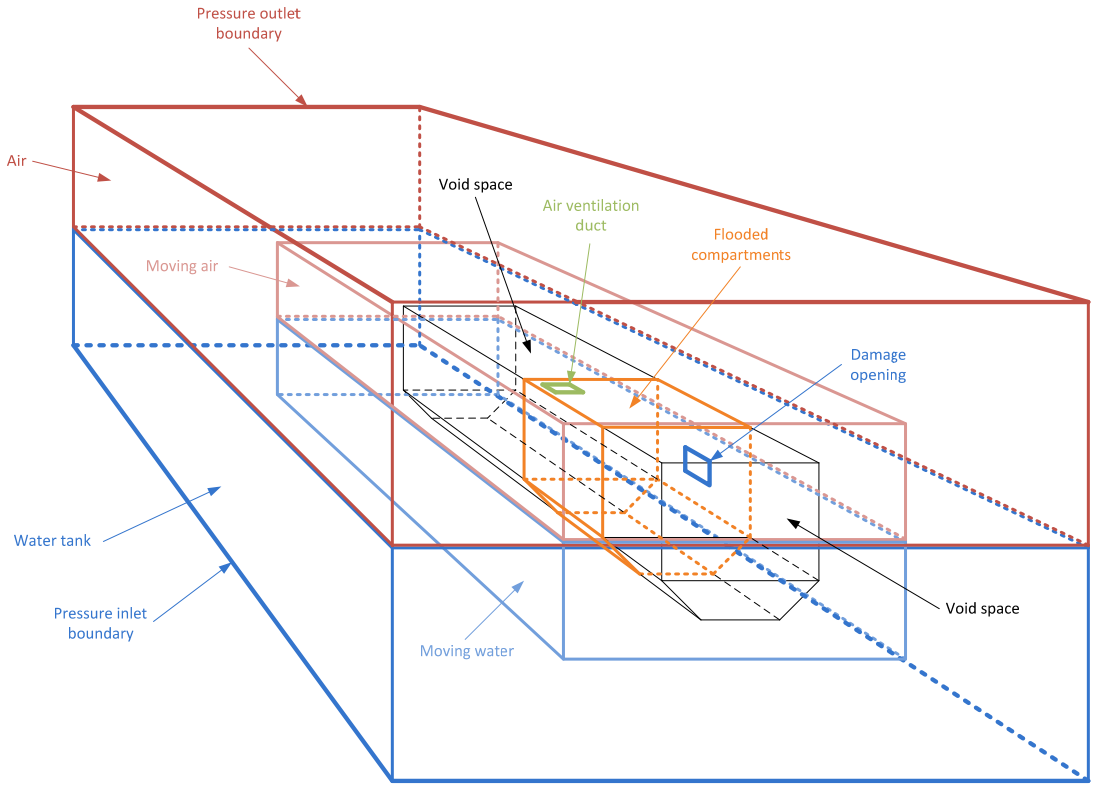

Figure 41: Schematic view of dynamic flooding domain

7.2.3 Design and Creation of the Grid

The design and creation of the grid is an important factor in CFD calculations and can have a lasting effect on the calculation results. Therefore, several points have to be considered:

- Which type of grids can be used, a quadrilateral/hexahedron, a triangle/tetrahedron or a hybrid grid, see Figure 42: Cell types?
- How can numerical diffusion be avoided?
- How complex is the geometry and the flow?
- What degree of resolution is required in each region of the domain?
- Is sufficient computer memory available for a certain number of cells and models?

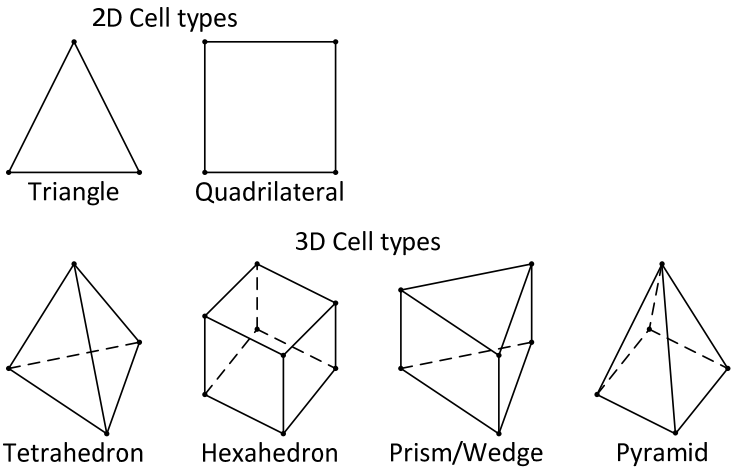

Figure 42: Cell types

Most relevant to the choice of the grid is to minimise numerical diffusion. Hence, ideally the flow should be aligned with the mesh which can be achieved by the use of quadrilateral or hexahedral mesh. When the flow is complex the use of triangular or tetrahedral mesh is recommended. Furthermore, the amount of numerical diffusion is inversely related to the resolution of the mesh. Especially these two criteria have to be considered when the mesh is designed.

Moreover, the grid resolution is a factor that influences both, the accuracy of the results and the computational expenses. It is desirable to find a balance between accuracy and computational expense. This can be done by carrying out grid dependency studies. Grids with different resolutions are compared to validation data. When the CFD results start to settle down at reasonable values the ideal grid has been found.

In almost the same manner as in previous section, it has to be distinguished between the static and the dynamic flooding case. The meshing strategy for both cases is different due to the presence of ship motion in the dynamic case.

Static case:

All walls and openings of the domains in the static case are meshed with quadrilateral cells. The volumes in the domains consist of hexahedral cells. On one hand the use of structured mesh, in contrast to unstructured mesh, limits the number of cells and therefore saves computational resources; on the other hand this structured mesh can cause numerical diffusion. Effects of numerical diffusion can be reduced by using higher order discretization schemes, see chapter 6.3.3.

The resolution of the entire mesh is defined by the maximum resolution of the smallest opening that still gives reasonable and sufficiently accurate results compared to validation data.

Dynamic case:

For the walls of the flooded compartments quadrilateral cells were used while triangular cells were used for all doors and damage openings in order to ensure that a sufficient number of cells are available for flow calculation through the smallest openings. As a result a hybrid tetrahedron mesh is used for all compartments.

For the walls of the moving rigid water and air domain around the ship triangular cells were used. The meshed volume has to comply with the standard of the mesh of the flooded compartment, so the volume has to be a hybrid tetrahedron mesh.

The walls of the water tank and the air domain above the water tank were equipped with triangular cells; ergo the volume is meshed with tetrahedrons. Reason for meshing the water tank and air domain with tetrahedral cells are the methods used for deforming the mesh. During the update process of the mesh the spring-based smoothing method and the face region remeshing method are applied, see chapter 6.5.3. The spring-based smoothing method can deal with both, tetrahedral and non-tetrahedral cell zones, but since not all possible combinations of node pairs in non-tetrahedral cells are idealised as springs which brings forward highly skewed cells the use of tetrahedral cell zones is recommended. The local remeshing method that

is used to remesh regions with deteriorated cell quality or degenerated cells can only be applied to triangular or tetrahedral cell regions.

The difference in mesh design between the static and the dynamic case is also demonstrated in Table 1.

Location of surface or volume	Mesh static case	Mesh dynamic case
Doors / damage openings	quadrilateral	triangular
Walls flooded compartment	quadrilateral	quadrilateral
compartments	hexahedral	hybrid tetrahedron
Walls moving grid	-	triangular
Moving volumes (air/water)	-	hybrid tetrahedron
Walls water tank / reservoir	quadrilateral	triangular
Volume water tank / reservoir	hexahedral	hybrid tetrahedron

Table 1: Mesh for static and dynamic case

7.3 Solver Execution

7.3.1 Set-up of the Numerical Model

After the geometry has been designed, the numerical set-up needs to be created. This is done by following this roadmap, see Figure 43:

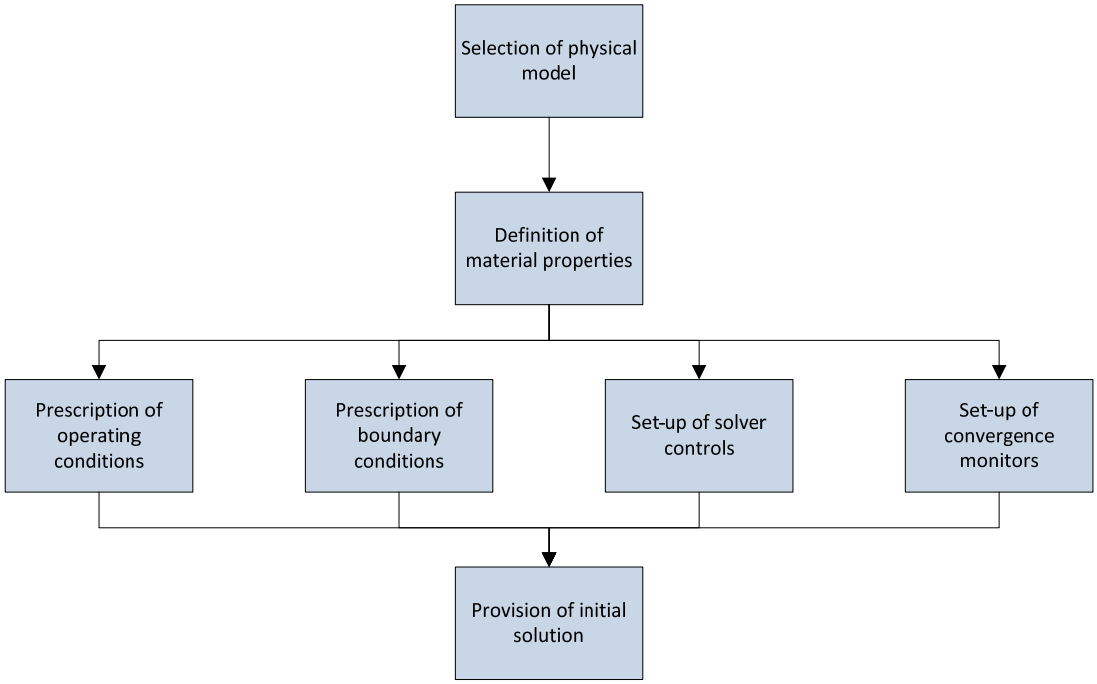

Figure 43: Roadmap of the set-up of the numerical model

In the next few sections the set-up of the numerical model will be explained for the static and the dynamic flooding case. Generally, the two flooding cases are set-up similarly; the only difference is the prescription of the boundary condition, the set-up of the dynamic mesh for the dynamic flooding case and the provision of the initial solution.

7.3.1.1 Physical Model and Material Properties

Multiphase model

Static and dynamic case:

First and foremost all involved physical models have to be selected. As previously mentioned flooding of a ship involves a free-surface and therefore the occurrence of at least two phases. It results in the selection of an appropriate multiphase model, see chapter 6.2. The VOF (volume of fluid) model might come in handy for several reasons. The VOF algorithm, see chapter 6.2.2, can handle two immiscible fluids such as water and air and can track the interface between the two phases

which is ideal for free-surface problems. The geometric reconstruction scheme, chapter 6.2.3, can be used to capture the interface between the phases. This interpolation scheme is most accurate and applicable for both, structured and unstructured meshes. When the geometric reconstruction scheme is used the VOF model can only be solved with the explicit scheme which is useful as for time-dependent calculations where time-accurate intermediate transient behaviours of the VOF solution are of interest. In contrary the implicit interpolation scheme can be used for steady-state solution which is not the case for flooding simulations. Furthermore, the VOF model is capable of calculating the effects of surface tension and wall adhesion.

However, the VOF algorithm has some limitations that have to be considered when setting up the numerical model. Firstly, the VOF algorithm is not working with the density-based solver, see chapter 6.3.6. It only works with the pressure-based solver, chapter 6.3.5, due to the rapid change of density in the VOF model. Besides only one compressible ideal gas can be used. Every space must be filled with either a single phase or a combination of the phases and no void space is allowed.

When a time-dependent VOF calculation is performed, the time-step used for the volume fraction calculation is not the same as the time-step used for the rest of the transport equations. For that reason the time-step is refined based on the Number. The Courant Number is a dimensionless number that compares the time step in a calculation to the characteristic time of transit of a fluid element across a control volume, see chapter 6.3.3 for details:

$$\frac{\Delta t}{\Delta x_{cell} / v_{fluid}} < C \tag{7.3.1}$$

In the region near the fluid interface, the volume of each cell is divided by the sum of the outgoing fluxes. The resulting time represents the time it would take for the fluid to empty out of the cell. The smallest such time is used as the characteristic time of transit for a fluid element across a control volume, as described above. For example, if the maximum allowed Courant number is 0.25, the time step will be

chosen to be at most one-fourth the minimum transit time for any cell near the interface, *Fluent (2006)*.

Naturally gravitational force, which can be treated as a large body force, acts upon the entire domain. Unfortunately, this has a negative effect on the convergence of segregated algorithm, because the body force and pressure gradient terms in the momentum equation are almost in equilibrium. Thus, a body force correction term is introduced in the face flow rate equation (6.3.39) and as a result also in the equation (6.3.37) of the net flow rate into the cell in order to achieve a realistic pressure field. Taking this action will improve the solution convergence and make the solution more robust.

The phases in the VOF model are characterised by two or more materials and their properties. For flooding simulations relevant properties include:

- density
- heat capacity
- thermal conductivity
- viscosity
- molecular weight
- standard state enthalpies
- kinetic theory parameters

These parameters should be set accordingly. For flooding simulations usually two phases, water and air, are used but when flooding simulations are carried out on tankers or other cargo vessels additional phases like oil or liquid chemicals can be included. The air phase can have two different density properties: air is either incompressible and its density is constant, or compressible and the ideal gas law is used, see C.1.5. Usually air is defined as primary phase and water as secondary phase.

Turbulence model

Static and dynamic case:

With respect to turbulent flow a turbulence model needs to be chosen. The semi-empirical standard *k-*ε turbulence model, see chapter 6.4, is known for its simplicity. Compared to other two-equation turbulence models like the RNG *k-*ε turbulence model, the realizable *k-*ε turbulence model or the *k-*ω turbulence model the standard *k-*ε turbulence model requires the least computational effort and gives sufficiently accurate results. Though the performance of the RNG or realizable *k-*ε model might be slightly better but it is also aim to optimise computation time and find a balance between time and accuracy.

In general turbulence is also affected by the presence of walls which is the case with complex deck geometries. The solution variables near walls have large gradients, the tangential velocity fluctuations are reduced by viscous damping while the normal fluctuations are reduced by kinematic blocking. All this causes an increasing turbulence in the outer part of the near-wall region because large gradients in mean velocity augment the production of turbulence kinetic energy.

Near-wall regions can be subdivided into three “turbulence” layers: the innermost viscous sublayer where viscosity plays a dominant role, the outmost fully-turbulent sublayer where turbulence plays an important role and an interim layer between the laminar and the fully-turbulent layer where viscosity and turbulence are equally important. This effect can be treated by wall functions or the near-wall models.

Wall functions are semi-empirical functions that comprise formulas for near-wall turbulent quantities and laws-of-the-wall for mean velocity and other scalars. Three different kinds of wall functions can be used with the standard *k-*ε model:

- Standard Wall Functions
- Non-Equilibrium Wall Functions
- Enhanced Wall Treatment

Among the three the standard wall functions are widely used in engineering applications with high Reynolds numbers. The non-equilibrium wall functions additionally consider the effects of pressure gradient and strong non-equilibrium. That is why non-equilibrium wall functions are recommended for use in complex flows involving separations, etc. with rapidly changing pressure gradients. The enhanced wall treatment approach is a near-wall modelling method that combines a two-layer model with enhanced wall functions. A fine near-wall mesh is premise in order to resolve the laminar sublayer which severely increases the computational expense. Taking all the listed features of the wall functions into account the standard wall functions are a good choice for flooding simulations.

7.3.1.2 Operating Conditions

Static and dynamic case:

The environment where the flooding takes place is defined by several important parameters called the operating conditions. One of these parameters is the operating pressure p_{op}. It is defined as the absolute pressure p_{abs} minus the gauge pressure p_{gauge}:

$$p_{op} = p_{abs} - p_{gauge} \tag{7.3.2}$$

Gauge pressure is the pressure relative to the local atmospheric or ambient pressure. The operating pressure is of significance because it determines the density for incompressible ideal gas according to the ideal gas law (equation (7.3.3)) and therefore has to be set properly.

$$\rho = \frac{p_{op}}{\frac{R}{M_{\omega}}} T \tag{7.3.3}$$

For compressible low Mach number flows the operating pressure is of significance in order to avoid roundoff error problems. Roundoff error problems occur in low Mach number flows because the overall pressure drop is small compared to the

absolute static pressure and the influence of numerical roundoff can be enormous. For flooding simulations the operating pressure is set to atmospheric pressure.

Another environment-describing parameter is gravity which has to be set accordingly.

For improved convergence the operating density can be defined. Normally the operating density ρ_0 is computed by averaging over all cells. The operating density will be used to determine the hydrostatic pressure p_s' from the well known pressure p_s.

$$p_s' = p_s - \rho_0 g x \tag{7.3.4}$$

For flooding calculations the operating density ρ_0 is the density of air at atmospheric pressure.

7.3.1.3 Boundary Conditions

The boundary conditions define the flow on the boundaries of the physical model. In flooding simulations four boundary conditions are used:

- Wall boundary condition
- Interior boundary condition
- Pressure inlet boundary condition
- Pressure outlet boundary condition

Wall boundaries are used for all borders that are neither openings such as doors or pipes nor define any fluid flow at a cell face. They feature a no slip shear condition, are stationary walls and do not support heat flux.

All internal openings that are not closed such as doors, damage openings, tubes, ducts, etc., are allocated as interior boundary condition. Interior boundary conditions leave the flow unaffected and let fluids flow between two fluid volumes.

Static case:

Pressure inlet boundaries are installed at the bottom of the water reservoirs connected to the damage openings. The flow is assumed to be normal to the boundary. The pressure inlets provide a constant gauge total pressure equal to the hydrostatic pressure of an adjacent water column. Furthermore the turbulence intensity and viscosity ratio is specified. The turbulence intensity *I* is defined as the ratio of the root-mean-square of the velocity fluctuations *u'* to the mean flow velocity u_{avg}, *Fluent (2006)*.

$$I \equiv \frac{u'}{u_{avg}} \cong 0.16\left(\mathrm{Re}_{D_H}\right)^{-1/8} \tag{7.3.5}$$

If the flow has a low Re number and is less turbulent, the turbulence intensity is low; vice versa if the Re number is high and the flow fully turbulent, the turbulence intensity is high. For flooding cases a low Re number is expected at the damage opening, therefore a turbulence viscosity around 1% can be assumed. Likewise the turbulence viscosity is set. The turbulence viscosity ratio μ_t/μ is direct proportional to the Re number:

$$\mathrm{Re}_t \equiv \frac{k^2}{(\varepsilon \nu)} \tag{7.3.6}$$

Usually μ_t/μ is small in most free stream flows and turbulence parameters are set so that $1 < \mu_t/\mu < 10$.

To ensure that the reservoir is always filled with water, a constant flow volume fraction of water has to be set for the secondary phase water at the pressure inlet boundary condition.

Pressure outlet boundary conditions are placed on top of the air ventilation ducts. In principle pressure outlet boundaries work in the same way as pressure inlet boundaries. The only difference is that they let the fluid escape. A backflow condition can be used and should be set to air for the secondary phase water, so that air can escape and enter the domain in order to keep the atmospheric pressure

constant. The turbulence intensity and the turbulence viscosity are set to the same values as has been done for the pressure inlet boundary conditions. As the gauge pressure at the pressure outlets is unknown the value is set to t = 0 and will be extrapolated from the upstream conditions.

Dynamic case:

In principle the set-up of the boundary conditions for the dynamic case is similar to the set-up of the static case but differs slightly due to the configuration of the geometrical model.

Pressure inlet boundary conditions are placed on the bottom of the water tank to ensure a constant water level throughout the simulation. The flow is assumed to be normal to the boundary face. A constant gauge total pressure is given equal to the static pressure of the water column from the bottom of the tank to the initial water level at point in time t=0. A flow of volume fraction of water is set for the secondary phase water which means that the water tank will be refilled with water to maintain a constant water level. The turbulence intensity and viscosity are defined as in the static case: the turbulence intensity I is 1% and the turbulence viscosity ratio is set to 10.

Above the water tank a region of air is situated representing the atmosphere with all its physical properties. On top of this region a pressure outlet boundary is placed with a backflow condition of air. So, air can escape and enter as the pressure in the atmosphere changes and maintain a constant air pressure. The turbulence intensity and the turbulence viscosity are set to the same values as has been done for the pressure inlet boundary conditions. As the gauge pressure at the pressure outlets is unknown the value is set to zero and will be extrapolated from the upstream conditions.

Dynamic Mesh and Six DOF Solver

Dynamic case:

All of the above described physical models are applicable to the dynamic model. Additionally, the dynamic mesh method, see chapter 6.5, is applied which simulates the ship motion caused by the ingressing floodwater. To account for motion in six degrees-of-freedom the six DOF solver, chapter 6.5.4, has to be included.

When a mesh is deformed different mesh update methods ensure that the mesh moves and that the volume mesh is updated in the deforming regions at the boundary. One of these methods is the spring-based update method described in chapter 6.5.3. This method requires the definition of the spring stiffness; a value of 0 indicates that there is no damping on the springs, whereas a value of 1 indicates full damping on the spring. A spring stiffness of 0.5 every 5 to 30 iterations has been found to be ideal for flooding simulations.

The boundary node relaxation controls how the node position on the deforming boundaries is updated:

$$\vec{x}^{n+1} = \vec{x}^{n} + \beta \vec{x}^{m,converged}_{spring} \tag{7.3.7}$$

where β is the boundary node relaxation. A value of 0 switches off smoothing on deforming boundary zones and a value of 1 indicates no under-relaxation. For flooding simulation smoothing is used and the value set to 1.

The convergence tolerance and number of iterations controls the solution of the equation (6.5.11) for the net force on all nodes. This equation is solved until the specified number of iterations has been performed or if the solution is converged for the time step:

$$\left(\frac{\Delta \vec{x}^{m}_{rms}}{\Delta \vec{x}^{1}_{rms}} \right) < \text{convergence tolerance} \tag{7.3.8}$$

where $\Delta\vec{x}^{1}_{rms}$ is the interior and deforming nodes root-mean-square (RMS) displacement at the first iteration. It has turned out that a value of 10^{-3} for the convergence tolerance and a value of 5 to 30 for the number of iterations depending upon the magnitude of the motion are suitable for dynamic flooding simulations but still should be adapted depending on the case.

In order to avoid skewed or invalid elements in the mesh the remeshing algorithm is used. The quality of the cell elements can be improved by selecting the option *must improve skewness*. Minimum length scale specifies the lower limit of the cell size below which the cells are marked for remeshing and, vice versa, the maximum length scale specifies the upper limit of the cell size above which the cells are marked for remeshing. Also, the maximum skewness for the mesh can be set. A rough estimate of these values can be determined by checking the mesh scale information of the current mesh. For an improved mesh quality face remeshing can be used to remesh triangular faces and to create very regular meshes at the border of the moving boundaries. When this option is used the maximum face skewness has to be defined. As first guess this information can be obtained by examining the mesh scale information.

For the ship motion gravitational force needs to be set in the six DOF options. Furthermore, the dynamic mesh zones need to be defined. All zones are defined as rigid body zones performing a rigid body motion. The six DOF solver is used on all zones following the motion defined in the user defined function. To define the motion required inputs for the user defined function are the mass of the ship and the moment of inertia in three axes which is specified from the location of the centre of gravity. All zones except the moving air and water zone account for forces and moments; thus the passive six DOF solver option is disabled except for the moving zones.

7.3.1.4 Solver Set-up

The solution parameters are controlled and defined in the solution control. Four equations will be solved:

- Flow equation
- Volume fraction
- Turbulence equation
- Energy equation

Temporarily, each of these equations can be individually switched on or off. During the flooding calculations normally all equations are switched on.

Under-relaxation factors, see chapter 6.3.5, can be set in order to control the update of the computed variables at each iteration step. Under-relaxation factors are set to lower values when the residuals are continuously increasing instead of decreasing. For most flows under-relaxation factors do not need to be modified but if there is an unstable or divergent behaviour observed, the under-relaxation factors for pressure, momentum and turbulence (k and ε) can be decreased to minimum values of 0.2, 0.5, 0.5 and 0.5 in order to achieve convergence.

In chapter 6.3.5 different pressure-velocity coupling methods were presented. At this stage numerical theory of the pressure-based algorithm has to be implemented and an appropriate pressure-velocity coupling algorithm should be selected. It can be chosen from four different algorithms:

- SIMPLE
- SIMPLEC
- PISO
- Coupled

Static case:

Among the listed algorithms the PISO algorithm is highly recommended for transient flows especially when large time steps are used. It features skewness and neighbour correction. Neighbour correction is an iterative process where velocities are corrected inside the solution stage of the pressure correction equation in order

to satisfy the momentum and continuity equations. For transient problems this method can significantly decrease the number of iterations required for convergence. For transient flooding simulations this option is utilised. Skewness correction can be used when meshes are highly skewed. Basically, when a mesh is skewed the relationship between the mass flux correction at the cell face and the difference of the pressure correction at the adjacent cell is harsh. So the pressure-correction gradient is recalculated with a few iterations and the mass flux corrections are updated with the new pressure correction gradient. This method can drastically reduce convergence issues with skewed grids. As for the static flooding simulations a structured mesh is used, the mesh is not likely to be skewed and therefore the skewness correction method is not used. When neighbour and skewness corrections are used simultaneously on the same pressure correction equation divergence can be provoked. Hence, this can be avoided by carrying out one or more iterations of skewness correction for each iteration step of neighbour correction which improves the accuracy of the mass flux correction according to the normal pressure correction gradient.

The discretization scheme for the convection terms of the governing equation of momentum and energy can and should be selected. Following discretization schemes are available:

- First order upwind
- Second order upwind
- QUICK
- Power law
- Third-order MUSCL

Generally, the first order upwind discretization scheme gives acceptable results for a flow that is aligned with the grid and which grid is structured. QUICK, like the second order upwind scheme, provides better accuracy than the first order upwind discretization scheme. The QUICK discretization scheme is preferably used for swirling flows. During flooding model tests swirling could be observed in large

compartments, which proves the application of the chosen discretization scheme. QUICK can be used for quadrilateral or hexahedral cells only.

When the VOF model is chosen only two pressure interpolation schemes are available:

- PRESTO!
- body-force-weighted

The PRESTO! (PREssure STaggering Option) scheme uses the discrete continuity balance for a "staggered'' control volume about the face to compute the "staggered'' pressure. This scheme is – again – recommended for swirling flows.

An interpolation scheme for the volume fraction itself can be selected when the physical model VOF is applied. Following options are available:

- Geometric reconstruction
- CICSAM
- Modified HRIC
- QUICK

The geometric reconstruction discretization scheme, see chapter 6.2.3, gives a sharp image of the interface between two phases. It is applicable for both structured and general unstructured meshes and the most accurate among the volume fraction interpolation schemes.

Dynamic case:

Different pressure-velocity algorithms may all have advantages and disadvantages but the coupled algorithm has some features that are interesting for the use with dynamic flooding simulations. First of all the coupled algorithm is more robust and has a better performance compared to the segregated algorithms. Secondly, it can also be used for transient flows with poor mesh quality or very coarse meshes and still gives acceptable results when the time step size is large. Additionally the

Courant-Friedrichs-Lewy condition should be adjusted according to following equation:

$$\Delta t = \frac{2CFL \cdot V}{\sum_f \lambda_f^{\max} A_f} \tag{7.3.9}$$

where Δt is the time step, *CFL* is the Courant-Friedrichs-Lewy number, *V* is the cell volume, A_f is the face cell, and $\lambda_f^{\max}$ is the maximum of the local eigenvalues. The use of a large Courant number can achieve fast convergence. The Courant number is, as already mentioned before, a local time stepping method which adjusts the solution at each control volume with the cell time step that is defined by the local stability limit of the time-stepping scheme.

The flow in the dynamic case is never aligned with the grid as an unstructured grid is used. Therefore, the discretization scheme of choice is the second order upwind scheme to obtain accurate results.

As for the static case the dynamic case uses PRESTO! for the pressure interpolation scheme.

The interpolation scheme for volume fraction is the geometric reconstruction scheme.

7.3.1.5 Convergence Monitor Set-up

Static and dynamic case:

The convergence during the solution process can be monitored by checking residuals and surface and volume integrals. Ideally, the residuals will go to zero as the solution converges but actual computers do not have infinite precision. So the residuals can drop between six and twelve orders of magnitude before hitting round-off. The conservation equation for a variable ϕ at cell *P* after discretization is

$$a_P \phi_P = \sum_{nb} a_{nb} \phi_{nb} + b \tag{7.3.10}$$

where a_P is the centre coefficient, a_{nb} are the influence coefficients for the neighbouring cells, and b is the contribution of the constant part of the source term S_c in $S = S_c + S_P\phi$ and of the boundary conditions. Therefore is

$$a_P = \sum_{nb} a_{nb} - S_P \tag{7.3.11}$$

The unscaled residual R^ϕ computed by the pressure-based solver is the difference between the left and the right term in equation (7.3.10) summed over all the computational cells P:

$$R^\phi = \sum_{\text{cells } P} \left| \sum_{nb} a_{nb}\phi_{nb} + b - a_P\phi_P \right| \tag{7.3.12}$$

The residuals specified in equation (7.3.12) are problematic because it is hard to judge if convergence is achieved when residuals cannot be compared with the flow rate ϕ. For that reason residuals are scaled with a scaling factor obtained from the flow rate ϕ through the domain. This scaled residual may be written as

$$R^\phi = \frac{\sum_{\text{cells } P} \left| \sum_{nb} a_{nb}\phi_{nb} + b - a_P\phi_P \right|}{\sum_{\text{cells } P} \left| a_P\phi_P \right|} \tag{7.3.13}$$

For the momentum equations the equation is defined as

$$R^\phi = \frac{\sum_{\text{cells } P} \left| \sum_{nb} a_{nb}\phi_{nb} + b - a_P\phi_P \right|}{\sum_{\text{cells } P} \left| a_P v_P \right|} \tag{7.3.14}$$

where v_P is the magnitude of the velocity at cell P.

The unscaled residual for the continuity equation is defined as

$$R^c = \sum_{\text{cells } P} \left| \text{rate of mass creation in cell } P \right| \tag{7.3.15}$$

It follows from the above that the scaled residual for the continuity equation is formulated as

$$\frac{R^{c}_{\text{iteration } N}}{R^{c}_{\text{iteration } 5}} \tag{7.3.16}$$

The denominator of equation (7.3.16) is the largest absolute value of the continuity residual in the first five iterations.

The scaled residuals discussed above are already very good indicators of the convergence of a solution. An additional indicator for convergence can be how much a residual has decreased during calculations. This method is called normalised and may be written as:

$$\overline{R}^{\phi} = \frac{R^{\phi}_{\text{iteration } N}}{R^{\phi}_{\text{iteration } M}} \tag{7.3.17}$$

The scaled or unscaled residuals are divided by the maximum residual value after M iterations. Normalization in this manner is sometimes useful in judging overall convergence.

Absolute residual criteria for continuity, velocity and turbulence are set to 10^{-3} and scaling is enabled. The scaled residual is a more appropriate indicator of convergence for flooding problems than the unscaled residual. If the residual is less than that value, this particular equation is supposed to have converged for a time step. The lower the value of the absolute residual criteria is, the more time steps an equation needs to achieve convergence. Again a balance between time and accuracy has to be found.

At the end of each time step velocity and pressure are monitored on all surfaces that represent openings like doors, windows, damage openings, tubes, etc. Also the volume average of the volume fraction for each volume on the ship is monitored. These values are plotted in a chart over the flow time as an additional convergence

indicator. When the values of these additional convergence indicators do not change anymore the iteration can be stopped.

7.3.2 Computation and Monitoring of the Solution

7.3.2.1 Computation of the Solution

Before the calculations can be started the flow field in the entire domain has to be initialised. Because zone motion occurs in the dynamic case the initial velocities are relative to the motion of each cell zone, so the reference frame is relative to the cell zone. When there is no cell motion such as in the static case both options, absolute and relative to the cell zone, are equivalent.

Following values can be initialised:

- Gauge pressure
- Velocities in x, y and z-direction
- Turbulence (kinetic energy and dissipation rate)
- Temperature
- Volume fraction for the primary phase

Gauge pressure and velocities will be zero in the beginning, before flooding starts. Turbulence kinetic energy and dissipation rate are set to 10^{-3} and the temperature is set equally to the temperature measured during the model tests. The entire domain will be filled with air first (volume fraction of the primary phase is set to 1) to ensure that there are no other phases left that could influence the final results. In the next step regions that include water such as the water tank and the moving water zone will be patched and filled with water. Therefore patched regions will be set to the primary phase of air with a value of zero.

For the initiation of the CFD calculation a few more inputs have to be entered. One of the crucial and important values is the time step size which is the magnitude of Δt. Normally, the time step size can be determined by satisfying equation (7.3.1)

which is related to the Courant number, but in order to model transient phenomena properly the time step size Δt should be at least an order of magnitude smaller than the smallest time constant in the system being modelled. When the number of iterations per time step for a converged solution does not exceed 5-10 iterations the choice of the time step size is good. The time step size can be gradually increased as the calculation proceeds, because in the beginning of the simulation unsteady problems only have transients that usually stagnate quickly. As an additional indicator for the choice of a sufficiently small/large time step size the contours of the Courant number within the entire domain can be plotted. Then the Courant number should not exceed a value of 20-40 in most sensitive transient regions of the domain.

7.3.2.2 Monitoring of the Solution

During the calculation the convergence of the solution has to be judged permanently. An indicator of convergence is the residuals of the solution which can sometimes be misleading. There are two reasons for the occurrence of misleading residuals: a good initial guess of the flow field and a poor initial guess. If the initial guess was good, the initial continuity residuals may be very small causing large scaled residual for the continuity equation. On the other hand, if a poor initial guess was done such as for k and ε equations where an initial guess is difficult, the initial continuity residuals may be very large causing low scaled residuals which become unstable with non-linear sources. In general, it is a good idea to judge residuals from its behaviour and its trend. Residuals should always show the trend to remain low or to decrease then convergence can be concluded.

However, convergence can also be judged when the normalised residuals drop by three orders of magnitude. A typical situation is when the initial guess was good. Then the residuals might not drop three orders of magnitude. Another situation is when respective variables are nearly zero everywhere; a drop of residuals by three orders of magnitude cannot be expected. Also, if the governing equations contain non-linear source terms which are zero in the beginning of the calculation and build

up slowly during the calculation, residuals may not drop by three orders of magnitude.

Judgment of convergence from residuals as described above render moot, so alternatively other relevant quantities like volume fraction of water should be examined in the zones of interest. From experience it is known what the volume fraction of water in a flooded compartment should look like. When the compartment is near the damage, water will flood in rapidly and cause an increasing volume fraction. As time is progressing and head pressure at the damage opening and water pressure in the compartment are equalising, volume fraction of water will decrease and converge towards zero. If the solution is still unconverged the convergence tolerance may be dropped.

7.4 Post Processing

7.4.1 Examination of the Results

When the calculations are finished data has to be validated with results from model tests. For that reason simulation data and data obtained from model tests have to be available in due form and processed appropriately. The results can be examined by a combination of data evaluation and visual comparison of screenshots with pictures from model tests. In model tests several different data can be collected such as:

- water height in the compartments
- flow velocity at openings
- vertical force on compartments
- ship motions

These data usually has some noise which has to be removed for a better comparison. Moreover, it is sometimes difficult to calibrate measurement devices correctly. For example, when the water height in compartments is measured data

has to be scaled as it sometimes exceeded the limits for the maximum and minimum compartment height. It has been observed during some model tests that the actual calibration factors were larger than the results of the calibration. This can happen because the conductivity of the medium changes rapidly from dry to wet and, additionally, the water used for the tests adds impurities after several test runs.

Therefore, data has been scaled in order to compensate any issues regarding with calibration factors. Additionally a regression analysis applying the Epanechnikov method, see appendix B.2, has been undertaken in order to smooth out the curves and to remove noise. When several model tests were carried out that examined the same conditions so that many sets of similar data were available the data was averaged in order to obtain a single data set.

After the CFD calculation surfaces have been added in the CFD model to represent physical measurement devices like hot wire probes for water height measurements. The solution of water volume fraction is then integrated on this surface which gives the water height at that position.

Other values like flow velocity at openings, vertical forces on deck or on the ship and ship motions have been monitored during the calculation and can be directly compared to model tests.

For a visual comparison with photos of the model tests, images of the CFD simulation have to be produced. To make the water surface in the CFD model visible Isosurfaces need to be created on the interface between the phase water and air. Isosurfaces display results on cells that have a constant value for a specified variable, in the case of flooding the volume fraction of either air or water.

Once CFD results have been compared with data from model tests several different conclusions can be drawn. Obviously a desirable conclusion would be that the results agree very well and that the simulation and the model tests were carried out in an optimal way. Sometimes the results do not agree very well so either the CFD

model or the physical model or both have to be revised. This will be discussed in the next section.

7.4.2 Consideration of Revisions to the Model

In case of an unsuccessful validation of model data a revision to the model should be taken into consideration. Following key questions can help to identify possible errors.

- Are the physical models appropriate?
- Are the boundary conditions correct?
- Is the grid adequate?

Problems that occurred during the set-up of the case studies are listed below but could be solved by taking above questions into account.

Special care has been taken on the choice of the physical model. Especially when the model accounts for compressible air attention has to be brought to the position of air ventilation ducts and their cross section size. If a duct is in the wrong position air might escape either too quickly or too slowly. This can influence the entire flooding process and finally give deviating values. An air ventilation duct with a small cross section may have high flow velocities which can lead to difficulties in achieving convergence. As a result time step size has to be decreased according to the Courant number. To avoid decreased time step size the cross section of the air ventilation ducts should be increased accordingly.

In some rare cases when the domain is small it can happen that two boundary conditions are too close to each other. These boundary conditions can influence each other and falsify the computed results. Typical examples are pressure inlets for damage openings or pressure outlets for air ventilation ducts. This situation can be avoided by the use of long ducts but then the head pressure has to be corrected accordingly.

The quality of the grid can have a massive influence on the CFD results. For flooding simulations a common problem is the correct modelling of small openings on deck where a fluid is supposed to flow through. When the number of cells used for such small openings is too small numerical diffusion can be caused and convergence may not be achieved. Therefore a sufficient number of cells is obligatory but at the same time it has to be ensured that the total number of cells is not increasing disproportionately high. Ideally, a grid dependency study is carried out to find out if the solution changes significantly with grid adaption, or if the solution is grid independent.

Whenever such an error caused by one of the previously mentioned situations occurs, the simulation has to be restarted after correction of the problem. This can be quite time consuming because sometimes an error occurs in an advanced state of the simulation when some time has already been spent on the calculation. Unfortunately this fact is hardly to avoid in order to achieving good results.

7.5 Concluding Remarks

The implementation of the numerical and physical methods has been discussed in this chapter. It is noticeable that the approach of implementation is strictly structural whereas its workflow is - similar to the philosophy of the actual numerical computation - iterative. However, an iterative workflow is very important in achieving satisfying numerical results due to the complexity of a CFD model where errors in the design or set-up are not easy to discover. Unfortunately, that is the crux of the matter and makes the use of CFD so difficult. It can be quite expensive in time to find a possible error in extremely complex mesh geometries or in the set-up of the numerical simulation or in the selection of the physical model itself. Once numerical results are available they should be compared to validation data or results from other numerical methods. The problem herein is that it has to be ensured that data used for validation is correct which is sometimes not easy to judge. For simple measurements such as the water height in a compartment of a

flooded ship deck, the correctness of the data can be judged even with common sense. But when it comes to complex procedures like the measurement of flow velocity through an opening which can be done with PIV (particle image velocimetry) the judgement of the correctness and accuracy of the obtained results is arguable.

However, to reduce the risk of inaccurate results in CFD calculations the implementation of the numerical methods should be done with diligence and prudence. Experience with flooding simulation taught that special attention should be turned to:

- The grid design and creation. Especially the dynamic case which involves ship motion and is therefore using the dynamic mesh updating method, the mesh has to be of superior quality. The duration of the calculation is mainly influenced by the time step size that has to be used for dynamic meshing.
- The boundary conditions. A good geometrical positioning of the faces that represent the boundaries and reasonable input for the boundary conditions that is consistent with numerical methods presented in chapter 6.
- The solver set-up. The right choice of solution parameters that can deal with the geometry and the physical methods adopted. More difficult is the initial guess of parameters like k and ε for the turbulence but then the recommendations in chapter 7.3.2.2 what to do if the guess was poor or good should be followed.
- The examination of the results. Here it is important to process the data in an appropriate way, so that it can be compared easily to the validation data. Thus, all possibility of doubt should be excluded that the validation data may not be accurate enough.

In the following chapter two case studies are presented to assess previously described methods and to verify the applicability of the numerical method.

8 Case Studies

8.1 General Remarks

In this chapter three case studies are presented that have been performed in order to check the capability of the applied method to deal with realistic ship geometry and damage cases.

The first case study deals with the flooding of deck 4 of the sunken Ro-Ro ferry M/V Estonia. It accounts a fixed and horizontally levelled out ship without any motion or inclination. Detailed information on the modelling and set-up of the calculations can be found in *Strasser (2008). Blok and Luisman (2008)* carried out the model tests with which the CFD model was compared.

The second case study is based on model tests with a box-shaped barge done in the towing tank of TKK Ship Laboratory in January 2006. A detailed description of the model test set-up and the measurements is given in *Ruponen (2006)*. The CFD calculations include a solver for gravitational time-varying restoring force of the hull in calm water, which means that position of the freely floating hull is updated every time step. Additionally, the CFD calculations address air as compressible medium.

The third case study is a continuation of the PRR02 damaged compartment, *Cho et al. (2005)*, which already has been used in the 24th ITTC Benchmark Study on numerical prediction of damage ship stability in waves. The CFD simulation shows scale effects and measures pressure and velocity at the damage opening. As the calculation addresses air as compressible medium the air pressure in occasionally occurring air pockets is derived.

8.2 Case 1: Research Study of Sinking Sequence of M/V Estonia

8.2.1 Details of the Ro-Ro Ferry M/V Estonia

The Ro-Ro ferry M/V Estonia (Figure 44) which sunk in 1994 in the Baltic Sea was used for a case study and validation of the method. This section gives a brief overview about some facts of the incident and general details about M/V Estonia.

The main characteristics of the vessel are listed in following table (Table 2):

Length over all (L_{OA})	155.40	m
Length between perpendiculars (L_{PP})	137.40	m
Breadth	24.20	m
Depth to bulkhead deck	7.65	m
Maximum draft	5.60	m
Deadweight at max. draft	3,006	dwt
Light weight	9,733	t
Gross tonnage	15,598	
Propulsion power	4 x 4,400	kW
Electrical power	4 x 1,104	kW
Bow thrusters	800 + 590	kW
Maximum number of passengers	2,000	
Maximum service speed	21	knots
IMO number	7921033	

Table 2: Main Characteristics of M/V Estonia

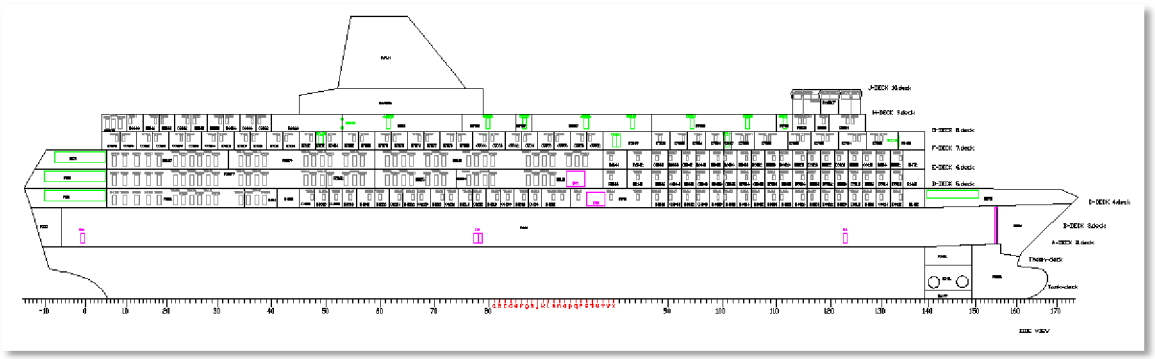

Figure 44: Side View of M/V Estonia

During the journey from Tallinn to Stockholm the ferry got into rough but not extreme weather conditions. Around 01:00 am in the morning of the 28th September 1994 the visor at the bow collapsed and left the ramp fully open so that large amounts of water could enter the car deck. After a few minutes the vessel got list of approximately 40° to the starboard side while engines stopped working due to a lack of lubricating oil pressure. Waves were pounding against windows and doors on deck 4 and broke some of them in the aft section of the deck, so floodwater was allowed to enter the accommodation. At that point water could enter further decks above deck 4 and the vessel started to sink stern first. About 01:50 am the ship disappeared from the sea surface. Computer-generated images, see Figure 45, illustrate the development of list and sinking of M/V Estonia.

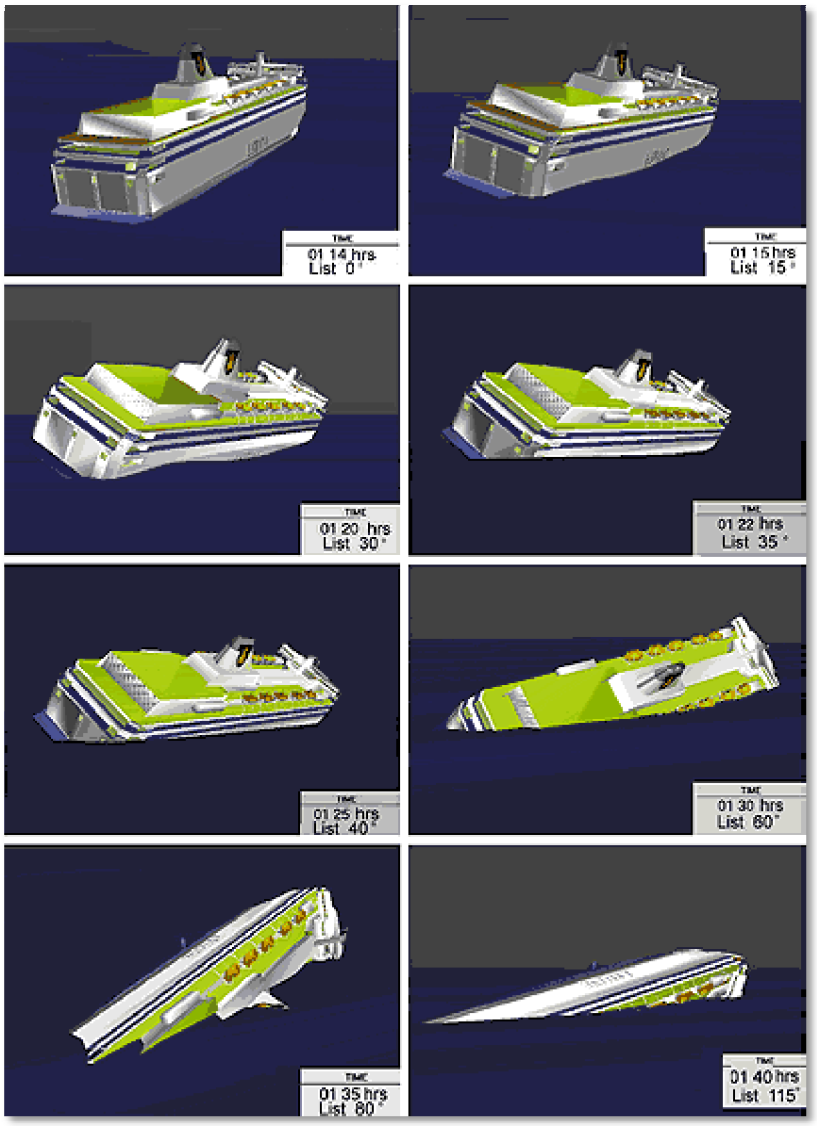

Figure 45: Development of the list and sinking of M/V Estonia in a computer-generated time line, *The_Government_of_the_Republic_of_Estonia (1997)*

In the simulation special attention was turned to deck 4 (Figure 46) because the increasing amount of water on the car deck could have made the aft windows on deck 4 the first flooding point to other areas which finally caused M/V Estonia to sink.

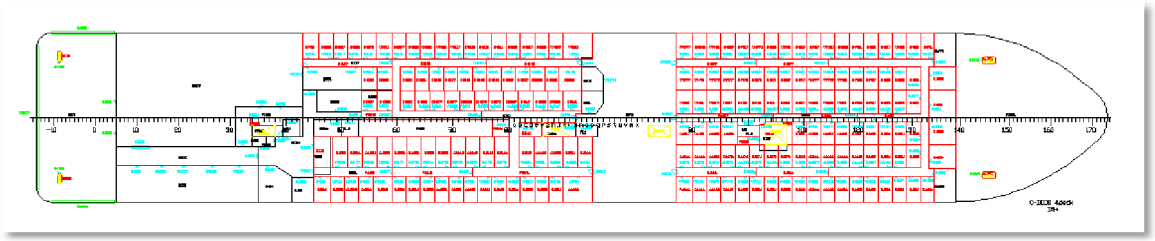

Figure 46: Deck 4 of M/V Estonia

8.2.2 Design Requirements

The design requirements for the numerical and the physical model were decided in agreement with SSRC and MARIN at a project meeting at Chalmers University, Gothenburg, January 2007. The consortium agreed on following requirements for the numerical and physical simulations:

- Modelling of M/V Estonia deck 4, which is an accommodation deck directly over the car deck.
- Application of a simplified compartment and cabin layout which includes more than 20 separate spaces and more than 20 door openings.
- All doors between the compartments and passageways are fully open.
- The model is flooded through five big windows at the starboard stern end.
- An inflow pressure head of 2 m above the top of the window frame is adopted. This assures for the model experiments that the model is flooded in a reasonable time without having too high flow velocities that result in high hydrodynamic forces that could destroy the model. Moreover, this simplification was necessary because for model tests it is difficult to provide a variable head pressure on the damage opening when the model is horizontally fixed.
- The model is fixed and level in horizontal fashion without any motion or inclination.
- The compartments are fully ventilated, so no air pockets can develop.

8.2.3 Modelling of Deck 4

Deck 4 of M/V Estonia was an accommodation deck situated directly above the car deck. The layout of the deck shows a great variation of compartments, varied in both size and purpose. Among the various compartments there was a night club, conference areas, public lounges and many cabins; in conclusion this characterises a highly compartmentised space.

For the CFD calculations as well as for the model tests a simplified interior layout was chosen. Only bulkheads including their openings were modelled and the walls of all the cabins were neglected. The engine case was completely watertight and no water could enter during the whole flooding process. The main dimensions of the model are given in Figure 47 and Table 3.

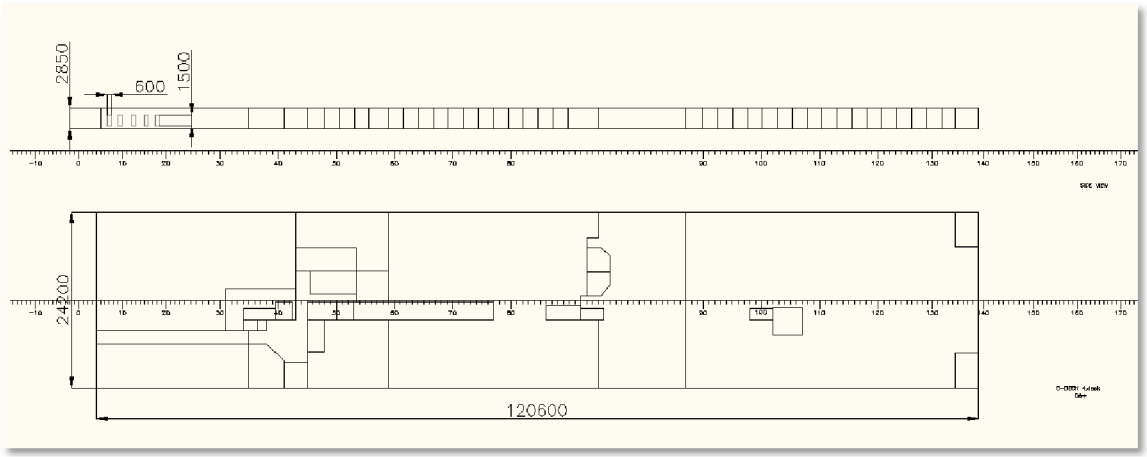

Figure 47: General view of the model

Length over all:	120.60	m
Breadth:	24.20	m
Height:	2.85	m
Flooded volume:	8126.262	m^3
Height damage opening:	1.5	m
Breadth damage opening:	0.6	m

Table 3: Main dimensions of the model

It was assumed that all connecting doors, apart from doors leading to the lift shafts, were open to simulate the worst case scenario. Flooding would take place at its fastest when all doors are open. Closed doors would not prevent the ship from being flooded as the water would spill through the gap under the door and the door would finally collapse due to the high floodwater pressure on one side. So, closed doors might slow down the flooding process. Additionally, staircases and shafts leading to lower or upper decks were closed.

The model was flooded from five windows in the starboard aft corner of deck 4 where the conference area was located. The number of five broken windows was assumed as fact that once some windows are broken the pressure difference on the remaining windows is relieved. These five windows will also be called damage openings throughout this research work. The damage openings were connected to water reservoirs which were permanently refilled with water. Faces on the bottom of the water reservoirs were defined as pressure inlet in order to apply the requested constant head pressure. They are located 1.9 m below the upper edge of the damage opening and provide a constant head pressure of 38.190 kPa which corresponds to pressure head of an inflow pressure head of 2 m above the top of the damage opening. This setup is necessary to correlate model tests with the numerical simulation, see chapter 8.2.2 and section test arrangement in chapter 8.2.5. Figure 48 shows the arrangement of the water reservoirs.

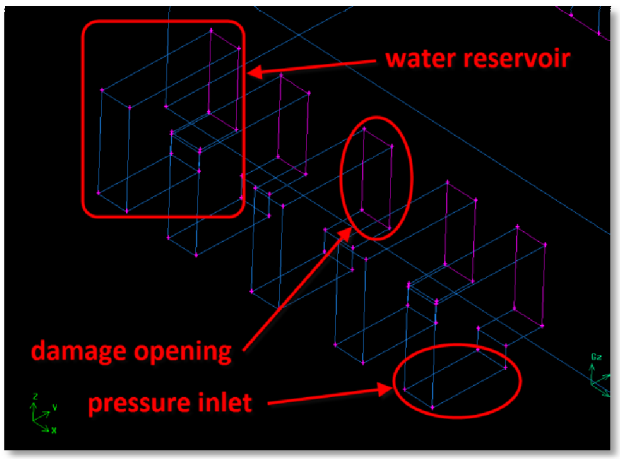

Figure 48: Water reservoirs

The model was kept in a fixed and horizontal position without any motions although in reality the ship would heel over.

All compartments were ventilated and equipped with air ventilation ducts (Figure 49) in order to allow the compartments to be fully flooded and to avoid trapped air. On top of the air ventilation ducts a pressure outlet boundary condition ensures the pressure equalisation. The air pressure remains equal to atmospheric pressure throughout the whole duration of the simulation.

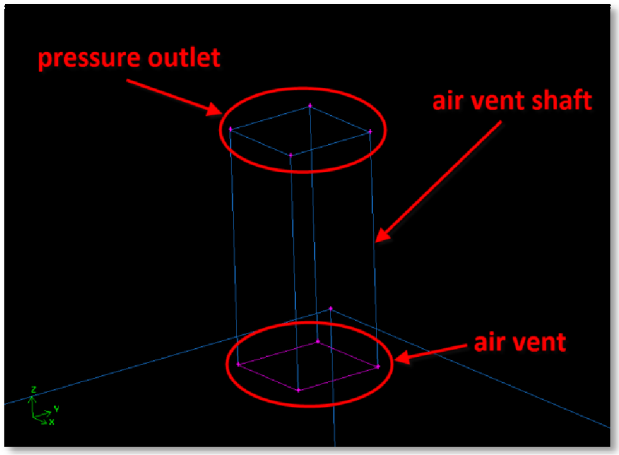

Figure 49: Air ventilation shaft

The entire numerical model of deck 4 of M/V Estonia was created in full scale with the grid generator GAMBIT. The wall thickness of the deck and bulkheads was not taken into account and also the instrumentation used for the model tests on deck was ignored, so that the permeability in all modelled compartments could be taken as unity.

The numerical model consists of three main volumes (deck, air ventilation ducts and water reservoirs) which are separated in sub-volumes. The geometrical model can be investigated in Figure 50. A structured hexahedral mesh with a constant grid spacing of 0.2m was chosen. The number of cells for each main volume is given in Table 4 .

Volume	Number of cells
Deck (including all compartments)	1.019.844
20 air ventilation shafts	1.872
5 water reservoirs (water domain)	1.680

Table 4: Number of cells for each main volume

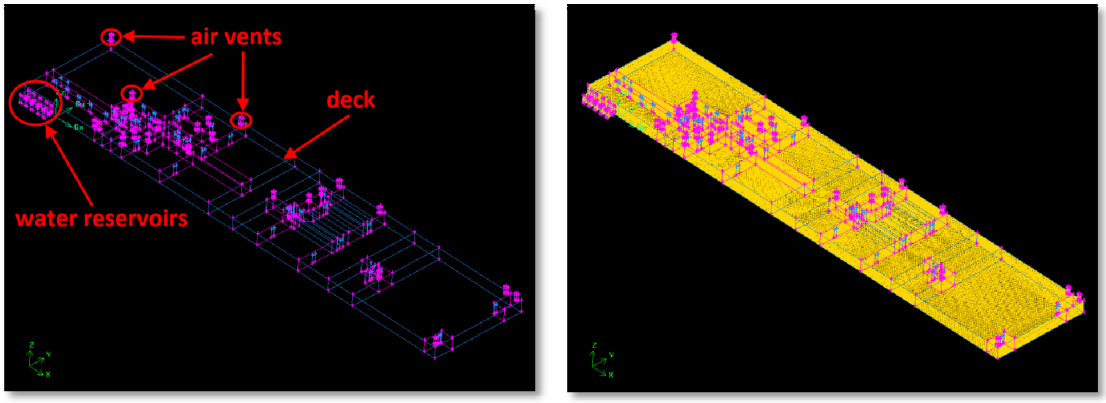

Figure 50: Model of the volumes and meshed model

8.2.4 Simulation Parameters

The simulation parameters will only be explained in a short because they have already been discussed in a very detailed form in chapter 7.3.

The CFD calculation was carried out with the commercial solver FLUENT on an eight nodes dual core cluster. For the entire duration of the calculation the full capacity of the eight nodes (16 CPUs) cluster was used.

The geometry of the deck 4 of M/V Estonia has been imported from GAMBIT to FLUENT as a mesh file. It has been checked for any geometrical errors or highly skewed elements and the domain has been reordered by using the Reverse Cuthill-McKee method, which reduces cache and disk swapping during the calculation, *Cuthill and McKee (1969)*.

The VOF algorithm has been applied and two phases were set up; water with a density of ρ = 1.025 kg/m^3 and a viscosity of ν = 1.003 10^{-3} kg m^{-1} s^{-1} and

incompressible air with a density of ρ = 1.225 kg/m^3 and a viscosity of ν = 1.7894 10^{-5} kg m^{-1} s^{-1}. Additionally, the standard *k*-ε turbulence model has been applied using standard wall functions as near wall treatment as high Reynolds numbers were expected when the water enters the deck. Air pressure remained equal to atmospheric pressure of 101.325 kPa during the whole simulation time. The operating density was set to ρ_0 = 1.225 kg/m^3 for overriding an on all cells averaged density.

Pressure inlet boundary conditions were set at the bottoms of the water reservoirs, which provided a constant head pressure of 38.190 kPa and constantly refilled the reservoir with water in order to reproduce the setup of the model tests. On top of the air ventilation shafts the boundary conditions were set to pressure outlet conditions to allow incompressible air to escape or enter the domain. All other faces were set to wall boundary conditions apart from the internal openings, which were set to interior boundary conditions.

Equations are solved implicitly and pressure based. Solution equations for flow, the volume fraction equations and turbulence are solved as shown in Table 5:

Solution control	**Mode**
Discretization	
Pressure	PRESTO!
Momentum	QUICK
Turbulence Kinetic Energy	QUICK
Turbulence Dissipation Rate	Power Law
Volume Fraction	Geo-Reconstruct
Pressure-Velocity Coupling	PISO

Table 5: Solution control for flow and volume fraction equations

The initial condition was that deck and the air vent shafts were completely filled with incompressible air and the water reservoirs were completely filled with water. A time step of 0.025 seconds was chosen according to the requirements of the

dimensionless Courant Number, see chapter 6.3.3, which compares the time step in a calculation to the characteristic time of transit of a fluid element across a control volume.

During the calculation forces and moments on walls, volume fraction, flow velocities and pressure were monitored. The results of the calculations are presented in chapter 8.2.6.

8.2.5 Model Tests

The model tests were carried out by MARIN in order to fulfil the M/V Estonia Consortium Agreement WP 3, Task 3.3, Subtask 3.3.1: "Flooding through complex internal spaces". It was aimed to obtain physical model data which can be used to compare and to validate the results of numerical codes employed for the computational simulation of the sinking sequence of M/V Estonia, see *Blok and Luisman (2008)* for details.

Model

To meet this objective a model of deck 4 was built in acrylic plastic and completely filled with water from a container. The model scale adopted was λ=20 and the model was segmented into three pieces in order to withstand the heavy water load during the flooding process. The main dimensions of the model are listed in Table 6.

Length over all:	6.0	m
Breadth:	1.20	m
Height:	0.145	m
Flooded volume:	1.015	m^3
Height damage opening:	0.075	m
Breadth damage opening:	0.03	m

Table 6: Main dimensions of the model in model scale λ=20

The inner sub-dividing walls in CFD calculations usually have a thickness of zero but the walls in the physical model of deck 4 had to have a thickness to provide enough stiffness. That is the reason for slightly differing volumes compared to the numerical model. The physical model was equipped with bottom drains to quickly drain the model. Furthermore, the three top plates of the model could be completely removed for easy access into the model. On the top plates air ventilation ducts were installed to ensure that air can escape and to avoid trapped air. The outer walls of the model were constructed from very thick acrylic plastic to provide sufficient stiffness and to avoid flexing of the model. At the stern end on the starboard side of the model five windows were cut into the acrylic plastic side walls. These five windows represented the damage openings.

Test arrangement

The five openings were connected through a trapezoid mouth piece inlet to the water inlet pressure stabilization container. This container was equipped with an overflow to provide a constant head pressure at the damage opening. The water inflow could be controlled with a butterfly valve. Two water supply containers were connected to the water inlet pressure stabilization container for a constant refill of water. Water supply to the water inlet pressure stabilization container could be controlled with a butterfly valve. These containers could hold a supply of three times the volume of the entire deck. For a better visual observation the water in the containers was dyed green.

The equipment was set-up for a constant head pressure of 2 m above the top window frame of the five starboard aft windows which translates to 10 cm water column pressure head on model scale.

The three segments of the model rested on three six-component force transducers to measure vertical forces.

At the start of any test the butterfly valve of the supply containers is opened. When water is spilling through the overflow of the water inlet pressure stabilization

container, a 10 cm pressure head is attained and the inlet to the model will be opened by quickly opening of the butterfly valve on top of the trapezoid mouth piece. The model will then be filled with water.

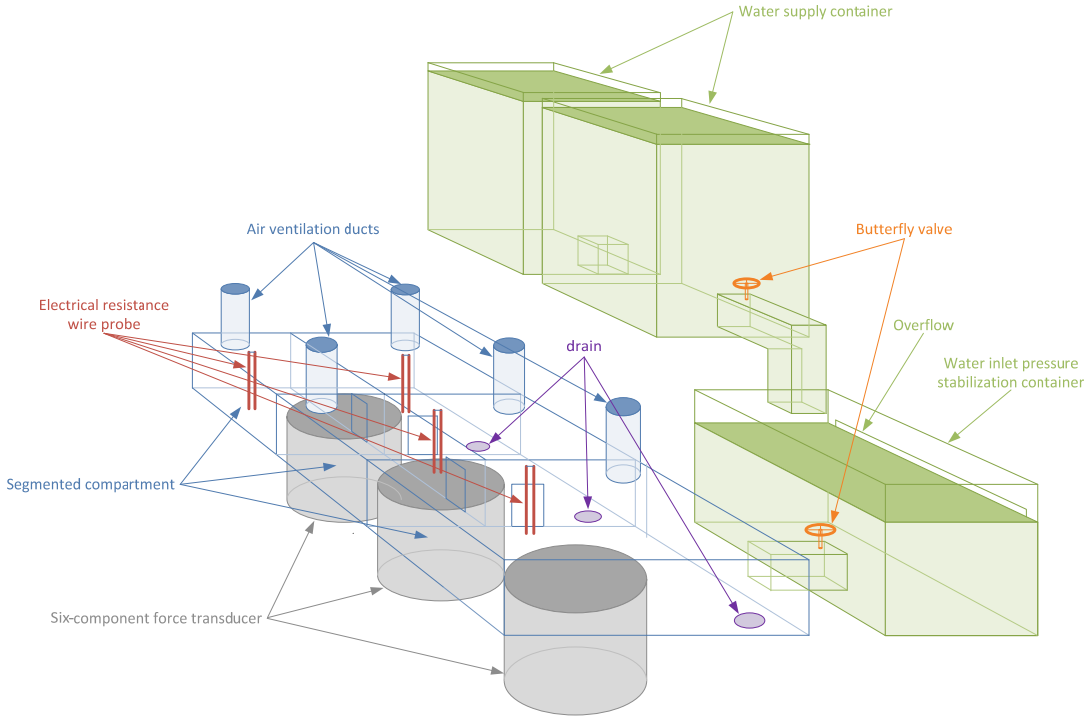

Figure 51: Schematic view of test arrangement

Measurement instrumentation

The water height was measured at 20 locations inside the model using electrical resistance wire probes. They were hanging from the top of the compartment and were not fixed at the bottom; therefore the wires were constructed thicker as normally.

To obtain a total amount of water and its centre of gravity as a function of time, the model was set on three six-component force transducers. Each transducer was composed of three vertical strain-gauge rods that together carried the full weight of on segment of the model. The measurement function of the transducer is, according to the requirements, to vectorially separate the force vector into three x-

y-z coordinate force directions, or moments, respectively. Basically, strain gauge platform balances with computer separation of forces and moments are used.

Measurement of the flow velocity of floodwater through the doors at some five locations was done by measuring the force exerted on a rod hanging behind the door. The conversion from force measurement to flow velocity was done using the equation (8.2.1) for fluid dynamic drag.

$$F = C_d \frac{1}{2} \rho V^2 A \tag{8.2.1}$$

where F is the force, C_d is the drag coefficient, ρ is the density, V is the flow velocity and A is the wetted frontal area of the force probe. This velocity should be understood as velocity averaged over the water depth at the location of the force probes. Naturally, that measurement of flow velocity is not simple and the reliability of such measurement has to be handled with care.

Additionally to all the measurements videos and still photos were taken to visualise the progress of the flooding through the complex geometry.

8.2.6 Data Comparison

8.2.6.1 Time History of the Flooding Process

In the calculation three dimensional images were created in order to visualise the flooding progress on deck 4 of M/V Estonia. Isosurfaces have been created on the interface between the two phases, water and air, to make the floodwater visible.

In the beginning floodwater enters the conference area R251 of deck 4 violently and with high flow velocity. The first few compartments are almost flooded instantly. As the floodwater progresses it finds a number of openings and spreads into the next arrangement of compartments which gradually fill up with water. Once the floodwater reaches the larger open-spaced compartments the flooding process starts to slow down. Reason for that is that the conference room is already filled up

with water so the pressure difference between the water reservoir and the conference room is almost equalised. Floodwater that flows off from the conference room R251 will be replenished by floodwater from the water reservoir to conserve the pressure equilibrium. This principle of pressure conservation propagates from compartment to compartment until the whole deck is filled with floodwater. When the water reaches the most forward compartments are reached a cascade of water levels can be observed that rise at more or less the same pace. It can also be observed that the flooding time increases significantly when the floodwater reaches the upper edge of the internal openings. This phenomenon will be discussed in chapter 8.2.6.2. The progression of the floodwater on deck 4 of M/V Estonia is shown in some snapshots in the following time history (Figure 52 - Figure 73).

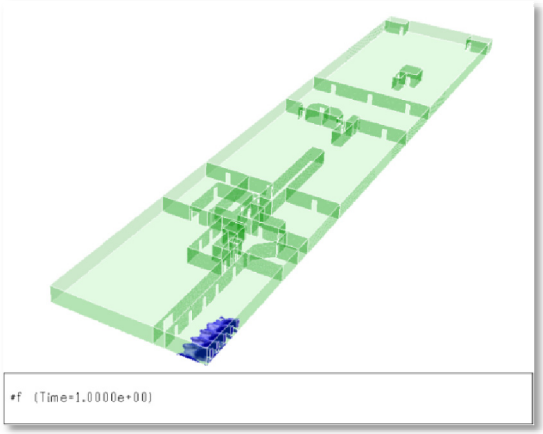

Figure 52: Progressing floodwater after 1 second

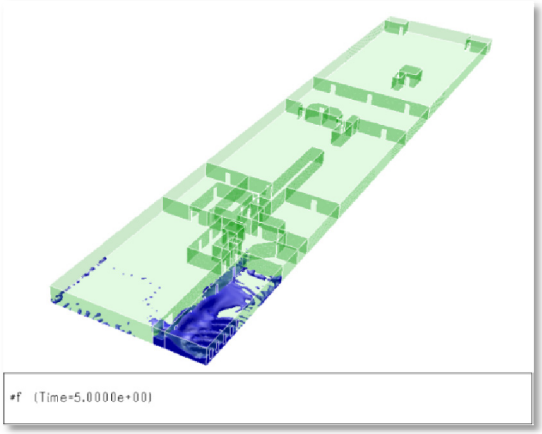

Figure 53: Progressing floodwater after 5 seconds

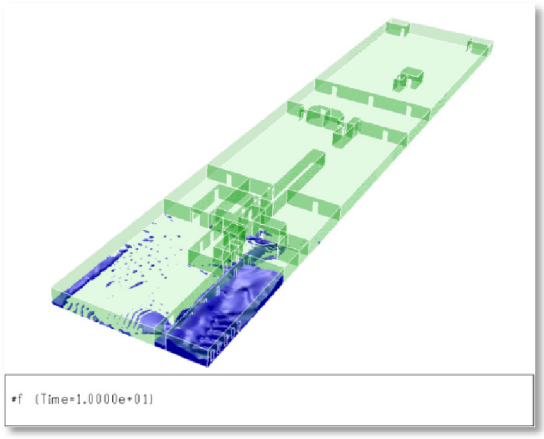

Figure 54: Progressing floodwater after 10 seconds

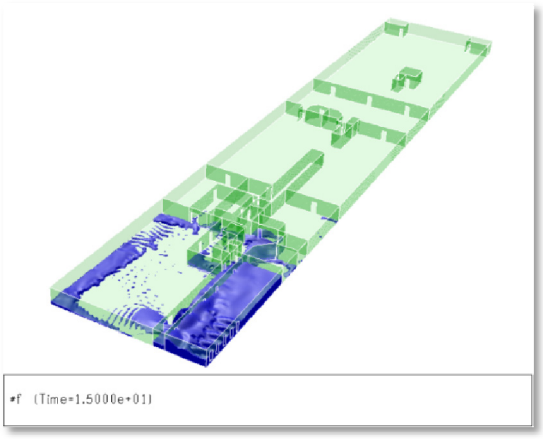

Figure 55: Progressing floodwater after 15 seconds

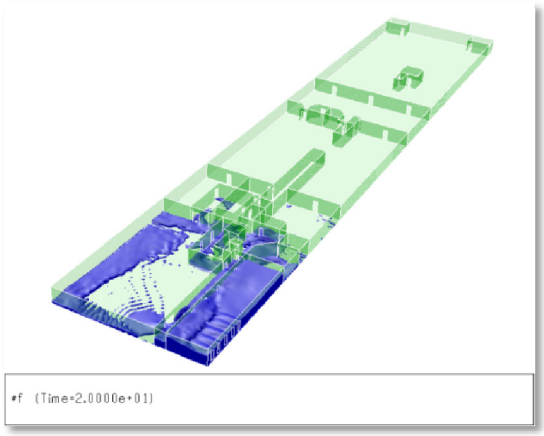

Figure 56: Progressing floodwater after 20 seconds

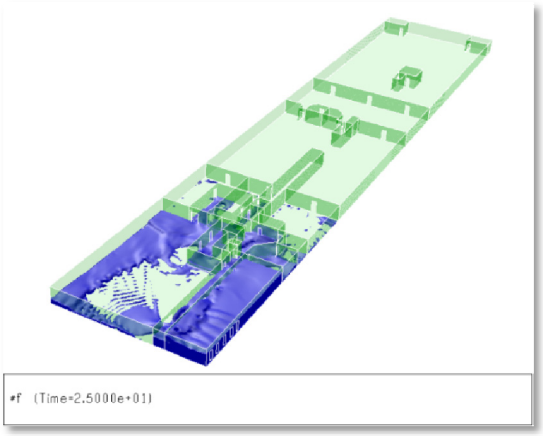

Figure 57: Progressing floodwater after 25 seconds

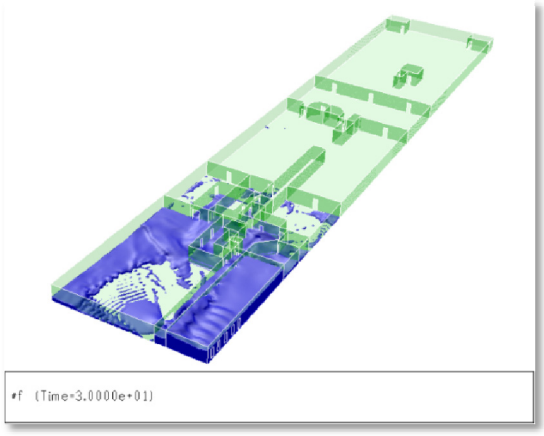

Figure 58: Progressing floodwater after 30 seconds

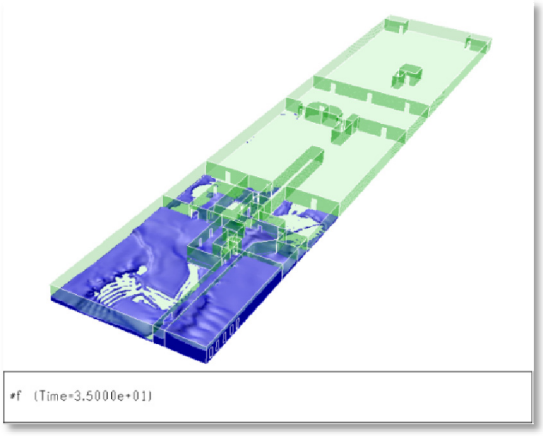

Figure 59: Progressing floodwater after 35 seconds

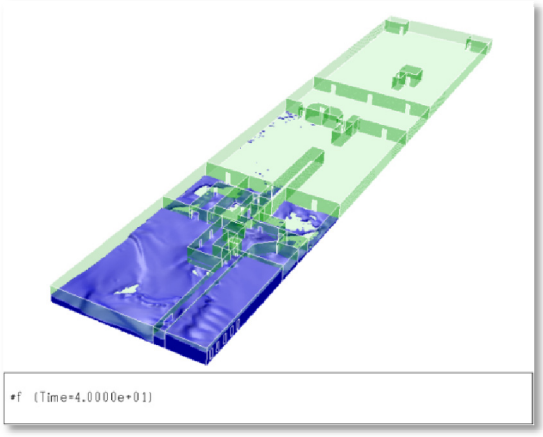

Figure 60: Progressing floodwater after 40 seconds

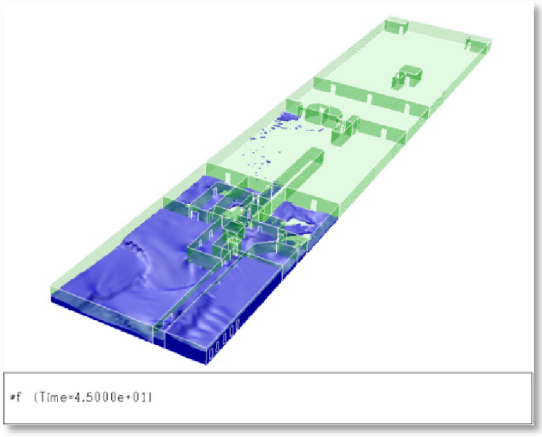

Figure 61: Progressing floodwater after 45 seconds

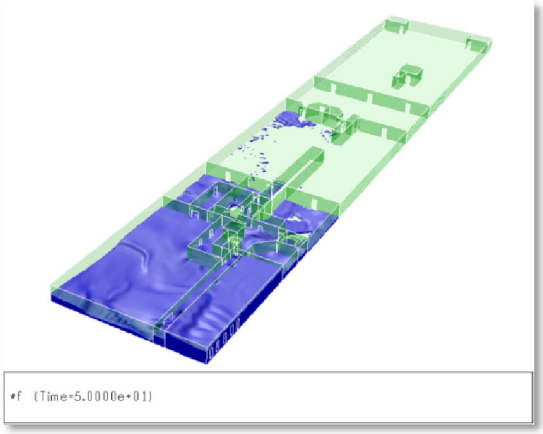

Figure 62: Progressing floodwater after 50 seconds

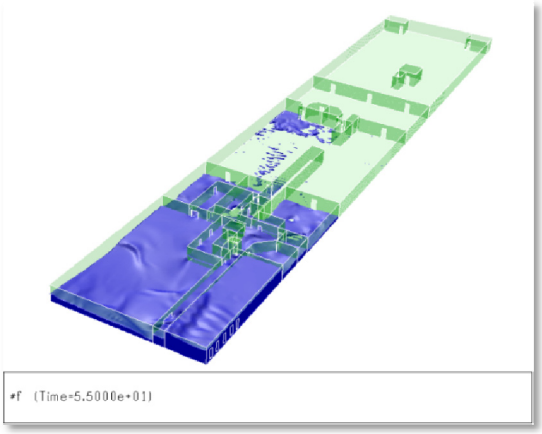

Figure 63: Progressing floodwater after 55 seconds

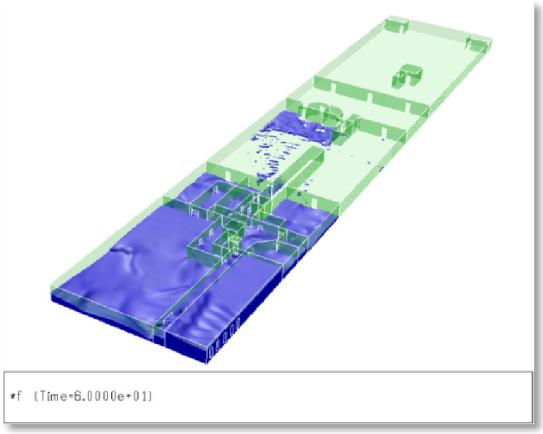

Figure 64: Progressing floodwater after 1 minute

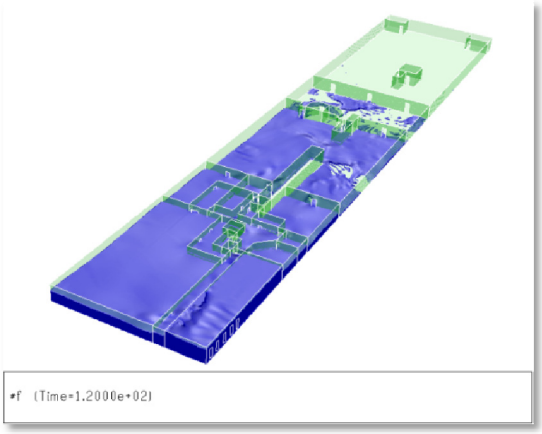

Figure 65: Progressing floodwater after 2 minutes

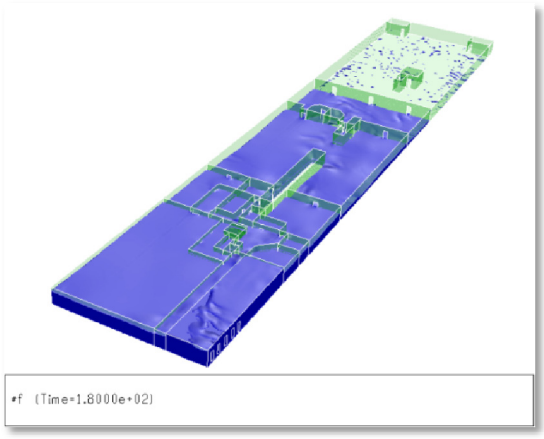

Figure 66: Progressing floodwater after 3 minutes

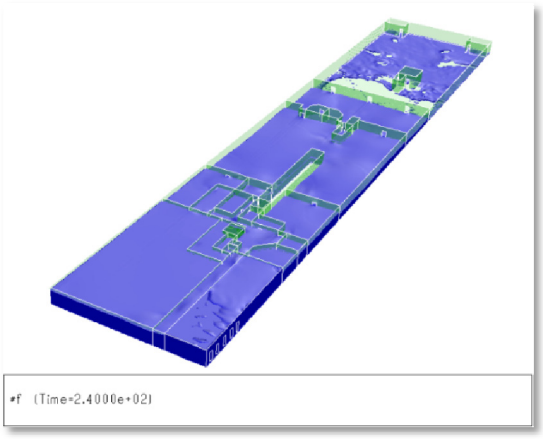

Figure 67: Progressing floodwater after 4 minutes

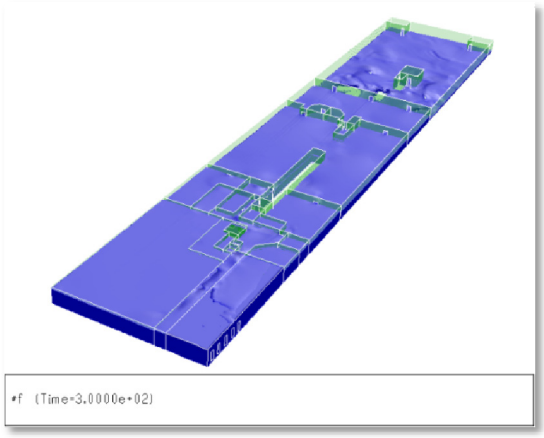

Figure 68: Progressing floodwater after 5 minutes

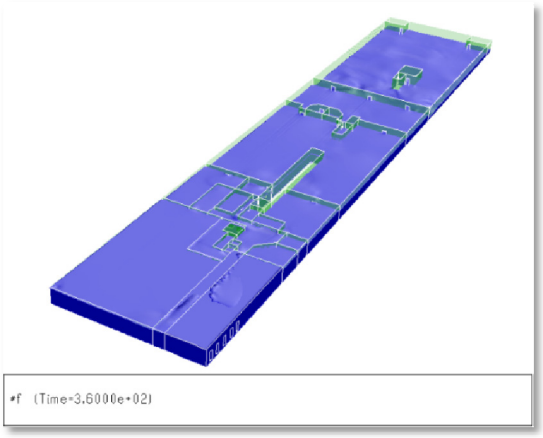

Figure 69: Progressing floodwater after 6 minutes

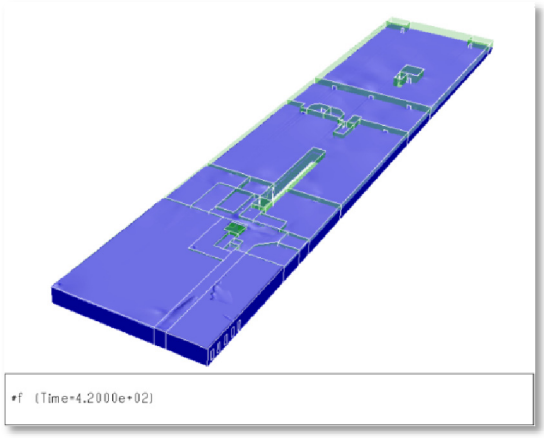

Figure 70: Progressing floodwater after 7 minutes

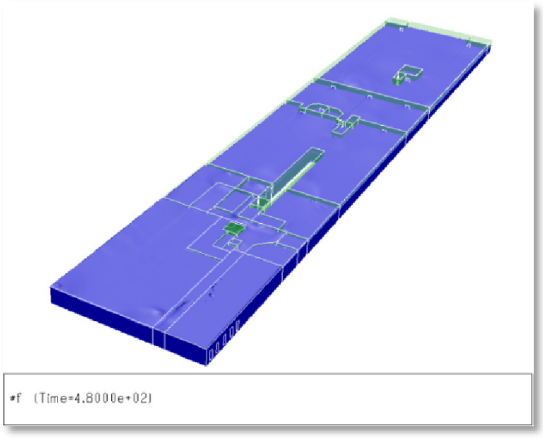

Figure 71: Progressing floodwater after 8 minutes

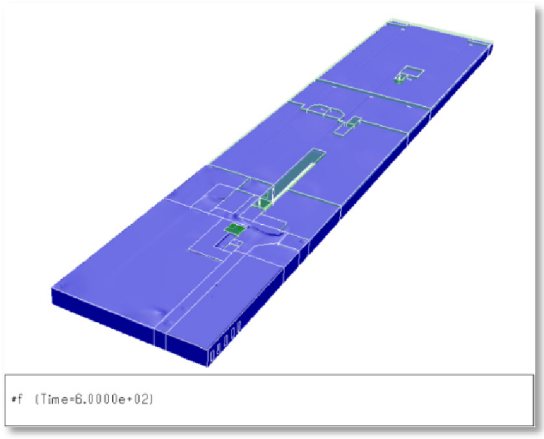

Figure 72: Progressing floodwater after 10 minutes

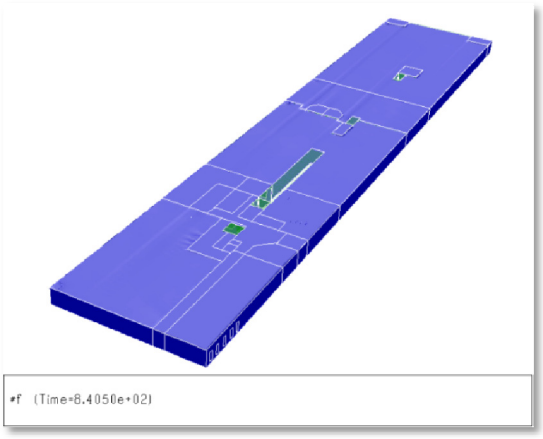

Figure 73: Progressing floodwater after 14 minutes

A detailed comparison between MARIN's model tests and the CFD calculation of the aft part of deck 4 was carried out to show similarities in the wave pattern of the floodwater surface, see Figure 74 - Figure 85. The CFD images show isosurfaces, velocity vectors and turbulence intensity (see chapter 7.3.1.3).

As expected, the floodwater velocity and turbulence intensity is higher in the area of doors and compartments near the damage opening than anywhere else. Flow velocity and turbulence intensity decreases the more floodwater has entered a compartment and the further the compartment is away from the damage opening.

Following figures show a good agreement with model tests and visualise comparable wave patterns in the simulation and the model tests at the same time instant.

Flooding scenario 6 seconds after floodwater penetration

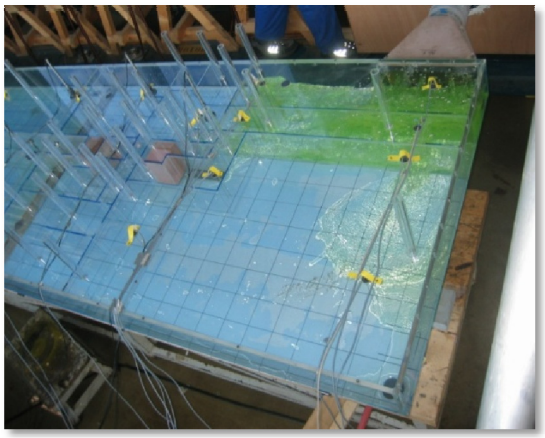

Figure 74: Model test after 6 seconds

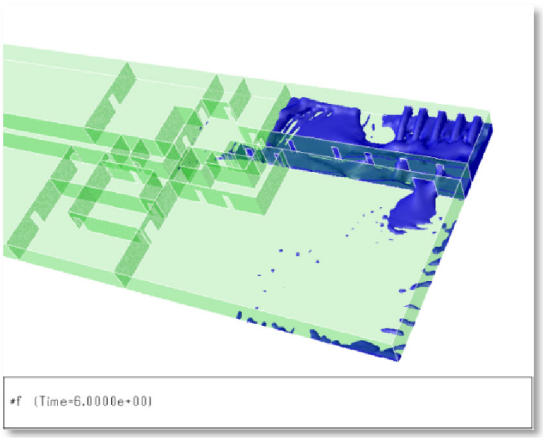

Figure 75: CFD isosurfaces after 6 seconds

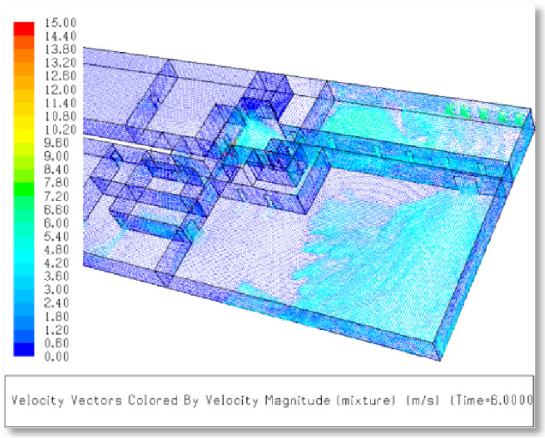

Figure 76: CFD velocity vectors after 6 seconds

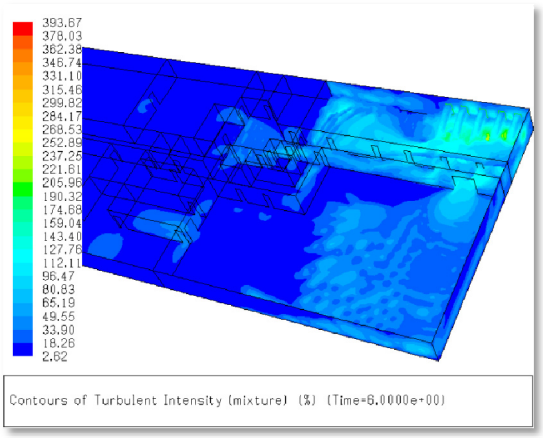

Figure 77: CFD turbulence intensity after 6 seconds

Flooding scenario 33 seconds after floodwater penetration

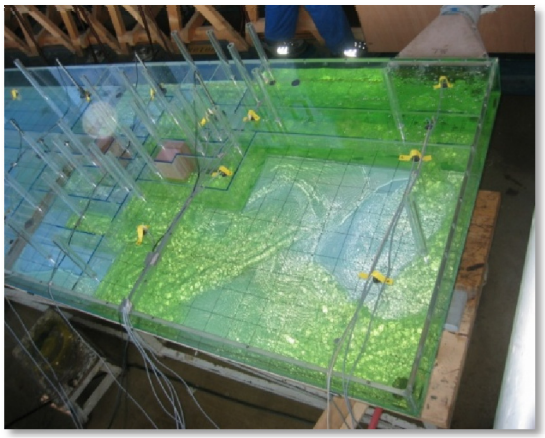

Figure 78: Model test after 33 seconds

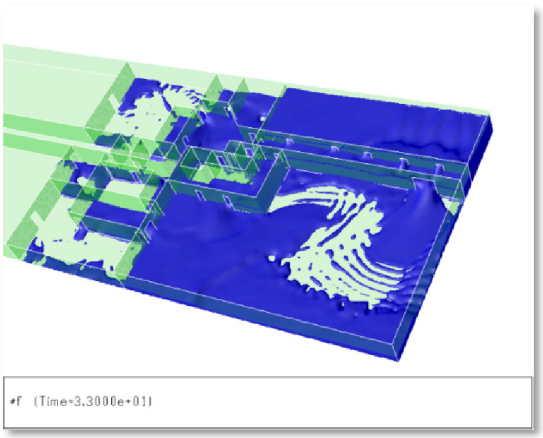

Figure 79: CFD isosurfaces after 33 seconds

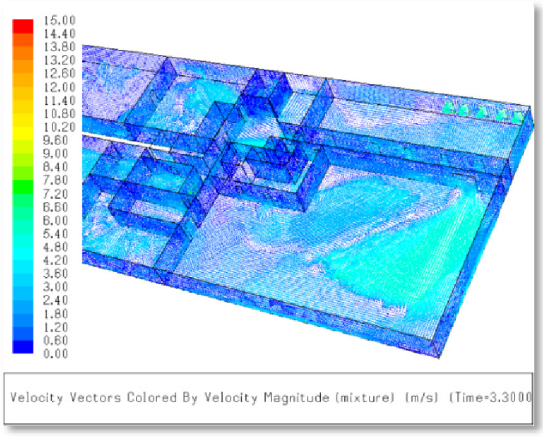

Figure 80: CFD velocity vectors after 33 seconds

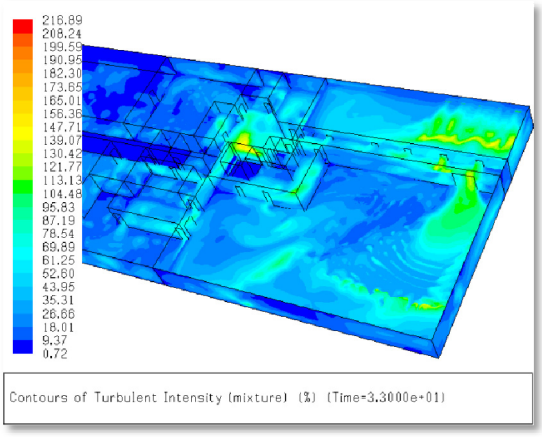

Figure 81: CFD turbulence intensity after 33 seconds

Flooding scenario 46 seconds after floodwater penetration

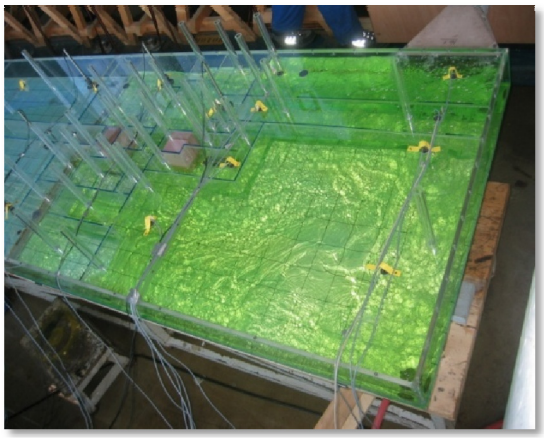

Figure 82: Model test after 46 seconds

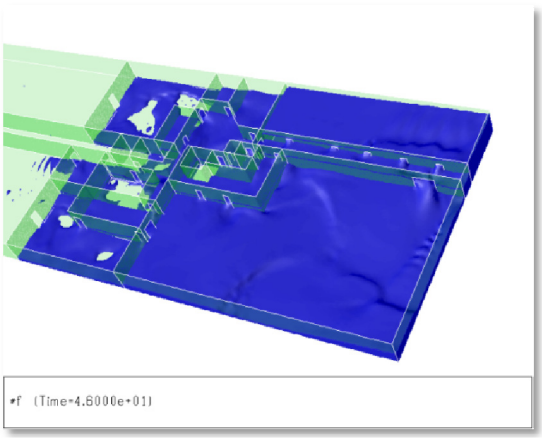

Figure 83: CFD isosurfaces after 46 seconds

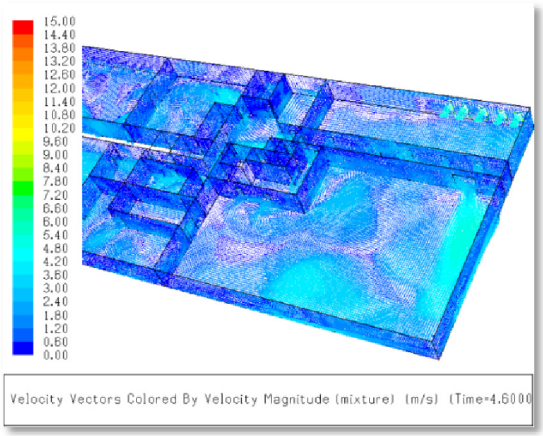

Figure 84: CFD velocity vectors after 46 seconds

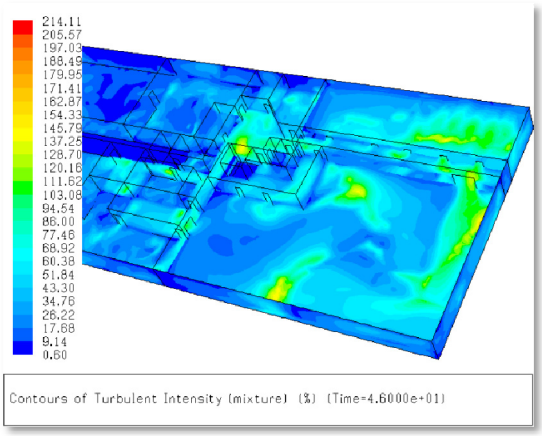

Figure 85: CFD turbulence intensity after 46 seconds

8.2.6.2 Water Level Height

The water level is measured in some selected large compartments. The probes are placed in the middle of the compartment in line with an opening in order to obtain measurands for direct incident floodwater flow. The location and identification of the probes can be found in Appendix A.1.1 and Appendix A.1.8.

MARIN uses probes that are based on the “hot wire” technique whereas each probe consists of two parallel stainless steel wires with a diameter of approximately 2 mm. The distance between the centres of the wires is 15 mm. For that reason the probe cannot measure the water height precisely in a single point but the accuracy is considered to be better than 0.5 mm. In cases of small water heights surface tension may decrease the measuring accuracy of the probes.

In the CFD model the water height is measured with “numerical” probes represented by faces with the dimension of the real probes which are added into a second identical geometrical model of deck 4 of M/V Estonia. After calculating the volume fraction for the whole deck, interpolation files are created with the first geometry and applied to the second model. The volume fraction of the wetted area on the probes is then determined and the water height calculated. The reason for this procedure is that the water flow is not influenced by the “numerical” probes. Additionally, this procedure saves computational resources and time.

Data from MARIN had to be scaled as its values for water height sometimes exceeded the limits for the maximum and minimum compartment height. Reason for that is the observation during the test program that the actual calibration factors were larger than the results of the calibration. This can happen because the conductivity of the medium changes rapidly from dry to wet and, additionally, the water used for the tests adds impurities after several test runs.

For a better comparison with results of CFD simulation, data from MARIN has been averaged and a regression analysis applying the Epanechnikov method, see Appendix B.2, has been undertaken in order to smooth the curves out. Results for

all probes can be compared in Figure 86 - Figure 105. Assignment of the captions used in the figures can be found in Appendix A.2, Table 32.

In some cases the data compared to the model tests features some discrepancies due to the use of different geometries. A direct correlation between small deviations in the data comparison and geometrical discrepancies listed in Appendix A.3, Table 33 can be noticed.

Generally, the accuracy of the CFD calculations and of the model tests in reverse is confirmed.

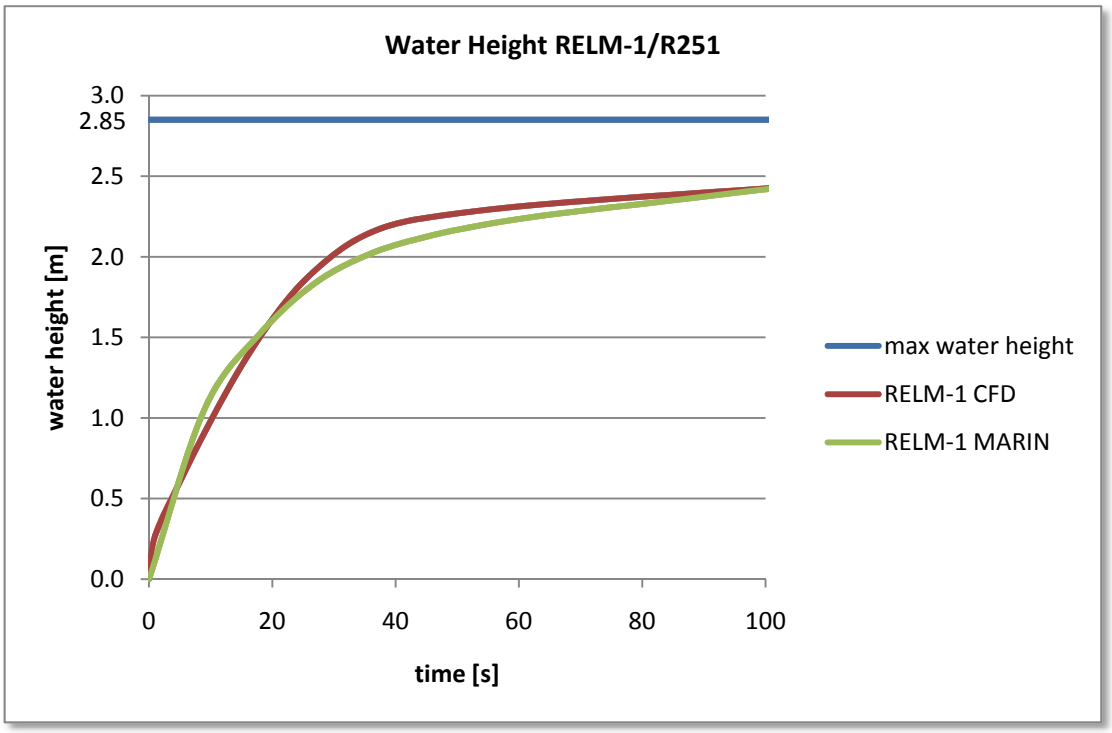

Figure 86: Comparison of RELM-1

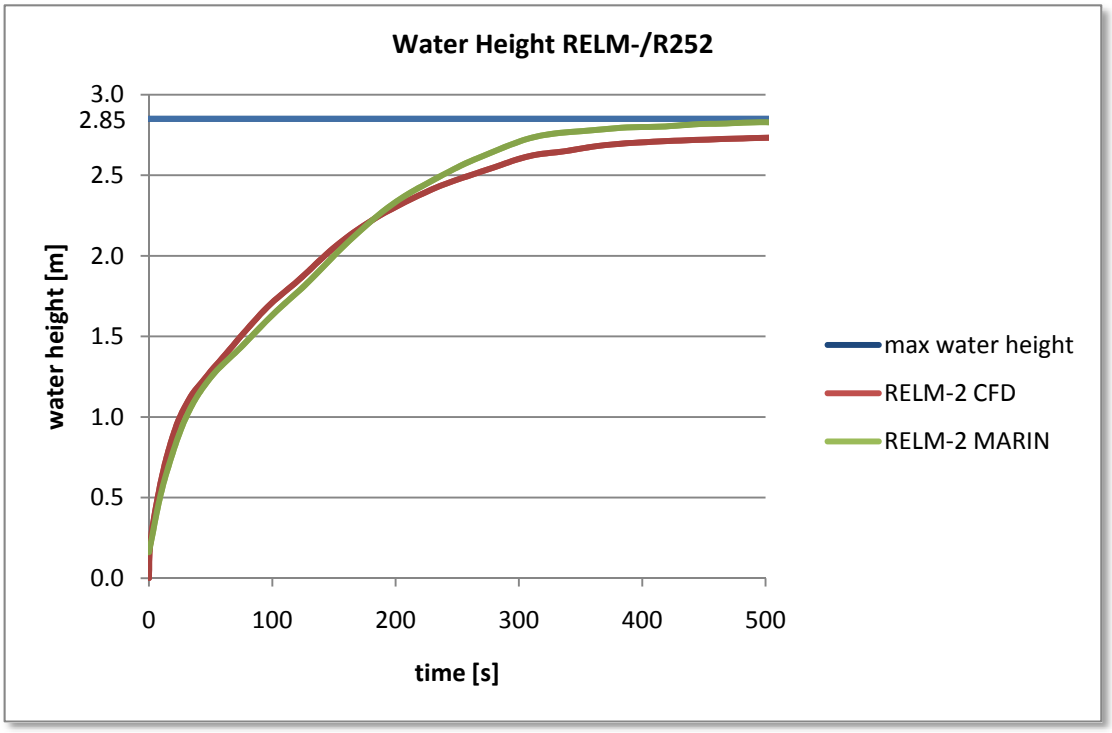

Figure 87: Comparison of RELM-2

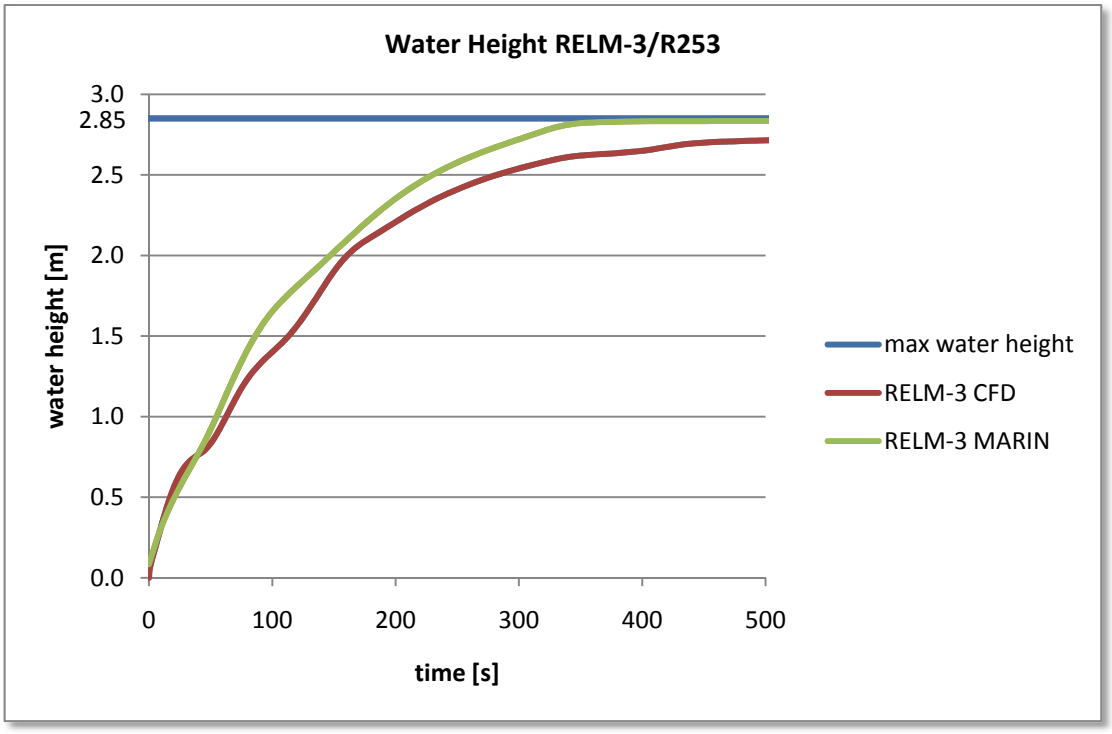

Figure 88: Comparison of RELM-3

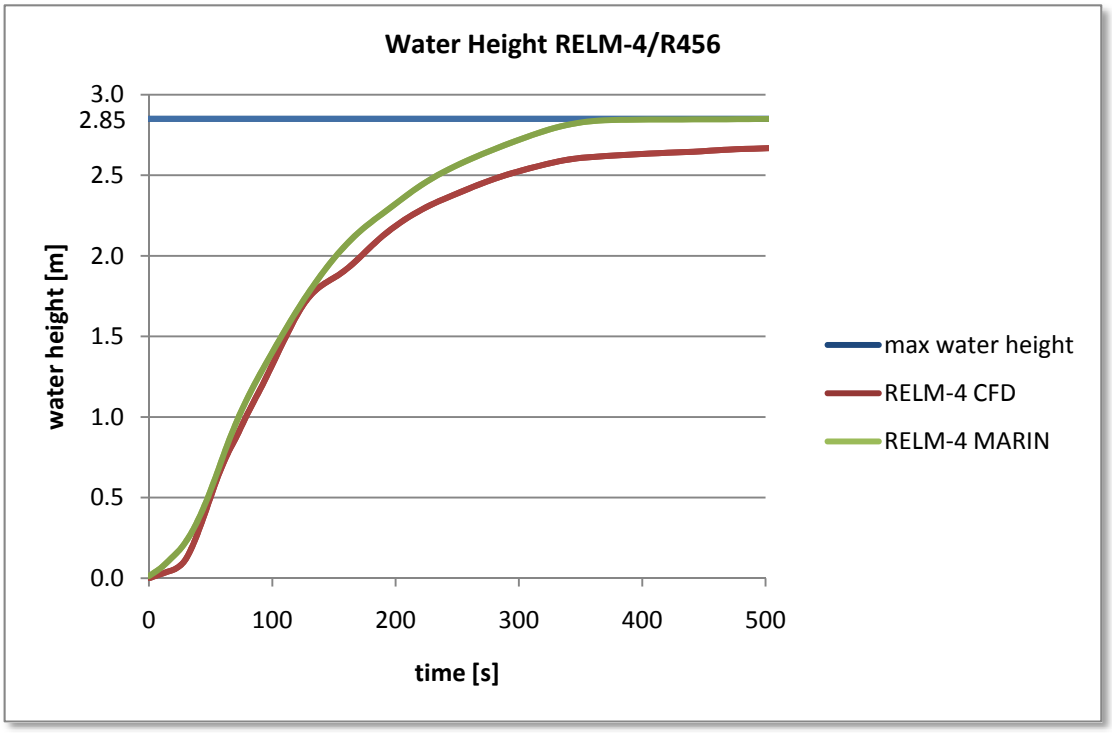

Figure 89: Comparison of RELM-4

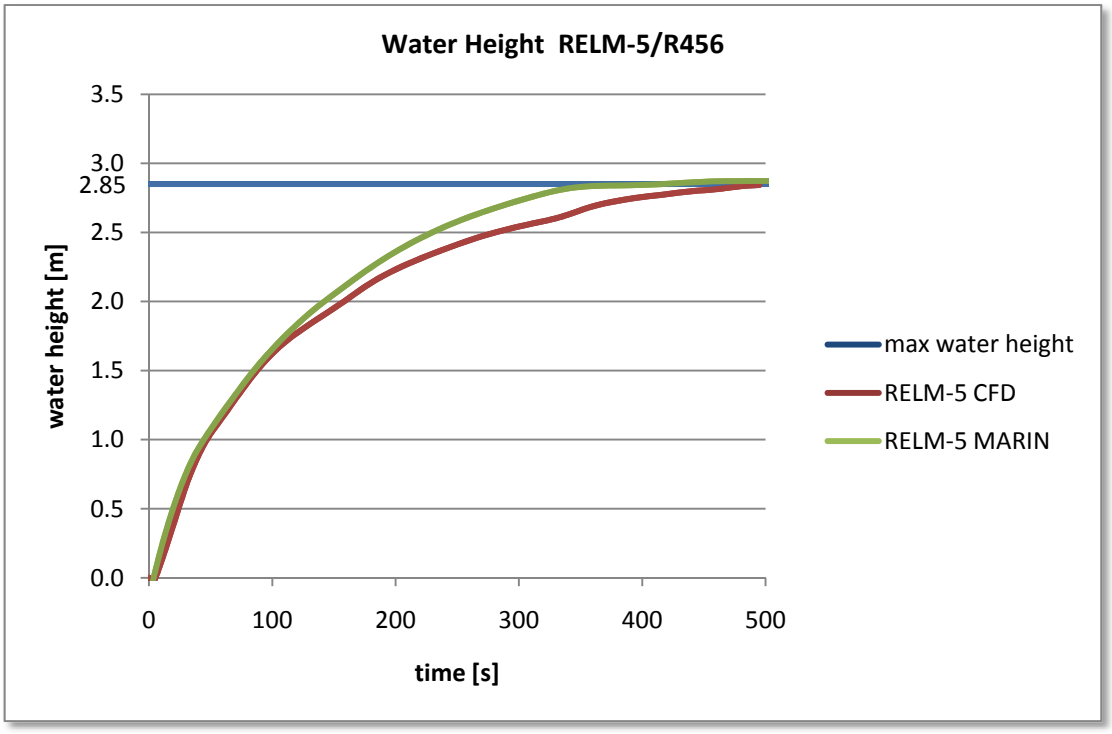

Figure 90: Comparison of RELM-5

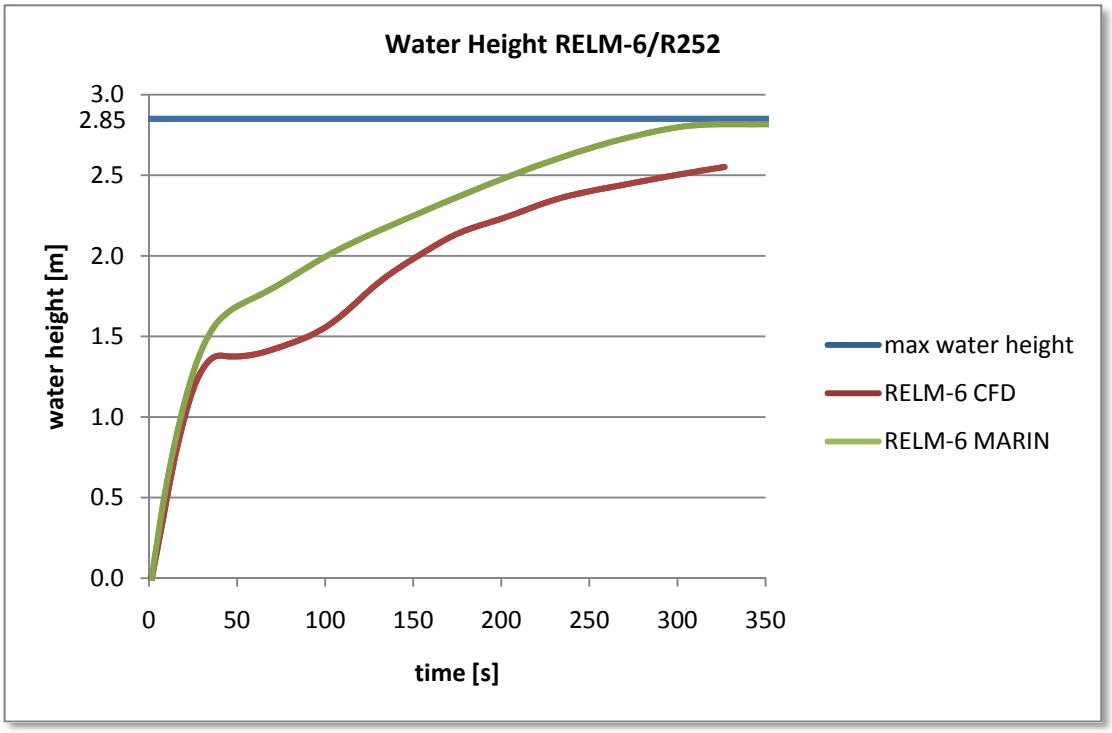

Figure 91: Comparison of RELM-6

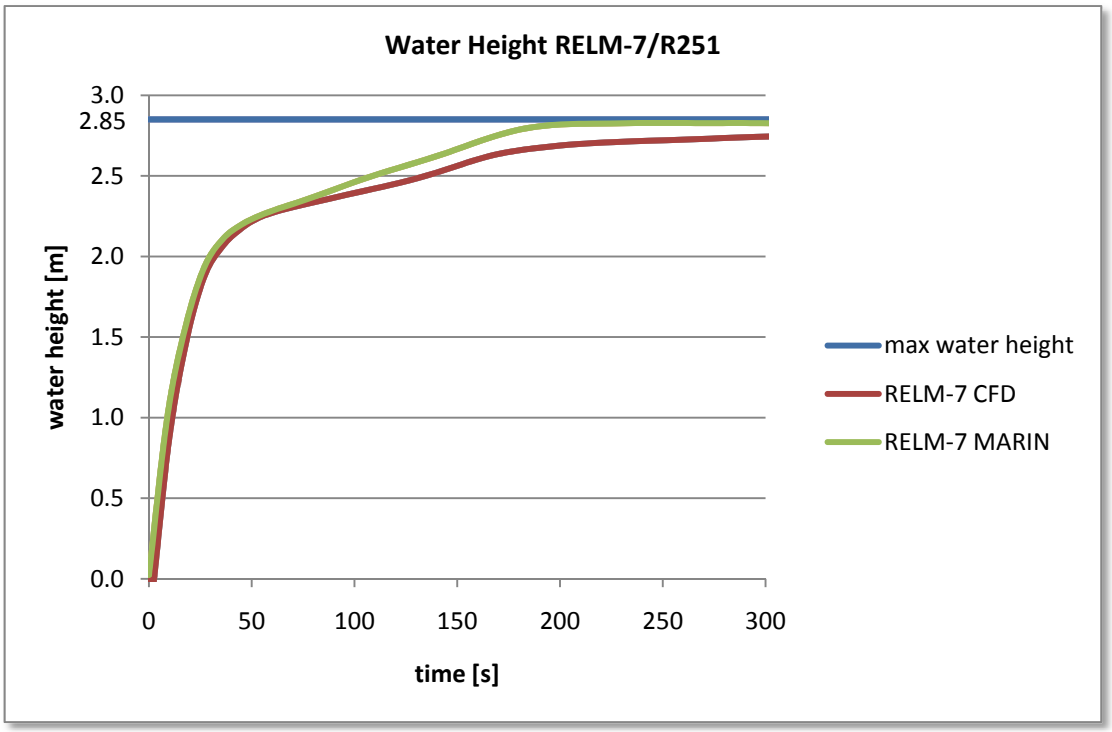

Figure 92: Comparison of RELM-7

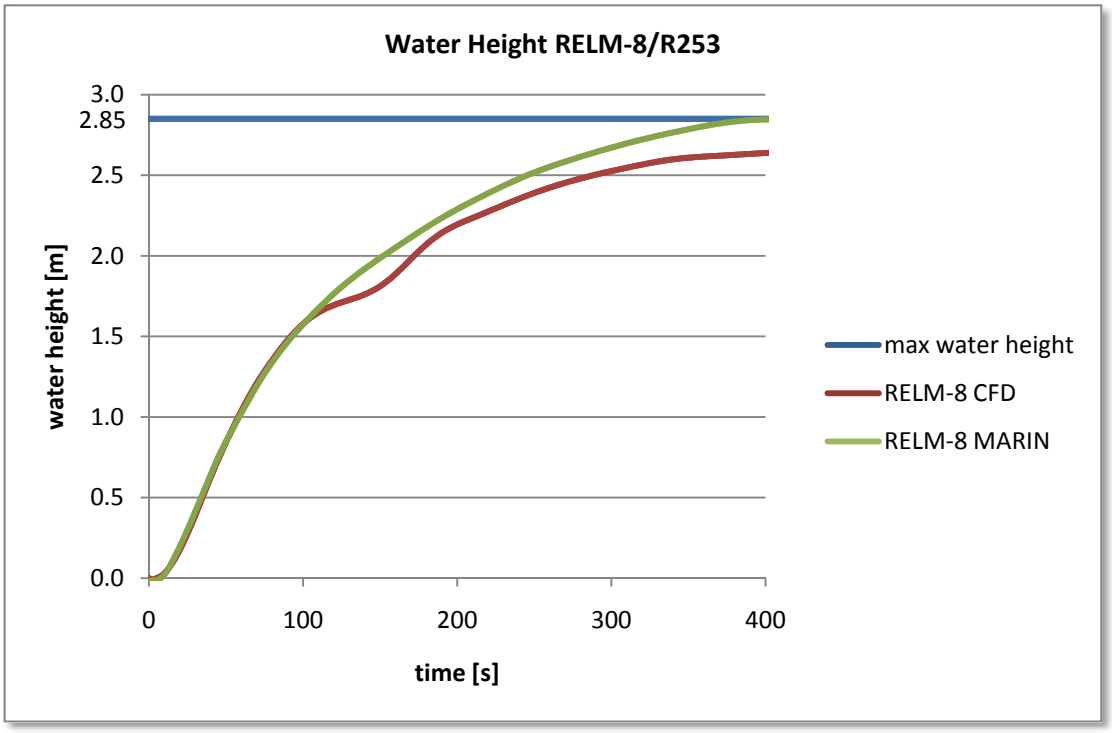

Figure 93: Comparison of RELM-8

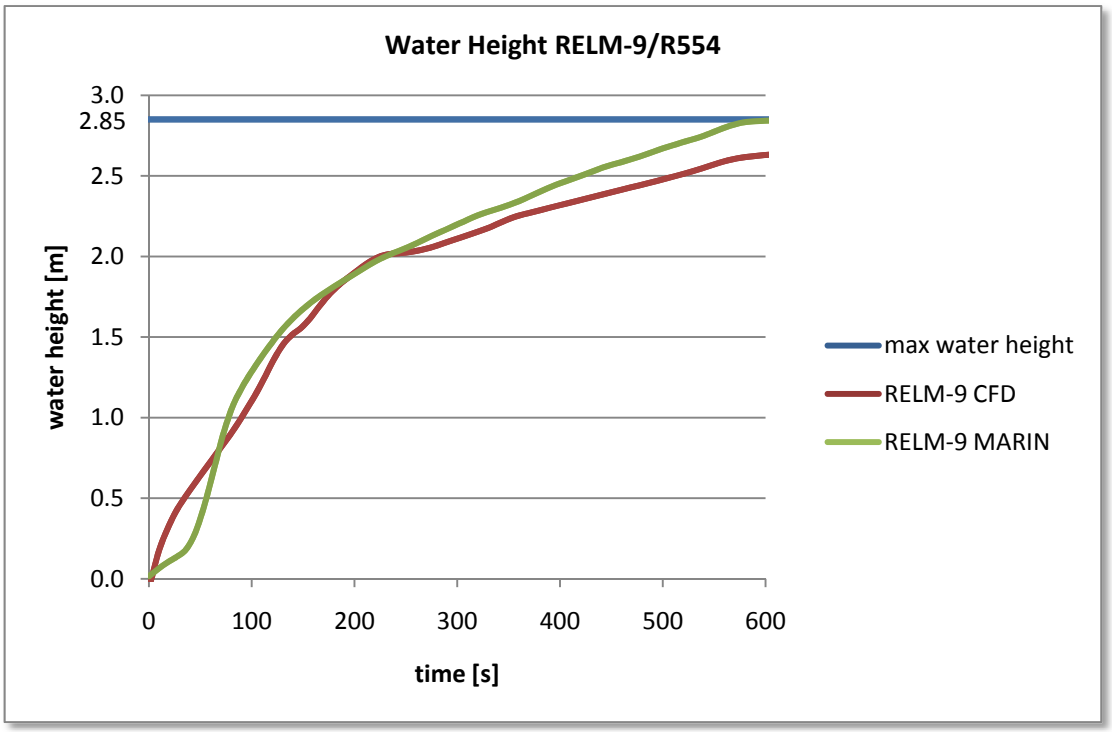

Figure 94: Comparison of RELM-9

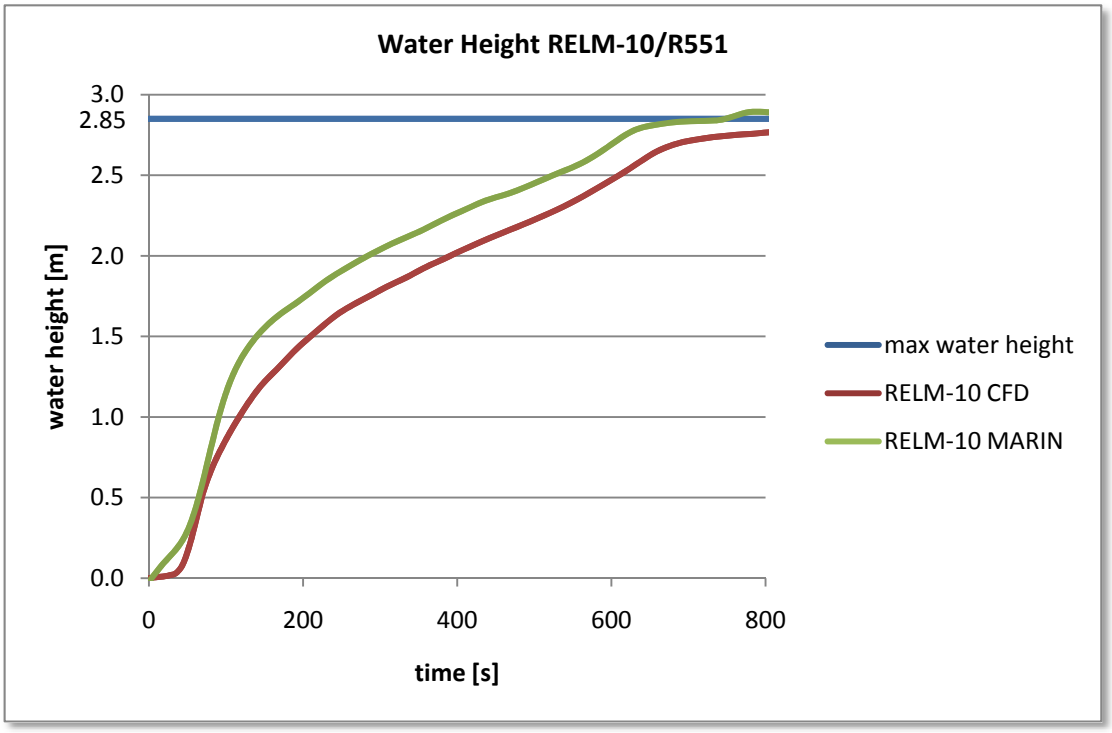

Figure 95: Comparison of RELM-10

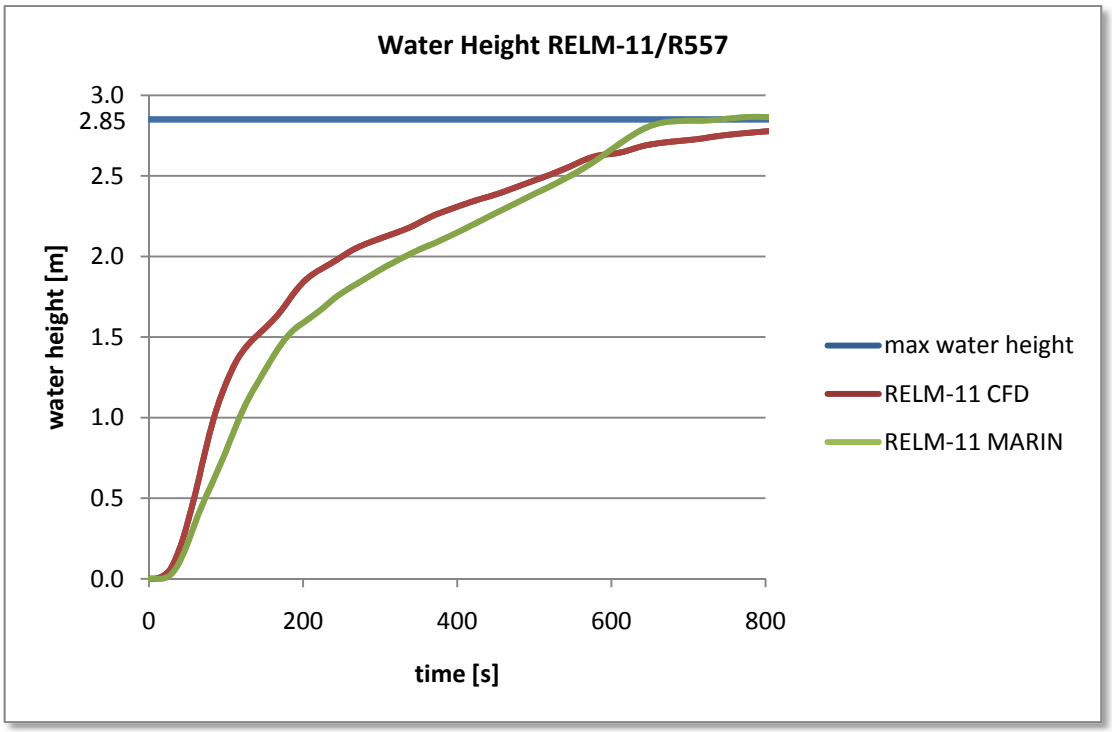

Figure 96: Comparison of RELM-11

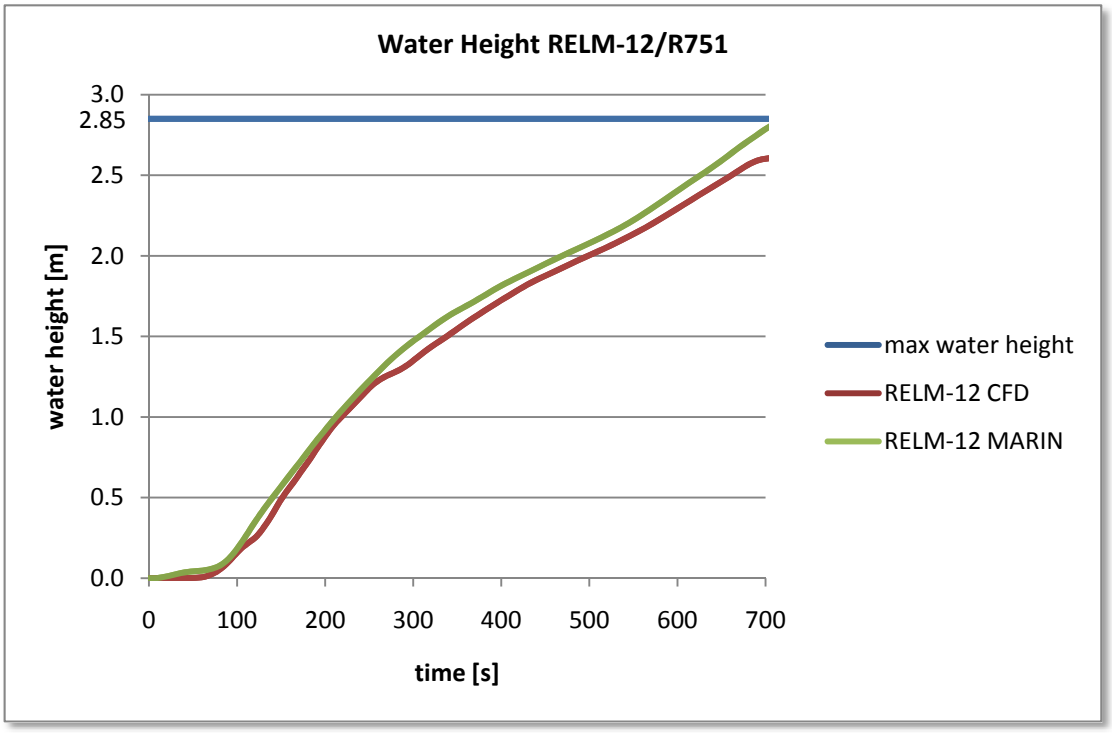

Figure 97: Comparison of RELM-12

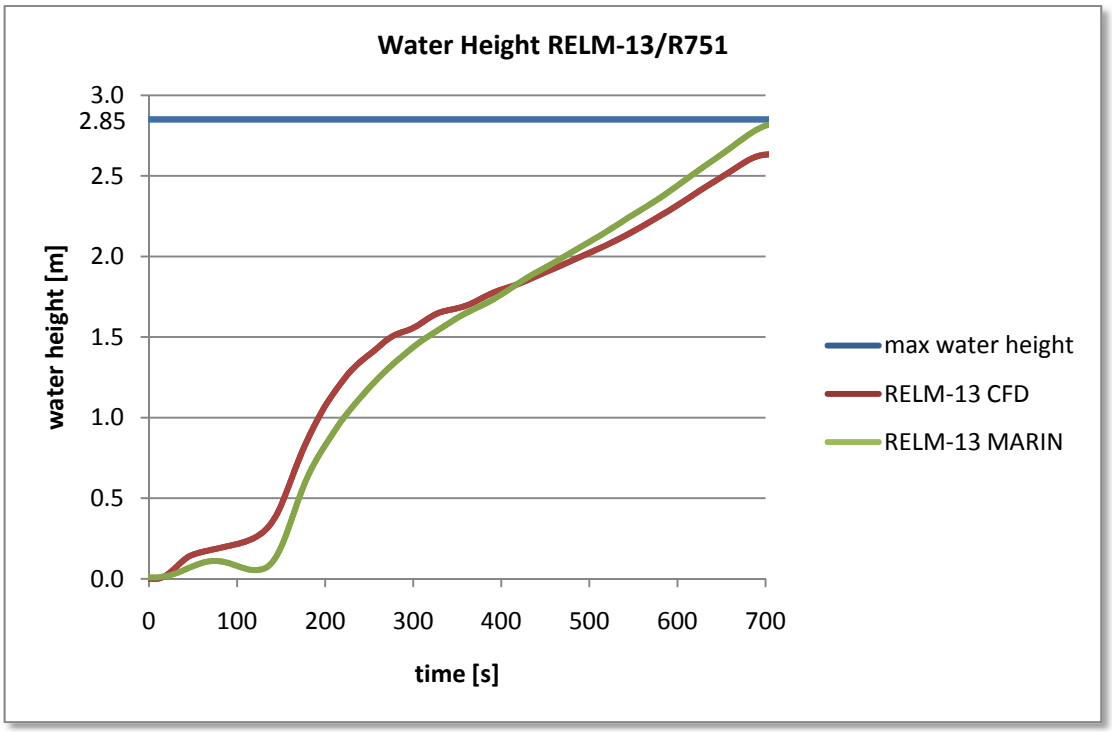

Figure 98: Comparison of RELM-13

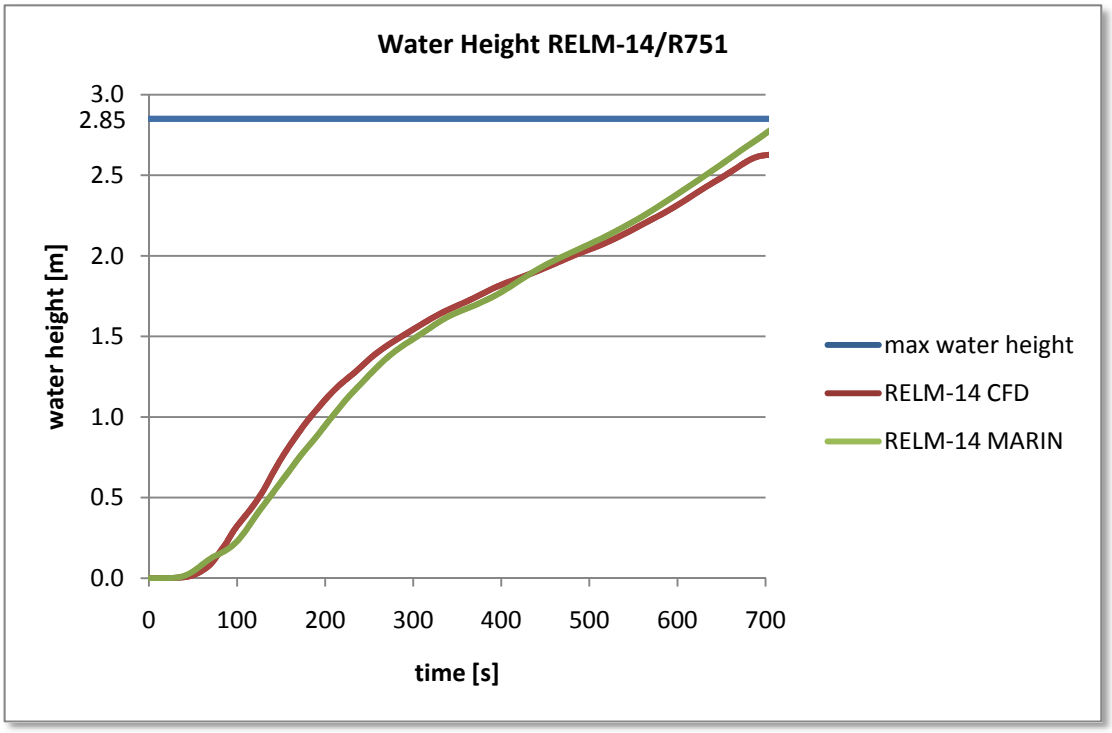

Figure 99: Comparison of RELM-14

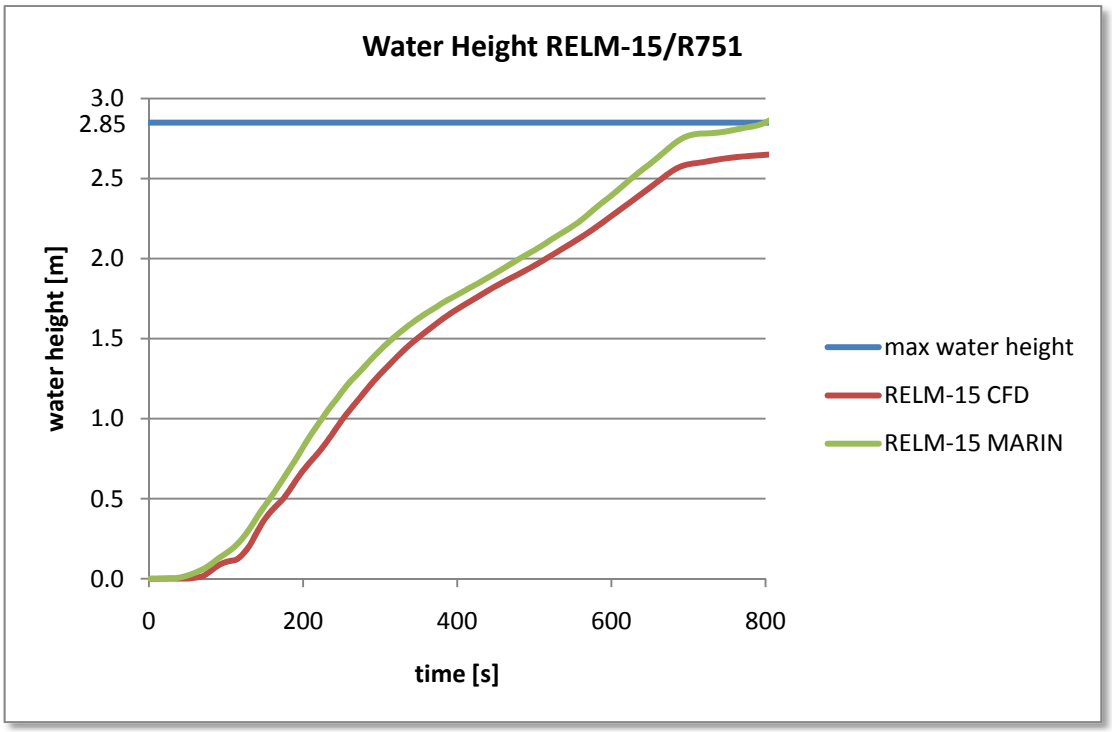

Figure 100: Comparison of RELM-15

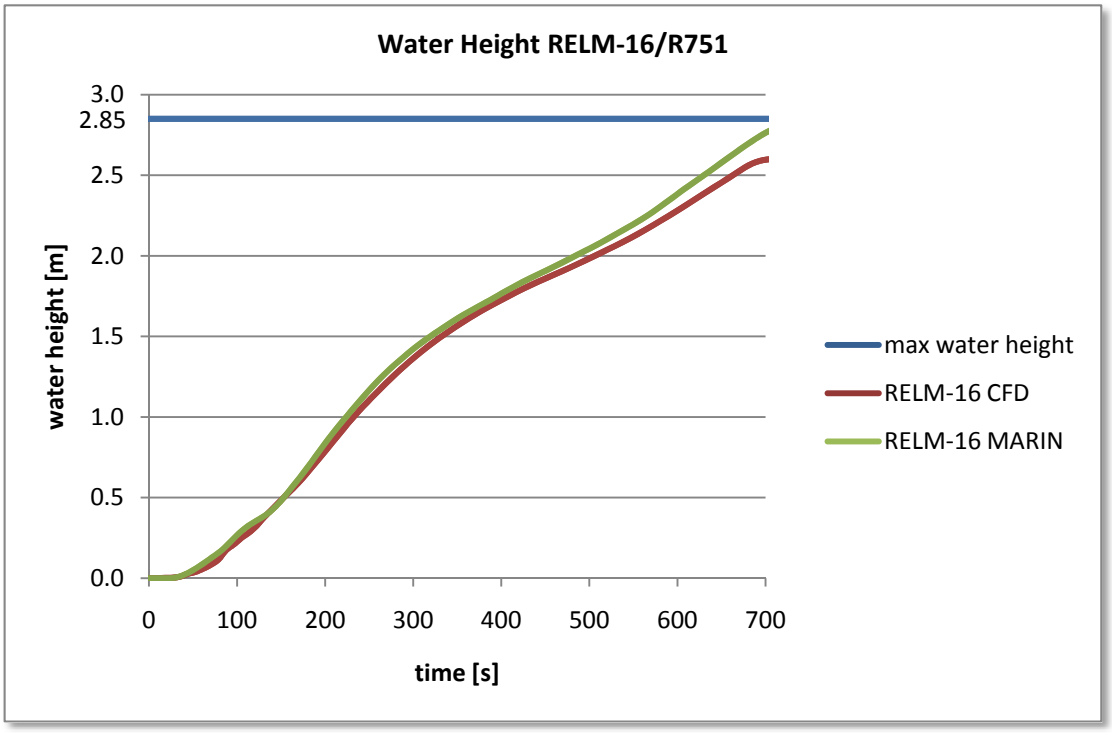

Figure 101: Comparison of RELM-16

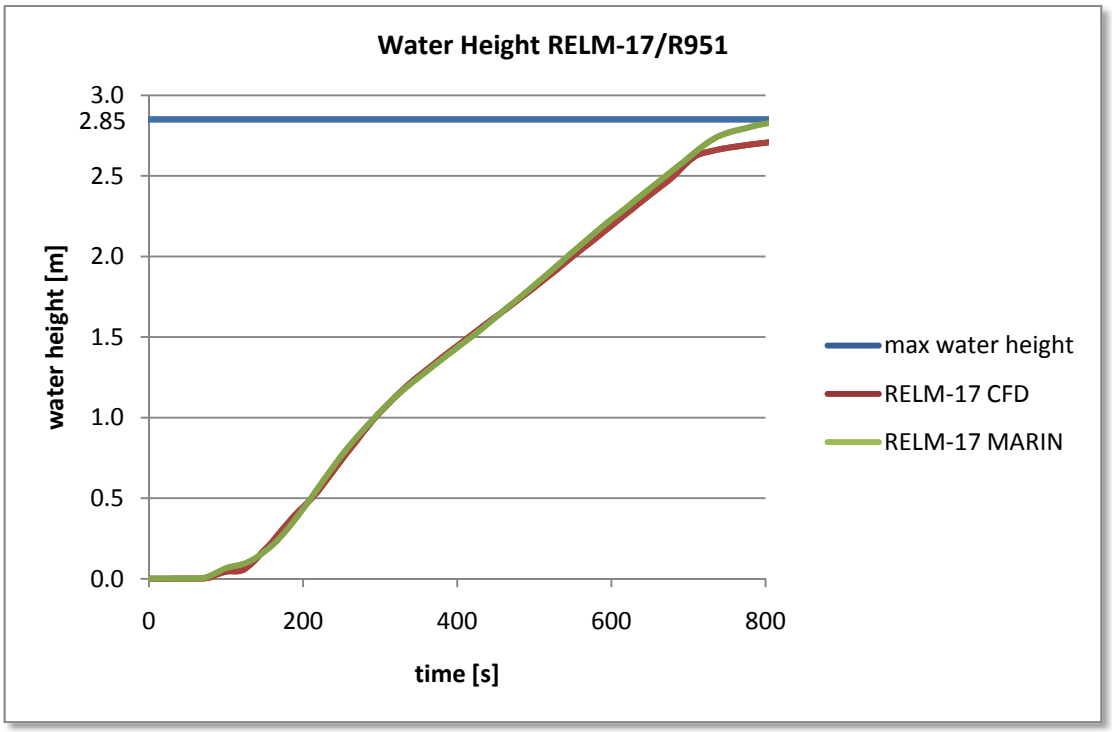

Figure 102: Comparison of RELM-17

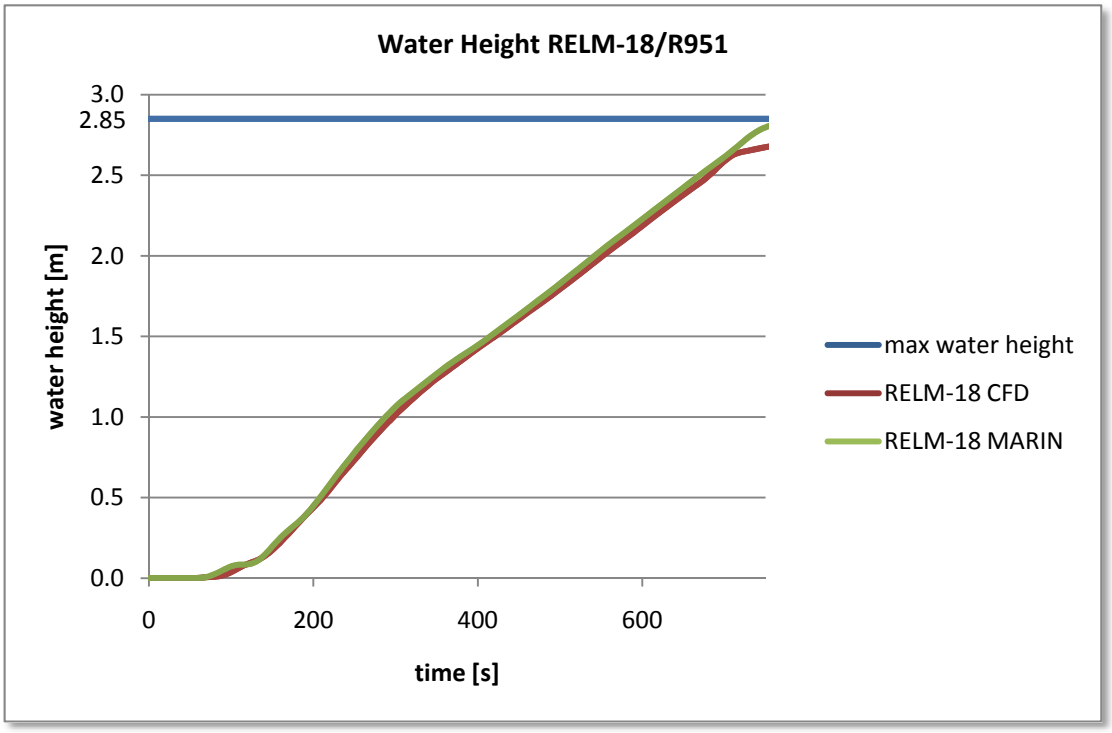

Figure 103: Comparison of RELM-18

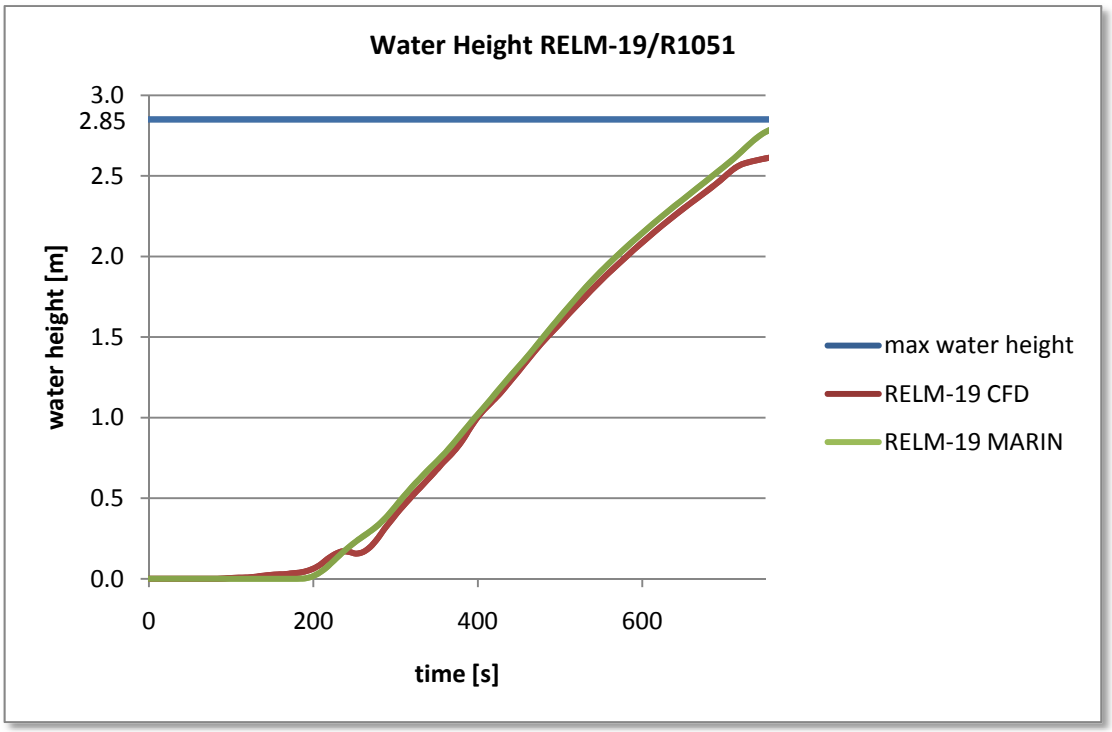

Figure 104: Comparison of RELM-19

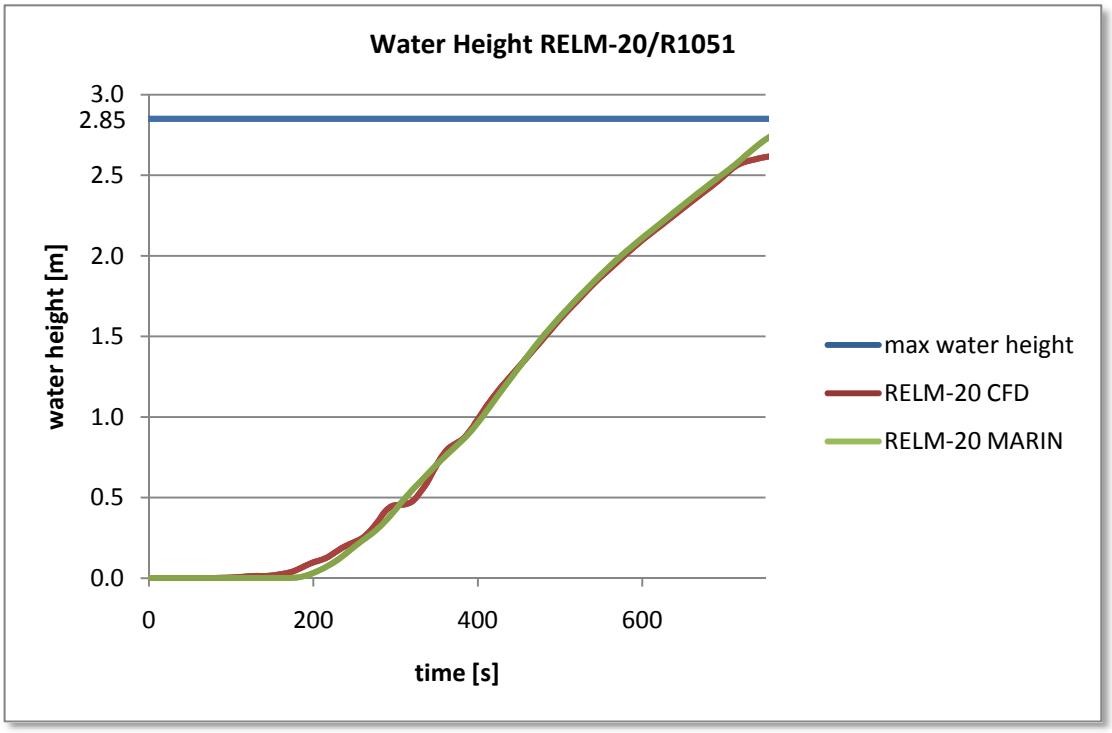

Figure 105: Comparison of RELM-20

When the data of the water height has been analysed and compared to experimental data it has been observed that all data lines in the water height charts had a bend at a certain point where the flooding slowed down though the compartment was fully ventilated. This bend occurs when the floodwater inside a room reaches the upper edge of the opening which raises the assumption that this bend shows a correlation between floodwater height and height of the openings as can be seen in Figure 106.

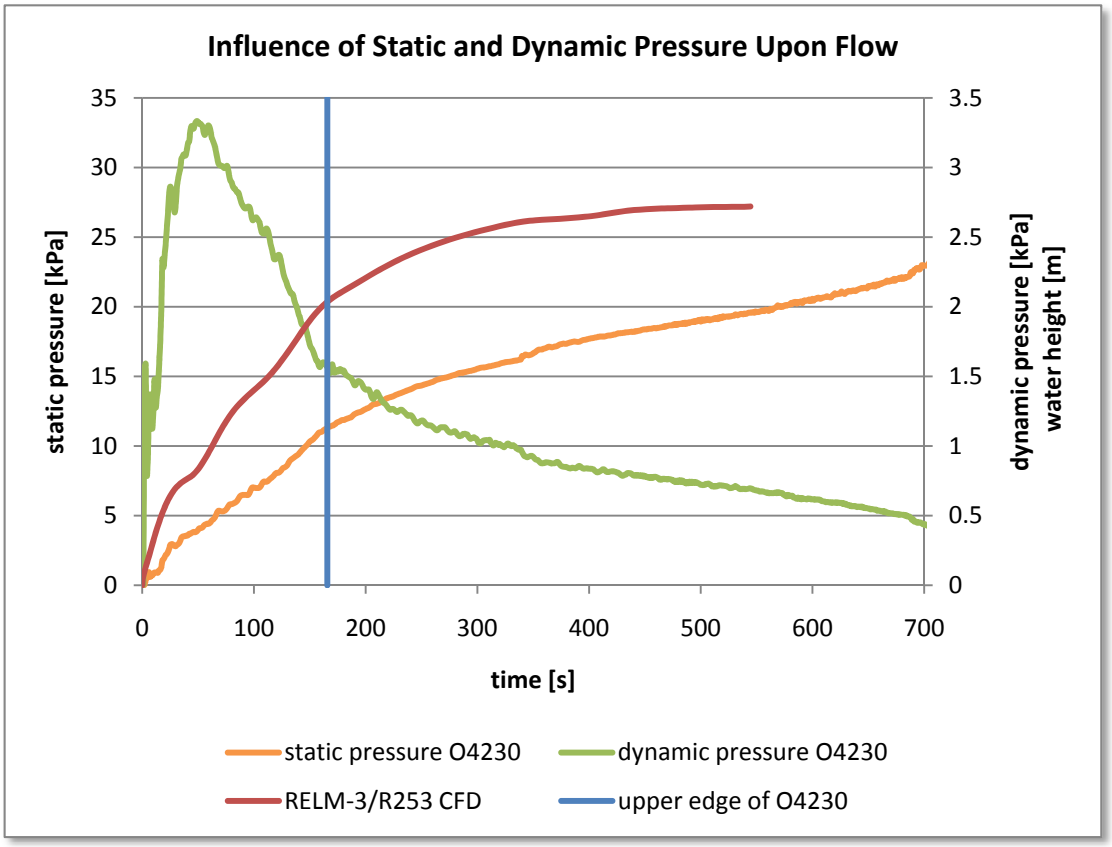

Figure 106: Influence of static and dynamic pressure on flow

This effect can be trivially explained with the Bernoulli equation (8.2.2) between two points. Point 1 lies in front of the opening and point 2 is in the opening.

$$p_1 + \frac{1}{2}\rho u_1^2 + \rho g H(t) = p_2 + \frac{1}{2}\rho u_2^2 \tag{8.2.2}$$

where p is air pressure, ρ is density, u is flow velocity and g is gravitational acceleration, see Figure 107.

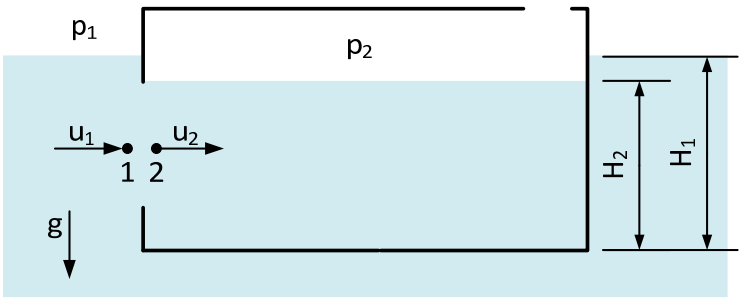

Figure 107: Effect explained by Bernoulli equation

When the rooms are fully vented, $p_1=p_2$ and air pressure has no effect on the floodwater flow. Figure 86 shows the water height level in the room which is directly connected to the water reservoirs through the damage openings. As the water reservoir outside room R251 is always replenished with water the damage opening has a constant head pressure distribution on the damage opening surface facing the water reservoir. When the water level inside room R251 rises, the pressure outside of the damage opening is counteracted by the developing static and dynamic pressure inside the room. Thereby, the dynamic pressure is less significant for the reduction of the pressure on the damage opening and smaller in magnitude than the static pressure. Due to the decreasing pressure difference behind and in front of the damage opening the flow through the damage openings slows down. This is demonstrated in Figure 86 where the water level seems to be constant up to a height of 2.2 m which is exactly the upper edge of the damage opening. In other words: the higher the water level rises inside the room the less energy is available to fill up the room with floodwater. The flooding stops when the pressure in the room and in the water reservoir is equal. This effect applies to all rooms that are connected through openings and can be observed in every compartment, see Figure 86 - Figure 105.

8.2.6.3 Volume Fraction of Flood Water

The volume fraction of water which entered deck 4 was monitored and compared to five model tests carried out by MARIN. Alternatively, the calculations were compared to the in-house numerical tool, PROTEUS3, which is a time domain solver that treats water as lump mass concentrated at its centre and the free surface is kept plane but is allowed to incline as a result of dynamic interaction between floodwater and ship. PROTEUS3 uses the hydraulic model for the calculation of the flow velocities by applying Bernoulli's equation as the momentum equation.

It should be mentioned that both, MARIN's model tests and Safety @ Sea's numerical simulation with PROTEUS3, used slightly different deck geometries compared to the CFD calculations. It can be agreed that MARIN's different deck geometry has hardly any influence on the comparison of the final results while Safety @ Sea's deck geometry can have some influence on the comparison of the final results due to some closed doors in the middle part of the deck. The difference in the geometry can be found in Appendix A.2, Table 33.

Data from MARIN is adapted as only vertical forces were measured with the three six-component force transducers. This data has to be converted into water volume by dividing the force with the water density.

In general the results of the CFD calculation match well with the model tests up to the point when floodwater reaches the top of the compartments and remaining little air bubbles cannot fully escape from the compartments through the air vents. The calculation then becomes instable and iterations tend to diverge and as a result the time step and relaxation factors have to be lowered.

PROTEUS3 results compare well only in an early stage of flooding, maybe because the geometry used for PROTEUS3 simulations was slightly different to the geometry used for CFD and MARIN model tests. These geometrical differences can be found in Appendix A.3. The results of the comparison can be seen in Figure 108. Assignment of the captions used in the figures can be found in Appendix A.2, Table 32.

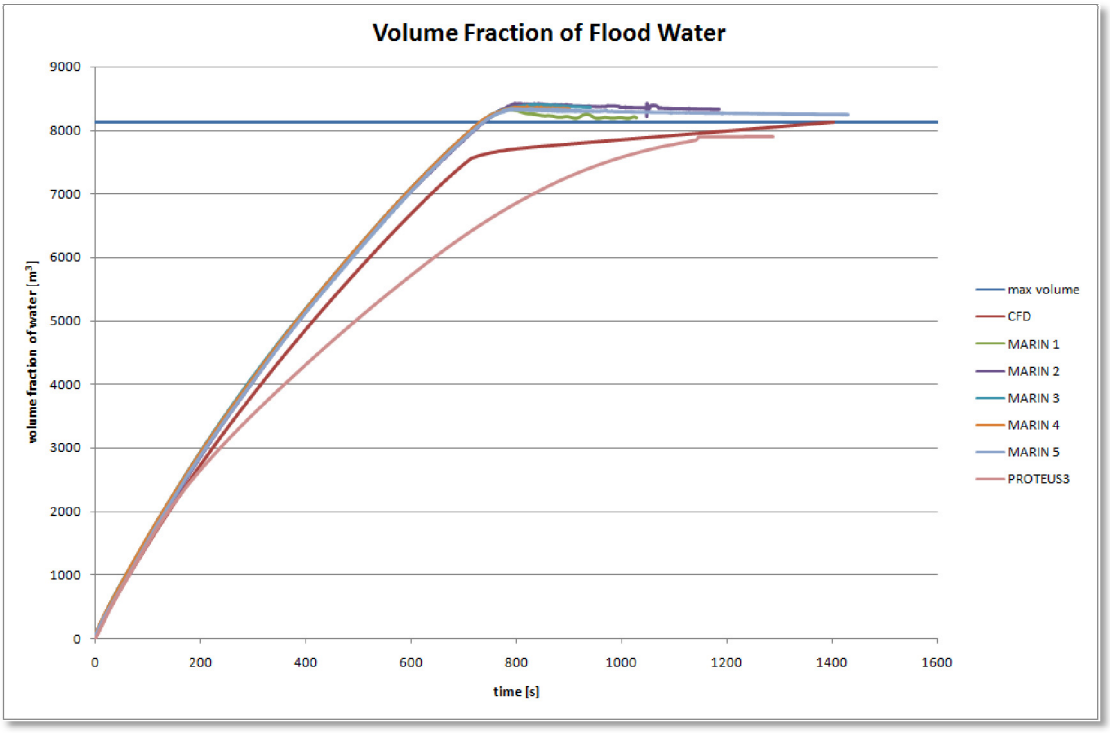

Figure 108: Volume fraction of floodwater on deck 4

8.3 Case 2: Box-Shaped Barge

8.3.1 Details of the Box-Shaped Barge

In this case study calculations were carried out with a box-shaped barge (Figure 109). Originally the model of the box-shaped barge was built to provide experimental data for the validation of numerical simulation methods. In reality, the barge does not exist in full scale, but it is representing a simple example of a floating structure with several compartments that are free to flooding. The size of the compartments and internal openings was selected in a way that the flooding behaviour would be complex enough to be similar to progressive flooding of a passenger ship. All main characteristics of the box-shaped barge are given in Table 7.

Length over all (L_{OA})	40	m
Breadth	8	m
Height	8	m
Design draft	5	m
Block coefficient at design draft	0.906	
Volume of buoyancy	1450	m^3

Table 7: Main Characteristics of the box-shaped barge

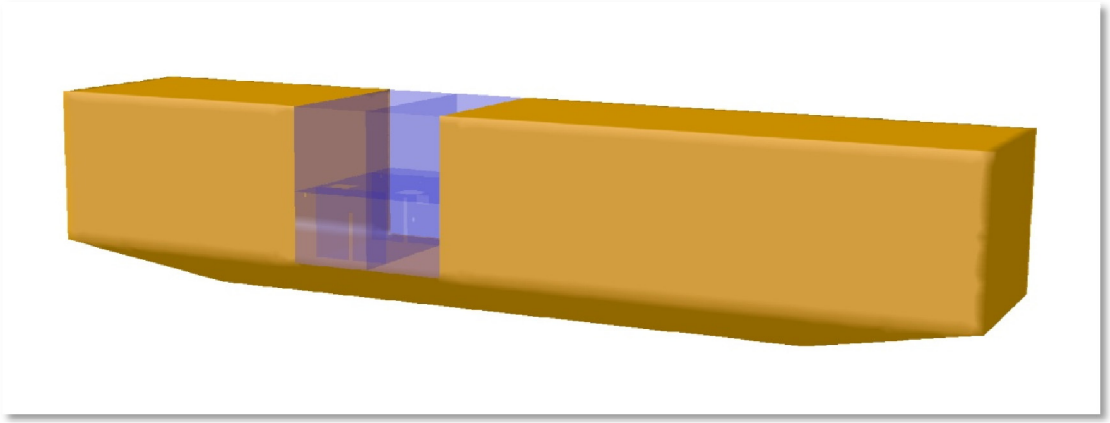

Figure 109: 3D view of the box-shaped barge

8.3.2 Design Requirements

The design was already used for a numerical study carried out by *Ruponen (2006)*. It concerns test case No. 6 which is side damage through a large opening in the forward compartment of the barge. The design requirements were kept the same for the physical and numerical models:

- Modelling of a box-shaped barge with an arrangement of floodable compartments which are located slightly forward from the mid-section of the barge.
- Application of a simplified compartment layout which includes 8 separate spaces and 12 openings.
- Depending upon the case, some openings are fully open and some are closed. The model is flooded through a large opening representing damage at the starboard side of a compartment.
- An initial draft of 0.5 m in model scale is adopted which corresponds to an inflow pressure head of 0.165 m above the top of the damage opening. Due to appearing quasi-static ship motions in calm water during the flooding process the inflow pressure head will vary according to the new draft positions and therefore corresponding hydrostatic pressure in the water tank.
- The model can float freely and both aft and forward trim is levelled to zero.
- The compartments are only partly ventilated, so that air pockets can develop.

8.3.3 Modelling of the Box-Shaped Barge

The box-shaped barge was modelled according to the design requirements in the previous section. A general view of the model can be observed in Figure 110 which is dimensioned in model scale λ=10. In Table 8 the main characteristics of the barge are listed.

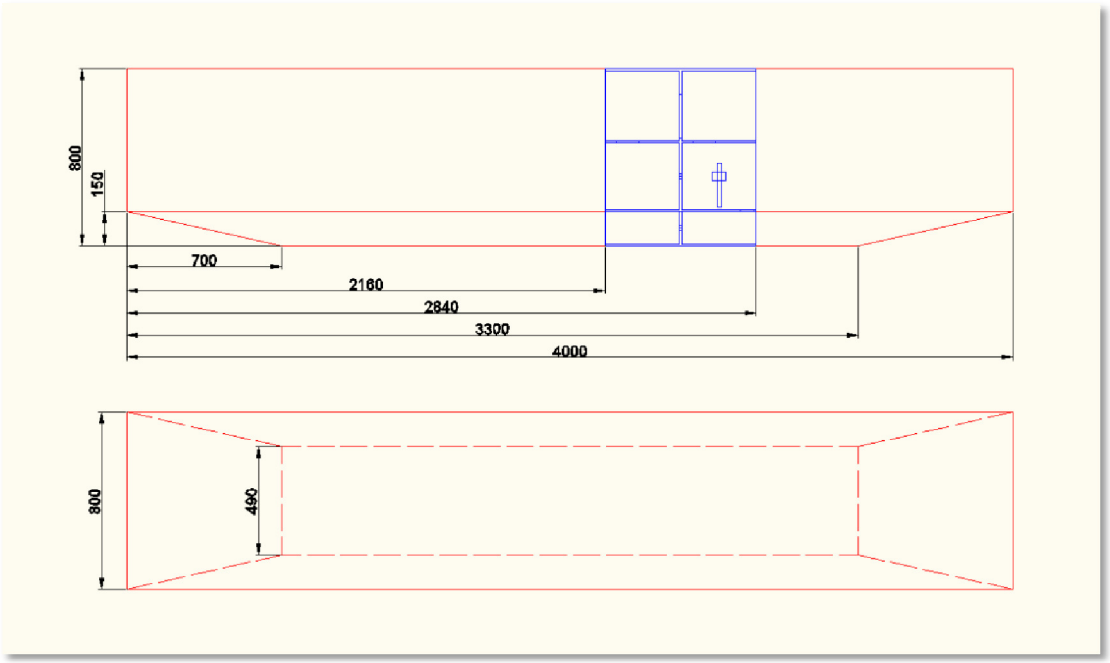

Figure 110: General view of the box-shaped barge

Length over all (L_{OA})	4.000	m
Breadth	0.800	m
Height	0.800	m
Design draft	0.500	m
Block coefficient at design draft	0.906	
Volume of buoyancy	1.450	m^3

Table 8: Main dimensions of the numerical model in model scale λ=10

Main attention was paid to the design of the flooded compartment and its details. Compared to the model used in the model test, internal walls of the numerical model had to have zero thickness which added slightly more volume to the rooms in the numerical model but had no severe influence on the results of the calculation. The dimensions of the compartment and its details are presented in Figure 111 - Figure 113. Walls are represented by blue lines and openings by black lines, respectively.

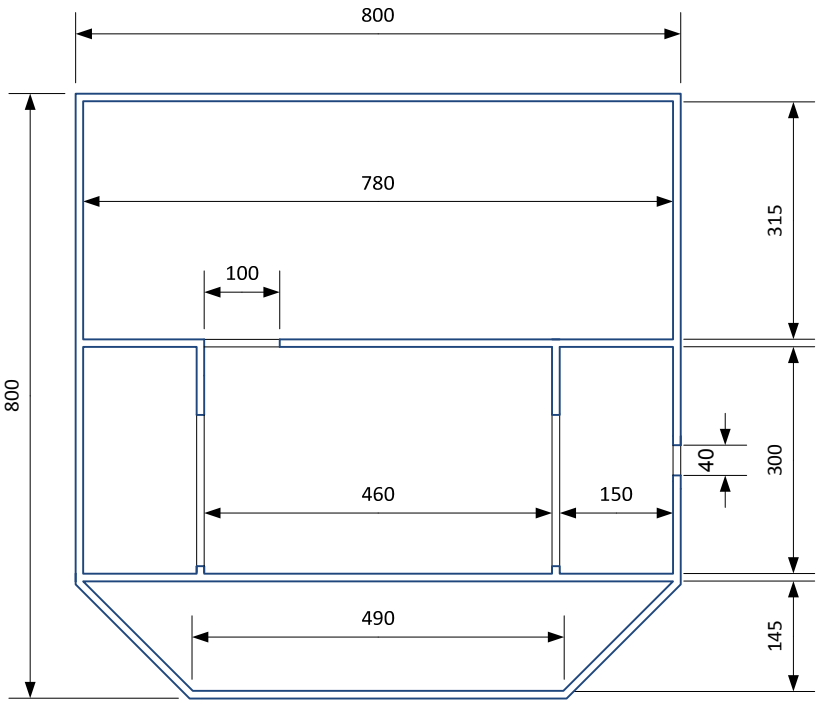

Figure 111: Cross-section of the forward compartment

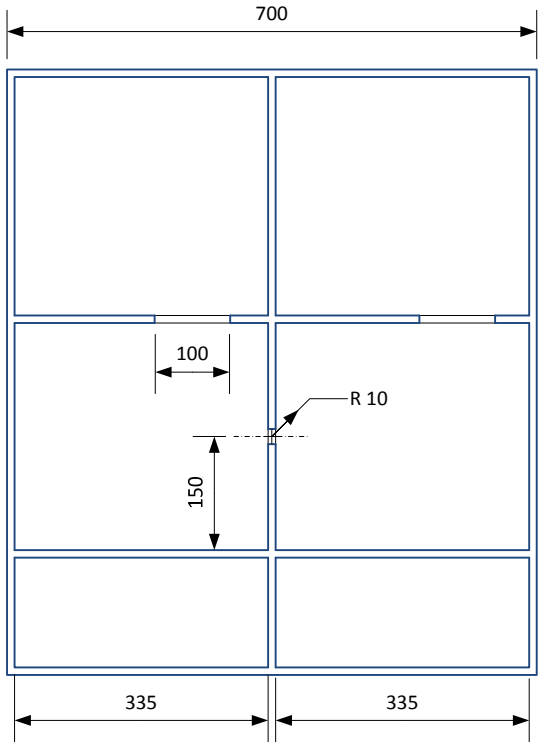

Figure 112: Side view of the compartments

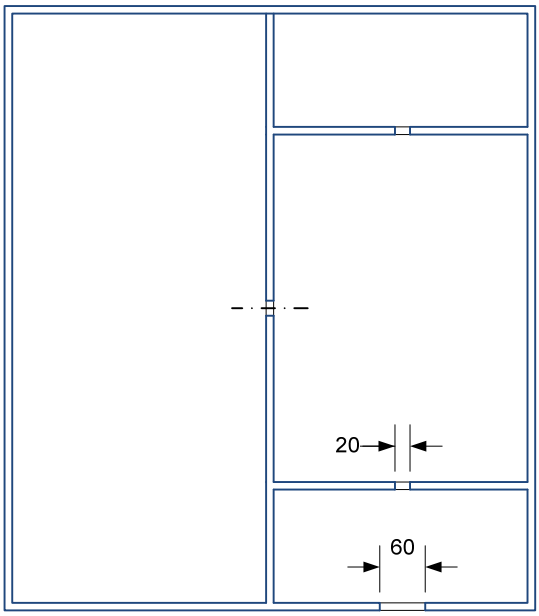

Figure 113: Top view of the lower compartment

The flooded compartment is located forward from the mid-section of the barge. The layout of the compartment consists of 8 separate rooms that are connected trough doors, pipes, manholes or staircases. The lower part of the compartment consists of two rooms representing the double bottom DB1 and DB2. A manhole on the ceiling of DB2 is leading to deck 1. As this manhole was closed while performing the model test no water could flow into the double bottom, therefore double bottoms DB1 and DB2 were not modelled for the numerical simulation.

Rooms are defined by a three/four digit code. R means room, the first number denotes the longitudinal position of the room where 1 is the aft compartment and 2 is the forward compartment. The second number defines the deck number so that 1 is the lower deck or tank top and 2 is the upper deck. The port and starboard side are marked by the additional letters P and S, respectively. All rooms are presented in Figure 114.

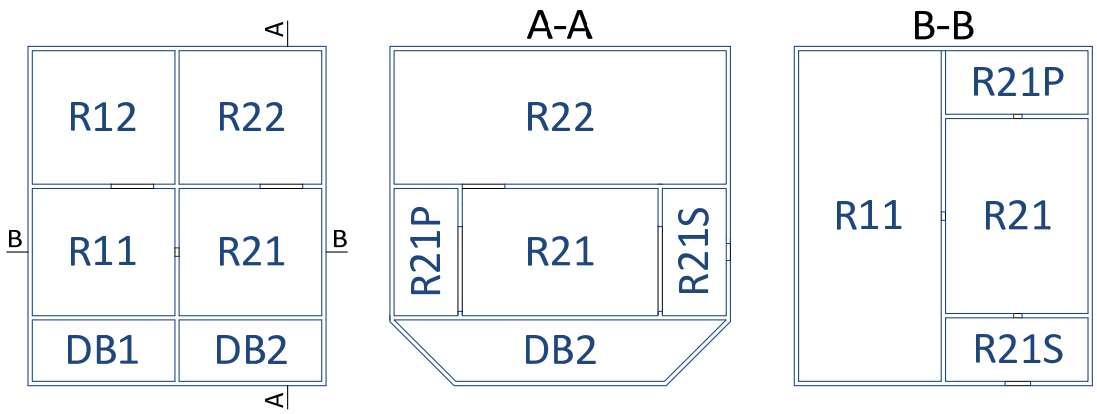

Figure 114: Identification of compartments

All rooms are connected through openings which are listed in following Table 9. Only open connections are modelled while closed connections are neglected. The dimensions of the openings are given in x-y-z direction.

Identification		**Connecting**	**x [mm]**	**y [mm]**	**z [mm]**
FDP	Fire door port	R21↔R21P	20		200
FDS	Fire door starboard	R21↔R21S	20		200
DP	Damaged pipe	R11↔R21		∅20	
SC1	Staircase aft	R11↔R12	100	100	
SC2	Staircase forward	R21↔R22	100	100	
DAS	Damage opening starboard	R21S↔Sea	60		40

Table 9: Identification and dimension of openings

The compartment was flooded from an opening in the centre of room R21S. Damage opening DAS was connected to the moving water domain in the water tank. As the barge was allowed to float freely the head pressure at the damage opening was dependent upon the draft of the barge.

The entire hull of the barge was surrounded by two moving domains: the moving water domain and the moving air domain. With the barge in the middle, the two domains exceeded the main dimensions of the barge by 0.25m in each direction.

This arrangement of the moving domains and the barge itself was surrounded by two static domains: the water domain and the air domain which represented the water tank and the space above the water tank, see Figure 41 and Figure 115. Details of the identification of the modelled domain can be found in chapter 7.2.2.

As done in case 1 presented in chapter 8.2.3 the numerical model of the box-shaped barge was meshed with the grid generator GAMBIT. A mixture of structured and unstructured mesh was applied to the model. All walls of the compartment were meshed with a structured quadrilateral mesh while all openings were meshed with triangles due to the small size of the openings and to ensure converging flow calculations. As a result the volume mesh of the compartment is a hybrid mesh. The walls of the hull were meshed with triangles but the volume of the hull was not meshed and left as a void space. The moving domains surrounding the hull and the compartment were meshed with triangles and the volume mesh was a hybrid mesh because of the structured mesh used for the compartment walls. Larger triangles were used for the walls of the water and air domain and the volume meshed turned out to be meshed with tetrahedrons. The number of cells used for the box-shaped barge is listed in Table 10 and an image of the meshed model can be seen in Figure 115 and Figure 116.

Volume	**Number of cells**
Compartment	723.514
Moving water	570.922
Moving air	569.676
Water	281.586
Air	175.287

Table 10: Number of cells for each main volume

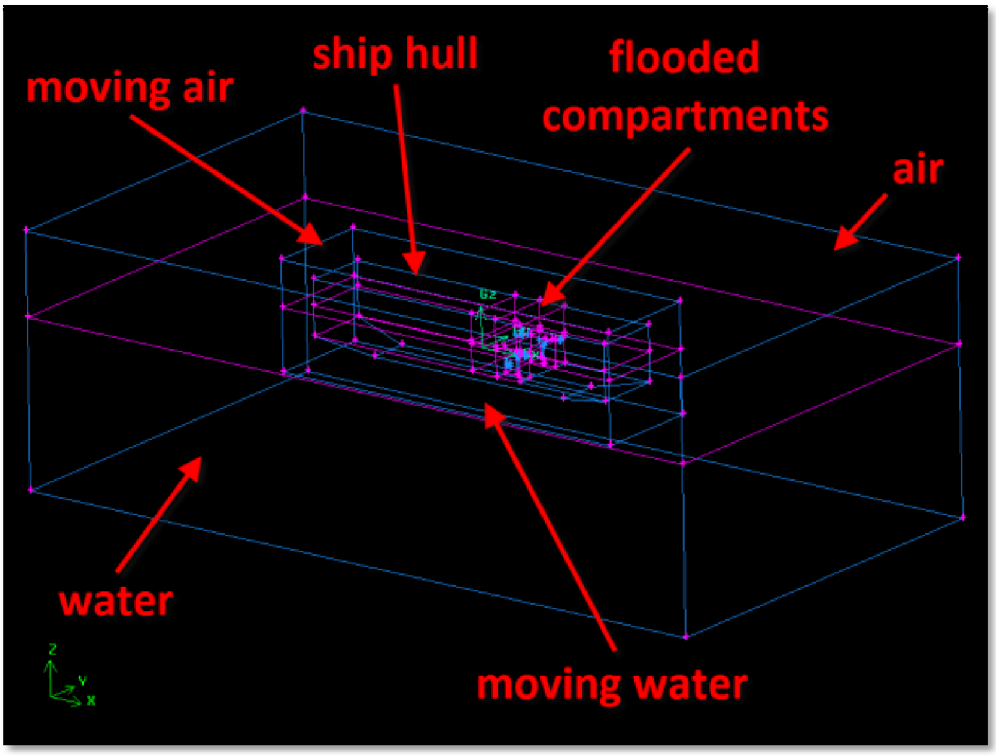

Figure 115: Model of the volumes

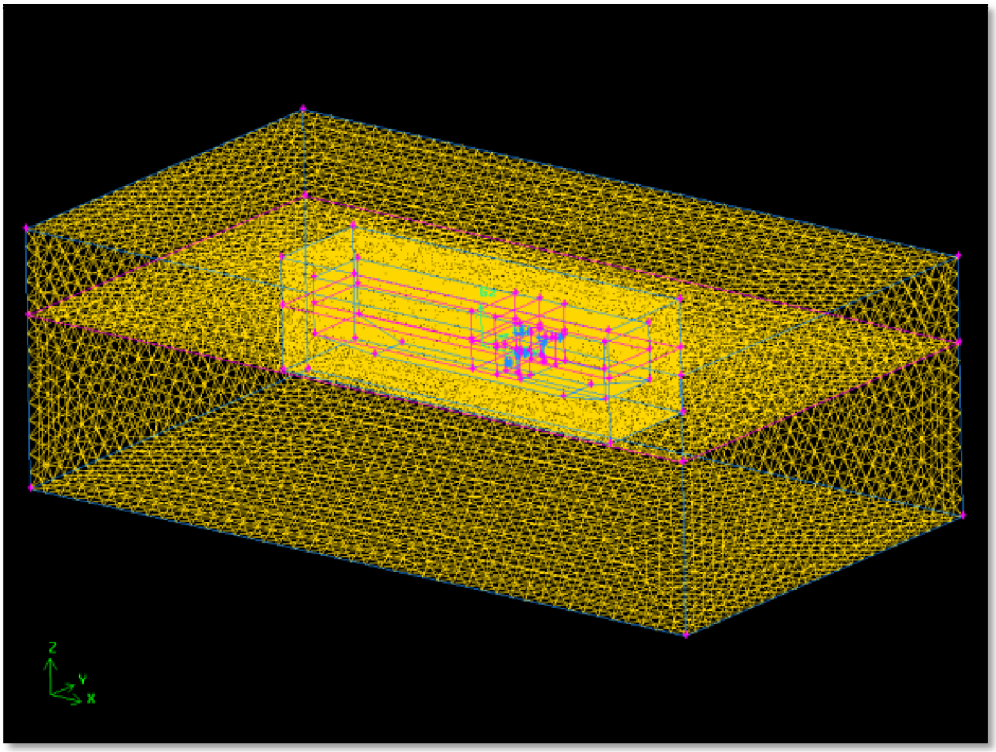

Figure 116: The meshed volumes

8.3.4 Simulation Parameters

Here, too, the set-up of the simulation parameters is similar to case study 1 in chapter 8.2.4.

Again, the calculations were carried out on an eight node dual core cluster and full computing power has been used.

The geometry of the box-shaped barge has been imported to FLUENT, checked for errors and highly skewed elements followed by an optimisation of the domain order by applying the Reverse Cuthill-McKee method.

Two phases were defined, compressible air with a density following the ideal gas law and a viscosity of $\nu = 1.7894\ 10^{-5}$ kg m^{-1} s^{-1} and water with a density of $\rho = 1.025$ kg/m^3 and a viscosity of $\nu = 1.003\ 10^{-3}$ kg m^{-1} s^{-1}. The VOF algorithm treating the interface between these two phases was applied. In the beginning of the simulation a highly turbulent flow was expected at the damage opening therefore the standard k-ε turbulence model with standard wall functions as near wall treatment was employed. The surrounding air pressure was set equal to atmospheric pressure of 101.325 kPa. The operating density was adjusted to $\rho_0 = 1.225$ kg/m^3 in order to override density which is averaged on all cells.

Pressure inlet boundary conditions were set at the bottom of the water tank providing a constant head pressure of 19.620 kPa to keep the water level in the tank at a constant height. It has to be noted that a constant head pressure on the bottom of the water tank does not indicate a constant head pressure on the damage opening as the barge is allowed to float freely in the domain. The pressure distribution on the damage opening behaves as described by the Bernoulli equation (8.2.2) in chapter 8.2.6.2. Moreover, the inflow pressure of the damage opening adjusts to the draft position of the CFD model of the barge and is therefore dependent on the hydrostatic pressure in the water tank at the immersion depth of damage opening and the hydrostatic counter pressure of floodwater developing inside the compartment, see chapter 8.2.6.2 for details. On top of the air domain

the boundary conditions were set to pressure outlet conditions to allow air to escape or enter the domain. All other faces were set to wall boundary conditions apart from the internal openings and the damage opening, which were set to interior boundary conditions.

Finally the dynamic mesh algorithm was applied by defining rigid zones that were allowed to be moved and remeshed and rigid zones that were only allowed to be moved. The moving water and moving air mesh that surrounded the ship hull was allowed to be moved and remeshed while the ship hull and the flooded compartments were only allowed to move. For the correct calculation of the six DOF motion the mass and the moment of inertia in three axes had to be defined, see Table 11.

Mass of the box-shaped barge	1450	kg
Moment of inertia along the x-axis I_{xx}	176	kg m^2
Moment of inertia along the y-axis I_{yy}	2235.3	kg m^2
Moment of inertia along the z-axis I_{zz}	2209.4	kg m^2

Table 11: Mass and moment of inertia of the box-shaped barge

Equations are solved implicitly and pressure based. Solution equations for flow, volume fraction, turbulence and energy are solved as shown in Table 12:

Solution control	Mode
Discretization	
Pressure	PRESTO!
Density	Second Order Upwind
Momentum	Second Order Upwind
Turbulence Kinetic Energy	Second Order Upwind
Turbulence Dissipation Rate	Second Order Upwind
Energy	Second Order Upwind
Volume Fraction	Geo-Reconstruct
Pressure-Velocity Coupling	Coupled
Courant Number	1.000.000

Table 12: Solution control for flow and volume fraction equations

The initial condition was that the air domain and the moving air domain were completely filled with compressible air and the water tank and moving water domain were completely filled with water. A time step of 0.0025 seconds was chosen according to the requirements of the dimensionless Courant Number and the requirements of the applied remeshing algorithm. When ship motion is large and a relatively large time step is used the remeshing algorithm might not be able to remesh all cells so that holes could appear in the remeshed zones. The solution of the governing equations would then diverge and the calculation would certainly crash. To avoid this, the time step has to be sufficiently small.

During the calculation volume fraction and flow velocities were monitored. The results of the calculations will be presented in chapter 8.3.6.

8.3.5 Model Tests

The model tests were performed by HUT (Helsinki University of Technology) Ship Laboratory in January 2006 which was jointly funded by NAPA Ltd and HUT Ship Laboratory. It was aimed to obtain physical model data which can be used to

compare and to validate the results of a numerical code employed for the computational simulation by *Ruponen (2007)*.

Model

The model consists of three blocks; the forward and aft block constructed of wood and the mid-section made from acrylic plastic in order to make it see-through. A steel-structured backbone is installed on top of the model in order to prevent the model from flexing and to avoid high tension in the acrylic plastic compartment, see Figure 117. Moreover, the acrylic plastic compartment has no direct connection with the forward and the aft block. The model scale adopted is λ=10. The main dimensions of the model are listed in Table 13.

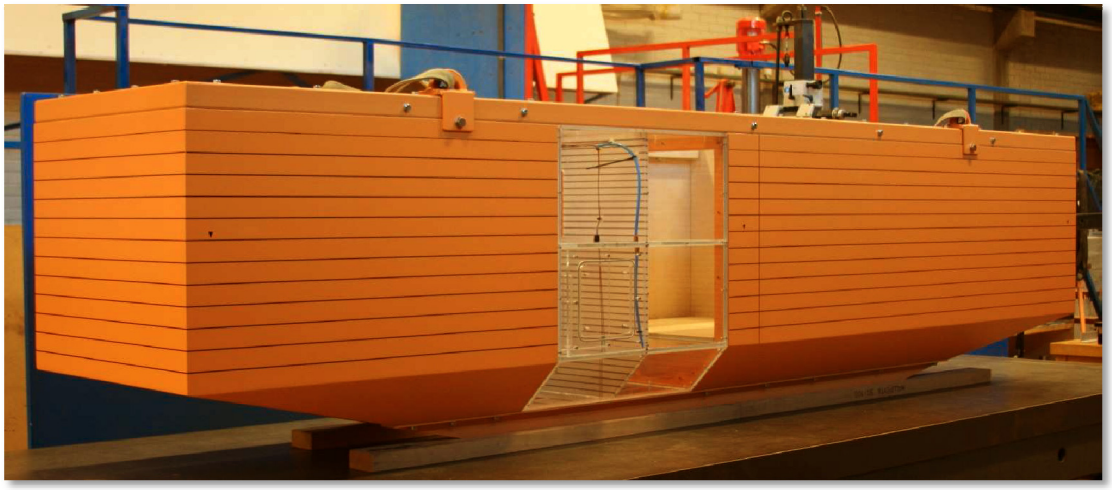

Figure 117: Box-shaped barge with backbone structure, *Ruponen (2006)*

Length over all (L_{OA})	4.000	m
Breadth	0.800	m
Height	0.800	m
Design draft	0.500	m
Block coefficient at design draft	0.906	
Volume of buoyancy	1.450	m^3

Table 13: Main dimensions of the physical model in model scale λ=10

The acrylic plastic compartments are divided by two decks and a transverse watertight bulkhead. The inner sub-dividing walls in CFD calculations usually have a thickness of zero but the walls in the physical model had to have a thickness of 10 mm to provide enough stiffness. Compartment R11, R21, R12 and R22 are fully vented while compartment R21P and R21S are ventilated with small pipes.

The top plate of the compartments is equipped with ventilation holes, discharging and ventilation pipes and holes for sensor cables and therefore made removable.

On the bottom of the double bottom the physical model is equipped with drains to quickly drain the model. The lower compartments have suction pipes installed in order to drain the model in that area. To avoid unwanted ventilation the lower end of the suction pipes are close to the bottom of deck 1.

Test arrangement

In the beginning the model is set into the water tank with empty compartments, see Figure 118. The initial intact conditions for a draft of 0.5m are given in Table 14.

Draft, T	0.500 m
Heel, ϕ	0.0°
Trim, θ	0.0°
Vertical centre of buoyancy, KB_0	0.270 m
Initial metacentric radius, B_0M_0	0.118 m
Initial metacentric height, GM_0	0.110 m
Vertical centre of gravity, KG	0.278 m

Table 14: Initial conditions

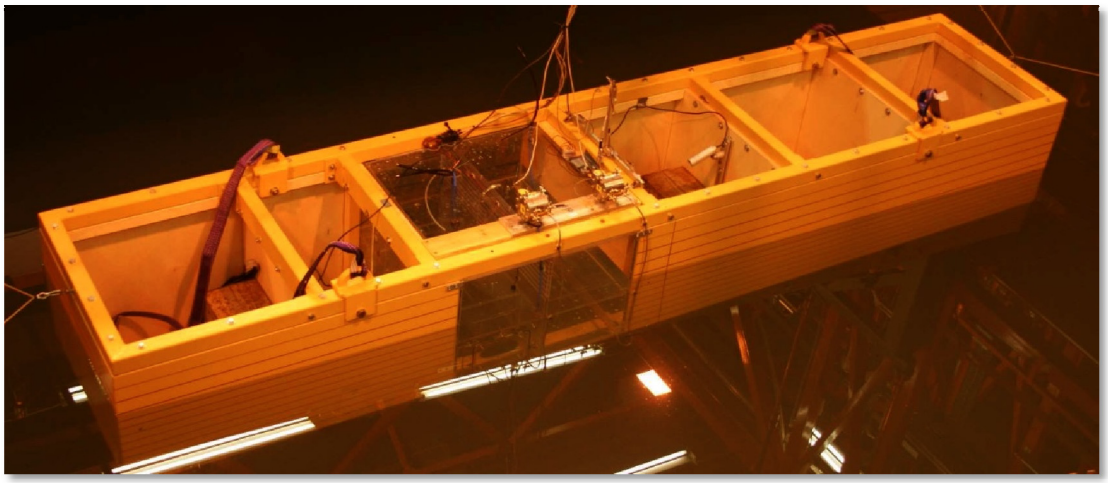

Figure 118: Model in equilibrium floating position, *Ruponen (2006)*

The damage opening is closed with a tight plug which is tied to a string. When the surrounding water is calm the damage opening is opened by pulling the plug with the string so that water is allowed to flow into the compartments. Immediately, as water flows into the compartment the ship will start to heel towards the side of the damage. The hull will also trim and sink which is recorded by the measurement equipment. When no more water can flow into the ship and the ship does not move anymore it has reached the final equilibrium position as shown in Figure 118 and the test run is finished.

Measurement instrumentation

The water height is measured in all of the 8 compartments inside the model using electrical resistance wire sensors. For the reasons stated in chapter 8.2.6.2 about electrical resistance wire sensors the same precision of measurements applies. The sensors are placed near the corner of each room that will be the lowest corner as the model heels and trims due to flooding. All sensors were calibrated and adjusted in a way that they were linear throughout the measurement range from dry to fully submerged.

Ship motions are measured with a camera based solution for measuring six degrees-of-freedom motions of objects in space. The camera system captures the position of

three LEDs that are installed on a frame on top of the model. By knowing the position of the LEDs, the translational and rotational motions of the centre of gravity in intact condition can be determined. It is clearly stated intact condition because when the ship is damaged and floodwater enters the ship the centre of gravity usually changes but the LED frame will stay on its position. The heeling angle, the trim angle and the vertical motion of COG are recorded. All the other motions are not relevant to flooding in calm water.

Additionally to all the measurements videos and still photos were taken to visualise the progress of the flooding through the complex geometry.

8.3.6 Data Comparison

8.3.6.1 Time History of the Flooding Process

In the beginning water enters compartment R21S from the starboard side through the damage opening DAS. The water ingress behaves in a jet-stream manner which is defined as a fast flowing and highly turbulent stream. As the damage opening DAS is in line with the fire doors FDS, water can flow straight from the sea to the mid-compartment R21. When the flood water reaches the damaged pipe DP in compartment R21, compartment R11 starts slowly to fill up; progressive flooding takes place. For that reason water flow into R21 slows down which causes the water levels in the side compartments to catch up. After approximately 19 seconds the water level in compartment R21 rises above both fire doors. This causes compression of air in the side compartments R21P and R21S. However, the compressed air can slowly escape through small ventilation openings leading to the void space in the forward part of the hull. About the same time instant the jet-stream through the damage opening trickles away and the internal turbulent wave pattern calms down. Roughly about 20 seconds later the water level reaches the staircase opening SC2 from where water can enter compartment R22. At time instant 191 seconds compartment R11 is completely full with floodwater. Then compartment R12 is allowed to be flooded. No further changes of the water level in

the compartments can be noticed after approximately 380 seconds which is equivalent to the TTF. The time history of the flooding process obtained by calculations is presented in Figure 119– Figure 132.

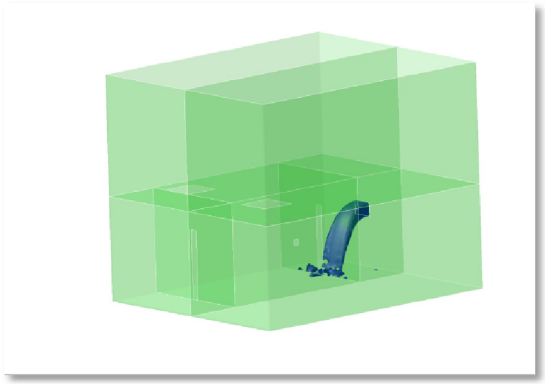

Figure 119: Progressing floodwater after 0.25 seconds

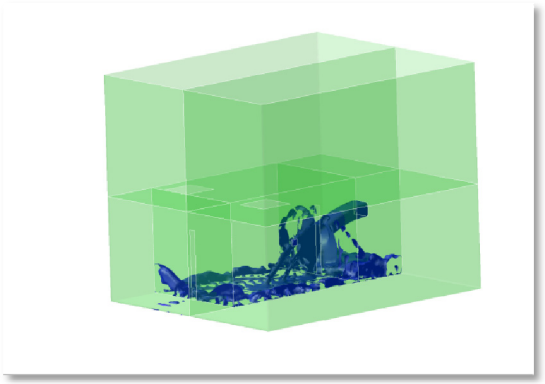

Figure 120: Progressing floodwater after 1 second

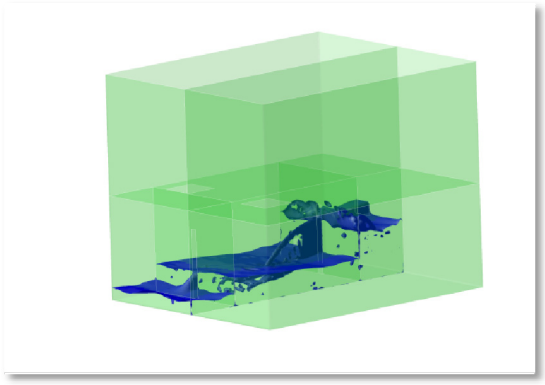

Figure 121: Progressing floodwater after 5 seconds

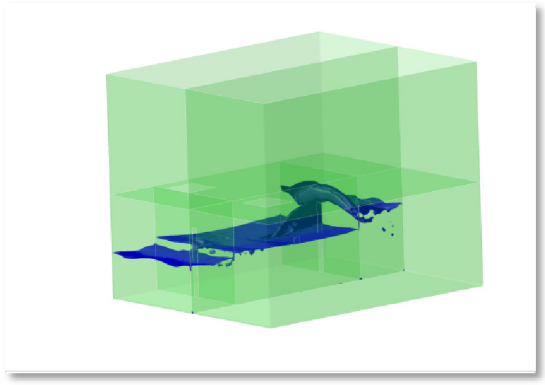

Figure 122: Progressing floodwater after 10 seconds

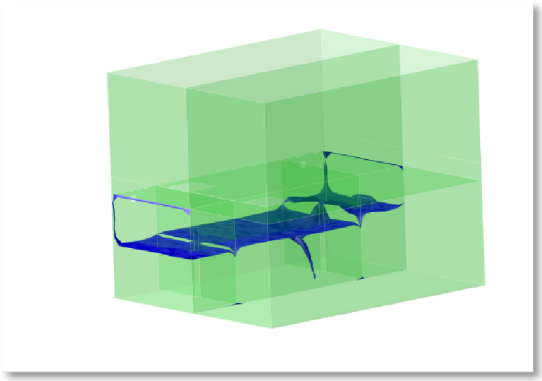

Figure 123: Progressing floodwater after 15 seconds

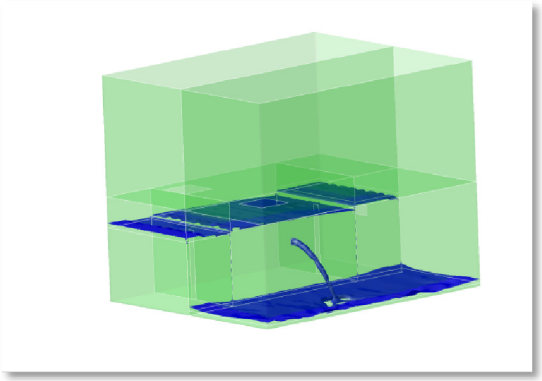

Figure 124: Progressing floodwater after 20 second

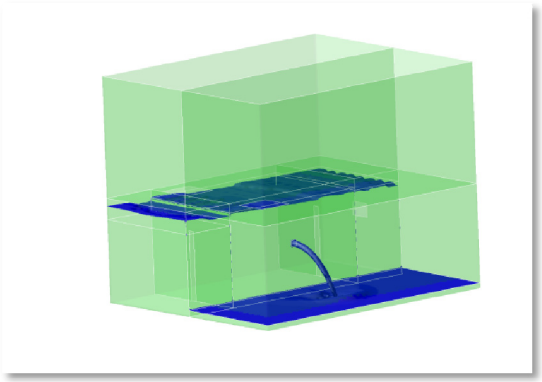

Figure 125: Progressing floodwater after 25 seconds

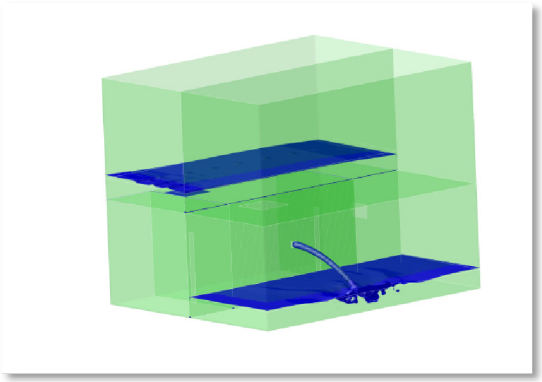

Figure 126: Progressing floodwater after 50 second

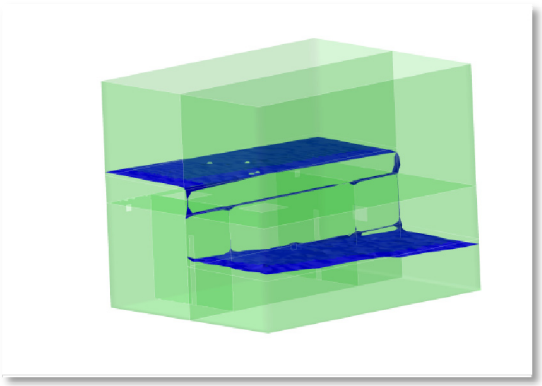

Figure 127: Progressing floodwater after 100 seconds

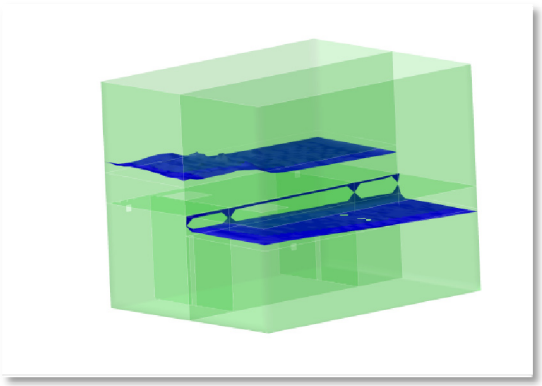

Figure 128: Progressing floodwater after 150 second

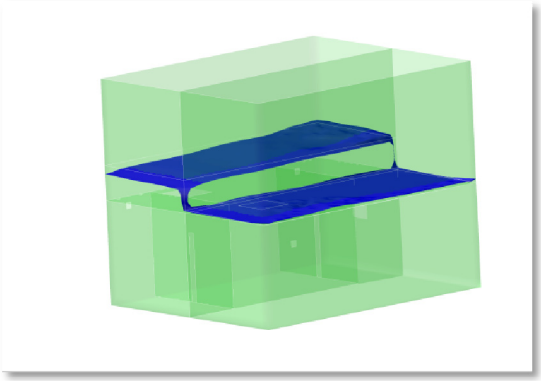

Figure 129: Progressing floodwater after 200 seconds

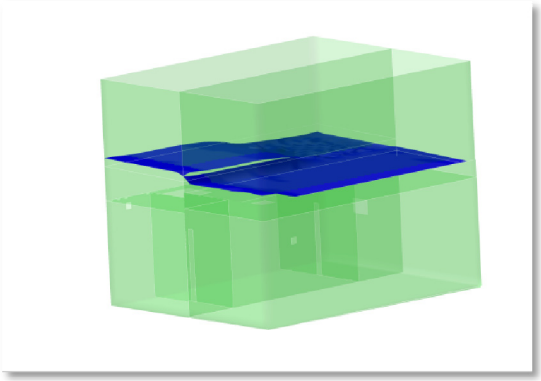

Figure 130: Progressing floodwater after 250 second

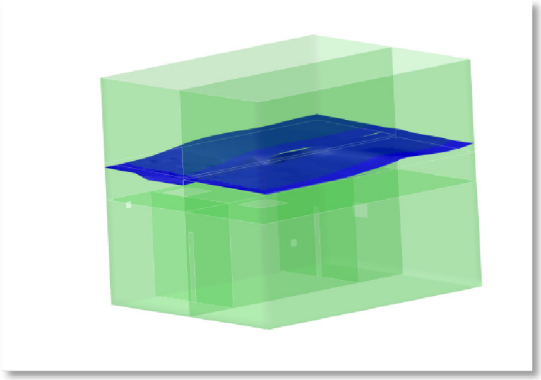

Figure 131: Progressing floodwater after 300 seconds

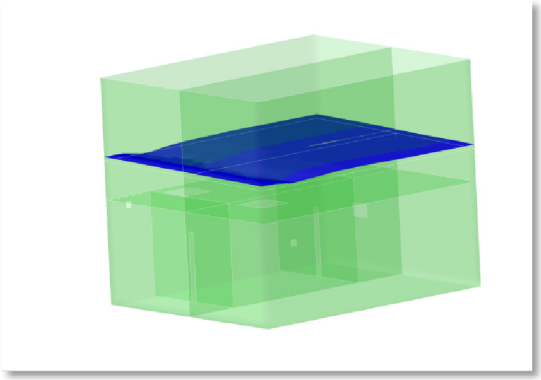

Figure 132: Progressing floodwater after 350 second

Some details of the floodwater ingress are shown in Figure 133 - Figure 144. Photos of the model tests are compared with images of the floodwater surface represented by isosurfaces. Also flow velocity vectors and the turbulence intensity of the floodwater are presented. In early stages of flooding the flow is very fast and the turbulence intensity very high. As the water level in the compartment raises the flow velocity and turbulence intensity decrease. Reason for that is that the static water pressure outside of the barge and the static water pressure in the compartments tend to equalise and therefore the pressure difference reduces.

Flooding scenario 0.7 seconds after floodwater penetration

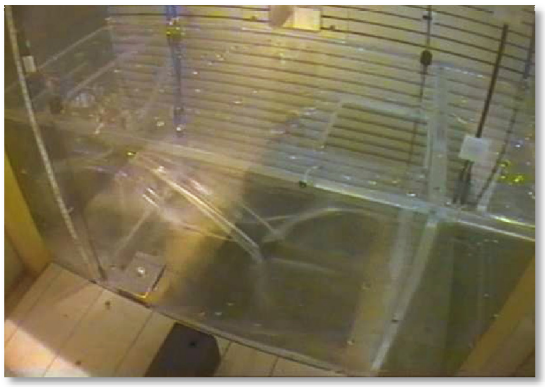

Figure 133: Model test after 0.7 seconds *Ruponen (2006)*

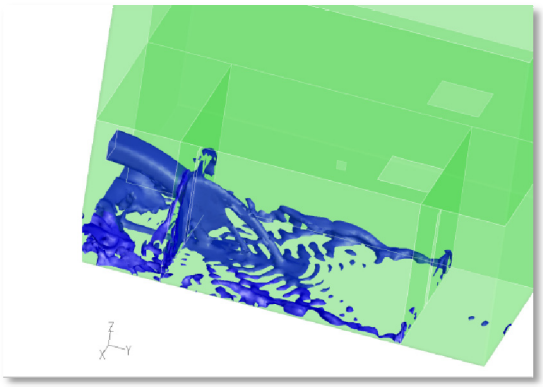

Figure 134: CFD isosurfaces after 0.7 seconds

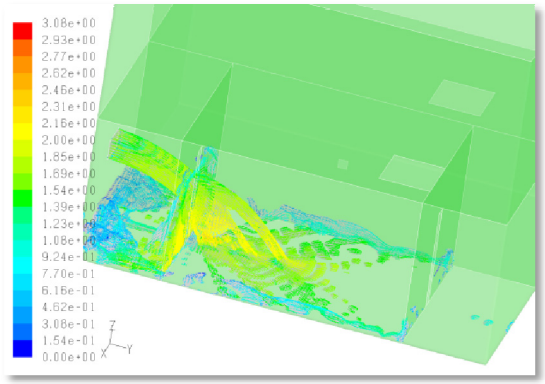

Figure 135: CFD velocity vectors after 0.7 seconds

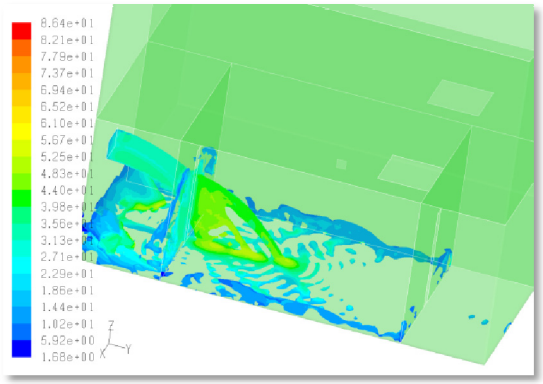

Figure 136: CFD turbulence intensity after 0.7 seconds

Flooding scenario 2.25 seconds after floodwater penetration

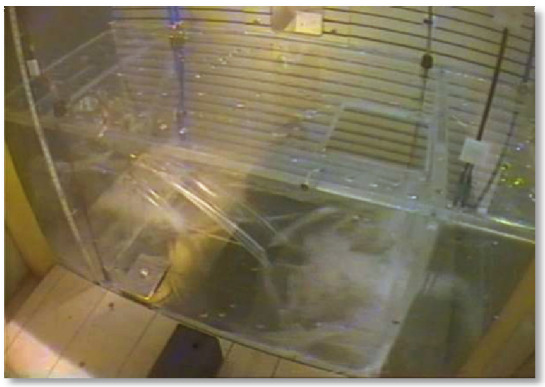

Figure 137: Model test after 2.25 seconds *Ruponen (2006)*

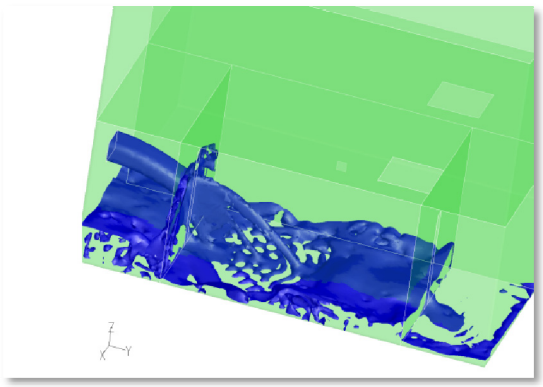

Figure 138: CFD isosurfaces after 2.25 seconds

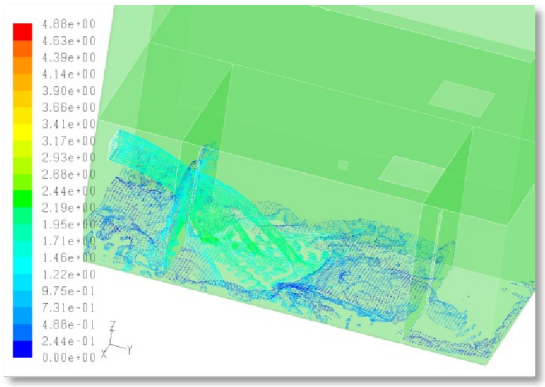

Figure 139: CFD velocity vectors after 2.25 seconds

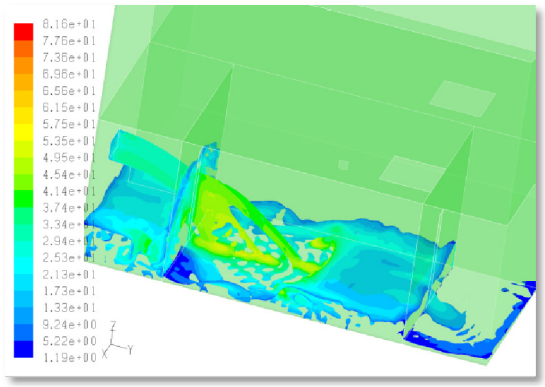

Figure 140: CFD turbulence intensity after 2.25 seconds

Flooding scenario 20 seconds after floodwater penetration

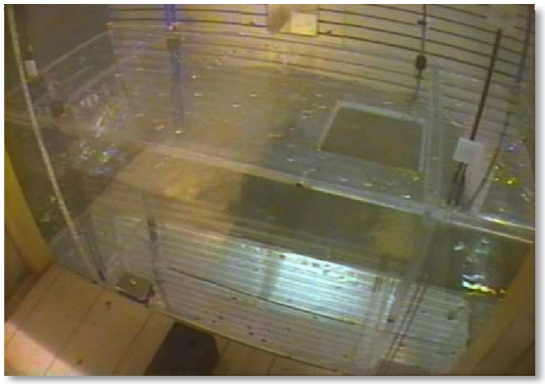

Figure 141: Model test after 20 seconds *Ruponen (2006)*

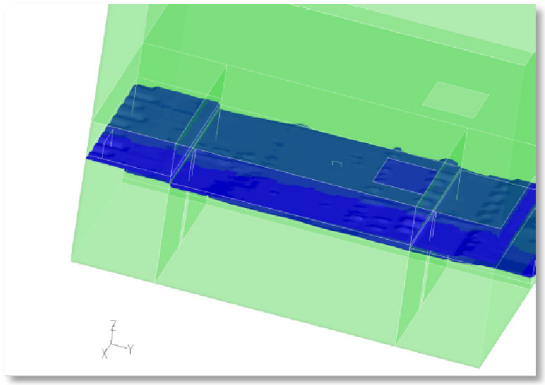

Figure 142: CFD isosurfaces after 20 seconds

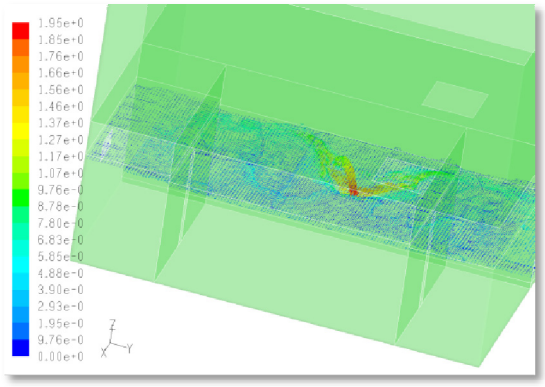

Figure 143: CFD velocity vectors after 20 seconds

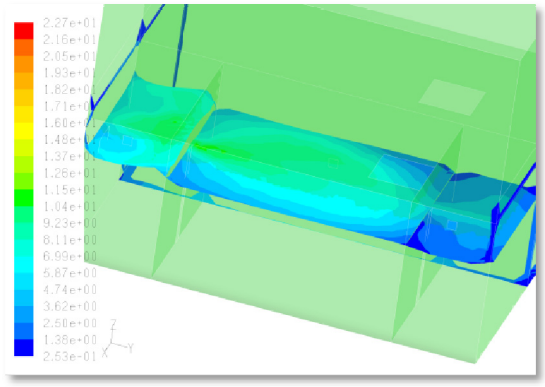

Figure 144: CFD turbulence intensity after 20 seconds

It was believed that the integration of a turbulence model only has a minimal influence upon the calculation results. A direct comparison of the laminar and turbulent conditions showed a different effect, see Figure 145 and Figure 146. The use of a proper turbulence model makes a significant impact on the results. It could be observed that in highly turbulent regions the laminar model overestimates the flow velocities, see Figure 147 and Figure 148. As a result more water flows into the damaged compartment which accordingly reduces the TTF. During progressive flooding when the flow is less or not turbulent this effect cannot be observed. It can be concluded that the use of a turbulence model in the transient phase of the flooding is very important.

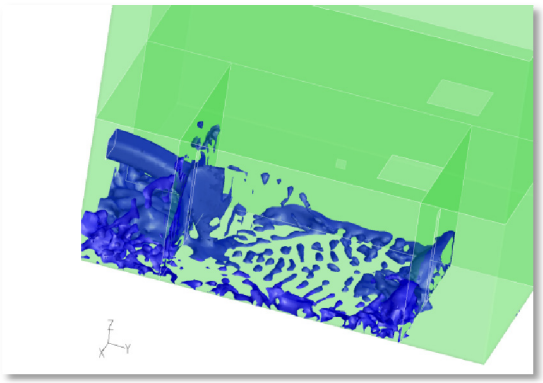

Figure 145: Laminar model

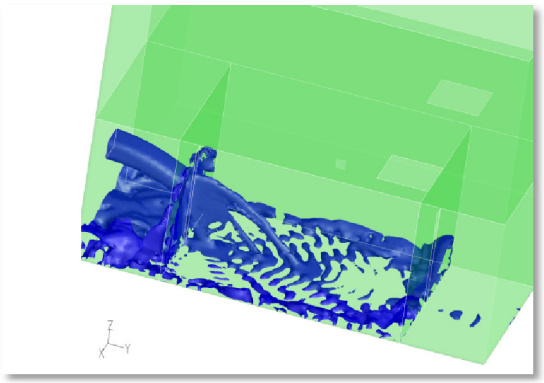

Figure 146: *k-ε* turbulence model

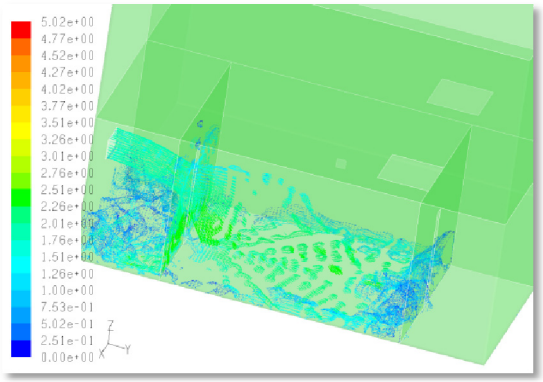

Figure 147: Velocity vectors laminar model

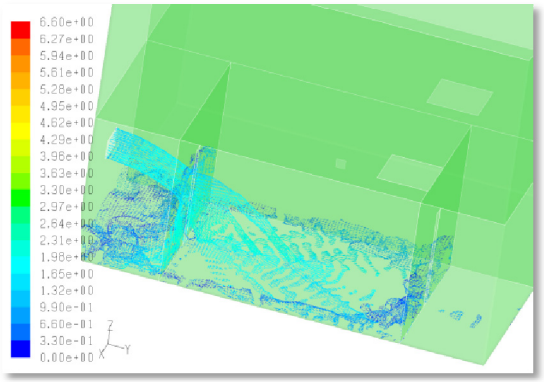

Figure 148: Velocity vectors *k-ε* turbulence model

8.3.6.2 Water Level Height

The water level is measured in all rooms in the corner that will be the lowest as the model heels and trims; in other words the position of the sensors is the forward starboard side of each room.

HUT uses sensors similar to that ones used by MARIN (see chapter 8.2.6.2). The distance between the wires and the wall is 5 mm if not other stated in Figure 149.

In the CFD model the water height is measured with “numerical” sensors represented by faces with the dimension of the real sensors. These sensors are added to the geometry after the CFD calculations are finished so that the surface of the sensors does not disturb the flow of the fluid. Because the hull is moving in six DOF in space it is difficult to determine the exact position of the sensors for each time step. Therefore a second identical model of the barge is introduced that is fixed and level in horizontal fashion without any motion or inclination. This second geometry includes each sensor at its designated location. The volume fraction of the moving numerical model is then interpolated to the fixed model. Finally the wetted surface of the sensors can be determined by integration of the volume fraction of water over the surface of the sensor. The water height is then obtained by dividing the wetted surface with the breadth of the sensor.

The location of the sensors is the same both for the physical model and the numerical model. Other than for the physical model the identification for the probes in the numerical model is defined by a three/four digit code where S means sensor followed by the code for the room location (see chapter 8.3.3). The location and identification can be found in figure Figure 149.

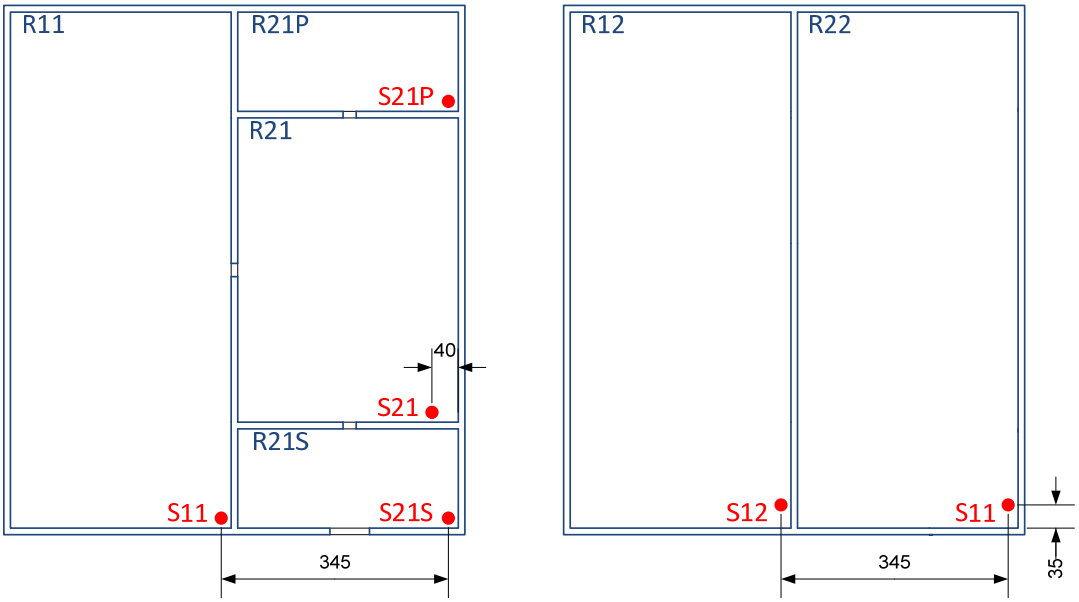

Figure 149: Location of the water height sensors from a top view

Data from HUT had to be scaled as the calibration factors of the sensors were smaller than the results of the calibration. HUT dealt with the same problem as MARIN did, namely that the conductivity of the medium changed rapidly from dry to wet which sustainably influenced the calibration of the sensors.

For a better comparison data from HUT was averaged and a regression analysis applying the Epanechnikov method, see Appendix B.2, had been undertaken in order to smooth the curves out. Results for all sensors can be compared in Figure 150 - Figure 155.

The graphs show that rooms that were directly affected by the floodwater ingress were filled up much faster than the other rooms which were progressively flooded. In Figure 150 it can be seen that the flooding slows down between a water height of 0.13 m and 0.14 m. When the water reaches the upper edge of the fire doors flooding slows down as well. This can be clearly identified by a bend in the charts at a water height of 0.2 m, see Figure 150 and Figure 152.

Room R21 is filled up constantly represented by an almost straight chart line even though at a certain point water is dispensed to room R11. Room R11 fills quickly by the time when the water in room R21 reaches SC2 and water can flow into room R22. Then the filling process in room R11 slows down until the room is completely full with floodwater.

Room R12 and R22 are slowly flooded as the height difference of the water level inside the compartment and outside of the hull is gradually decreasing. The flooding process stops when the water level inside the compartment is equal to the water level outside of the hull.

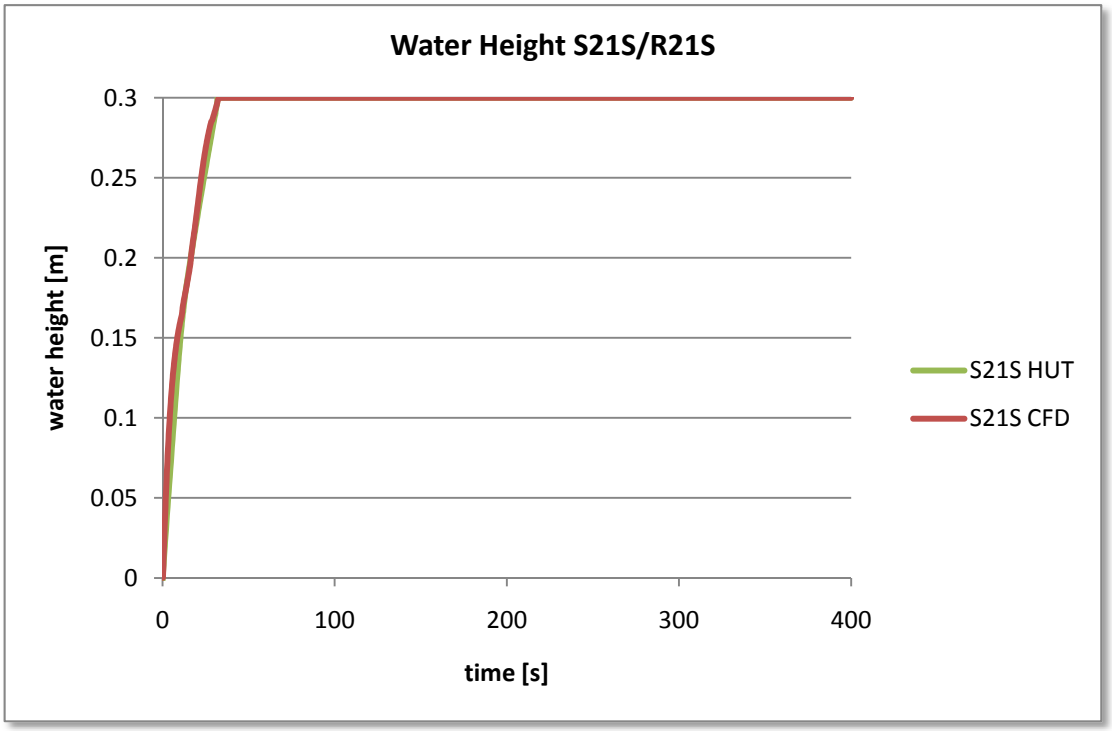

Figure 150: Water height in room R21S

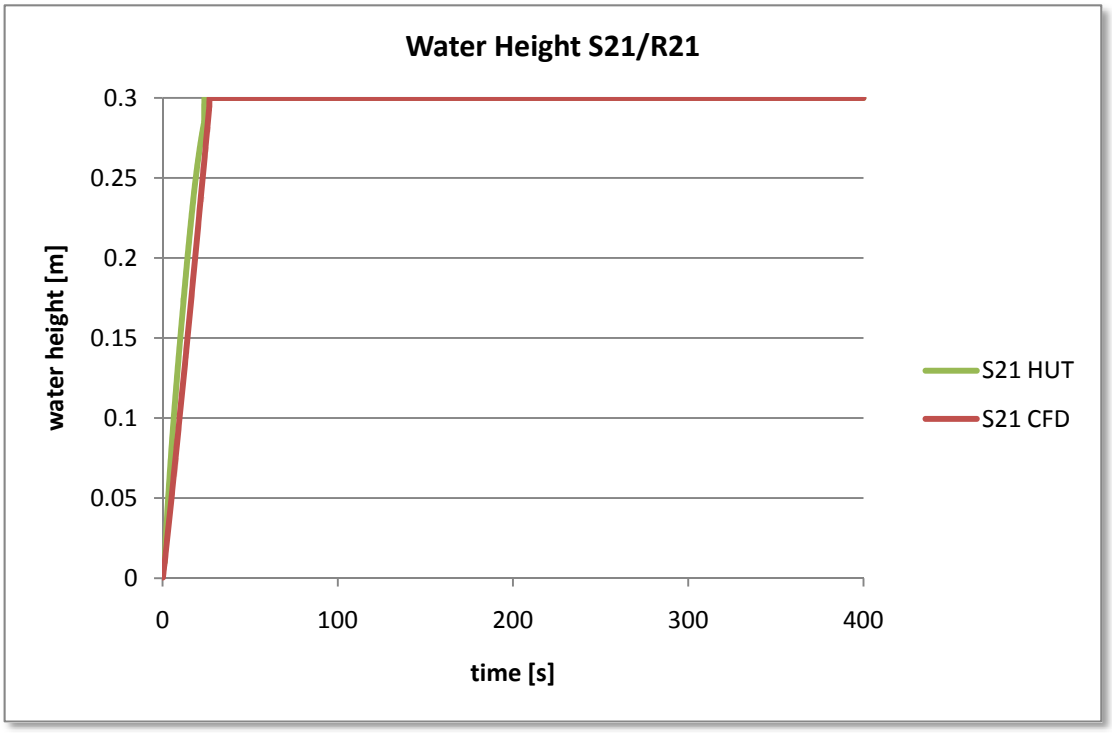

Figure 151: Water height in room R21

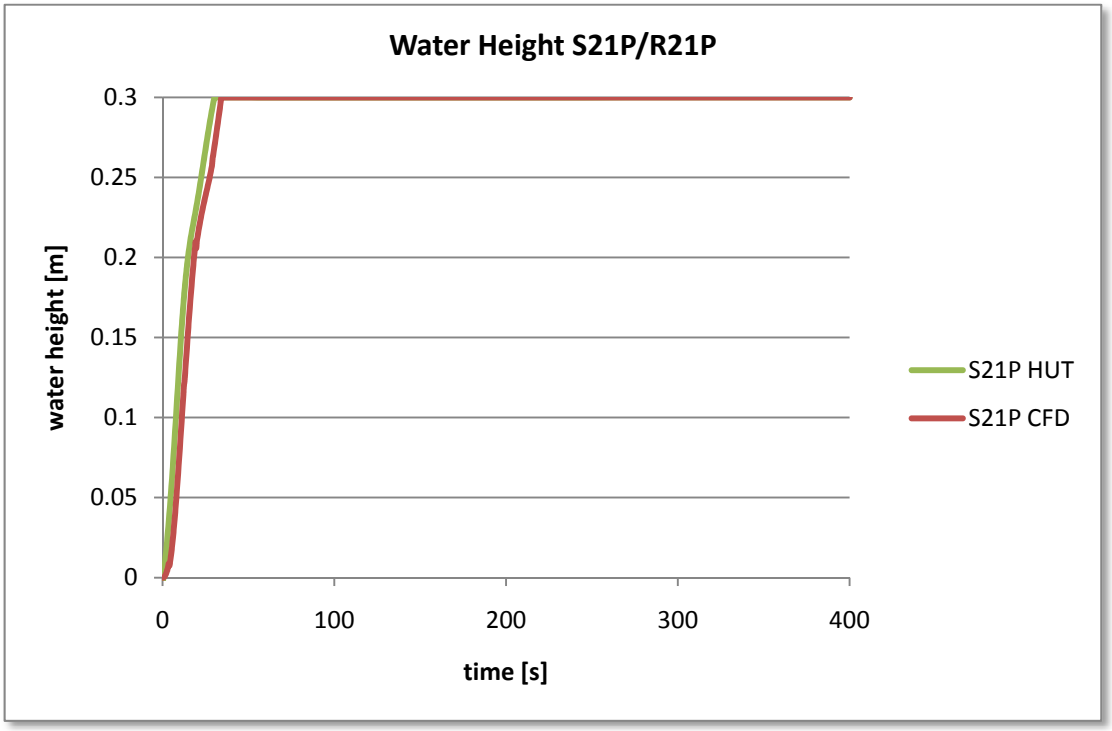

Figure 152: Water height in room R21P

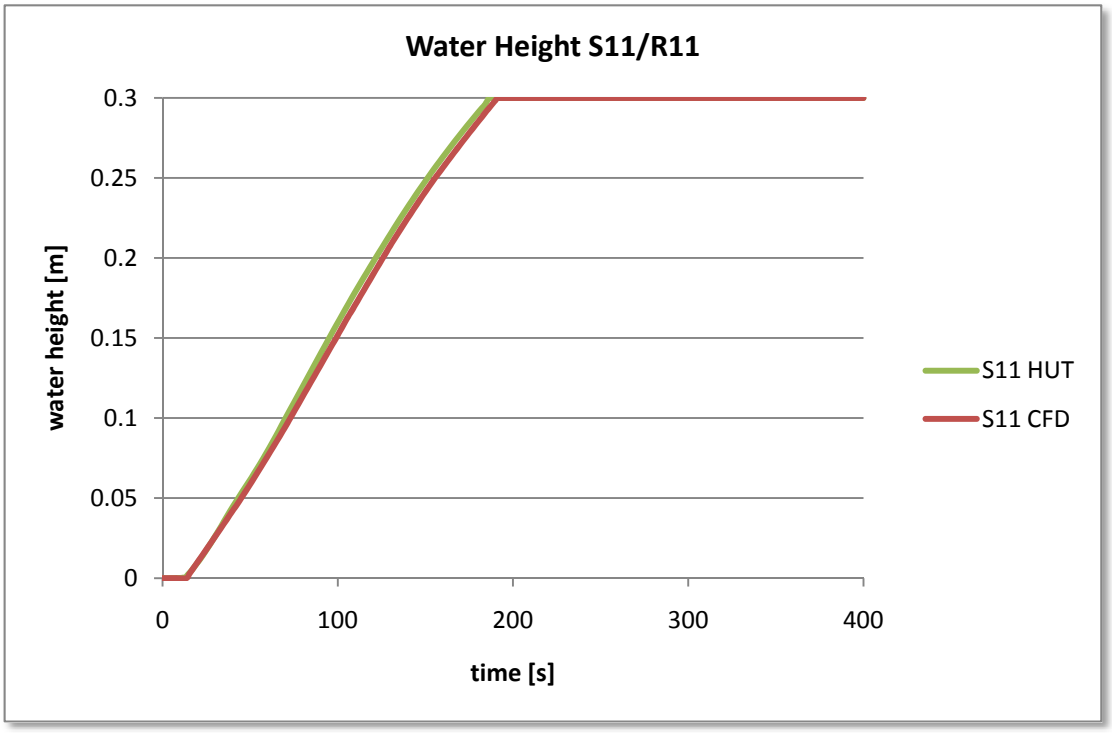

Figure 153: Water height in room R11

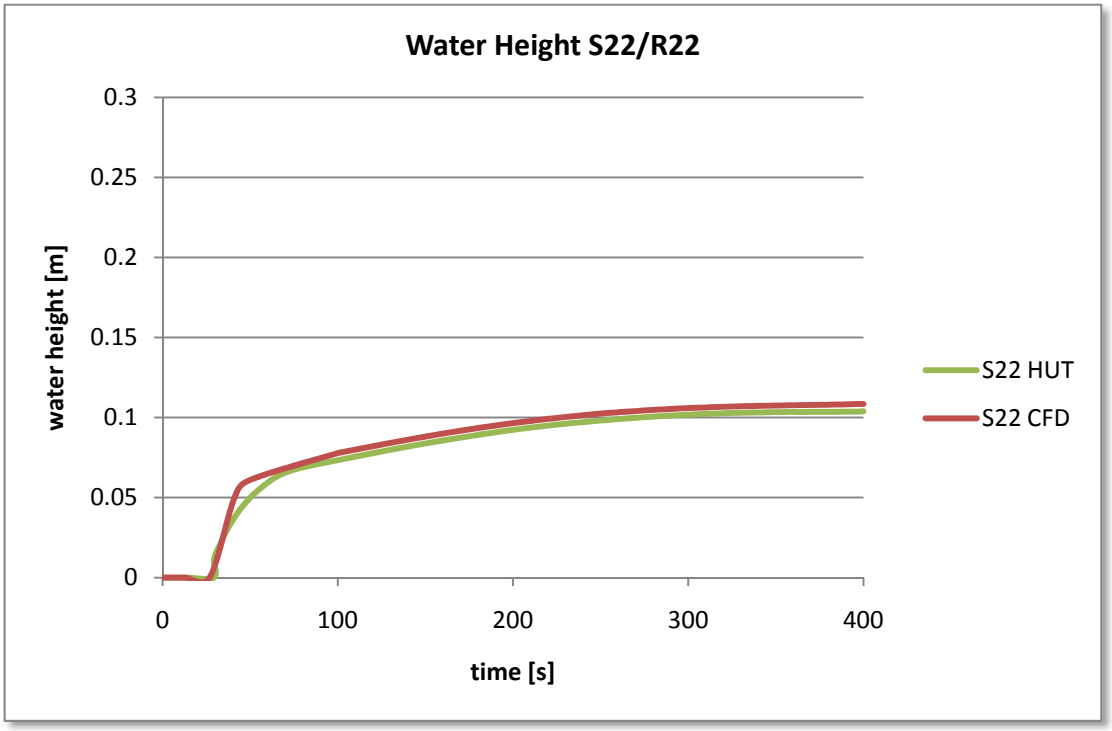

Figure 154: Water height in room R22

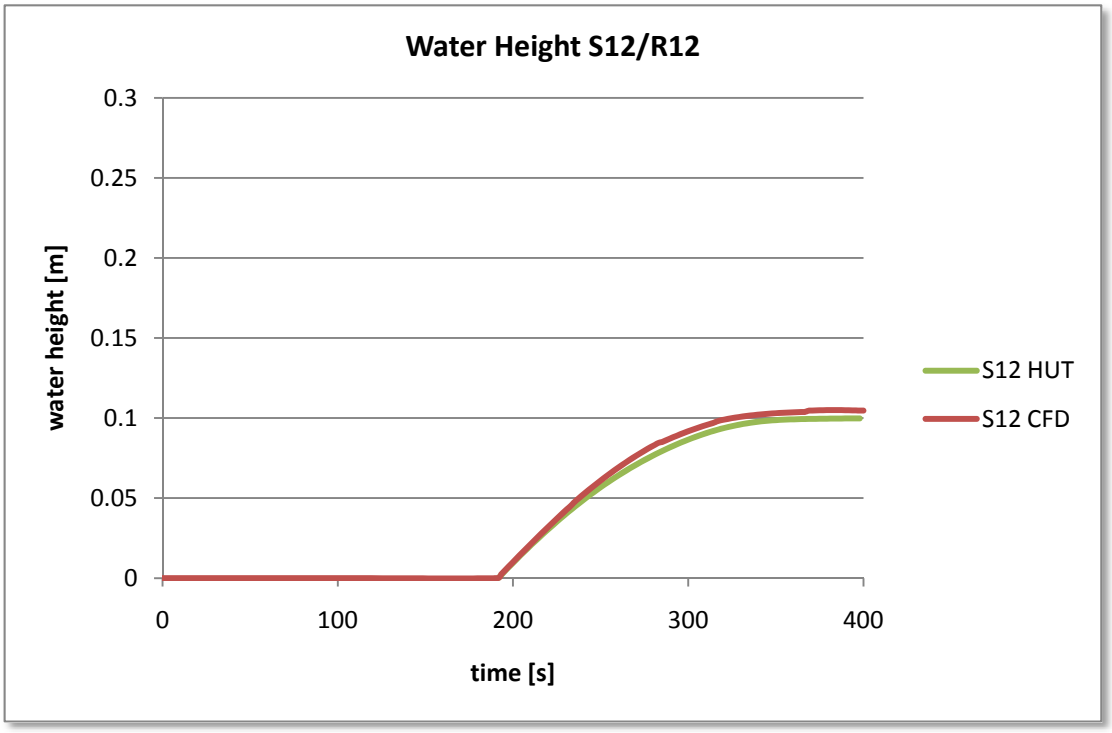

Figure 155: Water height in room R12

As already mentioned in section 8.3.6.1 the use of a turbulence model significantly influences the accuracy of the simulation results. Below the water heights are compared for a laminar and a turbulent CFD model in the transient phase of the flooding, see Figure 156. This chart is corresponding to Figure 145-Figure 148. In Figure 156 it is striking that the difference between data for water height in room R21P for laminar and turbulent flow at time instant 1 second is greater than the difference of the water height in room R21S. Reason for that is that the proportion of turbulent flow in room R21P is greater than its respective laminar proportion. Room R21S contrariwise has a larger proportion of laminar flow than turbulent flow and therefore the error is smaller. As the flooding is progressing the laminar proportion will dominate and the error will become smaller and smaller. Because the water height is only measured in a single point and the water height will differ due to its dynamic nature it is better to demonstrate this phenomenon by tracking the total water volume in each room. The total amount of floodwater volume is shown in Figure 157. In an analogous manner the laminar model predicts a greater water volume than the turbulent model.

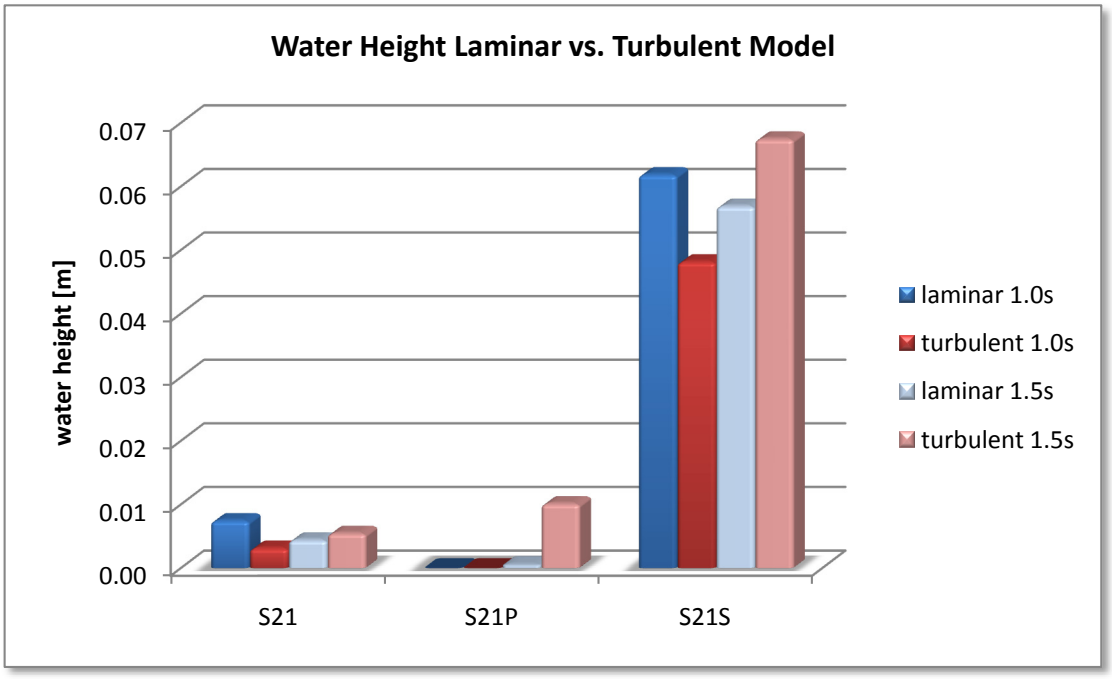

Figure 156: Water height in laminar and turbulent model

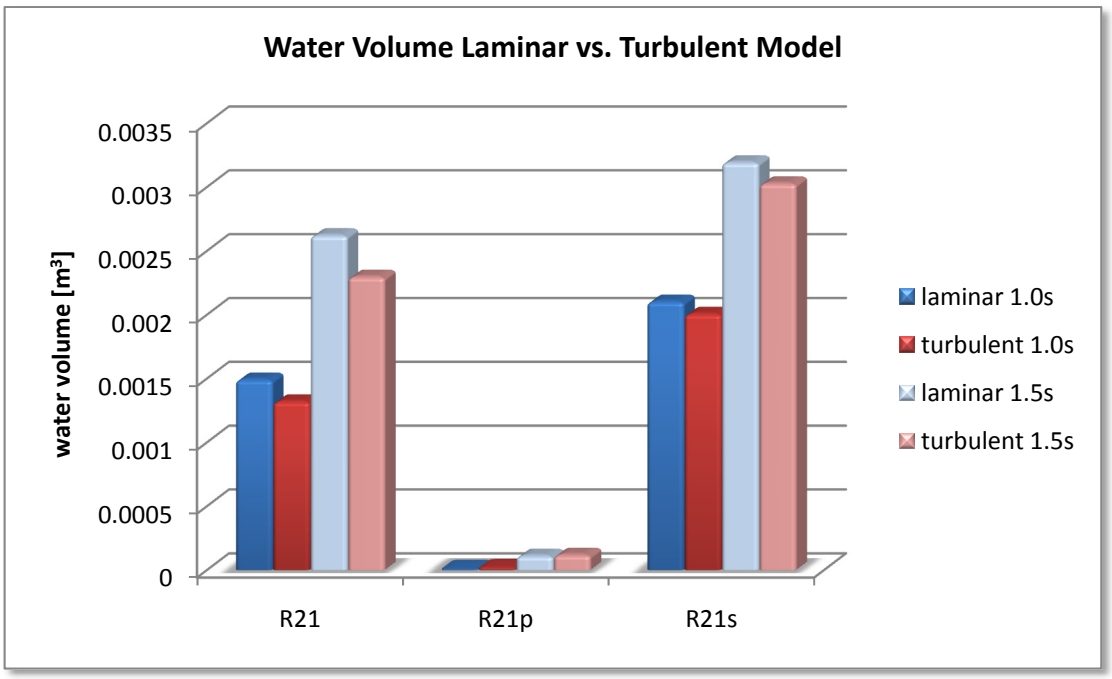

Figure 157: Water volume in laminar and turbulent model

8.3.6.3 Ship Motions in Calm Water (Quasi-static Calculations)

During the quasi-static calculation the ship motions in calm water are tracked whereupon special attention is turned to roll, pitch and heave motions. Unit for the heave motion is millimetres per second while pitch and roll motion are described by the covered angle per second.

In the beginning quasi-static ship motion in transversal direction, see Figure 158, is almost symmetrical because floodwater is allowed to spray directly from the sea through room R21S to room R21 and then further to room R21P. In addition, the internal fire doors FD1 and FD2 are larger in magnitude than the damage opening, so the floodwater tends to spread quicker on the lower deck than it can be replenished through the damage opening. For that reason the roll angle of the box-shaped barge remains small, even in the first 40 seconds during the transient flooding phase, and settles down at a stable level around approximately 0.05° in the progressive flooding phase. At the same time instant the trim angle increases significantly slower than in the beginning of the flooding which can be explored in Figure 159. In almost the same manner the sinkage of the barge behaves: the barge sinks quickly at the start of the flooding process, followed up by a slower vertical motion from time instant 40 seconds until the barge attains her final stable position, see Figure 160.

Applied method is in good agreement with model tests and demonstrates its applicability to quasi statically predict ship motions in calm water

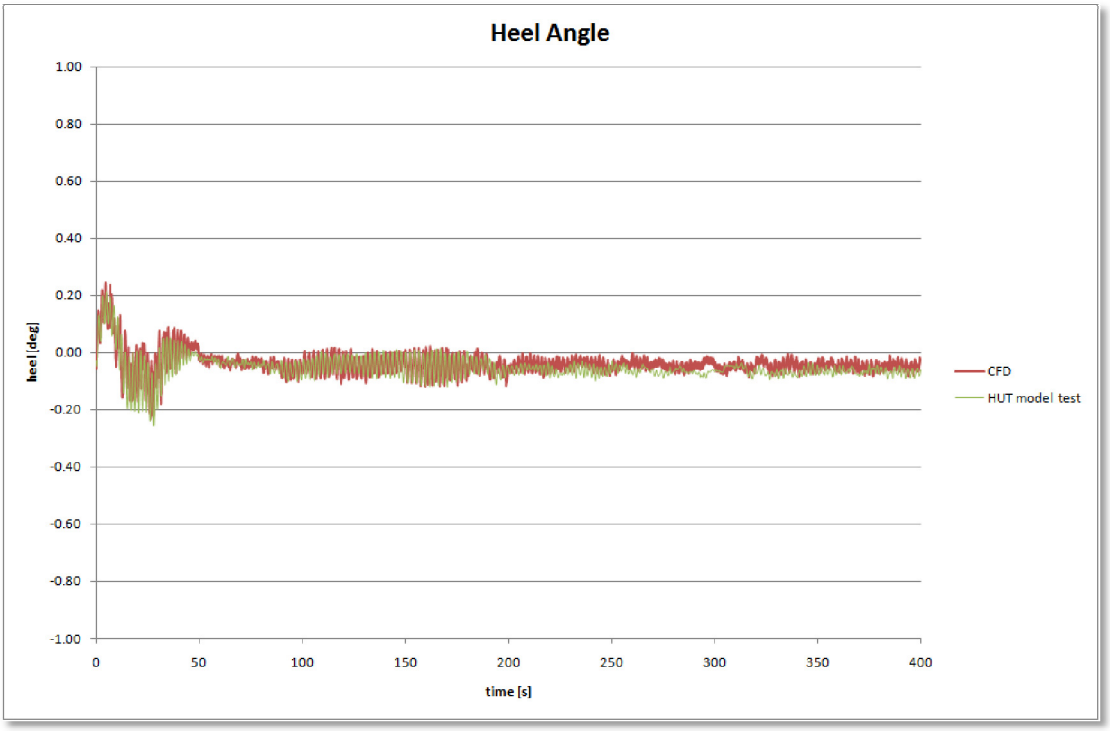

Figure 158: Heel angle of the box-shaped barge

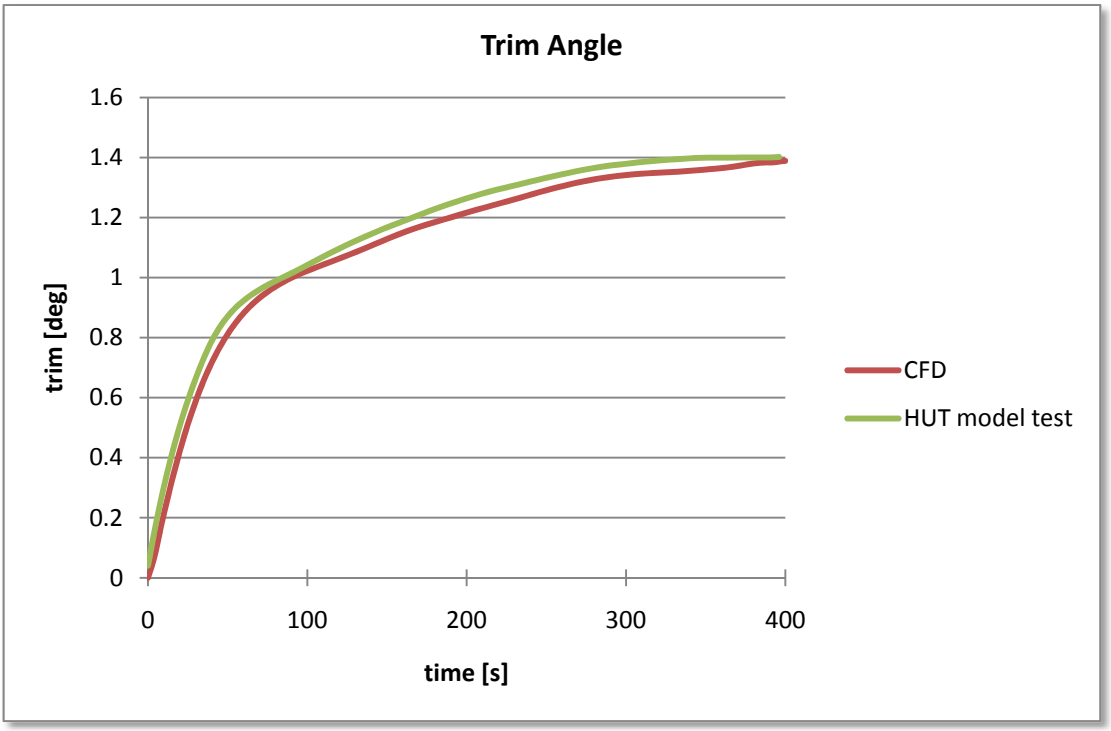

Figure 159: Trim angle of the box-shaped barge

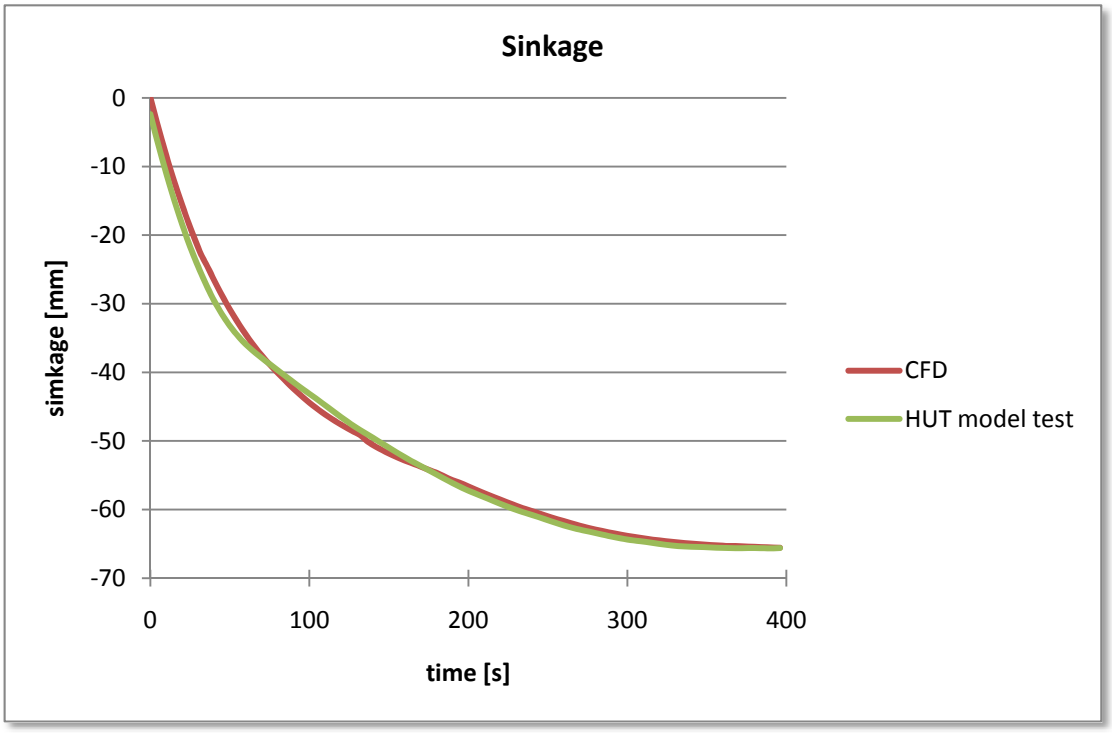

Figure 160: Sinkage of the box-shaped barge

8.4 Case 3: Damaged Compartment of an ITTC Ro-Ro Passenger Ship

8.4.1 Details of the ITTC Ro-Ro Passenger Ship

In this study a numerical simulation for the damaged part of a Ro-Ro passenger ship is conducted to investigate scale effects and to compare the influence of different damage opening shapes and positions on flooding in terms of a sensitivity analysis. Moreover, velocity and pressure is calculated on the damage opening which normally cannot be measured accurately by carrying out model tests. Additionally, the air pressure in occurring air pockets is calculated.

The main characteristics of the compartment are listed in following table (Table 15):

Model scale	48.57	
Damage side	Starboard	m
Length	26.714	m
Breadth	25.000	m
Height	9.025	m
Draft	6.400	m
Engine Blocks	13.18 x 5.73 x 3.2	m

Table 15: Main Characteristics of Damaged Compartment of ITTC Ro-Ro Passenger Ship

The geometry of the model is shown in Figure 9 and Figure 161.

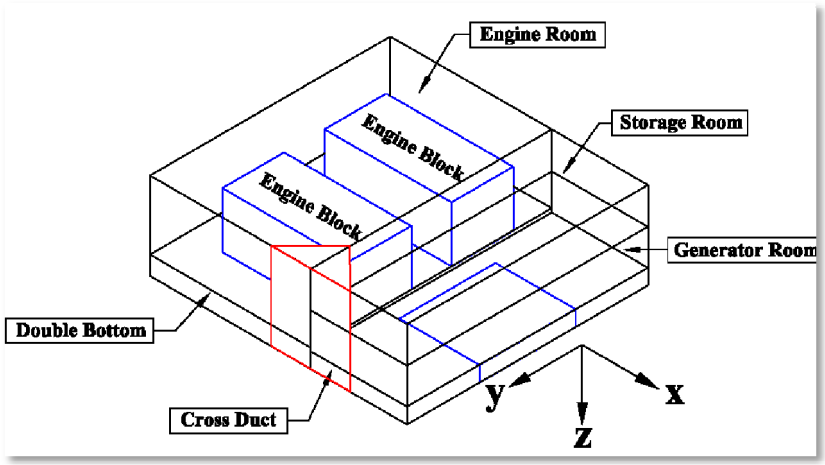

Figure 161: Geometry of Damaged Compartment of ITTC Ro-Ro Passenger Ship, *Cho et al. (2005)*

8.4.2 Design Requirements

The design was already used for a numerical study carried out by *Cho et al. (2005)*. It deals with a simple model with a large damage opening where the inside of the compartment is empty. A second model which is called real model has internal compartments and engine blocks and various geometrical shapes and positions of the damage opening. The design requirements for the numerical models were:

- Modelling of the damaged compartment of ITTC Ro-Ro Passenger Ship with and without an arrangement of floodable compartments.
- The model is flooded through various damage opening shapes and positions.
- A draft of 6.4 m in full scale is adopted.
- The compartments are only partly ventilated so that air pockets can develop.

8.4.3 Modelling of the Damaged Compartment of ITTC Ro-Ro Passenger Ship

The compartment was modelled according to the design requirements in the previous section 8.4.2. For the simple model, the geometry of damage opening 1 has been used, Figure 162. The geometry of damage openings 1-4 (Figure 162 - Figure 165) has been used when numerical simulations with the real model were performed. Walls are represented by blue lines while the damage openings are plotted in red.

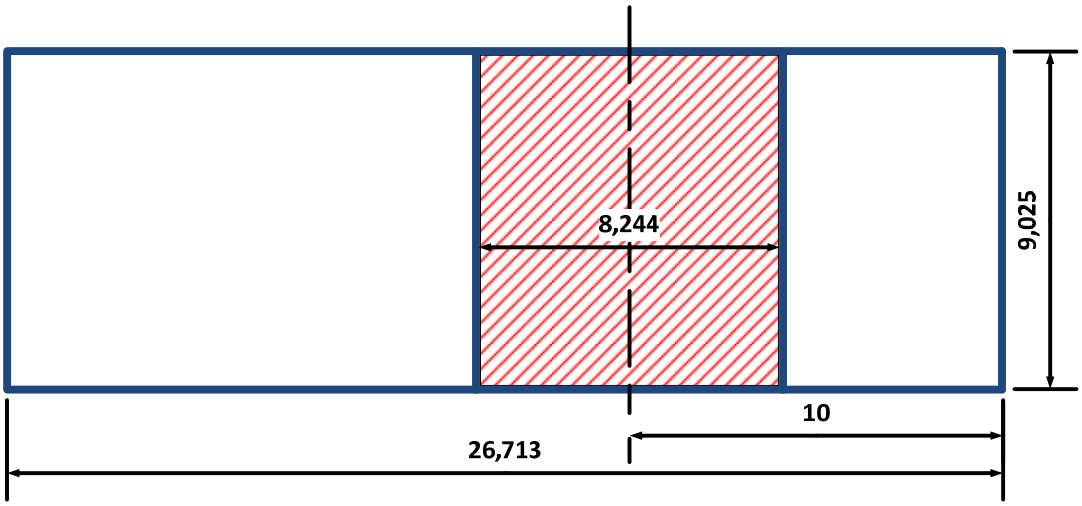

Figure 162: Geometry of damage opening 1

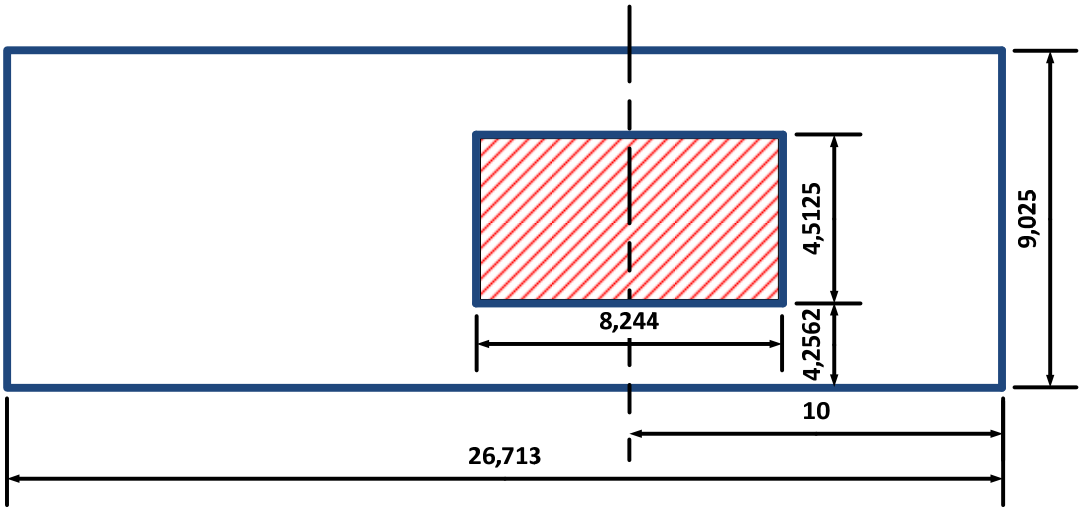

Figure 163: Geometry of damage opening 2

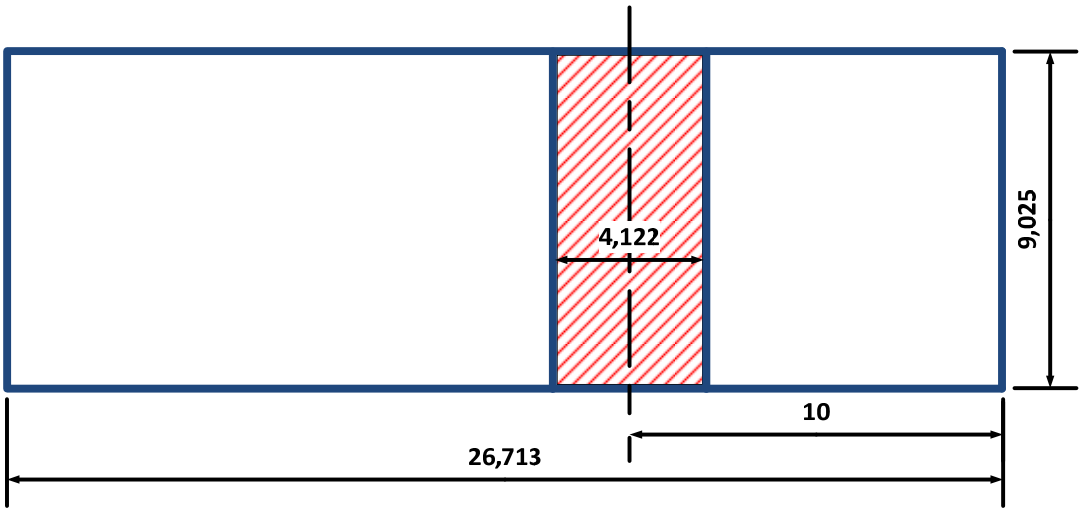

Figure 164: Geometry of damage opening 3

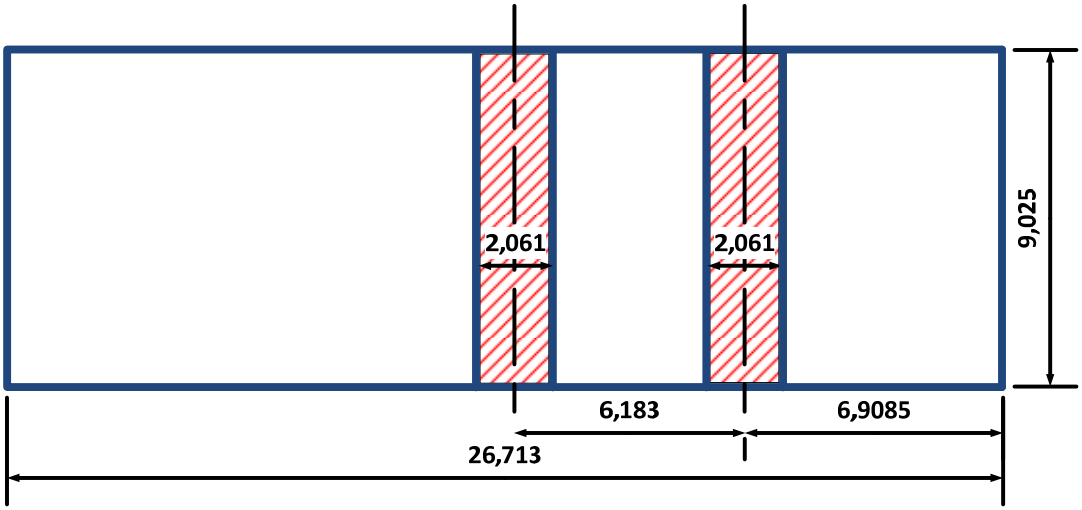

Figure 165: Geometry of damage opening 4

The layout of the real compartment consists of five separate rooms that are not connected to each other but are allowed to be flooded from the damage opening. The lower part of the compartment consists of two rooms representing the double bottom and the cross duct. On the lower deck in the forward part of the compartment the generator room is located and on the upper deck a storage room is to be found. In the aft part of the compartment the engine room spans the lower and the upper deck. Two rectangular blocks are representing the engines in the engine room.

The compartment was flooded from the damage opening on the starboard side. Similar to the Estonia case in chapter 8.2.3 the damage opening was connected to a water reservoir which was permanently refilled with water. Faces on the bottom of the water reservoirs were defined as pressure inlet in order to apply the requested constant head pressure. They were located 2.0 m below the lower edge of the damage opening so that the pressure inlet boundary condition had a sufficient distance to the damage opening which was defined as interior boundary condition. Again, as described in chapter 8.2.2 for case study 1, this simplification was necessary because for model tests it is difficult to provide a variable head pressure on the damage opening when the model is horizontally fixed. On top of the water reservoir above the water line a reservoir filled with air was situated. A pressure outlet boundary condition was defined on top of the air reservoir in order to allow air to exit and to enter the domain. The distance between upper edge of the damage opening and pressure outlet was 2.0 m. An ample distance between two different boundary conditions is necessary to ensure on one hand undisturbed floodwater flow through the damage opening and on the other hand to minimise the risk of diverging iterations. Figure 166 shows the arrangement of the boundary conditions, pressure inlet, pressure outlet and damage opening and the location of the water and air reservoir for the simple case with damage opening 1.

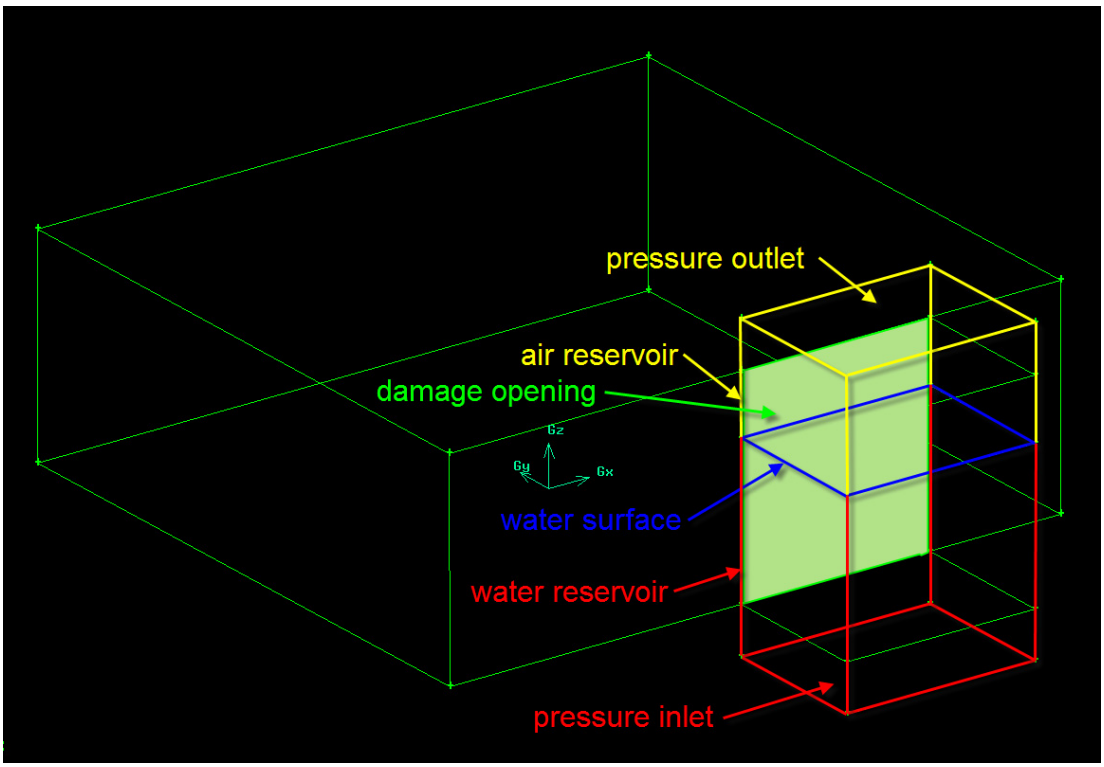

Figure 166: Water reservoir with boundary conditions

The model was kept in a fixed and horizontal position without any motions although in reality the ship would heel over.

Rooms were not directly ventilated but due to the fact that the water level outside the compartment was below the upper edge of the damage opening at any time, air was allowed to escape through the damage opening. Nevertheless, air pockets could develop in rooms that were located below the waterline. Throughout the whole simulation the operating air pressure remained equal to atmospheric pressure while the pressure of the trapped air in the rooms of the compartment was adjusted according to the ideal gas law.

The real model of the compartment of the ITTC Ro-Ro passenger ship was created in full scale with the grid generator GAMBIT. The simple model was created in full scale and in two different model scales namely λ=48.57 and λ=97.14 in order to

show scale effects due to physical or numerical phenomena. The wall thickness of the deck and the bulkheads was not taken into account.

The numerical model consisted of two main volumes; the compartment which was separated in sub-volumes representing all rooms and the water reservoir. The geometrical model of the simple model can be investigated in Figure 167 and the real model is shown in Figure 168. A structured hexahedral mesh with a constant grid spacing of 0.5m for the full scale model was chosen, respectively a constant grid spacing of 0.0103m and 0.00515m for the scaled models. The number of cells for each main volume is given in Table 16.

Volume	Number of cells	Computation time
Simple compartment full scale	47.700	≈ 6 h
Water reservoir full scale	5.408	
Simple compartment model scale 48.57	47.700	≈ 6 h
Water reservoir model scale 48.57	5.408	
Simple compartment model scale 97.14	47.700	≈ 6 h
Water reservoir model scale 97.14	5.408	
Real compartment with damage 1	47.632	≈ 18 h
Water reservoir connected to damage 1	5.824	
Real compartment with damage 2	47.632	≈ 22 h
Water reservoir connected to damage 2	5.824	
Real compartment with damage 3	47.632	≈ 25 h
Water reservoir connected to damage 3	5.824	
Real compartment with damage 4	47.632	≈ 20 h
Water reservoir connected to damage 4	5.824	

Table 16: Number of cells for each main volume and total computation time

Compared to the simulations that *Cho et al. (2005)* carried out, see Table 17, the performance of presented calculations was 800% - 2400% faster because less cells could be used due to the nonexistence of a large water/air domain surrounding the compartment.

Grid	3D/Structured grid		
Mesh	X	120~130	Total : 900,000 ~1,300,000
	Y	120~130	
	Z	60~90	
Computation time: 144~200 hour / P4 2.8 GHz			

Table 17: Computation time and number of cells, *Cho et al. (2005)*

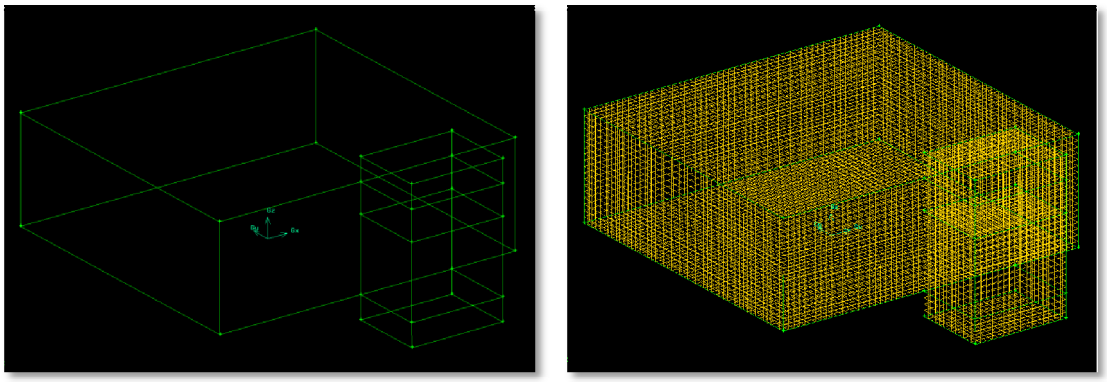

Figure 167: Model of volumes and the meshed model of the simple compartment

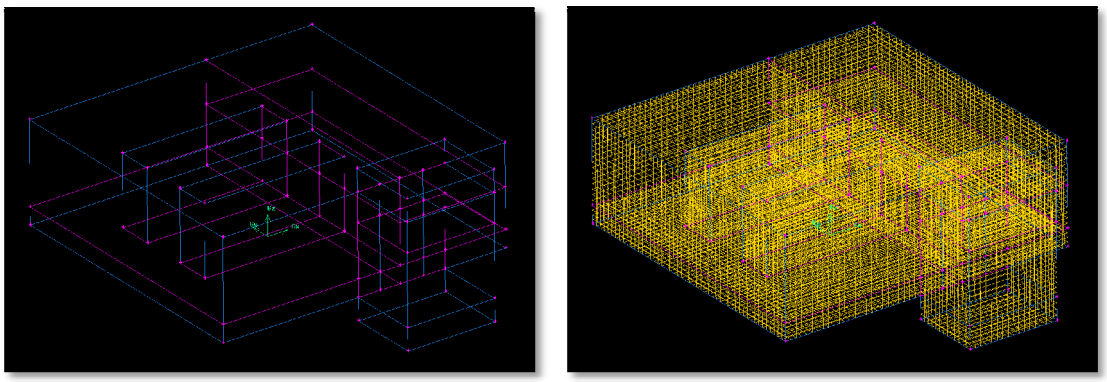

Figure 168: Model of volumes and the meshed model of the real compartment

8.4.4 Simulation Parameters

The simulation parameters are very similar to those used for case study 1 in chapter 8.2.4 and are discussed in a very detailed form in chapter7.3.

The CFD calculation was carried out with the commercial solver FLUENT on a standard P4 2.4GHz laptop.

The geometry of the compartment has been imported to FLUENT, checked for errors and highly skewed elements, followed by an optimisation of the domain order by applying the Reverse Cuthill-McKee method, *Cuthill and McKee (1969)*.

Two phases were defined, compressible air with a density following the ideal gas law and a viscosity of $\nu = 1.7894\ 10^{-5}$ kg m^{-1} s^{-1} and water with a density of $\rho = 1.025$ kg/m^3 and a viscosity of $\nu = 1.003\ 10^{-3}$ kg m^{-1} s^{-1}. The VOF algorithm treating the interface between these two phases was applied. In the beginning of the simulation a highly turbulent flow was expected at the damage opening therefore the standard k-ε turbulence model with standard wall functions as near wall treatment was employed. The surrounding air pressure was set equal to atmospheric pressure of 101.325 kPa. The operating density was adjusted to $\rho_0 = 1.225$ kg/m^3 in order to override density which is averaged on all cells.

Pressure inlet boundary conditions were set at the bottom of the water reservoir providing a constant head pressure to keep the water level in the reservoir at a constant height. According head pressure can be found in Table 18. On top of the air reservoir the boundary conditions were set to pressure outlet conditions to allow air to escape or enter the domain. All other faces were set to wall boundary conditions apart from the damage opening, which was set to interior boundary condition.

Model	**Head pressure [kPa]**
Simple compartment full scale	84.464
Simple compartment model scale 48.57	1.739
Simple compartment model scale 97.14	0.869
Real compartment full scale	84.464

Table 18: Head pressure at the pressure inlet

Equations are solved implicitly and pressure based. Solution equations for flow, volume fraction, turbulence and energy are solved as shown in Table 19:

Solution control	Mode
Discretization	
Pressure	PRESTO!
Density	Second Order Upwind
Momentum	Second Order Upwind
Turbulence Kinetic Energy	Second Order Upwind
Turbulence Dissipation Rate	Second Order Upwind
Energy	Second Order Upwind
Volume Fraction	Geo-Reconstruct
Pressure-Velocity Coupling	PISO

Table 19: Solution control for flow and volume fraction equations

The initial condition was that the air reservoir and the compartment were completely filled with compressible air and the water reservoir was completely filled with water. For the full scale model a time step of 0.01 seconds was chosen according to the requirements of the dimensionless Courant Number while for the models in scale 48.57 respectively 97.14 a time step of 0.001 seconds was selected.

During the calculation volume fraction of water and air in each room, flow velocity and pressure on the damage opening as well as air pressure in the air pockets were monitored. The results of the calculations will be presented in chapter 8.4.6.

8.4.5 Model Tests

The model tests were performed at the Maritime and Ocean Engineering Research Institute, KORDI, in Korea. It was aimed to obtain physical model data which can be used to compare and validate the results of a CFD code employed for computational simulation by *Cho et al. (2005)*.

Model

The model was made of transparent acryl plastic in order to observe the incoming floodwater. Two models were made to investigate the effect of ingressing floodwater on the inner compartments: a "simple model" with the inside empty and a "real model" having modelled internal compartments and engine blocks, see Figure 169. The effect of damaged inlets was also investigated by changing the geometry, size and position of the inlet. The model scale adopted is λ=48.57. The main dimensions of the model are listed in Table 20.

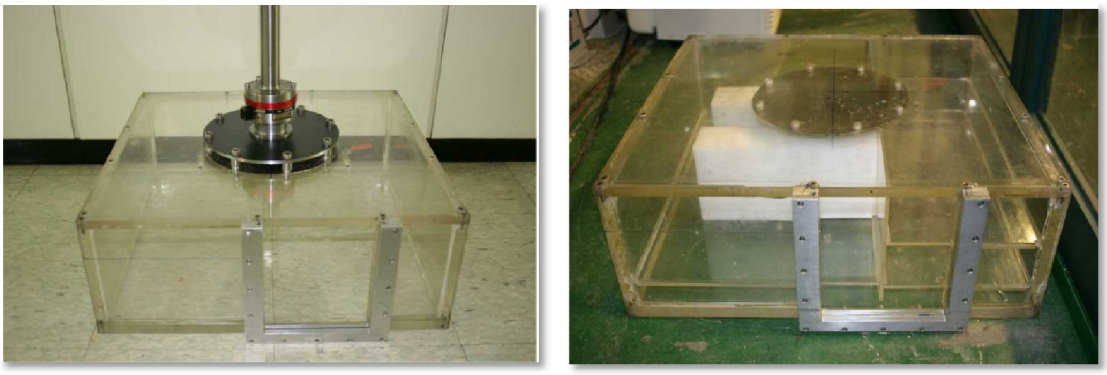

Figure 169: Simple and real model of the damaged compartment, *Cho et al. (2005)*

Model scale	48.57	
Damage side	Starboard	m
Length	0.550	m
Breadth	0.514	m
Height	0.185	m
Draft	0.131	m
Engine Blocks	0.271 x 0.118 x 0.066	m

Table 20: Main Characteristics of Damaged Compartment of ITTC Ro-Ro Passenger Ship

The acryl plastic compartments for the real model are divided by two decks and a transverse watertight bulkhead. The inner sub-dividing walls in the CFD calculations usually have a wall thickness of zero but the walls in the physical model had to have a thickness of 5 mm to provide enough stiffness.

Test arrangement

In the beginning the model is set into the water tank with empty compartments and the damage opening closed. The initial intact conditions are for a draft of 0.131 m. Then the damage opening is opened by pulling a slide; the opening procedure lasts about 0.12 seconds. When the slide is pulled, the model oscillated with natural frequency of the measuring system. The average of the measured values has been taken in order to exclude these unwanted effects.

Measurement instrumentation

Forces and moments were measured with a six-component force transducer which was attached on the centre of the top of the compartment. The water surface level of water inside the compartment could then be obtained from the measured vertical force acting on the model $F(t)$, by following equation.

$$F = \rho g S Z_w(t) + \frac{\rho S Z_w(t)}{t}\sqrt{2g\left(Z_{w0}(t) - Z_w(t)\right)} \tag{8.4.1}$$

where Z_w is the water level height in the compartment and S is the surface area of the compartment.

The floodwater flow at the damage opening was measured with high speed cameras which took 250 frames per second.

8.4.6 Data Comparison

8.4.6.1 Time History of the Flooding Process of the Simple Model

Again, in the calculation three dimensional images were created in order to visualise the flooding process of the empty compartment. The simulation case with the simple model does not focus on transient or progressive flooding but tries to show scale effects using a full scale model and two models scaled to λ=48.57 and λ=97.14. The flooding of the full scale compartment can be seen in the left column

of the image series (Figure 170, Figure 173, Figure 176, Figure 179 and Figure 182) and the flooding of the compartment in model scale λ=48.57 is shown in the middle column of the image series (Figure 171, Figure 174, Figure 177, Figure 180 and Figure 183). In the right column images of compartment in model scale 97.14 can be explored, (Figure 172, Figure 175, Figure 178, Figure 181 and Figure 184). Time steps for the simple model in model scale were converted with Froude's law, so that the images of the flooded compartment can be compared at the same time steps.

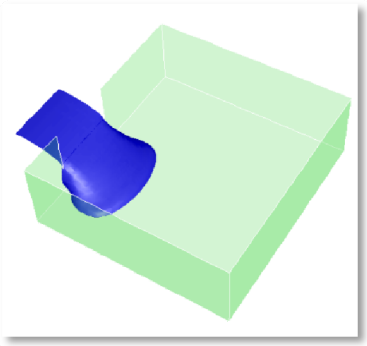

Figure 170: Flooding of simple model after 1 second

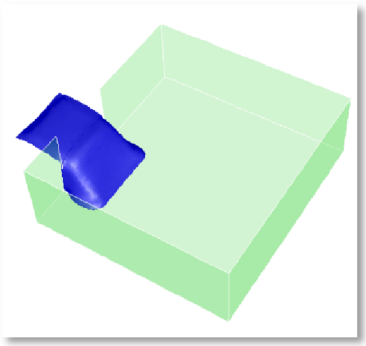

Figure 171: Flooding of simple model in model scale 48.57 after 1 second (converted with Froude's law)

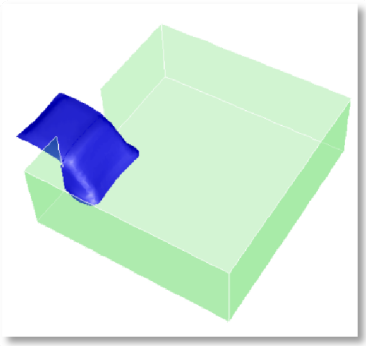

Figure 172: Flooding of simple model in model scale 97.14 after 1 second (converted with Froude's law)

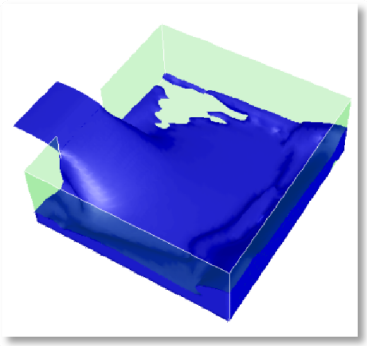

Figure 173: Flooding of simple model after 5 seconds

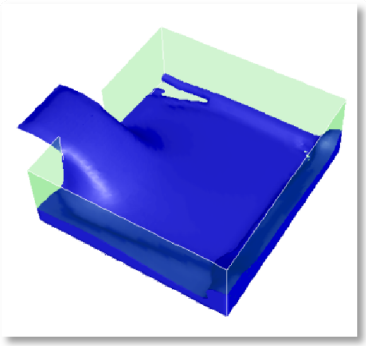

Figure 174: Flooding of simple model in model scale 48.57 after 5 seconds (converted with Froude's law)

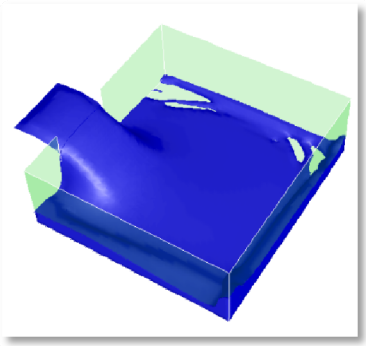

Figure 175: Flooding of simple model in model scale 97.14 after 5 seconds (converted with Froude's law)

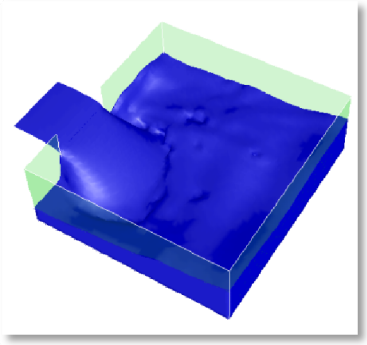

Figure 176: Flooding of simple model after 10 seconds

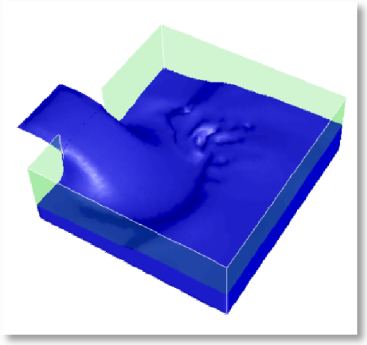

Figure 177: Flooding of simple model in model scale 48.57 after 10 seconds (converted with Froude's law)

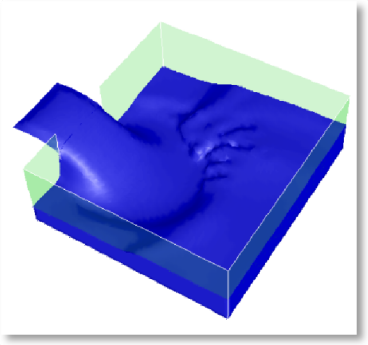

Figure 178: Flooding of simple model in model scale 97.14 after 10 seconds (converted with Froude's law)

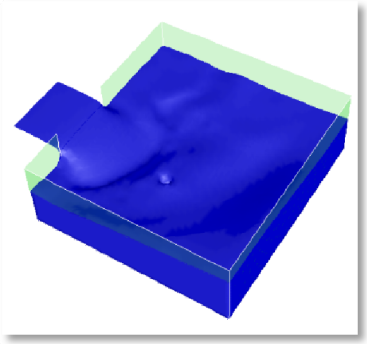

Figure 179: Flooding of simple model after 15 seconds

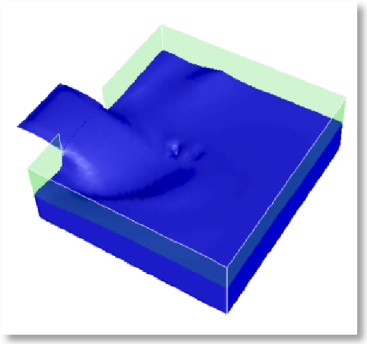

Figure 180: Flooding of simple model in model scale 48.57 after 15 seconds (converted with Froude's law)

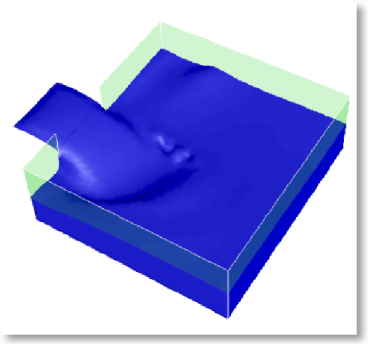

Figure 181: Flooding of simple model in model scale 97.14 after 15 seconds (converted with Froude's law)

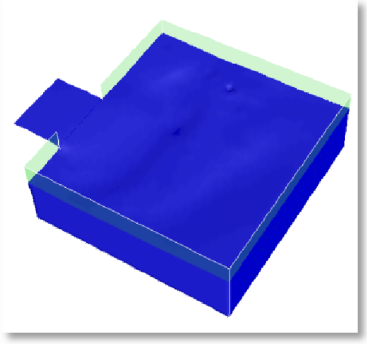

Figure 182: Flooding of simple model after 20 seconds

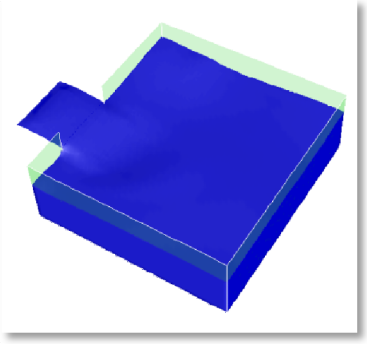

Figure 183: Flooding of simple model in model scale 48.57 after 20 seconds (converted with Froude's law)

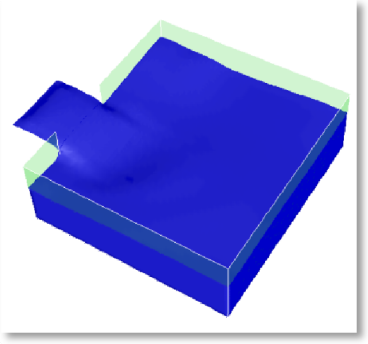

Figure 184: Flooding of simple model in model scale 97.14 after 20 seconds (converted with Froude's law)

In the beginning the floodwater enters the compartment violently with a high flow velocity. The full scale compartment fills up with water very quickly and reaches a water level of 6.4m corresponding to the given draft in only 21 seconds. The

compartment in model scale 48.57 requires 2.5 seconds more to be filled up with floodwater while the compartment in model scale 97.14 requires 5.5 seconds more than the full scale model. During the flooding process floodwater is constantly replenished by the water reservoir.

8.4.6.2 Scale Effects

The volume fraction of floodwater and air of the full scale model was monitored and opposed to the scaled models, see Figure 185. It can be observed that a faster flooding of the full scale model causes the remaining air to escape faster from the compartment. Air is allowed to escape from the compartment through the part of the damage opening which lies above the water line.

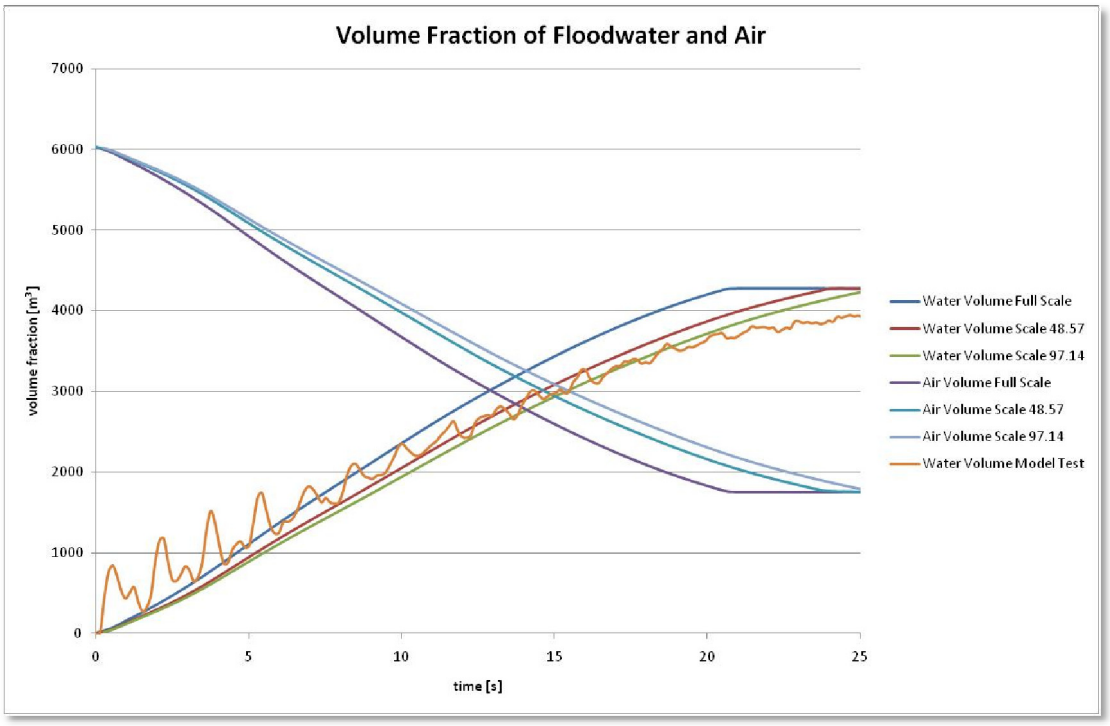

Figure 185: Comparison of volume fraction of floodwater and air of full scale and model scale

Scale effects are only small as the pressure remains small and does not increase rapidly throughout the simulation. Only in the beginning of the simulation a rapid

increase of pressure at the damage opening can be observed but this arises from the initial conditions. At time step 0 there is no pressure at the damage opening. When iteration is initiated the pressure at the damage opening has to be built up which happens in the first few time steps. The average pressure distribution on the damage opening can be seen in Figure 187. The minimal velocity difference between the full scale model and the scaled model results from the influence of the viscosity of the fluid on the flow, see Figure 186. According to *Ludwig Prandtl* the viscosity of a fluid has only influence on the flow in the boundary layer along some walls. In the centre of the flow the viscosity has no significant influence, *Siekmann and Thamsen (2008)*. This effect can be seen in the chart of the comparison of the average velocity, Figure 186. When the damage opening is scaled its centre moves closer to the surrounding perimeter of the damage opening and therefore closer to the boundary. As a matter of fact the flow velocity of the scaled model decreases compared to the full scale model because of the increased friction between the fluid particles which is described by the viscosity of a fluid.

As the wall thickness at the damage opening is zero a turbulent flow can only develop due to a flow separation at the sharp edge of the damage opening. A maximum Reynolds Number of $Re=4.16x10^4$ for the full scale model, a Reynolds Number of $Re=3.15x10^4$ for the model in model scale λ=48.57 and a Reynolds Number of $Re=3.21x10^4$ for the model in model scale λ=97.14 shows that the floodwater flows are comparable and that the model in model scale can represent full scale parameters. Although the agreement with full scale is not that good, this finding justifies the validation of full scale results of numerical calculation with results of model tests in model scale as has been done in the research study of sinking sequence of M/V Estonia, see chapter 8.2.

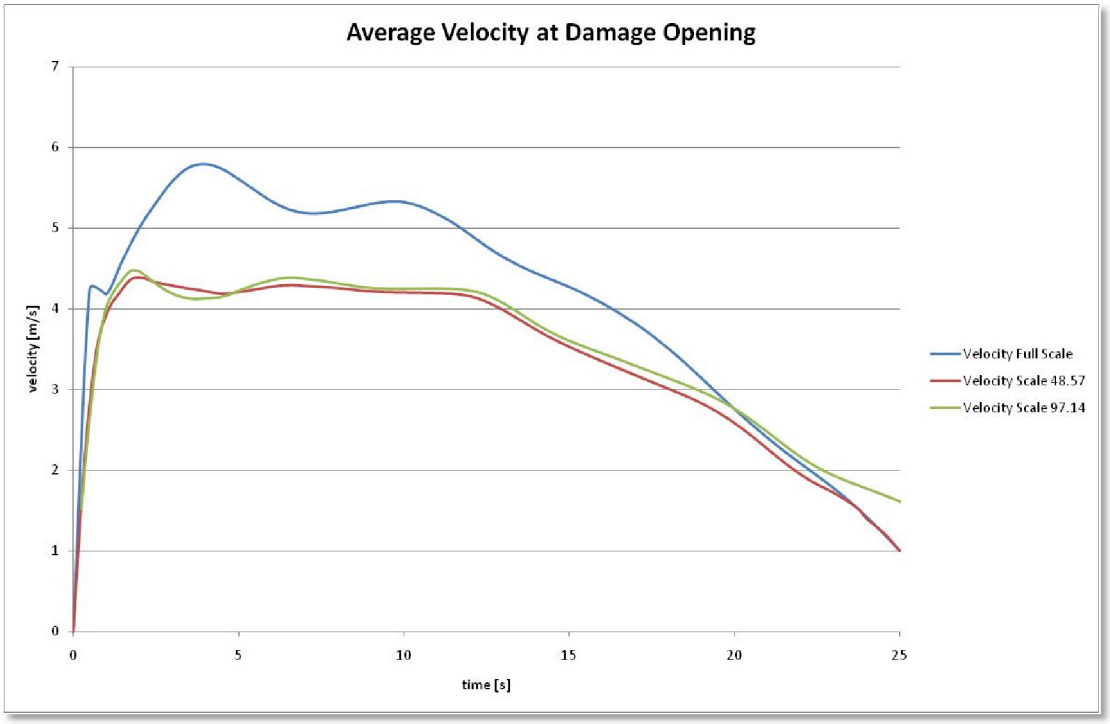

Figure 186: Comparison of average velocity at damage opening

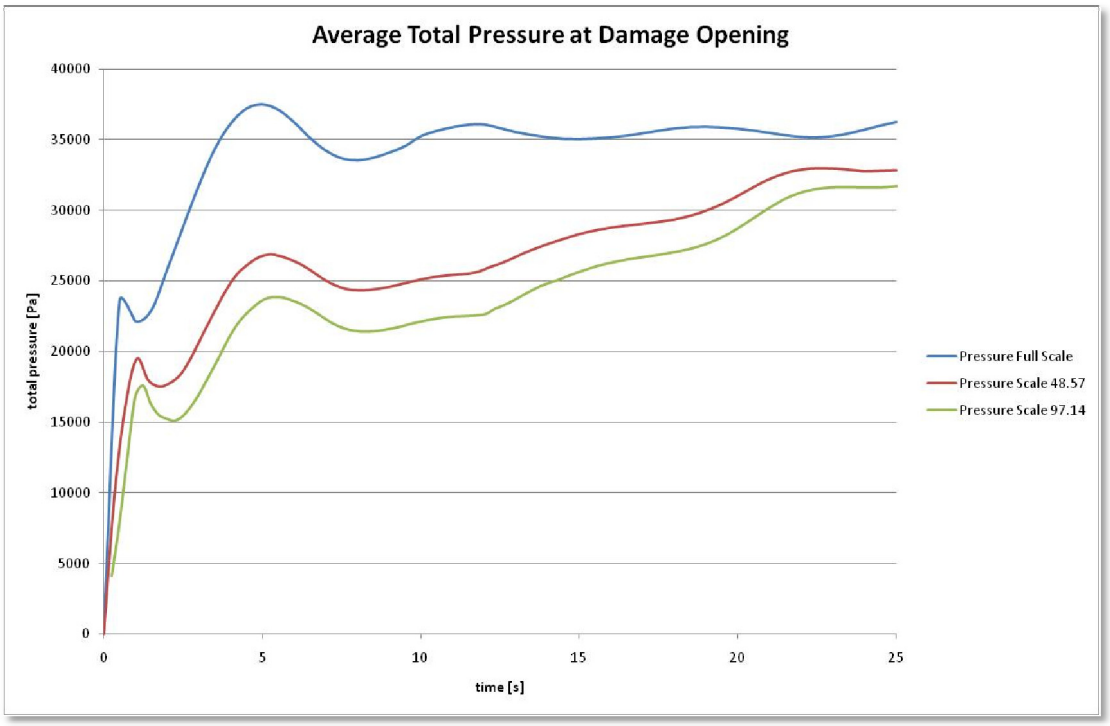

Figure 187: Comparison of average pressure at damage opening

8.4.6.3 Time History of the Flooding Process of the Real Model

In the case study with the real model flooding simulations with four different damage openings have been carried out. For all four cases the flow characteristic is similar. In the generator room and the storage room the floodwater reaches the opposite side of the damage opening and accumulates after a few seconds. Then the floodwater reflects from the wall opposite of the damage opening and generates a rotational flow at time instant of 10 seconds. In the Engine room the floodwater accumulates at the side of the damage opening because the two engine blocks are blocking the floodwater flow. After a few seconds the floodwater progresses to the opposite side. The total flooding durations for each damage case are as shown in the Table 21 below:

damage case	**time [s]**
damage case 1	32
damage case 2	38
damage case 3	45
damage case 4	45

Table 21: Duration of flooding

Screenshots of each flooding case for comparison can be found in the image series below. Flooding case 1 can be observed in Figure 188, Figure 190, Figure 192, Figure 194, Figure 196, Figure 198 and Figure 200. An impression of flooding case 2 is given in Figure 189, Figure 191, Figure 193, Figure 195, Figure 197, Figure 199 and Figure 201.

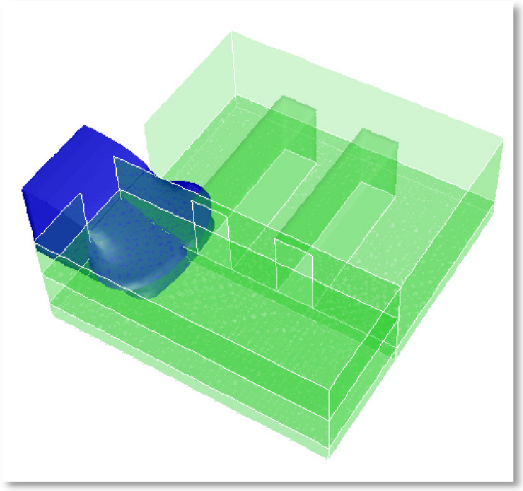

Figure 188: Flooding of real model through opening No. 1 after 1 second

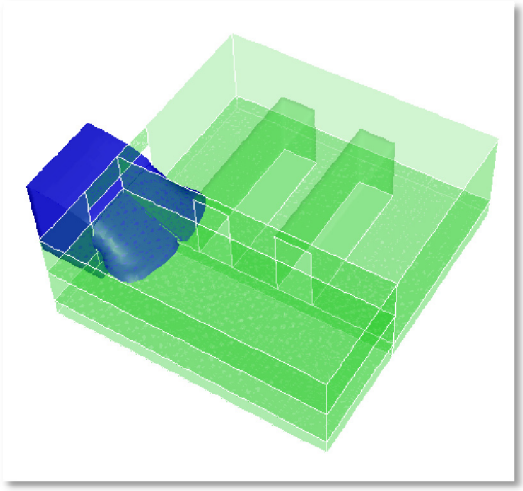

Figure 189: Flooding of real model through opening No. 2 after 1 second

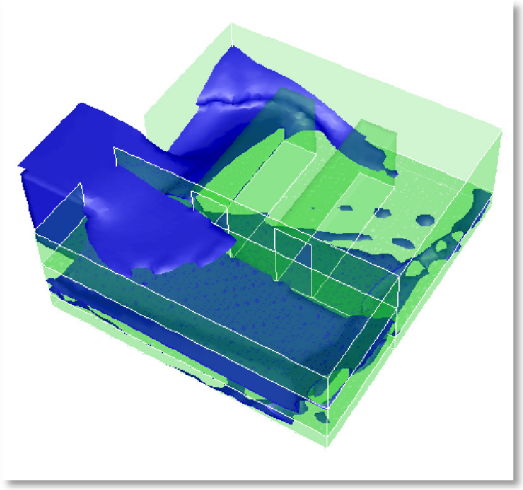

Figure 190: Flooding of real model through opening No. 1 after 5 seconds

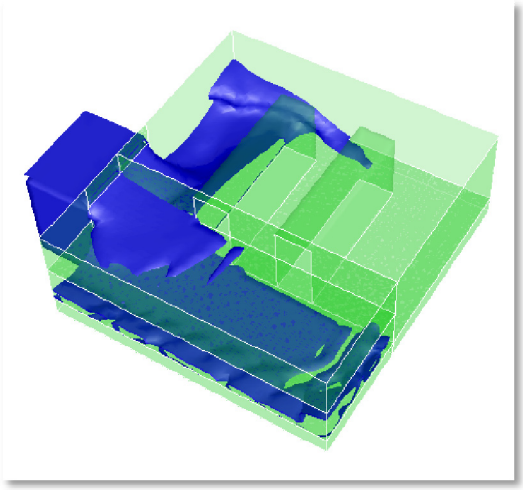

Figure 191: Flooding of real model through opening No. 2 after 5 seconds

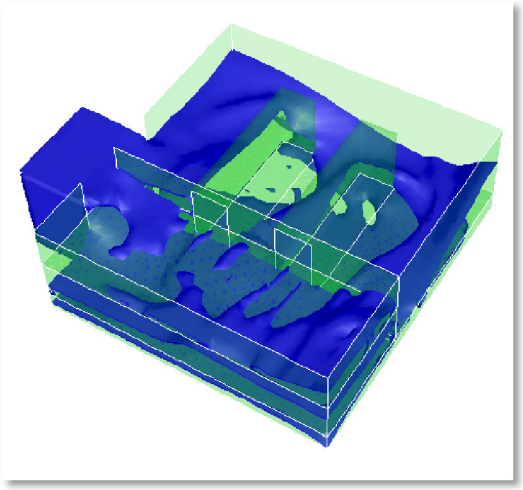

Figure 192: Flooding of real model through opening No. 1 after 10 seconds

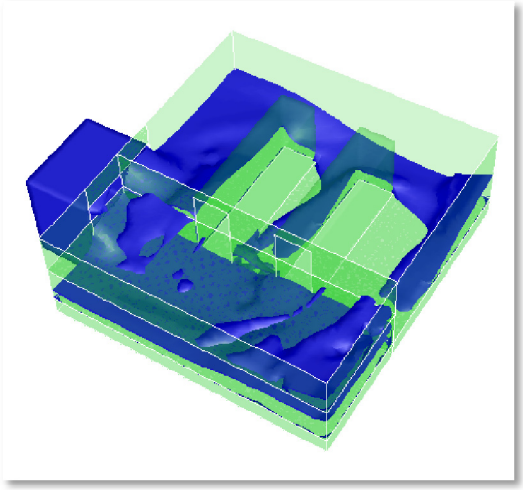

Figure 193: Flooding of real model through opening No. 2 after 10 seconds

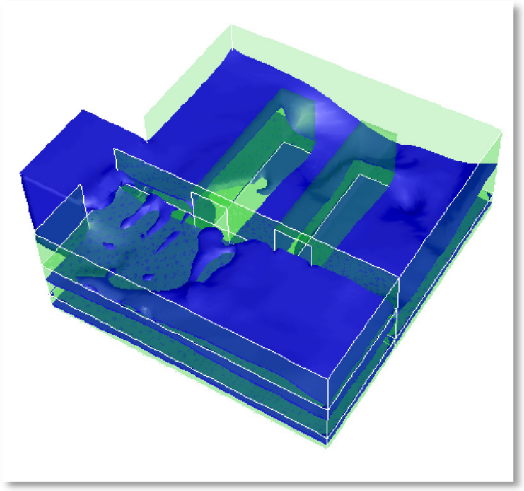

Figure 194: Flooding of real model through opening No. 1 after 15 seconds

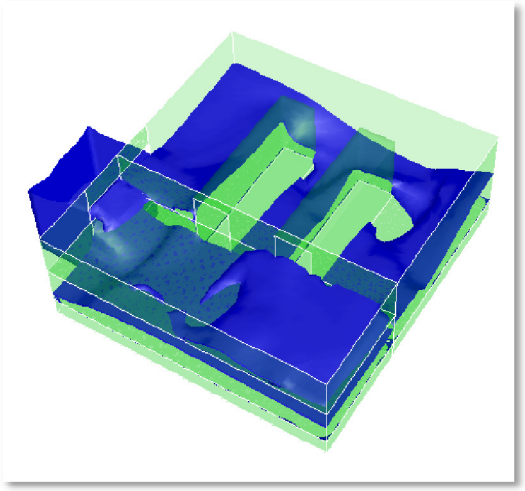

Figure 195: Flooding of real model through opening No. 2 after 15 seconds

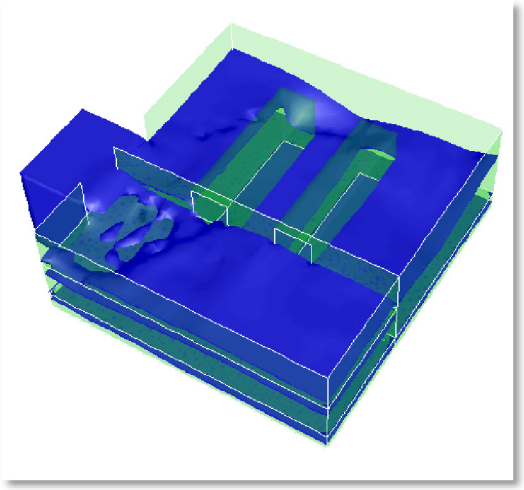

Figure 196: Flooding of real model through opening No. 1 after 20 seconds

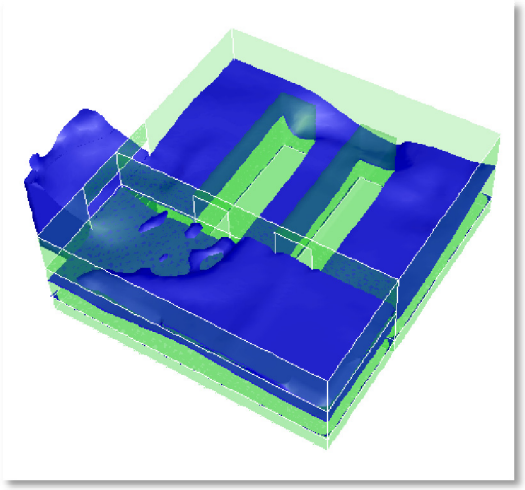

Figure 197: Flooding of real model through opening No. 2 after 20 seconds

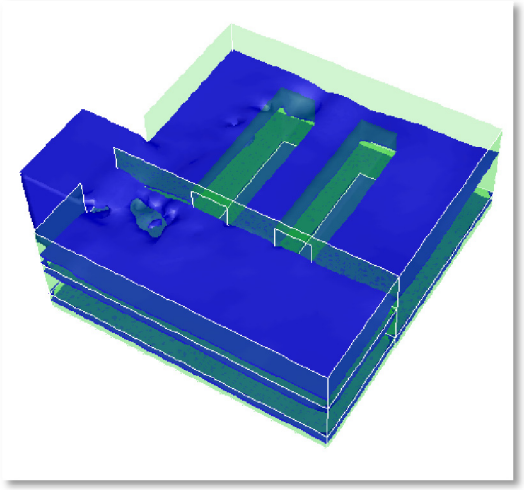

Figure 198: Flooding of real model through opening No. 1 after 25 seconds

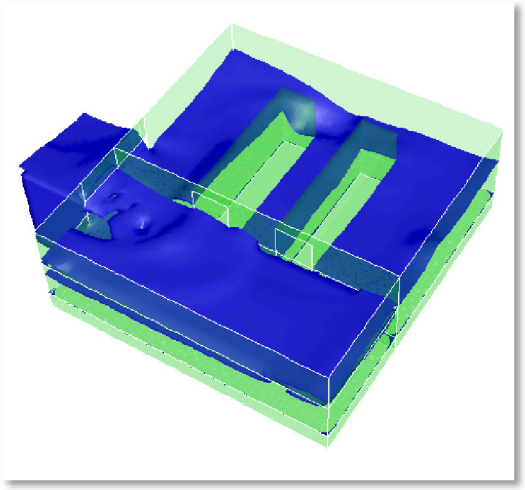

Figure 199: Flooding of real model through opening No. 2 after 25 seconds

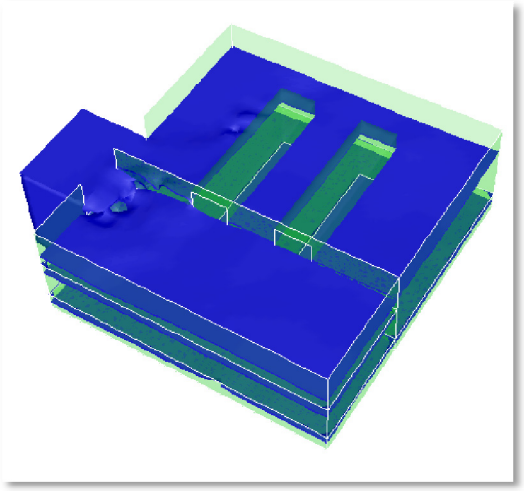

Figure 200: Flooding of real model through opening No. 1 after 30 seconds

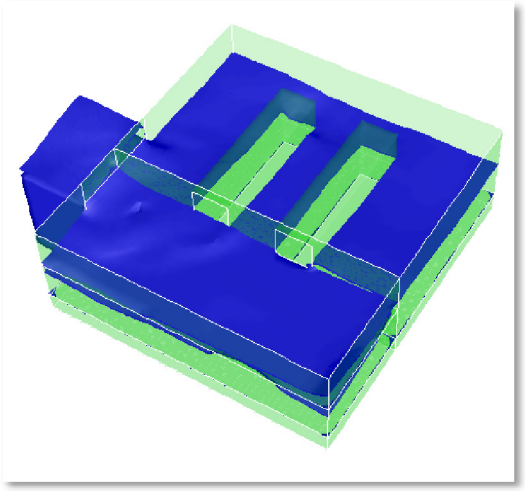

Figure 201: Flooding of real model through opening No. 2 after 30 seconds

Damage case 3 is shown in Figure 202, Figure 204, Figure 206, Figure 208, Figure 210, Figure 212 and Figure 214. Screenshots of damage case 4 are presented in Figure 203, Figure 205, Figure 207, Figure 209, Figure 211, Figure 213 and Figure 215.

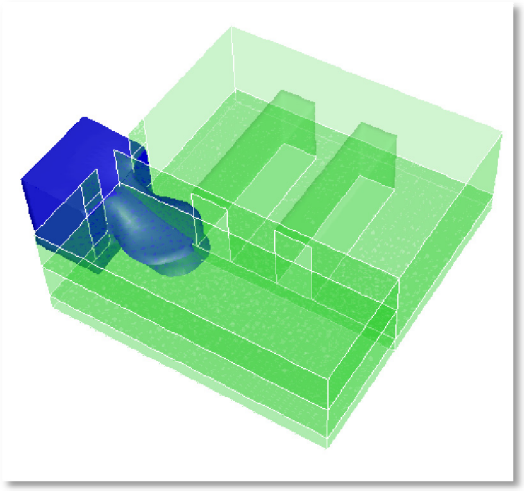

Figure 202: Flooding of real model through opening No. 3 after 1 second

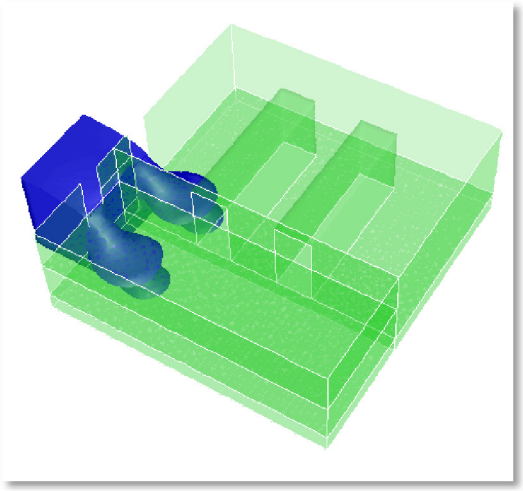

Figure 203: Flooding of real model through opening No. 4 after 1 second

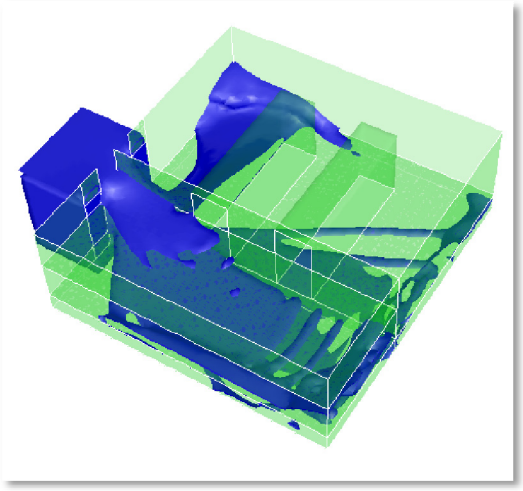

Figure 204: Flooding of real model through opening No. 3 after 5 seconds

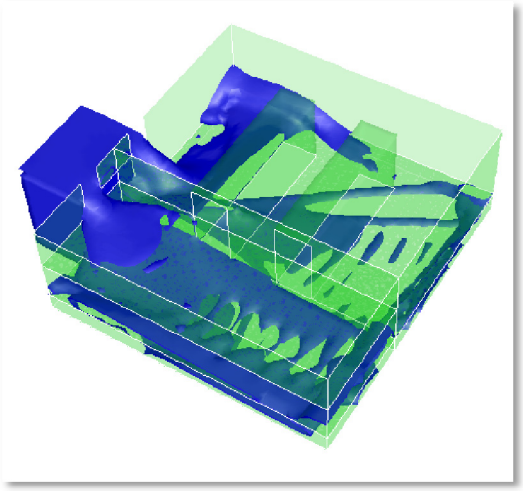

Figure 205: Flooding of real model through opening No. 4 after 5 seconds

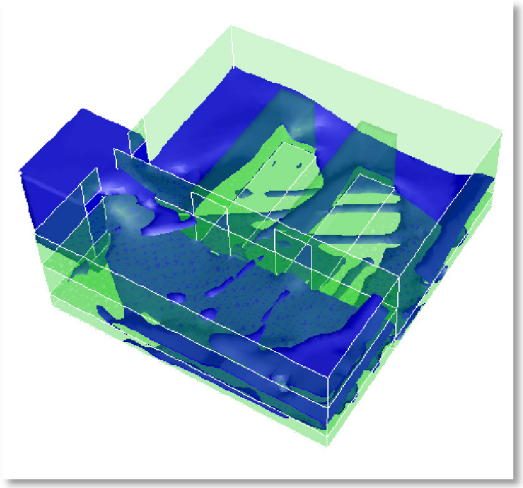

Figure 206: Flooding of real model through opening No. 3 after 10 seconds

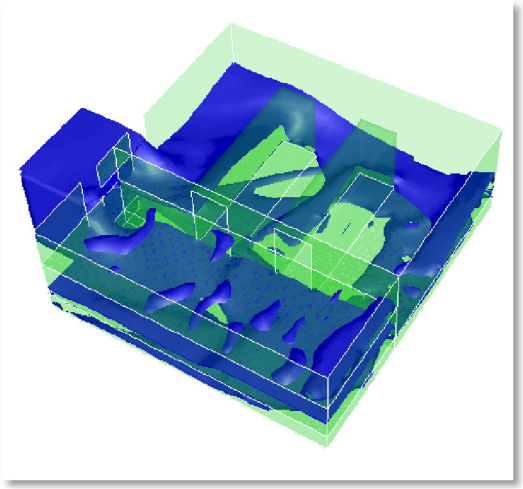

Figure 207: Flooding of real model through opening No. 4 after 10 seconds

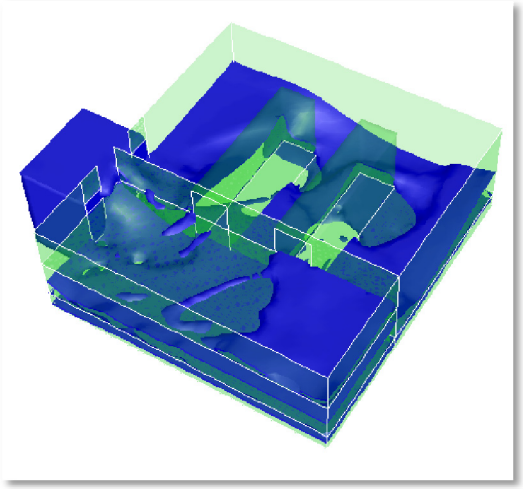

Figure 208: Flooding of real model through opening No. 3 after 15 seconds

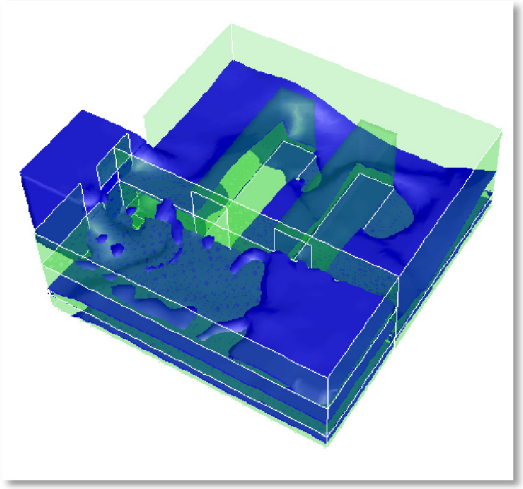

Figure 209: Flooding of real model through opening No. 4 after 15 seconds

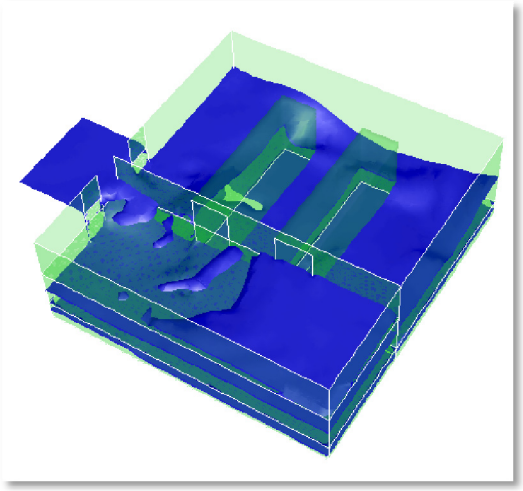

Figure 210: Flooding of real model through opening No. 3 after 20 seconds

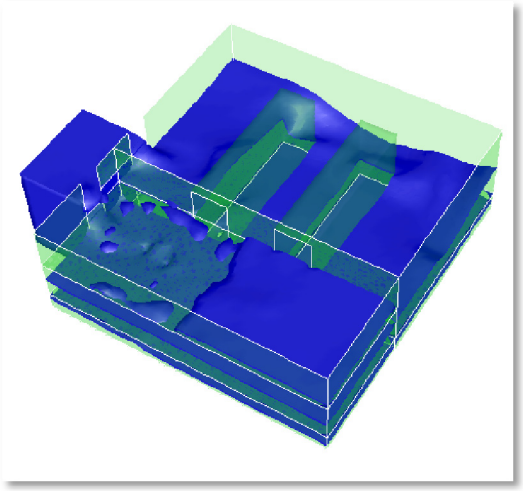

Figure 211: Flooding of real model through opening No. 4 after 20 seconds

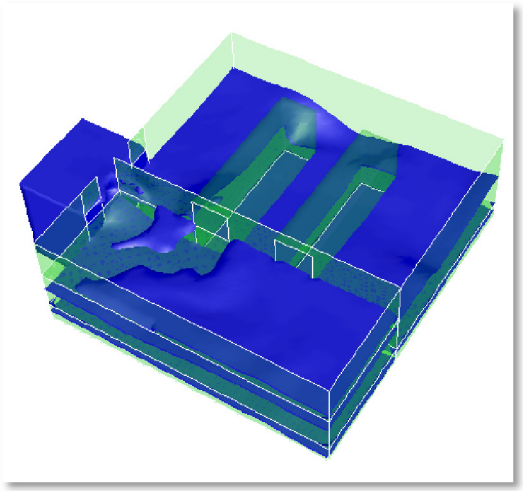

Figure 212: Flooding of real model through opening No. 3 after 25 seconds

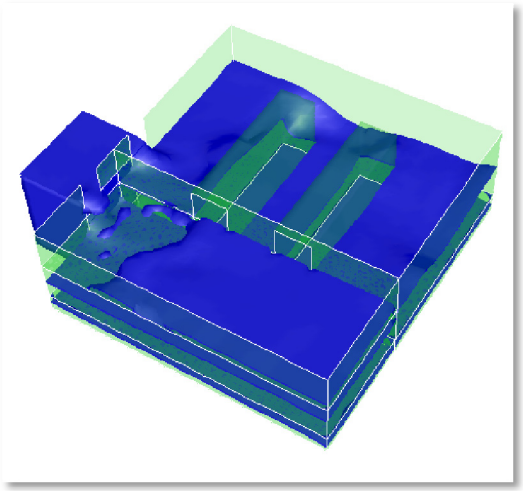

Figure 213: Flooding of real model through opening No. 4 after 25 seconds

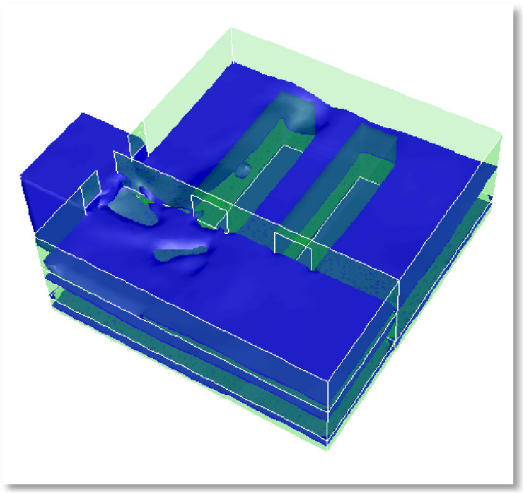

Figure 214: Flooding of real model through opening No. 3 after 30 seconds

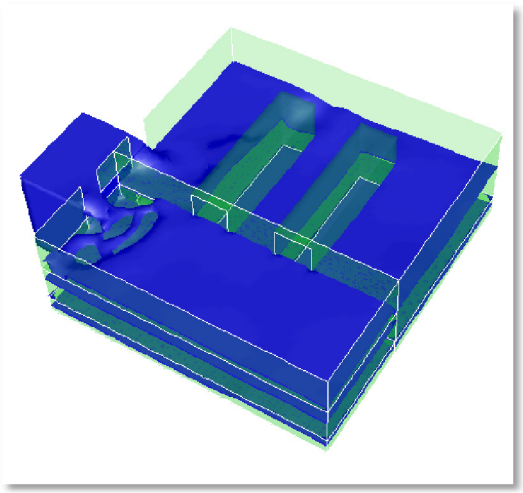

Figure 215: Flooding of real model through opening No. 4 after 30 seconds

8.4.6.4 Volume Fraction of Floodwater and Air

The volume fraction of floodwater and air is derived in all rooms. The volume fraction of floodwater and air increases almost linearly in the storage room and in the engine room where air can easily escape through the damage opening and no air pockets can develop, see Figure 220 - Figure 221 and Figure 224 - Figure 225. All other rooms can develop air pockets because air could only escape if the air pressure in the room is larger than the floodwater pressure at the damage opening. Therefore these rooms are flooded linearly up to the moment that air gets compressed which slows down the flooding process; this is illustrated in Figure 216 - Figure 219 and Figure 222 - Figure 223.

Special attention should also be turned to damage case 3 and 4. In this case the damage openings have the same magnitude of wetted area but have a different relative position along the starboard wall of the compartment. Also, the magnitude of the cross-section of the damage opening 4 is the same as the magnitude of the cross-section of damage opening 3 which is bifid by a transversal bulkhead. As expected the volume fraction of these cases is almost identical and their insignificant deviation results from a small amount of air that could escape easier from damage 4. This concludes that the horizontal position of a damage opening with consistent magnitude of wetted area has no significant effect on the flooding characteristics.

The compartment with damage opening 2 was flooded faster compared to the compartments with damage 3 and 4 though the damage openings had the same magnitude of cross-section. Reason for a faster flooding of compartment featuring damage opening 2 was that the wetted surface was larger compared to damage 3 and 4 which influences the celerity of the flooding process significantly. It can be concluded that the magnitude of the wetted surface of a damage opening has a significant influence on the time-to-flood of a compartment.

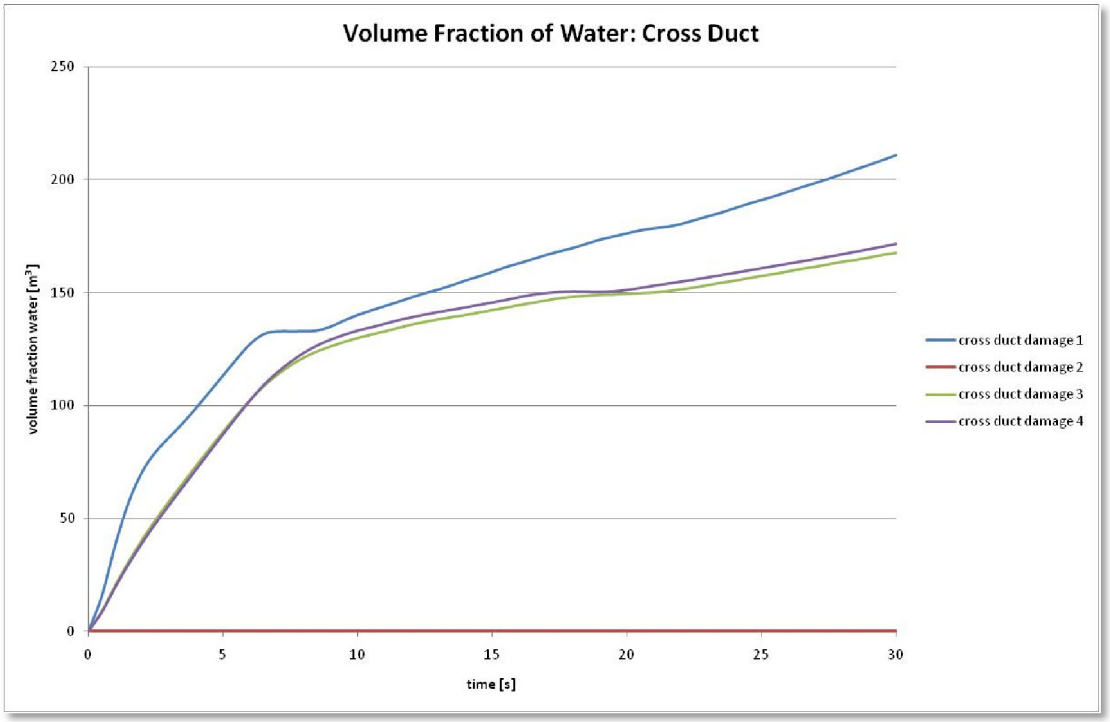

Figure 216: Volume fraction of floodwater in the cross duct

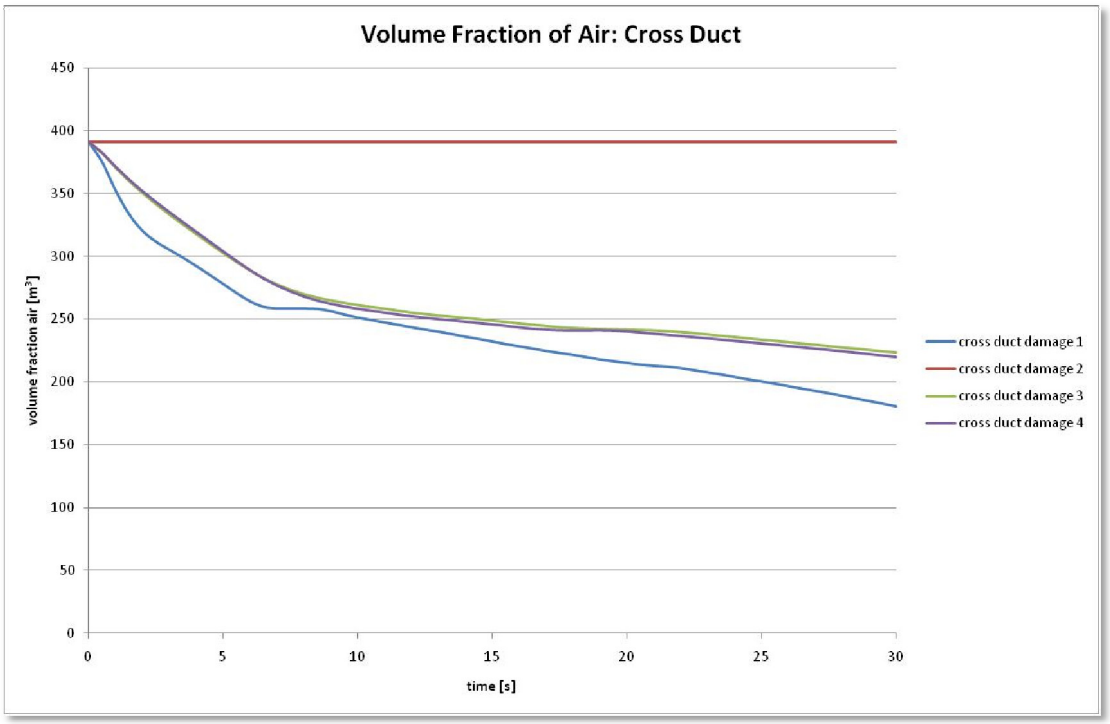

Figure 217: Volume fraction of air in the cross duct

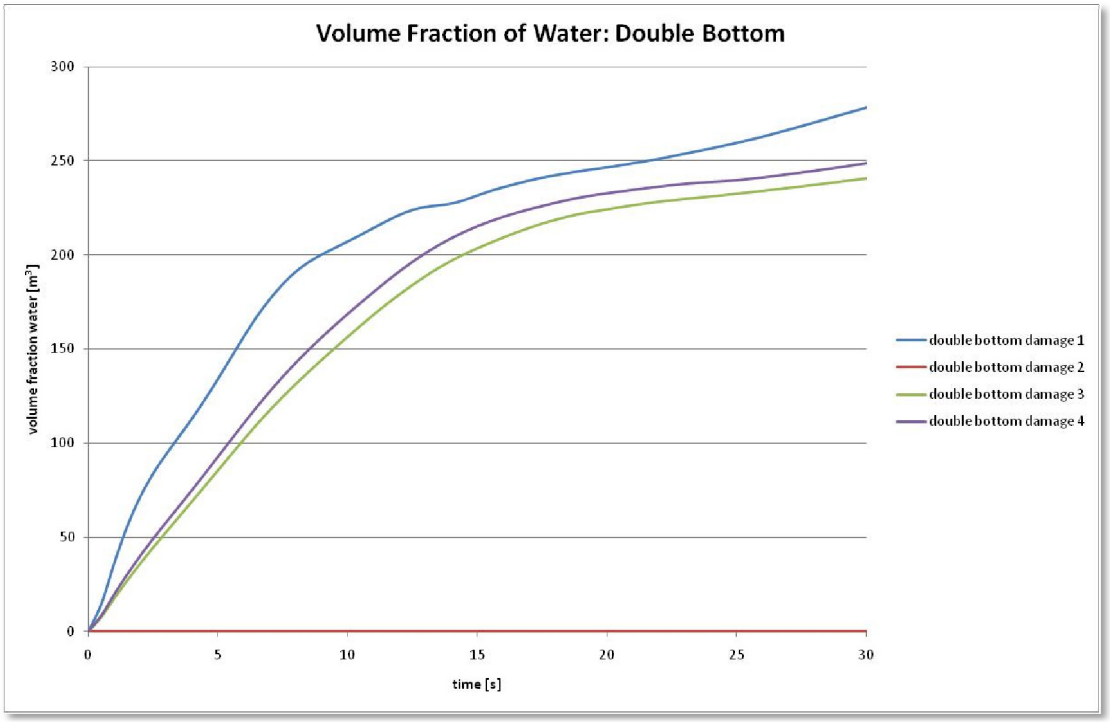

Figure 218: Volume fraction of floodwater in the double bottom

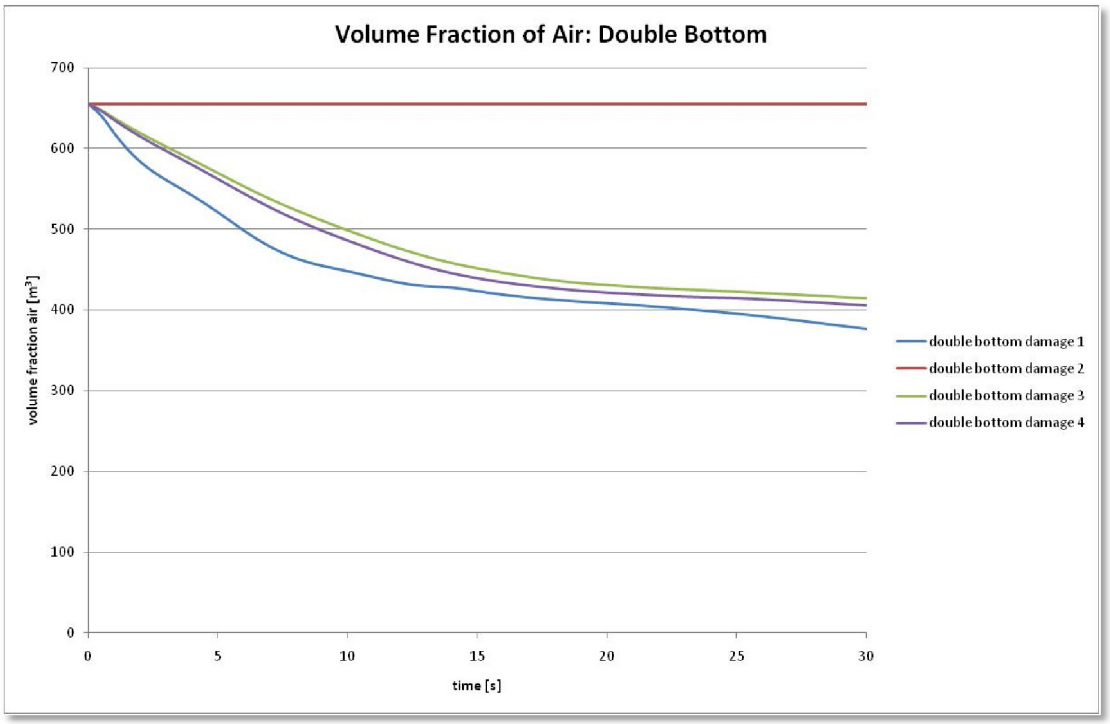

Figure 219: Volume fraction of air in the double bottom

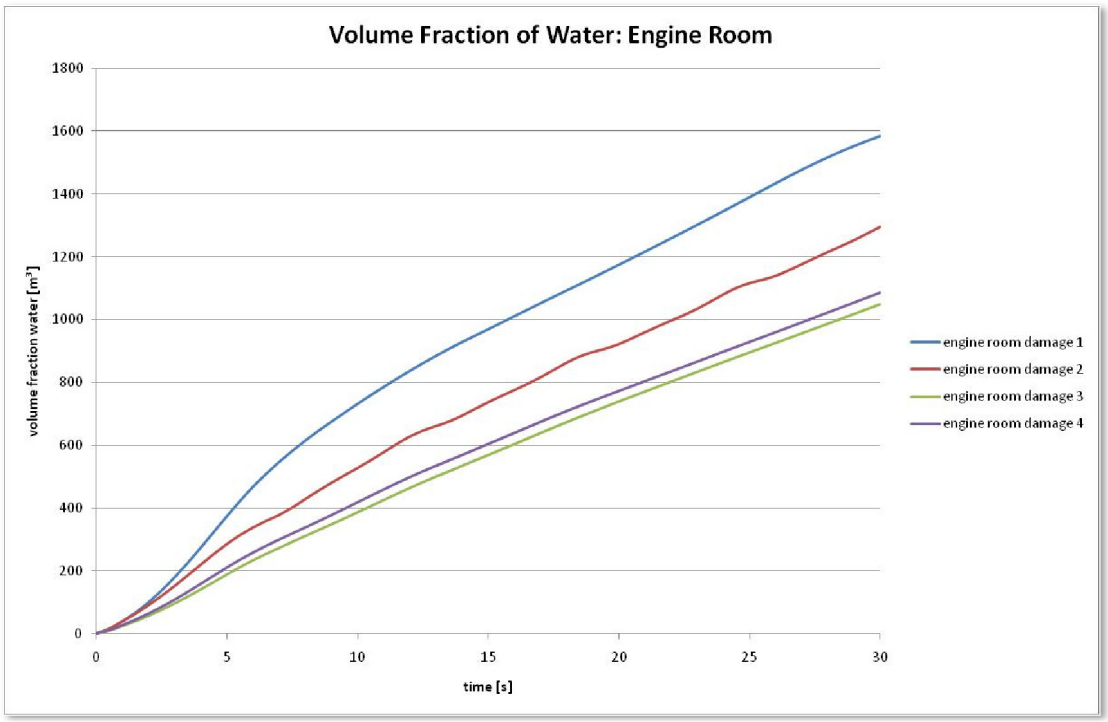

Figure 220: Volume fraction of floodwater in the engine room

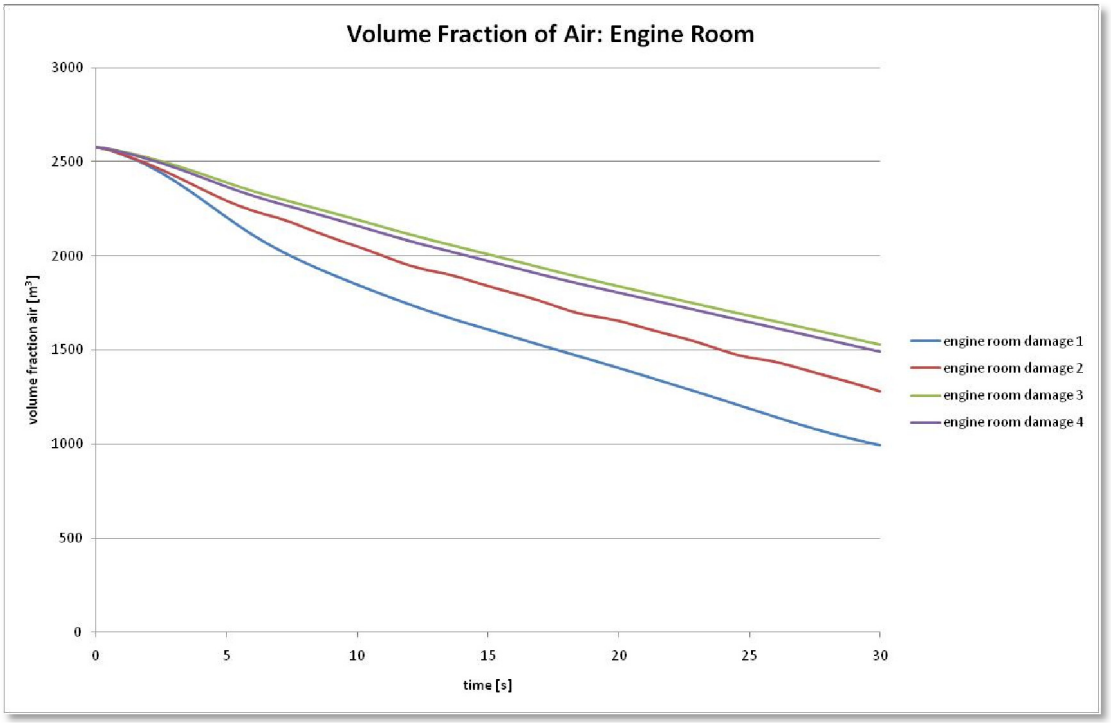

Figure 221: Volume fraction of air in the engine room

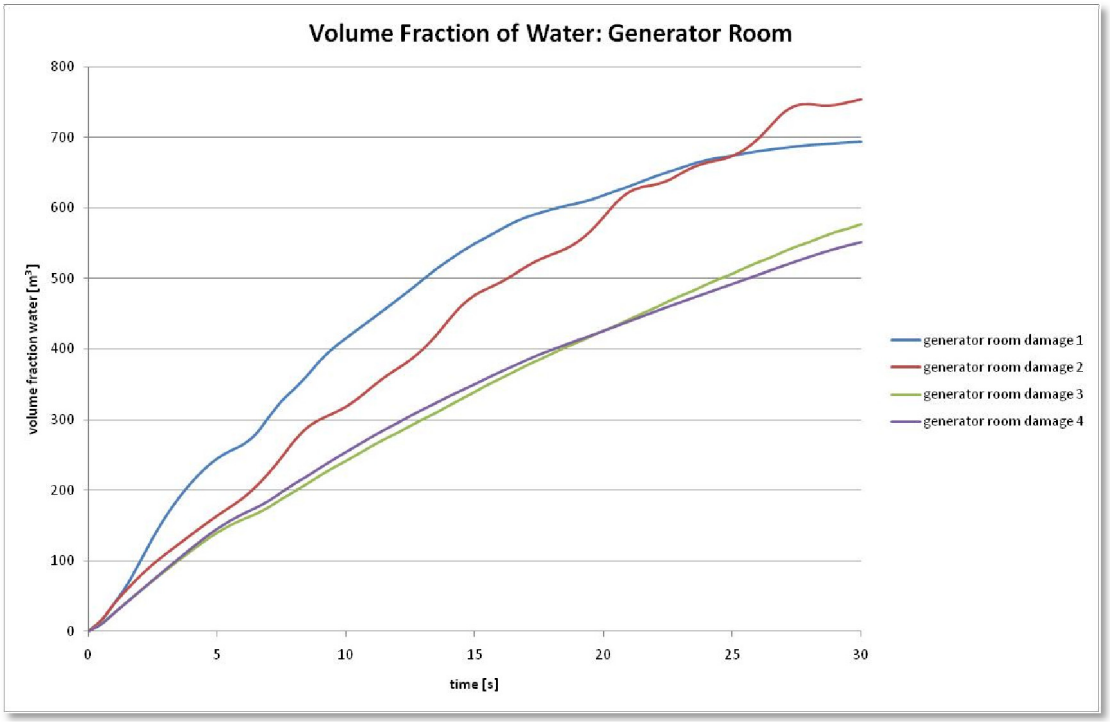

Figure 222: Volume fraction of floodwater in the generator room

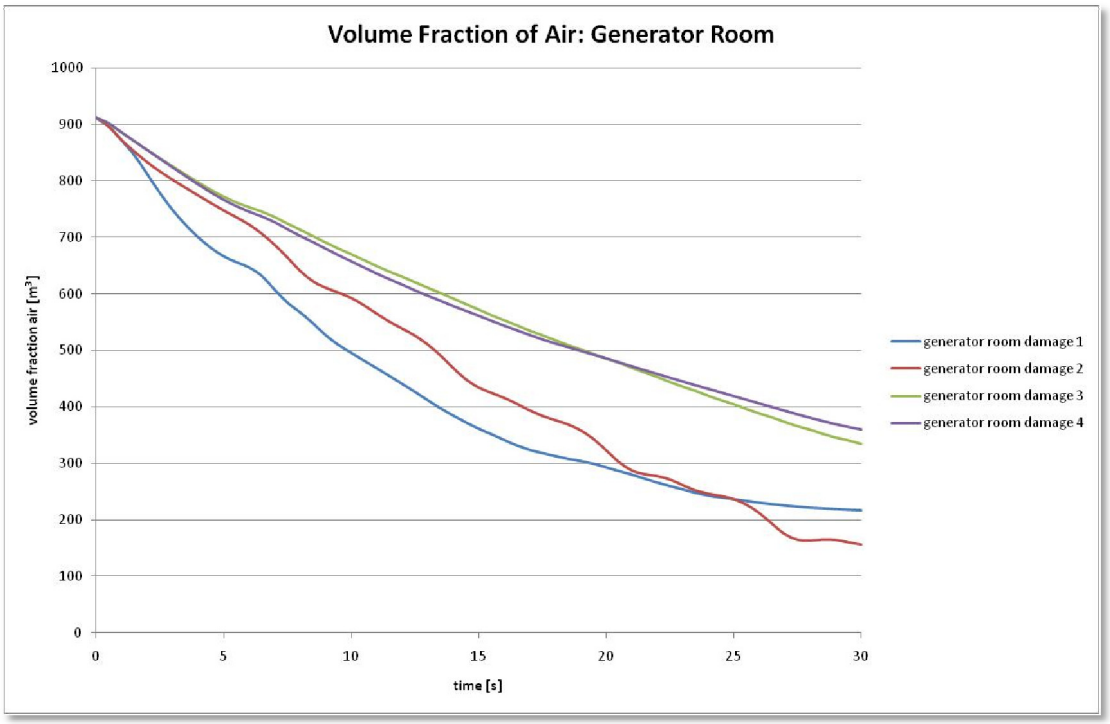

Figure 223: Volume fraction of air in the generator room

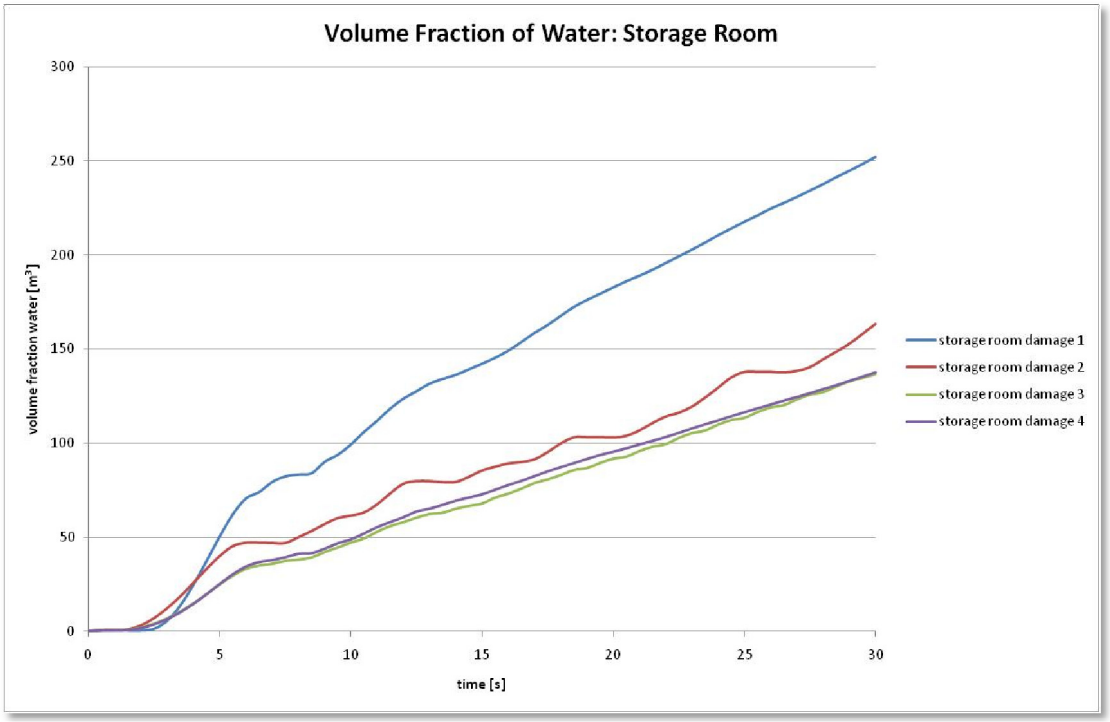

Figure 224: Volume fraction of floodwater in the storage room

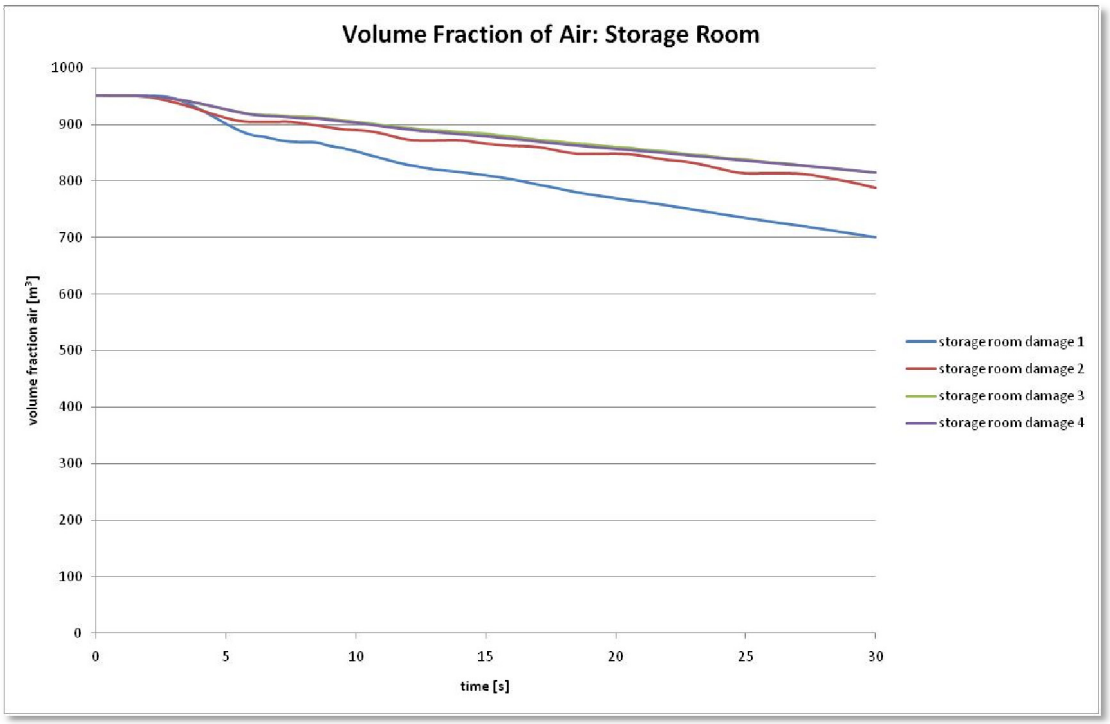

Figure 225: Volume fraction of air in the storage room

8.4.6.5 Air Pressure in Air Pocket

The average air pressure in the remaining space above the water surface in each room of the compartment was calculated. An increasing air pressure depends on various parameters such as high floodwater velocity at the damage opening which is directly proportional to an increasing pressure at the damage opening, limited or no ventilation and the position and shape of the damage opening. Generally, the air pressure increases in every room for the duration of flooding because compressible air is used in the simulation, see Figure 226 - Figure 230. There are two scenarios which can take place after the air pressure has increased: the air pressure does not change anymore and remains constant, or the air pressure drops down to ambient pressure. When the air pressure does not change anymore and remains constant either an air pocket has developed and the flooding of the compartment has stopped or air can slowly escape and is equally slowly replenished by floodwater – the pressure heads on both sides of the damage opening are in equilibrium. When the air pressure drops down to ambient pressure, flooding has stopped and remaining compressed air can escape from the compartment. Each of these scenarios can be found in some rooms of the compartment. In the double bottom and the cross duct air pockets develop and the flooding is stopped (case 1,3 and 4); in the generator room trapped air slowly escapes through the damage opening until it is completely filled with floodwater; in the storage and engine room remaining compressed air can escape through the damage opening and equalises with ambient air pressure.

Damage case 2 is distinguished from the other damage cases in such a way that air can only escape through a small slit of the damage opening because the draft line is only 0.27 m lower than the upper edge of the damage opening. So only a small fraction of the cross-section of the damage opening is not wetted and air can only escape when high air pressure inside the compartment has built up. Another reason why air cannot escape easily is that due to sloshing floodwater inside the compartment which sometimes covers the slit completely. Only when the wave crest is on the opposite side of the damage opening air can escape through the

unblocked slit. Therefore, the air pressure curve for damage case 2 results in a wavelike slope in the chart. Additionally, the sloshing period can be determined from the chart which is about 7 seconds for damage case 2. Subject to this phenomenon are primarily rooms on the upper decks such as the storage room and the engine room. Also rooms below the water surface like the generator room with comparatively lower pressure heads on the damage opening than in damage case 1, 3 and 4 show this phenomenon.

It can be concluded that the flooding process is significantly dependent on the vertical extent of the damage opening in conjunction with its position towards the water surface. The lower the damage opening is immersed the less air can escape and air pockets can develop.

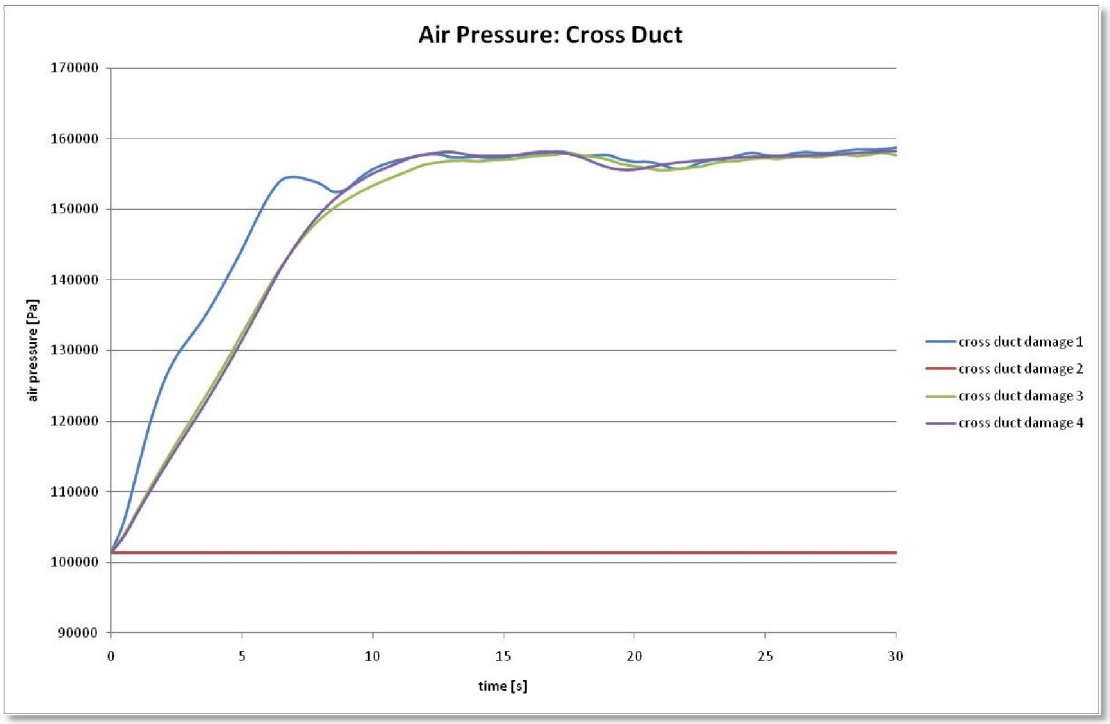

Figure 226: Air pressure of air pocket in cross duct

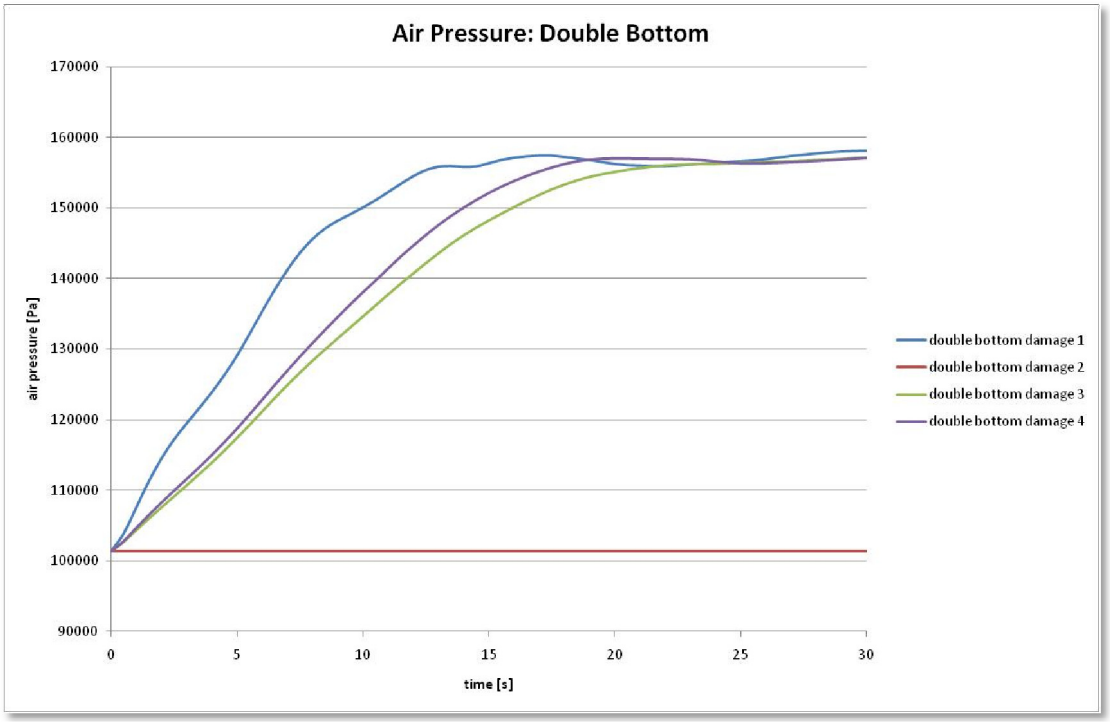

Figure 227: Air pressure of air pocket in double bottom

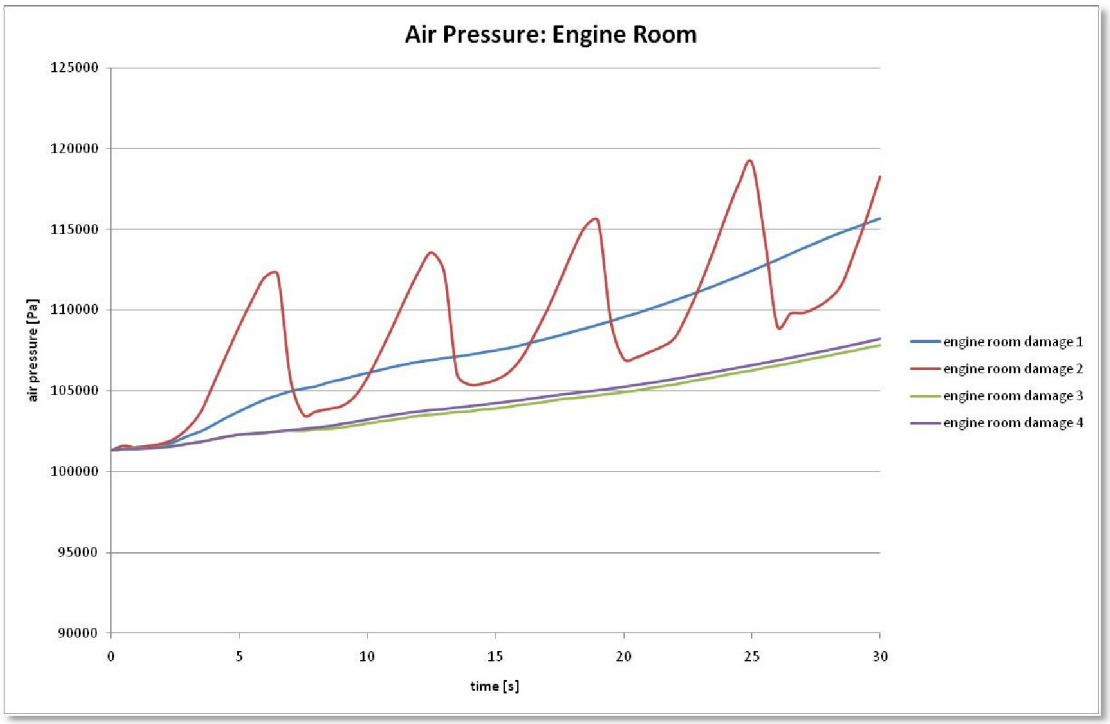

Figure 228: Air pressure of air pocket in engine room

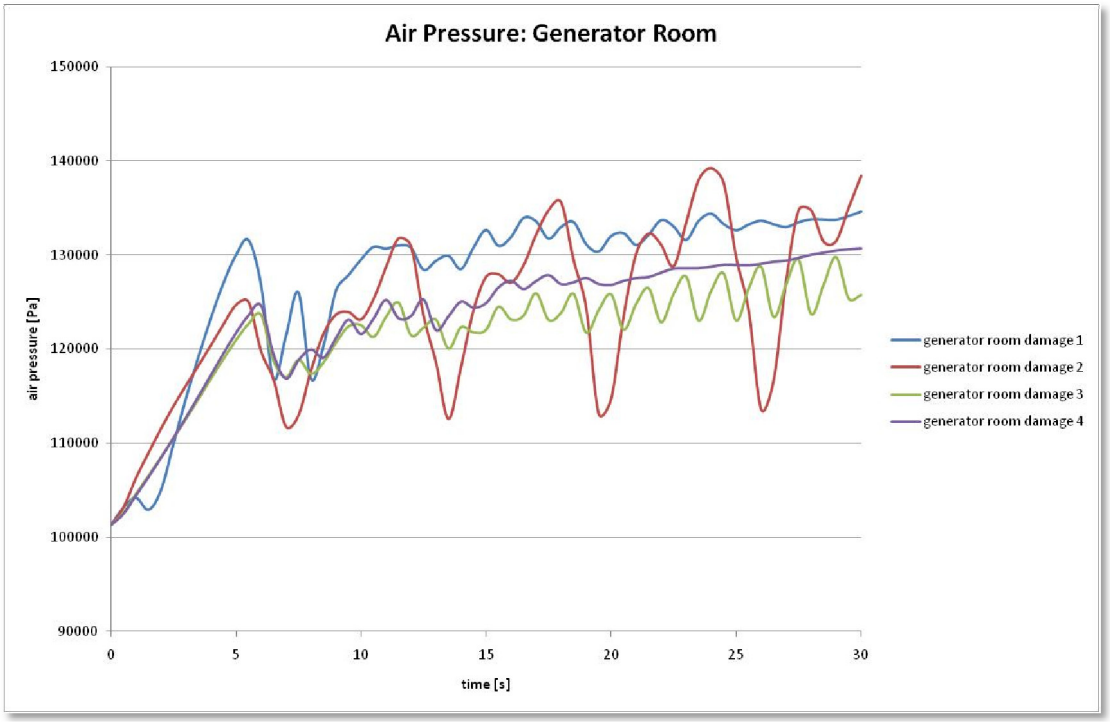

Figure 229: Air pressure of air pocket in generator room

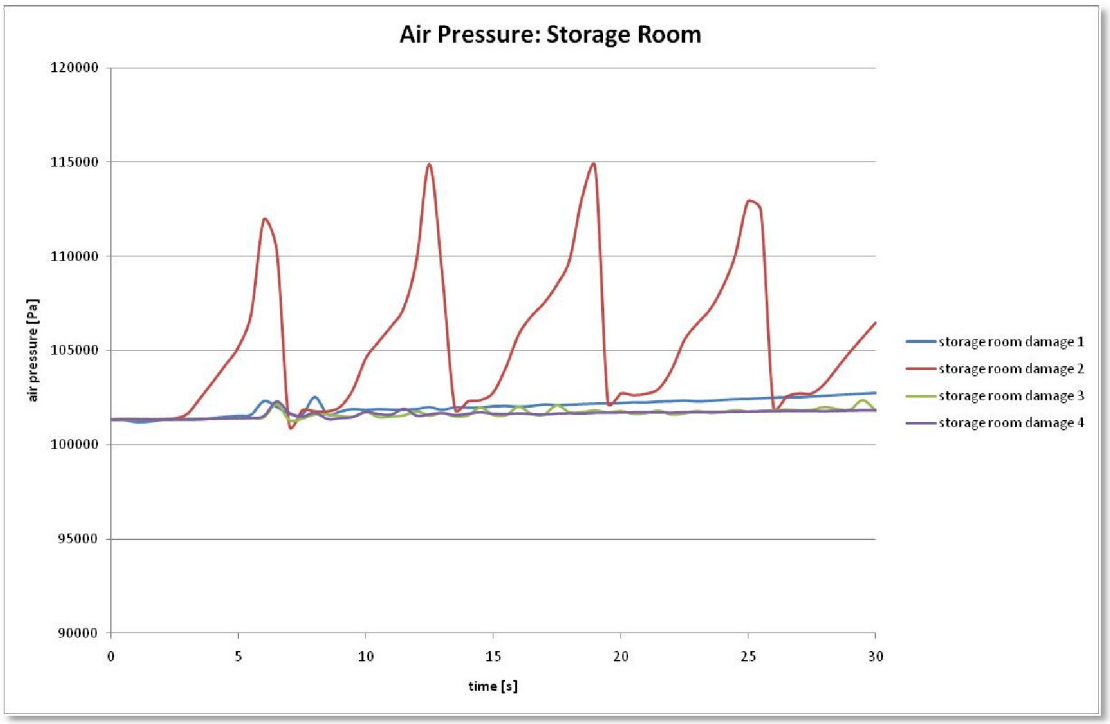

Figure 230: Air pressure of air pocket in storage room

8.4.6.6 Flow Velocity and Total Pressure at Damage Opening

Flow velocity and total pressure (static plus dynamic pressure) has been computed at the damage opening. For an appropriate reproduction of the flow parameters, the area of wetted surface of the damage opening had to be determined for each time step. With the aid of the VOF algorithm, see 6.2.2, only faces with a phase fraction of $0.5 \leq \alpha_q \leq 1$ were used for the definition of the wetted surface. From this surface the average velocity and the total pressure could be taken. In contrary to model tests this method is able to average velocity and pressure over the entire wetted surface of the damage opening. When model tests are carried out pressure or velocity is usually measured in one or a few representative locations (normally in the geometric centre of the wetted surface). Measurement devices have to be applied in a way that they allow an undisturbed flow but still take representative measurement values. The advantage of the CFD method is that velocity or pressure can be determined on any surface of interest without disturbing the flow at all.

Figure 235 and Figure 236 illustrate the relation between velocity and pressure at the damage opening; when the pressure increases the flow velocity drops and vice versa. Oscillation of pressure and velocity in the charts is caused by sloshing water and compressed air pockets inside the compartment. Again, damage case 2, Figure 232, shows extreme pressure and velocity fluctuations in the charts as air can only escape through a small slit (8.244m x 0.27m). The cross-sectional area of the slit is limited by the wavy water surface caused by sloshing and the upper edge of the damage opening; for that reason the slit is sometimes completely covered by a reflecting wave and air cannot escape. When the wave crest is on the opposite side of the damage opening air can easily escape through the unblocked slit.

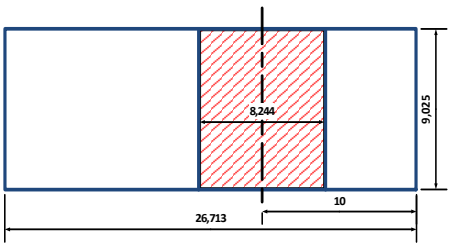

Figure 231: Damage opening 1

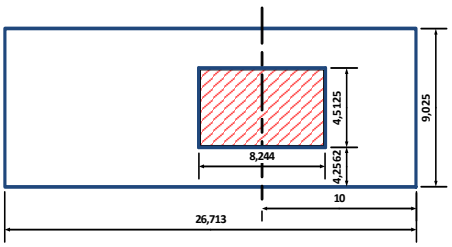

Figure 232: Damage opening 2

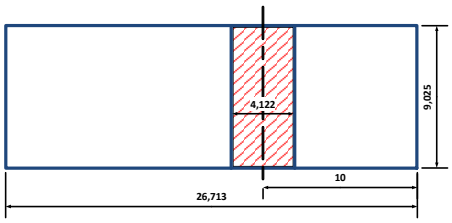

Figure 233: Damage opening 3

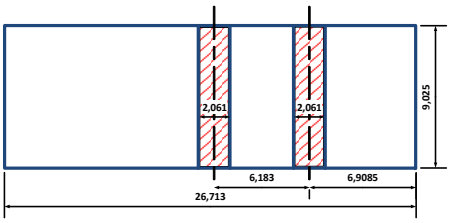

Figure 234: Damage opening 4

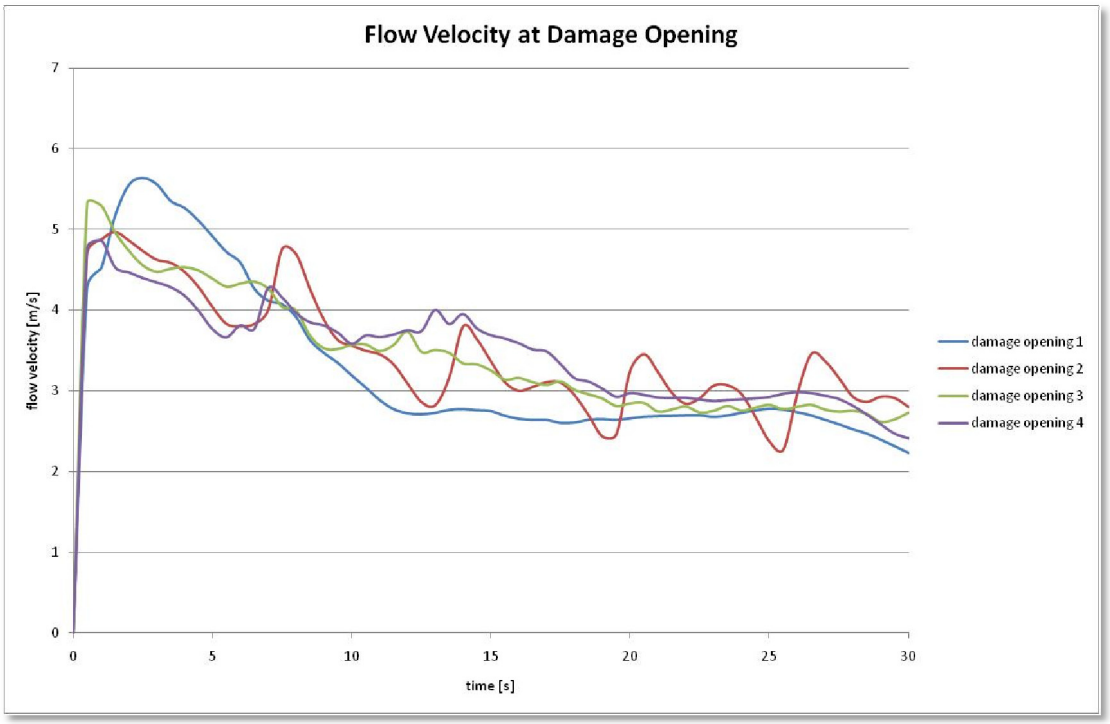

Figure 235: Flow velocity at damage opening

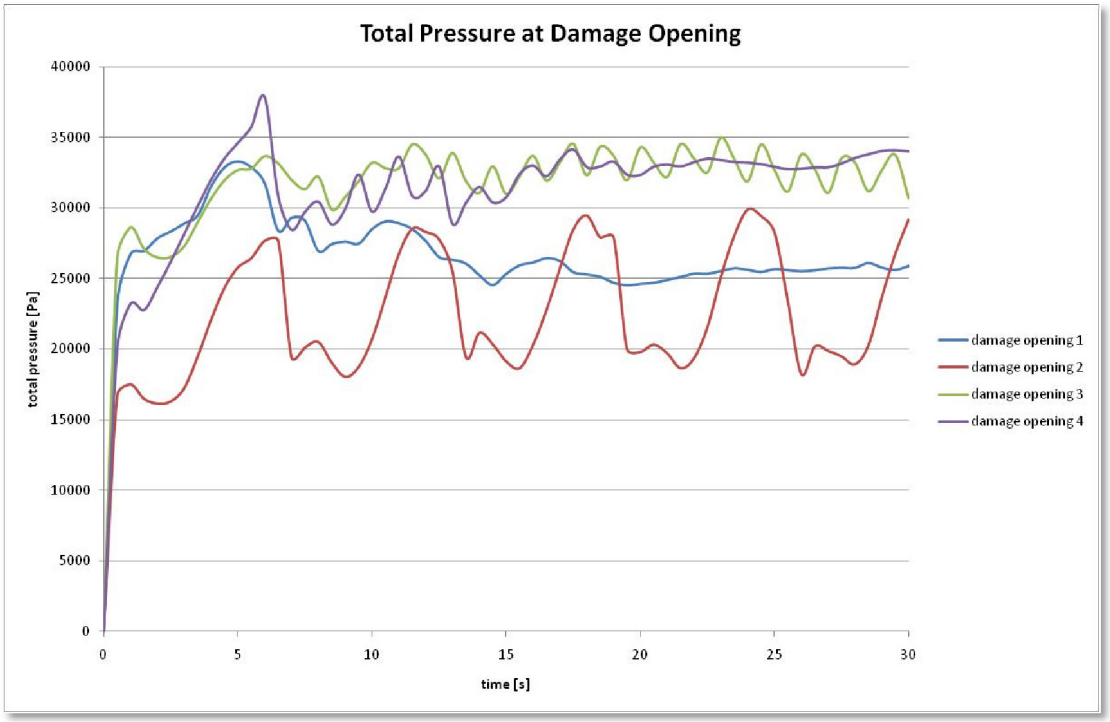

Figure 236: Total pressure at damage opening

As described in Appendix D.1 the discharge coefficient for each damage opening can be evaluated by taking the flow velocity and the pressure head at the damage opening into account, see equation (D.1.4). The discharge coefficients for each damage opening are presented in Table 22.

Damage opening	Average discharge coefficient C_d
Opening 1	0.639
Opening 2	0.755
Opening 3	0.620
Opening 4	0.636

Table 22: Average discharge coefficient for each damage opening

8.5 Summary of Results

Three different damage cases have been analysed with CFD calculations using existing software: deck 4 of M/V Estonia, a box-shaped barge and the damaged

compartment PRR02 of ITTC Ro-Ro passenger ship. The design requirements were different for each case but the principal of the calculations were the same. Main differences were that the model deck 4 of M/V Estonia was fixed disregarding any ship motion and that incompressible air was used in the simulation. A constant pressure head was adopted at the damage openings in order to provide the same floodwater inflow as has been achieved with the model tests at MARIN.

In contrary the box-shaped barge was allowed to float freely in a water tank and compressible air was used in order to treat possibly trapped air correctly.

The damaged compartment PRR02 of ITTC Ro-Ro passenger ship was also fixed disregarding any ship motion and compressible air was used to investigate scale effects and different flooding phenomena using various shapes and positions of damage openings. A pressure boundary condition was only attached to the bottom and the top of the water tank in order to keep the water level in the tank constant and in order to keep the water calm and to damp reflecting waves in the tank. The pressure at the damage opening depends on how deep the damage opening is submerged below the water surface of the tank which basically means that the pressure at the damage opening is the difference between the hydrostatic pressure in the tank and the hydrostatic pressure in the flooded compartment. The proportion of dynamic pressure is only of insignificant magnitude. This basic principle of pressure equalisation is applicable for all flooded compartments which are connected through an opening.

Regarding case study 3, the damaged compartment of an ITTC Ro-Ro passenger ship, a pressure boundary condition, in the same manner as in case study 1, is attached to the water reservoir that is continuously refilled with floodwater. Reason for applying a constant pressure head in the CFD model is to validate with model tests where the model was fixed and horizontally levelled out and the water surface in the tank was kept constant so that a constant pressure at the damage opening was allowed. The principle of pressure equalisation is also applicable in this case study.

The results of case study 1, M/V Estonia, and case study 2, the box-shaped barge, were compared and validated with model tests or, in regard to case study 1, additionally compared with another numerical simulation method. Case study 3, namely the damaged compartment PRR02, could only be validated for the simple model as all other data which were computed for demonstration purpose were not measured during the model tests.

The measured water height in case study 1 and 2 as well as the measured water volume in case study 3 was a good indicator for the accuracy of the calculations. In all cases the agreement of the results, especially local effects, was very good even in compartments that were flooded last due to their great distance to the damage opening within the labyrinth of compartments. It could be noticed that flooding always slowed down when the damage opening was fully submerged. Also, when the floodwater reached the upper edge of an internal opening the flooding process decelerated significantly. Reason for that is explained in chapter 8.2.6.2 which focused pressure and counter pressure effects on damage openings and openings in general.

MARIN, furthermore, measured the total amount of water which flowed into the compartments of the deck. Along with the measured water height this gave an indication of the quality of the measurement results, their consistency and repeatability, but moreover provided an additional set of data for validation of the numerical simulations. Generally, the correspondence between measured and calculated volume fraction is very good though the mesh is relatively coarse compared to case study 2. Therefore the selected time step size was larger than in case study 2 and the computation time of about two months for a simulation time of 900 seconds was comparatively short.

The calculated floating position of the box-shaped barge corresponds remarkably well with the measured values of the model tests. This accuracy is a result of the use of a very fine mesh at the moving boundaries and the choice of a small time step. On the other hand the computational cost for the simulation of 400 seconds

was so incredibly high that it took about four and a half months to complete the simulation.

The CFD simulation damaged compartment PRR02 of ITTC Ro-Ro passenger ship had a very low computational cost compared to the original calculations of *Cho et al. (2005)*. Due to a reduction of the number of cells by using a new approach the average computation cost could be reduced by 800% – 2400% compared to *Cho's* simulation model. Additionally, scale effects could be observed in case study 3 which result from viscosity effects of the fluid when it passes through an opening. It can also be seen that the size and the position of the damage openings have an influence on the flooding characteristics which is mainly affected by the development of air pockets and fluid viscosity effects due to large or small cross-sectional areas of the damage openings.

In the following chapters the final discussions of results and the conclusions obtained from this thesis will be given.

9 Discussion

9.1 General Remarks

The purpose of this research was to produce a reliable and accurate model to evaluate the influence of non-linear phenomena occurring during the progressive flooding of a ship. This could be achieved by analysing physical data of local flow characteristics with CFD in a detailed form

Traditionally, alternative numerical calculation methods are based on simplifications and assumptions. Such simplifications can either be treating the floodwater as lump mass whereas the water surface always remains horizontal, see *Jasionowski (2001)*, or the implementation of the widely used hydraulic model for the calculation of the flow velocities applying a pressure-correction technique, see *Ruponen (2007)*. Moreover, a drawback of above methods is that the discharge coefficients have to be estimated for each opening which has to be done by model tests. For CFD simulations an estimation of discharge coefficients is not necessary. Another drawback of hydraulic models is that the flooding is underestimated in the phase of transient flooding. On the opposite it could be verified that presented CFD simulation reproduces both flooding phases, the transient and the progressive phase, very well.

The above approaches give sufficiently accurate results in a very short computing time but depend upon some limiting assumptions and simplifications which is not the case with presented RANSE computations that are capable of providing more information on the flooding process at any desired location within the computing domain. More information has to be understood in terms of various kinds of physical data and local flow characteristics that can be collected dependent on the algorithms and methods that have been used. A short selection of data that can be collected is given in the Table 23 below. Data can be extracted from single points, surfaces and volumes within the computational domain which is an advantage over other numerical methods that do not use finite volume methods. This variety of

data, especially when it comes to local flow characteristics is also very difficult to obtain with model tests.

	Data	Location
Flux	Mass flow rate	Any boundary, any point on a boundary
	Total heat transfer rate	Any boundary, any point on a boundary
Force	Forces / Moments	Any wall, any point on a wall
Surface integrals / surface average volume integrals / volume average	Static / dynamic / total pressure	Any surface, any point on a surface Any volume, any point in a volume
	Density	Any surface, any point on a surface Any volume, any point in a volume
	Velocity, Reynolds number	Any surface, any point on a surface Any volume, any point in a volume
	Temperature, enthalpy, entropy, energy	Any surface, any point on a surface Any volume, any point in a volume
	Turbulent kinetic energy, turbulent intensity, turbulent viscosity, Prandtl number	Any surface, any point on a surface Any volume, any point in a volume
	Volume fraction	Any surface, any point on a surface Any volume, any point in a volume
	Skin friction coefficient, wall shear stress	Any surface, any point on a surface Any volume, any point in a volume

Table 23: Obtainable output of CFD calculation

A critical point of presented CFD method might be its high load of computing power and long simulation time. Compared to other numerical methods a finite volume

method is always more expensive in computing time due to the amount of cells being used and due to the iterative algorithms applied. On the other hand it could be demonstrated that by using a new approach the average computation cost could be reduced by 800% – 2400% compared to other CFD simulation methods, see case study 3 chapter 8.4.

The numerical model applied satisfies the requirement for detailed description of progressive flooding. It is also demonstrated that it is possible to achieve reasonably good accuracy in the quasi-static prediction of ship motions in calm water of a damaged vessel subject to progressive flooding without compromising on generality in terms of the use of commercial software.

The problems encountered in the development and validations of the model presented were manifold and complex, and occasionally their solution was not entirely satisfying. By stepwise optimisation of the geometrical model and by adaptive application of numerical methods the results could be improved.

Considering the great complexity of the task undertaken, this research has been successful. The study for slow progressive flooding confirmed that the approach applied can deal with a large number of flooded rooms and openings, including rooms with complex geometry.

Which difficulties have been met and how they were solved will be discussed in the next few sections of this chapter. Furthermore contributions and innovations of this study will be discussed as well as recommendations for future research work.

9.2 Case Studies

Three numerical case studies testing the quantitative capabilities of the developed method and their corresponding experimental studies to assess the time-to-flood and the stability of damaged ships constitute the validation studies.

9.2.1 Numerical Studies

Using previously tested available ship data the numerical model was investigated to provide a quantitative level of agreement in the TTF and all associated effects such as water height, quasi-static ship motions in calm water etc. The model data is of three different ships which do not only differ in type but also in the requirement of the set-up of the numerical calculation and their corresponding model tests. The first case concerns the accommodation deck 4 of the Ro-Ro ferry M/V Estonia which will be referred to as the static case because the deck is fixed and levelled out horizontally without regarding any ship motion and filled up with water through the damage openings by means of a water reservoir. Data from model tests was provided by MARIN.

The second case considers a layout of compartments in a box-shaped barge which will be referred to as the dynamic case because the vessel is allowed to float freely in calm water and the compartments are filled up with water coming from the same water tank the vessel is floating in. Data from model tests was provided from HUT Ship Laboratory.

The third case concerns a damaged compartment of an ITTC Ro-Ro passenger ship which is also referred to as a static case because the compartment is fixed and levelled out horizontally without regarding any ship motion. Similar to case study 1 the compartment is filled up with water through various different damage opening shapes by means of a water reservoir.

Overall the data obtained by the CFD calculations correlates very well with data from the model tests. Especially water heights are predicted very well in all cases though there are some insignificant inaccuracies in the water height towards the end of the simulation in case study 1 when floodwater almost touches the ceiling of the compartments. These inaccuracies are caused by numerical diffusion (see chapter 6.2.3) due to the design of a relatively coarse mesh and the use of a large time step. It is obvious that the results can be improved by mesh refinement and the choice of a smaller time step size as has been done with the case 2 and case 3.

The dynamic case, case study 2, and the second static case, case study 3, do hardly show numerical diffusion and predict water height very accurately. The drawback is that taking such actions as using a finer mesh and therefore selecting a smaller time step increase the computing time by severalfold.

Furthermore, a scale effect may not be excluded since the experiments for the static case 1 were carried out in model scale λ=20 while the corresponding numerical simulations were carried out in full scale. The existence of scale effects has been proven in case study 3 in a sensitivity analysis which also shows that these effects are dependent on the size of the damage opening; scale effect is smaller for larger openings and larger for smaller openings. Scale effects arise from viscosity effects of the fluid near the boundary layer of a damage opening. Although these effects are of minor significance this only slightly affects the comparability between the results of the experiments and the simulations since the flow through openings is a function of the area of the opening. Moreover, Reynolds numbers between different scales are in agreement which justifies a comparison of model test and CFD simulation in a different scale. In contrary, the numerical simulation and the experiments for the dynamic case were completely performed in model scale λ=10.

Above all, quasi-static ship motions in calm water have been tracked in the dynamic case study 2 showing a good agreement with the model tests. Quasi-static ship motions in calm water are generated by the dynamic mesh method in six degrees-of-freedom. Hence, the boundary on the moving mesh is modified with the spring-based update method and permanently remeshed. This method is ideal for small motions that occur during progressive flooding when roll motions are relatively small. For larger ship motions which can occur during transient flooding this method might not be ideal as a very fine mesh combined with a very small time step have to be used in order to obtain converging solutions. This requires enormously increased computing power and leads to an extended simulation time. Instead of using the dynamic mesh method motions could also be simulated by applying motion equations to the gravity vector of the fluids whereas two gravitational vectors have

to be used: one to simulate the sloshing water inside the compartments and another one to keep the surrounding water horizontal.

Since the boundaries are continuously remeshed during the simulation and due to the fact that a VOF algorithm is used which treats two different fluids it happens very often that a newly created cell “catches” some fluid from its neighbour cells. In case of flooding this can be either air or water or both. Figure 127 shows this effect clearly on the transverse bulkhead that is dividing the forward section from the aft section of the compartment. Unfortunately this effect cannot be avoided; it can only be minimised by using even smaller cell size. The amount of additional water or air in these cells is so small that the final results are not influenced at all.

During the simulation of the dynamic case 2 the ship hull was allowed to move in six DOF. When the model tests were performed it was paid attention to roll, heave and pitch motions; any occurrence of other motion was suppressed by attaching soft rubber strings to the model that were connected to the carriage. In the numerical simulation the model was not kept in position and slightly started to drift away from its initial position. As long as the water/air domain is large enough drifting does not cause any problem. When the domain is smaller or the drifting motion is large it could happen that the model comes too close to the wall boundaries of the domain which will result in the appearance of undamped wave systems that excite ship motions additionally. Reason for that is that the originally large cells at the wall boundaries of the water tank will be refined due to the dynamic mesh algorithm and therefore lose damping capabilities. So the solution to this issue is either to ensure that the domain is large enough or to neglect drifting motions.

It was observed that the use of a laminar model generally overestimates flow velocities of the fluid within the flooded compartments during the transient flooding phase. The k-ε turbulence model predicts flow velocities much better and gives very accurate values of water heights and associated floodwater volumes. However, the standard k-ε model is known to be slightly over-diffusive in certain situations. Additionally the standard k-ε model assumes that the flow is fully

turbulent which might not always be the case during progressive flooding. Though the results are satisfying it poses the question if an alternative turbulence model such as the k-ω turbulence model would give even better results. Like k-ε turbulence models, k-ω turbulence models are also two-equation models, and thus require about the same computational effort. Based on the Wilcox k-ω model it features a good handling for low Reynolds number effects, compressibility and shear flow spreading.

The implementation of all these physical models and the use of an appropriate mesh slow down the calculations extremely. Basically, most of the computing power is spent on the solution of the two-equation turbulence model and the dynamic mesh algorithm. On a numerical basis it is difficult to optimise the simulation time though there are solutions to be offered. The calculations in both validation cases were carried out with a constant time step size. Introduction of an adaptive time step could reduce calculation time. A small time step would be applied for large ship motions and high flow velocities and a larger time step would be set for small ship motions and lower flow velocities according to the estimate truncation error. An estimation of the truncation error can be obtained by using a predictor-corrector type of algorithm in association with the time integration scheme, *Fluent (2006)*.

A sensitivity analysis has been undertaken with case study 3, the damaged compartment of an ITTC Ro-Ro passenger ship. The influence of different damage opening shapes and positions on the flooding characteristics has been analysed and results can be found in Table 24. Generally, the magnitude of the area of a damage opening and the height of a damage opening has a significant influence on the flooding characteristics. Details of the sensitivity analysis can be found in chapters 8.4.6.2, 8.4.6.4, 8.4.6.5 and 8.4.6.6.

Factor	Change in Parameter	Effect in transient flooding phase	Effect in progressive flooding phase
Scale	Scale changed from 1:1 to 1:48.57 to 1:97.14	minor	minor
Damage size	Damage size changed from 8.244mx9.025m to 8.244mx4.5125m to 4.122mx9.025m to 2x2.061mx9.025m	significant	minor
Damage position horizontally	Damage position changed from centre of middle bulkhead to +/- 3.0915 m from centre middle bulkhead	minor	minor
Damage position vertically	Vertical extension of damage opening changed from 9.025 m to 4.5125 m, geometric centre in vertical axis kept constant	minor	significant

Table 24: Sensitivity analysis, changing parameters

Due to the fact that both complex cases, the static case 1 and the dynamic case 2, were time-consuming in mesh design and computing a solution, it can be concluded that this numerical model is not ideal to calculate many different cases yet. It should rather be understood as a more accurate and true-to-life simulation tool that verifies selected flooding cases on the basis of other faster numerical tools such as hydraulic models. Hydraulic models cannot reproduce the flooding process in detail, cannot show local flow characteristics and especially underestimate the flooding during transient heeling. Besides, the discharge coefficients have to be estimated for each opening. But, as mentioned before, they are very fast, give results with a satisfying accuracy and can evaluate thousands of cases in a fraction of the computing time of the presented model. In a couple of years it can be expected that computing power will have reached the level to carry out RANSE

calculations in an acceptable time so that many different flooding cases can be investigated.

9.2.2 Experimental Studies

Model tests have been carried out in different facilities with different modelling requirements but technicians and engineers faced the same difficulties in setting up the test arrangement in order to provide accurate data.

One of the main issues was the calibration of the water height sensors because the conductivity of the medium changes rapidly from dry to wet. Since the sensors are usually calibrated in wet conditions they are very sensitive in the beginning of the flooding when the surface of the sensors is not wetted. This influenced the measurement results slightly by underestimating the water height.

Another issue is that the sensors consist of two parallel electric wires with a certain mutual distance. When the surface is a wild mixture of water and air clashing against the sensors the accuracy of the results may be questionable. Generally, the use of water level sensors is well approved and traditionally used to measure wave heights during sea keeping tests. Alternatively, the water height could also be measured with ultrasonic probes or laser sensors that scan the remaining distance to the water surface. Unfortunately, ultrasonic probes are inaccurate due to their wide scanning range when waves are very steep so their use for transient flooding is very limited while for progressive flooding characterised by wavelets an application of these probes is possible. Laser sensors, on the other hand, are expensive and difficult to operate.

In the static validation case 1 the model was slightly leaking through small chinks in the conjunction between top plate and side walls of the compartment. These chinks occurred when larger rooms were completely filled up with water and the top plate started to flex due to the high pressure of the water. This also affected some probes that were not fully submerged because since they were mounted on the flexing top

plate they were slightly lifted and therefore measured lower water heights. The errors caused by the water loss and the flexing top plate were so small that it could be confidently neglected.

Additionally to water height measurements it was tried to measure flow velocity using force probes. Since there is no simple measurement device existent for such purpose this method should at least give a rough estimation of the flow velocity through some selected doors. The measured force was converted to water flow velocity averaged over the water depth by applying the dynamic drag equation for fluids. During the flooding these probes were susceptible to vibrations particularly in the transient flooding phase. Unfortunately, the quality of data in terms of accuracy and repeatability did not allow a comparison with computed data.

The dynamic case 2 showed the occurrence of air compression in some rooms. In the charts demonstrating the water height the curve noticeably flattens. It was omitted to measure the air pressure in these rooms which would have given valuable information about the flooding process and additional data for validation.

In the static validation case 3 the damage inlet is opened by pulling a slide which caused oscillating force and moment measurands in natural frequency. To avoid this unwanted effect data were averaged. Unlike validation case 1 and 2 the water height in the compartment was determined by measurement of the force in z-direction which naturally can only give the floodwater magnitude of the entire compartment. Therefore water level heights of single rooms could not be determined.

9.3 Main Contributions of Present Research

The main goal of this thesis was to design a setup for a valid numerical model to simulate the flooding process and in particular to investigate local flow characteristics during transient and progressive flooding. Based on the RANSE method for viscous effects such a model is presented accounting for turbulent

flows, compressible air and quasi-static ship motions in calm water in six degrees-of-freedom.

The secondary goal was to produce numerical results that are in agreement with experimental results on quantitative level. Some inadequacies of current numerical programs and ongoing research activities around the globe led to the pursuit of this goal.

By combination of existing numerical models and application of a consistent design and simulation strategy these goals could be achieved. All this was implemented into a commercial CFD solver, which makes this method realistic and available for many researchers and engineers without loss of generality. A special focus should be placed on the employment of the dynamic mesh method to quasi statically simulate ship motions in calm water in six degrees-of-freedom. To the best of the author's knowledge, in literature this method has not been found to be applied to internal flooding simulations for damaged ships and therefore constitutes a novelty in this research work.

Additionally, the k-ε turbulence model has been employed and tested. Employment of this turbulence model and comparison to the laminar model gave the important finding that a laminar model would overestimate velocities in the transient phase of the flooding and therefore would flood the compartment faster. In the same tenor it can be concluded that it does not make a significant difference to use either a laminar or turbulent model in the progressive phase of flooding as the differences between the models were marginal. This finding, prudently applied, can save additional computing resources and speed up the simulation time.

Another important point is that local flow characteristics can be determined at any location in the simulation domain. This is a clear advantage over physical model tests and also other numerical simulation methods employing hydraulic models.

Comparison of the numerical simulations with experimental simulations showed an excellent agreement on a qualitative and quantitative level. The results of the

numerical simulation lie in the range of the measurement error and therefore could theoretically replace experimental simulations. This statement should be taken with a pinch of salt and certainly validation with experimental results is still important. What it shows is the future trend that numerical simulations will be carried out predominantly while physical experiments will be reduced to a minimum which, on the other hand, increases effort and costs for physical experiments.

9.4 Present Approach

In order to identify dangerous situations leading to capsize or sink, a valid numerical model is a necessity as stated before. Therefore a finite volume method capable of dealing with free surface problems that can handle compressible and incompressible fluids and that can simulate motion in six degrees-of-freedom in space has been applied to three representative flooding scenarios. Basis for the calculations was the commercial numerical solver FLUENT.

The implementation of quasi-static ship motions in calm water was performed by the use of a six DOF solver. Various approaches were tried before it was decided to focus on the dynamic mesh method which certainly does not only have advantages but appeared to be ideal for the use of progressive flooding. The dynamic mesh model can be used in all flow cases where the shape of the domain, respectively the boundaries, is changing with time. These changes can be unspecified motions where the linear and angular velocities of the centre of gravity of a solid body are calculated based on the force balance on the body. This body can then move in six-degrees-of-freedom. Each time step the volume mesh is updated with the new position of the boundaries. In principle if enough computing power is available this method can also be adopted to true dynamic ship motions as only the force balance on the body is taken into account. However, it is a totally integrated approach and in contrary to coupled methods there is no need to exchange data which makes it extremely user-friendly.

Another issue was how to deal with trapped air and if it made a difference when using compressible air or incompressible air. Therefore air was treated as incompressible fluid with a constant density in validation case 1 and on the other hand treated as compressible fluid following the ideal gas law in validation case 2 and validation case 3.

In order to account for high Reynolds number flows a turbulence model was integrated. For a correct application of a turbulence model the mesh had to be of a certain quality in the region where turbulent flows were expected. The meaningfulness of the application of a turbulence model and its advantages and disadvantages will be discussed in chapter 9.2.1.

In the applied numerical model all methods have been introduced that provide data for validation with current state-of-the-art model tests. The author believes that the presented numerical model has room for improvement and additional features that occasionally cannot even be validated by model tests since it is sometimes difficult to measure certain data in experimental conditions. That is exactly what will be discussed in chapter 9.5.

9.5 Recommendations for Future Research Work

Several aspects were noticed during the course of this study that can extend the features of the numerical model and provide more value to the calculations.

A feature that definitely adds more value to the model is the integration of collapsing structures. In the presented CFD models it was assumed that either structures as doors and walls were indestructible or the existence of doors and walls was neglected to allow a free flow. There are two possible ways to integrate this feature: the use of sliding meshes or the replacement of the boundary conditions. The principle for both methods is the same; when the force on the structure exceeds a certain limit the wall boundary slides away or simply changes its

boundary condition from a wall boundary to an interior boundary. Latter method can lead to diverging solutions in extreme cases with high flow velocity.

Another feature that might be of interest especially in flooding simulations with Ro-Ro ferries is cargo shifting. When a Ro-Ro ferry encounters extreme motions the impact on the behaviour of the vessel by shifting vehicles on the car deck can be that enormous that the additional momentum as well as by the reduction of *GZ* could seriously affect the ship's stability. Numerically this could be handled by sliding meshes which represent the shifting cargo. For cargo that consists of smaller particles like coal or gravel this method might not be ideal as not every single particle can be modelled as a sliding mesh. It is better to treat this kind of cargo as a fluid with a very high viscosity.

So far presented CFD simulations have been carried out assuming that water surrounding the damaged vessel is calm. A more realistic environment could be created by bringing in the effect of sea state; this has already been implemented in various CFD codes but has not been done for damaged ships with internal flooding in combination with dynamic meshing. Waves could be generated by installing a movable flap on one side of the water domain that excites the fluid in the tank. Another approach to generate waves could be to move the gravity vector of the fluid in the water tank and the fluid in the air domain above. To avoid wave reflections on the side walls of the domain waves should be damped at the boundary. This can happen by applying a coarse mesh and a damping function at the wall boundary or by using open boundaries so that the wave simply runs out. As far as pressure boundary conditions are concerned there is no need to attach such a boundary condition at the bottom of the water tank as this would only damp the wavy water surface. Moreover, the water tank does not have to be refilled as the ship model is free to float while flooded in the tank. A pressure boundary above the water tank on top of the air domain allowing air to escape and to flow back into the domain, see Figure 41, is should be adopted in order not to influence wave formation by local air pressure variation; thereby the air pressure above the water tank can be kept at a constant level of atmospheric pressure.

Latter add-on to the simulation is problematic because it is difficult to obtain experimental validation data. Furthermore, a validation only makes sense if waves can be reproduced in a mutual way, in the numerical simulation and in the experimental simulation. This is easier to do for a regular wave pattern than for an irregular wave pattern.

In the same breath the influence of wind excitation should be mentioned since wind has a significant effect on vessels such as passenger ships with large lateral side area. This feature is easy to implement as it is only additional wind forces have to be added in the motion solver.

10 Conclusion

It is believed that the presented method has achieved the aim of the research work on a very sophisticated level. A variety of different modelling techniques and methods have been applied to accomplish the intention of creating a true-to-detail flooding simulation with a state-of-the-art CFD tool. Attention has also been turned to the applicability and universality which makes the method adaptive in a broad field.

To put it in a nutshell following concluding statements can be made:

- ✓ A horizontally fixed flooding model that corresponds very well to the small ship motions during the quasi-static phase of progressive flooding has been designed. It is optimised to allow a balance between computation efficiency and accuracy.
- ✓ A flooding model in calm water, freely moving and non-propelled has been designed that allows simulating both the highly dynamic phase during transient flooding and the almost quasi-static phase during progressive flooding.
- ✓ All physical phenomena such as free-surface effects, compressible air, turbulent flows and quasi-static ship motions in calm water in six degrees-of-freedom have been taken into consideration.
- ✓ It has been proven that the dynamic mesh method is capable of dealing with quasi-static ship motions in calm water and that it can be combined with numerical techniques such as the volume of fluid method and the adoption of compressible fluids.
- ✓ The developed numerical method proved to be effective when applied in real maritime casualty investigations, the loss of M/V Estonia. It also showed very good agreement with a fictitious damage case of a box-shaped barge that was also used as a validation model for ITTC.

- ✓ The case study for a damaged compartment of an ITTC Ro-Ro passenger ship demonstrated the existence of scale effects and showed good agreement with model tests.
- ✓ It has been verified that any kind of physical data at any desired location within the computing time can be collected from presented CFD model which makes it an ideal tool to demonstrate local flow characteristics.
- ✓ On basis of the application of the presented method to above mentioned case studies, valuable information about the flooding process could be collected.

References

Acikgoz, N., and Bottasso, C.L., 2007, *"A unified approach to the deformation of simplicial and non-simplicial meshes in two and three dimensions with guaranteed validity"*, Computers & Structures, Vol.85, 11-14: 2007. pp. 944-954.

AkyildIz, H., and Erdem Ünal, N., 2006, *"Sloshing in a three-dimensional rectangular tank: Numerical simulation and experimental validation"*, Ocean Engineering, Vol.33, 16: 2006. pp. 2135-2149.

Anderson, W., and Bonhus, D.L., 1994, *"An Implicit Upwind Algorithm for Computing Turbulent Flows on Unstructured Grids"*, Computers & Fluids, Vol.23: 1994. pp. 1-21.

Ataie-Ashtiani, B., Shobeyri, G., and Farhadi, L., 2007, *"Modified incompressible SPH method for simulating free surface problems"*, Fluid Dynamics Research, Vol.In Press, Corrected Proof: 2007.

Barth, T.J., and Jespersen, D., 1989, "*The Design and Application of Upwind Schemes on Unstructured Meshes"*, Technical Report AIAA-89-0366, Reno, Nevada.

Beck, U., 1986, *"Risk Society: Towards a New Modernity "*, Sage Publications: 1986.

Belenky, L., Weems, M., Liut, D., and Shin, S., 2003, *"Nonlinear Roll with Water-On-Deck: Numerical Approach"*, Proceedings of the 8th International Conference on Stability of Ships and Ocean Vehicles, Madrid, Spain, pp. 59-80.

Blok, J.J., and Luisman, H., 2008, "*Research Study of Sinking Sequence of MV Estonia - Model Experiments on MV Estonia: Flooding Tests of Superstructure Deck No. 4 - Final Report"*, Report No. 20374-1-RD, MARIN, Wageningen, The Netherlands, p. 126.

Brackbill, J.U., Kothe, D.B., and Zemach, C., 1992, *"A continuum method for modeling surface tension"*, Journal of Computational Physics, Vol.100, 2: 1992. pp. 335-354.

Caretto, L.S., Gosman, A.D., Patankar, S.V., and Spalding, D.B., 1972, *"Two Calculation Procedures for Steady, Three-Dimensional Flows with Recirculation"*, Proc. 3rd Int. Conf. Numer. Methods Fluid Dyn., Paris.

Chen, H.-C., and Yu, K., 2008, *"CFD simulations of wave-current-body interactions including greenwater and wet deck slamming"*, Computers & Fluids, Vol.In Press, Corrected Proof: 2008.

Chicken, J.C., and Posner, T., 1998, *"The Philosophy of Risk "*, Thomas Telford

Cho, S.K., Hong, S.Y., Kim, Y.H., and Lee, K.J., 2005, *"Investigation of Dynamic Characteristics of the Flooding Water of the Damaged Compartment of an ITTC RORO Passenger"*, Proceedings of 8th International Ship Stability Workshop: 2005. pp. session 4.1.

Chorin, A.J., 1968, *"Numerical Solution of Navier-Stokes Equations"*, Mathematics of Computation, Vol.22: 1968. pp. 745-762.

Courant, R., Friedrichs, K., and Lewy, H., 1928, *"Über die partiellen Differenzengleichungen der mathematischen Physik"*, *Mathematische Annalen*, Vol.100, No. 1: 1928. pp. 32-74.

Cuthill, E., and McKee, J., 1969, *"Reducing the Bandwidth of Sparse Symmetric Matrices"*, Proc. 24th Nat. Conf., 1122 Ave. of the Americas, New York, N.Y., p. 69.

de Goes, F., Goldenstein, S., and Velho, L., 2008, *"A simple and flexible framework to adapt dynamic meshes"*, Computers & Graphics, Vol.32, 2: 2008. pp. 141-148.

Fluent, 2006, *"Fluent 6.3 User's Guid"*, Fluent Inc., Lebanon.

Gao, Q., Kara, F., Shigunov, V., and Vassalos, D., 2005, "*A Numerical Study on Damaged Ship Hydrodynamics"*, The Ship Stability Research Center, Universities of Glasgow and Strathclyde, Glasgow, United Kingdom.

Gingold, R.A., and Monaghan, J.J., 1977, *"Smoothed particle hydrodynamics - Theory and application to non-spherical stars"*, Mon. Not. Roy. Astron. Soc., Vol.181: 1977. pp. 375-389.

Godderidge, B., Turnock, S., Tan, M., and Earl, C., 2008, *"An investigation of multiphase CFD modelling of a lateral sloshing tank"*, Computers & Fluids, Vol.In Press, Corrected Proof: 2008.

González, V., Talens, M., Riola, J.M., Valle, J., Queseda, T., and Espín, M., 2003, *"Numerical Prediction of the Behaviour of a Ro-Ro Ship after a Hull Side Damage"*, Proceedings of the 8th International Conference on Stability of Ships and Ocean Vehicles, Madrid, Spain, pp. 215-227.

Greene, A., 2000, "*A Process Approach to Project Risk Management*", Loughborough.

Hazards Forum, 1995, *"Safety-related system, Guidance for engineers"*.

Henkes, R.A.W.M., van der Flugt, F.F., and Hoogendoorn, C.J., 1991, *"Natural Convection Flow in a Square Cavity Calculated with Low-Reynolds-Number Turbulence Models"*, Int. J. Heat Mass Transfer, Vol.34: 1991. pp. 1543-1557.

Hirt, C.W., and Nichols, B.D., 1981, *"Volume of fluid (VOF) method for the dynamics of free boundaries"*, Journal of Computational Physics, Vol.39, 1: 1981. pp. 201-225.

Holmes, D.G., and Connell, S.D., 1989, *"Solution of the 2D Navier-Stokes Equations on Unstructured Adaptive Grids"*, AIAA 9th Computational Fluid Dynamics Conference.

IMO Resolution A.266 (VIII) 1973, *"Recommendation and a Standard Method for Establishing Compliance with the Requirements for Cross-Flooding Arrangements in Passenger Ships"*, adopted 20. November 2003.

IMO SLF46/INF.3 2003, *"Large Passenger Ship Safety: Time-to-Flood Simulations for a Large Passenger Ship - Initial Study"*, MARIN Report No. 17870-1-CPS.

IMO SLF47/INF.6 2004, *"Large Passenger Ship Safety: Survivability Investigation of Large Passenger Ships"*, submitted by Finland, 11. June 2004.

Issa, R.I., 1986, *"Solution of Implicitly Discretized Fluid Flow Equations by Operator-Splitting"*, J. Comp. Phys., Vol.62: 1986. pp. 40-65.

ITTC, 2005, *"The Specialist Committee on Stability in Waves. Final Report and Recommendations to the 24th ITTC"*, Proceedings of the 24th ITTC Conference, Edinburgh, United Kingdom, pp. 369-408.

Jasionowski, A., 2001, *"An Integrated Approach to Damage Ship Survivability Assessment"*, PhD Thesis, Ship Stability Research Centre, Universities of Glasgow and Strathclyde, Glasgow, United Kingdom.

Jasionowski, A., and Vassalos, D., 2001, *"Numerical Modelling of Damage Ship Stability in Waves"*, Proceedings of the 5th International Workshop on Stability and Operational Safety of Ships, Trieste, Italy, September 2001, p. 9.

Jones, D.A., and Clarke, D.B., 2003, *"An Evaluation of the FIDAP Computational Fluid Dynamics Code for the Calculation of Hydrodynamic Forces on Underwater Platforms "*, DSTO Platforms Sciences Laboratory, Australia: 2003.

Journée, J.M.J., Vermeer, H., and Vredeveldt, A.W., 1997, *"Systematic Model Experiments of Flooding of Two Ro-Ro Vessels"*, Proceedings of the 6th International Conference on Stability of Ships and Ocean Vehicles, Varna, Bulgaria, 22-27. September, 1997.

Katayama, T., and Ikeda, Y., 2005, *"An Experimental Study of Fundamental Characteristics of Inflow Velocity from Damaged Opening"*, Proceedings of 8th International Ship Stability Workshop, Istanbul Technical University, Turkey.

Kleefsman, K.M.T., Fekken, G., Veldman, A.E.P., Iwanowski, B., and Buchner, B., 2005, *"A Volume-of-Fluid based simulation method for wave impact problems"*, Journal of Computational Physics, Vol.206, 1: 2005. pp. 363-393.

Korkut, E., Atlar, M., and Incecik, A., 2004, *"An experimental study of motion behaviour with an intact and damaged Ro-Ro ship model"*, Ocean Engineering, Vol.31, 3-4: 2004. pp. 483-512.

Korkut, E., Atlar, M., and Incecik, A., 2005, *"An experimental study of global loads acting on an intact and damaged Ro-Ro ship model"*, Ocean Engineering, Vol.32, 11-12: 2005. pp. 1370-1403.

Koshizuka, S., and Oka, Y., 1996, *"Moving particle semi-implicit method for fragmentation of incompressible fluid"*, Nuclear Science and Engineering, Vol.123: 1996. pp. 421–434, 1996.

Launder, B.E., and Spalding, D.B., 1972, *"Lectures in Mathematical Models of Turbulence"*, Academic Press, London, England.

Lee, D., Hong, S.Y., and Lee, G.J., 2007, *"Theoretical and experimental study on dynamic behavior of a damaged ship in waves"*, Ocean Engineering, Vol.34, 1: 2007. pp. 21-31.

Leonard, B.P., 1979, *"A Stable and Accurate Convective Modelling Procedure Based on Quadratic Upstream Interpolation"*, Computer Methods in Applied Mechanics and Engineering, Vol.19: 1979. pp. 59-98.

Leonard, B.P., 1991, *"The ULTIMATE Conservative Difference Scheme Applied to Unsteady One-Dimensional Advection"*, Computer Methods in Applied Mechanics and Engineering, Vol.88: 1991. pp. 17-74.

Letizia, L., 1996, *"Damage Survivability of Passenger Ships in a Seaway"*, PhD Thesis, The Ship Stability Research Centre, Universities of Glasgow and Strathclyde, Glasgow, United Kingdom.

Liao, G., and Xue, J., 2006, *"Moving meshes by the deformation method"*, Journal of Computational and Applied Mathematics, Vol.195, 1-2: 2006. pp. 83-92.

Löhner, R., Yang, C., and Oñate, E., 2006, *"On the simulation of flows with violent free surface motion"*, Computer Methods in Applied Mechanics and Engineering, Vol.195, 41-43: 2006. pp. 5597-5620.

McBride, D., Croft, T.N., and Cross, M., 2008, *"A coupled finite volume method for the computational modelling of mould filling in very complex geometries"*, Computers & Fluids, Vol.37, 2: 2008. pp. 170-180.

Mustonen, P., 1998, *"Simulation Model of a Ship's Flooding Mechanism and Rolling Motion"*, Master's Thesis, Helsinki University of Technology, (in Finnish), Helsinki.

Nabavi, Y., Calisal, S.M., Akinturk, A., and Klaptocz, V., 2006, *"A Computational Investigation of the Three Dimensional Geometric Parameters' Effects on the Discharge Rate of a Ship Opening"*, Proceedings of the 9th International Conference on Stability of Ships and Ocean Vehicles, Rio de Janeiro, Brazil, 25-29 September.

Nichols, B.D., and Hirt, C.W., 1975, "*Methods for Calculating Multi-Dimensional, Transient Free Surface Flows Past Bodies*", Technical Report LA-UR-75-1932, Los Alamos National Laboratory.

Nieland, H., 1998, *"New Numerical Methods for CFD applied to Ship Hull Design"*, ERCIM News No.33 - April 1998: 1998.

Noh, W.F., and Woodward, P.R., 1976, *"SLIC (Simple Line Interface Methods)"*, In: Vande Voore, A.I., and Zandenberg, P.J. eds., Lecture Notes in Physics, Vol.59, pp. 330-340.

Palazzi, L., and de Kat, J.O., 2004, *"Model Experiments and Simulations of a Damaged Ship With Air Flow Taken Into Account"*, Marine Technology, Vol.41, 1: 2004. pp. 38-44.

Papanikolaou, A., 2003, *"Entwurf und Sicherheit von Ro-Ro Fähren"*, Handbuch der Werften 2003.

Papanikolaou, A., 2007, *"Review of Damage Stability of Ships: Recent Developments and Trends"*, Proceedings 10th International Symposium on Practical Design of Ships and Other Floating Structures (PRADS) 2007, Houston, October 2007.

Papanikolaou, A., 2009, *"Risk-Based Ship Design"*, Springer Verlag GmbH.

Papanikolaou, A., and Eliopoulou, E., 2004, *"Impact of the New Damage Stability Regulations on Ship Design"*, Procedures of the 2nd International Maritime Conference on Design for Safety, Sakai, Japan, 27-30 October 2004.

Papanikolaou, A., and Rusaas, S., 2002, "*Calculatory Procedures for the Determination of the Attained Subdivision Index of HARDER Sample Ships (Tasks 5.2 and 5.3)"*, HARDER Project, Deliverable 5-52-W-2002-01-2, summary included in SLF45/3/4.

Papanikolaou, A., and Spanos, D., 2002a, *"On the Modelling of Floodwater Dynamics and its Effects on Ship Motion"*, Proceedings of the 6th International Ship Stability Workshop, Webb Institute, 14-16 October 2002.

Papanikolaou, A., and Spanos, D., 2002b, *"On the Probability of Capsizing in Transient Flooding Conditions"*, Proceedings of the 2002 Stability Workshop, Webb Institute, October 13-16 2002.

Papanikolaou, A., Spanos, D., Boulougouris, E., Eliopoulou, E., and Alissafaki, E., 2003, *"Investigation in to the Sinking of the Ro-Ro Passenger Ferry Express Samina"*, International Conference on the Stability of Ships and Ocean Vehicles, Madrid, Spain.

Papanikolaou, A., Zaraphonitis, G., Spanos, D., Boulougouris, E., and Eliopoulou, E., 2000, *"Investigation into the Capsizing of Damaged Ro-Ro Passenger Ships in Waves"*, Proceedings of the 7th International Conference on Stability of Ships and Ocean Vehicles: 2000. pp. 351-362.

Pittaluga, C., and Giannini, M., 2006, "*Pressure Losses Estimation for Structural Double Bottom by CFD Technique"*, CETENA Technical Report, Genova, Italy.

Rhie, C.M., and Chow, W.L., 1983, *"Numerical Study of the Turbulent Flow Past an Airfoil with Trainling Edge Separation"*, AIAA Journal, Vol.21 (11): 1983. pp. 1525-1532.

Rider, W.J., and Kothe, D.B., 1998, *"Reconstructing Volume Tracking"*, J. Comp. Phys., Vol.141: 1998. pp. 112-152.

Rudman, M., 1997, *"Volume Tracking Methods for Interfacial Flow Calculations"*, Int. J. Num. Meth. Fl., Vol.24: 1997. pp. 671-691.

Ruponen, P., 2006, "*Model Tests for the Progressive Flooding of a Box-Shaped Barge"*, Report No. M-292, Helsinki University of Technology, Helsinki, Finland, p. 88.

Ruponen, P., 2007, *"Progressive Flooding of a Damaged Passenger Ship"*, PhD Thesis, Department of Mechanical Engineering, Helsinki University of Technology, Helsinki, Finland.

Santos, A., and Soares, G., 2006, *"Study of the Dynamics of a Damaged Ro-Ro Passenger Ship"*, Proceedings of the 9th International Conference on Stability of Ships and Ocean Vehicles, Rio de Janeiro, Brazil, 25-29 September.

Santos, T.A., Winkle, I.E., and Guedes Soares, C., 2002, *"Time Domain Modelling of the Transient Asymmetric Flooding of Ro-Ro Ships"*, Ocean Engineering, Vol.29: 2002. pp. 667-688.

Siekmann, H.E., and Thamsen, P.U., 2008, *"Strömungslehre"*, Springer-Verlag GmbH.

Skaar, D., and Vassalos, D., 2006, *"The Use of a Meshless CFD Method to Model the Progressive Flooding of a Damaged Ship"*, 9th International Conference on the Stability of Ships and Ocean Vehicles: 2006. pp. 8.

Snyder, D.O., Koutsavdis, E.K., and Anttonen, J.S.R., 2003, *"Transonic store separation using unstructured cfd with dynamic meshing"*, Technical Report AIAA-2003-3913, American Institute of Aeronautics and Astronautics, 33th AIAA Fluid Dynamics Conference and Exhibit.

Söding, H., 2002, *"Flow computations for ship safety problems"*, Ocean Engineering, Vol.29, 7: 2002. pp. 721-738.

Souto-Iglesias, A., Delorme, L., Pérez-Rojas, L., and Abril-Pérez, S., 2006, *"Liquid moment amplitude assessment in sloshing type problems with smooth particle hydrodynamics"*, Ocean Engineering, Vol.33, 11-12: 2006. pp. 1462-1484.

Souto Iglesias, A., Pérez Rojas, L., and Zamora Rodríguez, R., 2004, *"Simulation of anti-roll tanks and sloshing type problems with smoothed particle hydrodynamics"*, Ocean Engineering, Vol.31, 8-9: 2004. pp. 1169-1192.

Strasser, C., 2008, "*Research Study of Sinking Sequence of M/V Estonia - CFD Simulations on M/V Estonia: Flooding Simulations of Superstructure Deck NO.4 - Final Reports of the SSPA Consortium*", Report No. VIES01-RE-003.

Strasser, C., Jasionowski, A., and Vassalos, D., 2009, *"Calculation of the Time-to-Flood of a Box-Shaped Barge by Using CFD"*, Proceedings of 10th International Ship Stability Workshop, St. Petersburg, Russia.

Sueyoshi, M., and Naito, S., 2002, *"A Numerical Study of Very Large Motion of Floating Body by Particle Method"*, Asia Pacific Workshop on Marine Hydrodynamics, pp. 146-150, 2002.

Svensen, T.E., and Vassalos, D., 1998, *"Safety of Passenger/RoRo Vessels: Lessons Learned from the North-West European R&D Project"*, Marine Technology, Vol.35, No. 4: 1998. pp. 191-199.

Tagg, R., and Tuzcu, C., 2002, *"A Performance-based Assessment of the Survuval of Damaged Ships – Final Outcome of the EU Research Project HARDER"*, Proceedings of the 6th International Ship Stability Workshop, New York, U.S.A., 13-16. October, 2002.

The_Government_of_the_Republic_of_Estonia, 1997, *"Final report on the capsizing on 28 September 1994 in the Baltic Sea of the ro-ro passenger vessel MV Estonia*, Estonia, ISBN 9515316111, 1997.

van't Veer, R., and Serra, A., 2003, *"Large Passenger Ship Safety: Time to Sink Simulations"*, Proceedings of the Passenger Ship Safety Conference, Royal Institute of Naval Architects, London, United Kingdom, 25.-26. March 2003.

van't Veer, R., 2004, "*Time to Flood (TTF) Simulations for a Large Passenger Ship – Final Study*", Report No. 19289-1-CPS published as the IMO document SLF 48/Inf.2, MARIN, Wageningen, The Netherlands, 30.

van't Veer, R., and de Kat, J.O., 2000, *"Experimental and Numerical Investigation on Progressive Flooding in Complex Compartment Geometries"*, Proceedings of the 7th International Conference on Stability of Ships and Ocean Vehicles, Lainceston, Tasmania, Australia, pp. 305-321.

Vandoormaal, J.P., and Raithby, G.D., 1984, *"Enhancements of the SIMPLE Method for Predicting Incompressible Fluid Flows"*, Numer. Heat Transfer, Vol.7: 1984. pp. 147-163.

Vassalos, D., Guarin, L., and Konovessis, D., 2006, *"Risk-Based Ship Desogn: Concept, Methodology and Framework"*, 3rd International ASRANet Colloquium, 10 - 12th July 2006, Glasgow, UK.

Vassalos, D., Jasionowski, A., and Guarin, L., 2005, *"Passenger Ship Safety – Science Paving the Way"*, Proceedings of 8th International Ship Stability Workshop, Istanbul Technical University, Turkey, p. session 4.3.

Vassalos, D., and Turan, O., 1994, *"A Realistic Approach to Assessing the Damage Survivability of Passenger Ships"*, Transactions of Society of Naval Architects and Marine Engineers, SNAME, Vol.102: 1994. pp. 367-394.

Vassalos, D., Turan, O., and Pawlowski, M., 1997, *"Dynamic Stability Assessment of Damaged Passenger/Ro-Ro Ships and Proposal of Rational Survival Criteria"*, Marine Technology, Vol.34, 4: 1997. pp. 241-266.

Vermeer, H., Vredeveldt, A.W., and Journée, J.M.J., 1994, *"Mathematical Modelling of Motions and Damaged Stability of Ro-Ro Ships in the Intermediate Stages of Flooding"*, Proceedings of the 5th International Conference on Stability of Ships and Ocean Vehicles, Melbourne, Florida, U.S.A.

Versteeg, H.K., and Malalasekera, W., 2007, *"An introduction to computational fluid dynamics : the finite volume method"*, Pearson Education Ltd., Harlow, England ; New York.

Woodburn, P., Gallagher, P., and Letizia, L., 2002, *"Fundamentals of Damage Ship Survivability"*, Transactions of Royal Institute of Naval Architects, Vol.144: 2002. pp. 143-163.

Young, D.L., 1982, *"Time-dependent multi-material flow with large fluid distortion"*, Numerical Methods for Fluids Dynamics, Academic Press, New York (1982).

Zhao, Y., and Forhad, A., 2003, *"A general method for simulation of fluid flows with moving and compliant boundaries on unstructured grids"*, Computer Methods in Applied Mechanics and Engineering, Vol.192, 39-40: 2003. pp. 4439-4466.

Appendix A

A.1 Nomenclature Deck 4 of M/V Estonia

A.1.1 Deck Layout

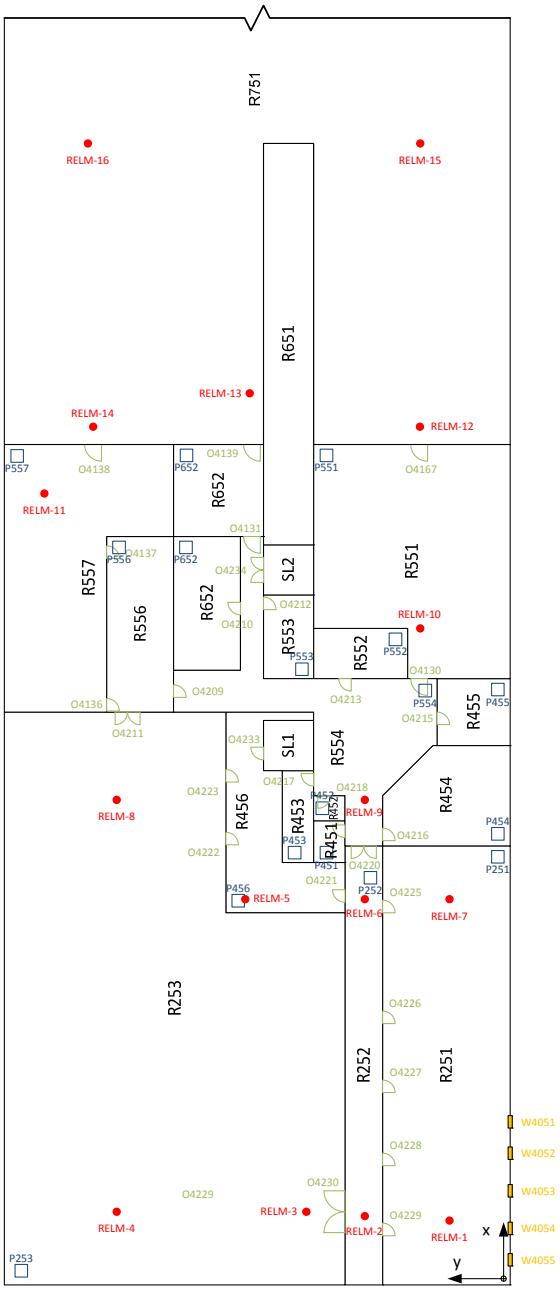

Figure 237: Deck layout aft to mid-ship

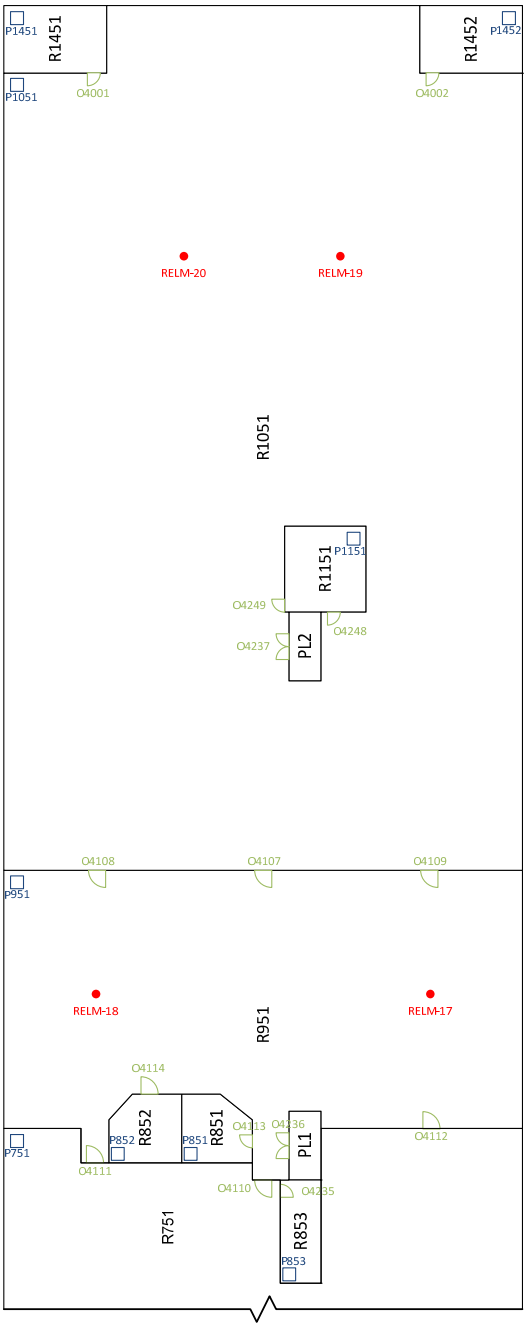

Figure 238: Deck layout mid-ship to forward

Figure 237 and Figure 238 illustrate the layout of deck 4 of M/V Estonia. For a better visualisation the deck is split into two parts, the forward and the aft part. The

nomenclature of the abbreviations used in the illustration will be explained in the following sections.

A.1.2 Flooded Compartments

The compartments, doors and windows of the model are identified with the same name throughout the thesis. “R” means room; some compartments are defined as “PL” and “SL” which stands for lift shaft. All flooded compartments and their identifications are presented in Table 25.

Compartment	Description	Volume
PL1	Lift	13.68 m^3
PL2	Lift	13.68 m^3
R251	Conference Room	354.654 m^3
R252	Corridor	104.652 m^3
R253	Night club / Bar / Cinema / Projector Room / Store	1089.042 m^3
R451	Storage	8.55 m^3
R452	Telephone	5.13 m^3
R453	Staircase	18.81 m^3
R454	Conference Room	75.24 m^3
R455	Office	31.92 m^3
R456	Pantry	89.946 m^3
R551	Corridor	269.268 m^3
R552	WC Gents	30.78 m^3
R553	Linen	27.36 m^3
R554	Corridor	152.418 m^3
R555	WC Ladies	58.368 m^3
R556	Staircase	76.608 m^3
R557	Corridor / Cabins	218.88 m^3
R651	Engine Case	131.328 m^3
R652	Cabins	53.922 m^3

R751	Cabins	1803.48 m^3
R851	Information	27.531 m^3
R852	Information Office	29.127 m^3
R853	Staircase / Cabins	25.992 m^3
R951	Hall / Luggage / Staircases	815.67 m^3
R1051	Cabins / Cleaning Room / Linen	2629.41 m^3
R1151	Staircase	43.32 m^3
R1451	Staircase	43.092 m^3
R1452	Staircase	43.092 m^3
SL1	Lift	16.416 m^3
SL2	Lift	16.416 m^3

Table 25: Identification of the flooded compartments

A.1.3 Water Reservoirs

The water reservoirs are attached to the damage opening respectively to the five open windows located at the starboard aft section of deck 4. They are identified with the letters “WR” throughout the thesis. The volume of the water reservoir is 2.385 m^3. Table 26 presents the identification and location of the water reservoirs.

Water reservoir	**Location**
WR4051	R251 Conference Room
WR4052	R251 Conference Room
WR4053	R251 Conference Room
WR4054	R251 Conference Room
WR4055	R251 Conference Room

Table 26: Identification and location of the water reservoirs

A.1.4 Air Ventilation Shafts

Air ventilation shafts, which are located on top of the flooded compartments, are assigned with the letters “AV”. The air ventilation volume is 0.54 m^3. Identification and location of the air ventilation shafts can be found in Table 27.

Air vent volume	Location	
AV251	R251	Conference Room
AV252	R252	Corridor
AV253	R253	Night club / Bar / Cinema / Projector Room / Store
AV451	R451	Storage
AV452	R452	Telephone
AV453	R453	Staircase
AV454	R454	Conference Room
AV455	R455	Office
AV456	R456	Pantry
AV551	R551	Corridor
AV552	R552	WC Gents
AV553	R553	Linen
AV554	R554	Corridor
AV555	R555	WC Ladies
AV556	R556	Staircase
AV557	R557	Corridor / Cabins
AV652	R652	Cabins
AV751	R751	Cabins
AV851	R851	Information
AV852	R852	Information Office
AV853	R853	Staircase / Cabins
AV951	R951	Hall / Luggage / Staircases
AV1051	R1051	Cabins / Cleaning Room / Linen
AV1151	R1151	Staircase
AV1451	R1451	Staircase
AV1452	R1452	Staircase

Table 27: Identification and location of the air ventilation volumes

A.1.5 Damage Openings

Five windows were chosen as damage opening, which are identified with the letter "W" throughout the thesis. "PI" identifies the pressure inlets, which are located on the bottom of the water reservoir. The dimensions of the windows and pressure inlets are 0.6 m x 1.5 m and their area is 0.9 m^2. The identification and locations of the windows are given in Table 28.

Opening	Pressure Inlet	Connection ←→		Open / Close
W4051	PI4051	R251	WR4051	●
W4052	PI4052	R251	WR4052	●
W4053	PI4053	R251	WR4053	●
W4054	PI4054	R251	WR4054	●
W4055	PI4055	R251	WR4055	●

Table 28: Dimensions and status of damage openings and pressure inlets

A.1.6 Internal Openings

Internal openings are identified throughout the thesis with the letter "O". During the test all openings are kept open apart from openings leading to lift rooms. All staircases on deck are closed as well, but will not be labelled in the thesis. The identification, dimension and the status of each opening is described in Table 29.

Opening	Dimensions				Connection ←→		Open / Close
	X [m]	Y [m]	Z [m]	Area [m^2]			
O4001		0.6	2	1.2	R1051	R1451	●
O4002		0.6	2	1.2	R1051	R1452	●
O4107		0.8	2	1.6	R951	R1051	●
O4108		0.8	2	1.6	R951	R1051	●
O4109		0.8	2	1.6	R951	R1051	●
O4110		0.8	2	1.6	R751	R951	●
O4111		0.8	2	1.6	R751	R951	●
O4112		0.8	2	1.6	R751	R951	●

O4113	0.6		2	1.2	R851	R951	●
O4114		0.8	2	1.6	R852	R951	●
O4130		0.8	2	1.6	R551	R554	●
O4131		0.8	2	1.6	R554	R652	●
O4136	0.8		2	1.6	R556	R557	●
O4137	0.8		2	1.6	R556	R557	●
O4138		0.8	2	1.6	R557	R751	●
O4139		0.8	2	1.6	R652	R751	●
O4167		0.8	2	1.6	R551	R751	●
O4209	0.6		2	1.2	R554	R556	●
O4210	0.6		2	1.2	R554	R555	●
O4211		1.2	2	2.4	R253	R556	●
O4212	0.6		2	1.2	R553	R554	●
O4213		0.6	2	1.2	R552	R554	●
O4215	0.6		2	1.2	R455	R554	●
O4216	0.6		2	1.2	R454	R554	●
O4217	0.6		2	1.2	R453	R554	●
O4218		0.6	2	1.2	R452	R554	●
O4219	0.6		2	1.2	R451	R554	●
O4220		1.2	2	2.4	R252	R554	●
O4221	0.6		2	1.2	R252	R456	●
O4222	1.2		2	2.4	R253	R456	●
O4223	0.6		2	1.2	R253	R456	●
O4225	0.6		2	1.2	R251	R252	●
O4226	0.6		2	1.2	R251	R252	●
O4227	0.6		2	1.2	R251	R252	●
O4228	0.6		2	1.2	R251	R252	●
O4229	0.6		2	1.2	R251	R252	●
O4230	2		2	4	R252	R253	●
O4233	0.6		2	1.2	R456	SL1	●
O4234	1.2		2	2.4	R554	SL2	●
O4235	0.6		2	1.2	R751	R853	●

O4236	1.2		2	2.4	R951	PL1	●
O4237	1.2		2	2.4	R1051	PL2	●
O4248		0.6	2	1.2	R1051	R1151	●
O4249	0.8		2	1.6	R1051	R1151	●

Table 29: Identification, dimensions and status of the openings

A.1.7 Air Ventilation Openings

Air ventilation openings are identified throughout the thesis with the letter "A" and the pressure outlets on top of the air ventilation volumes are declared with the letters "PO". The air ventilations are located on top of the compartments, are squared and have an area of 0.36 m^2. Table 30 gives information on the identification and location of the air ventilations.

Air vent opening	**Air vent pressure outlet**	**Air vent volume**	**Location**	
A251	PO251	AV251	R251	Conference Room
A252	PO252	AV252	R252	Corridor
A253	PO253	AV253	R253	Night club / Bar / Cinema / Projector Room / Store
A451	PO451	AV451	R451	Storage
A452	PO452	AV452	R452	Telephone
A453	PO453	AV453	R453	Staircase
A454	PO454	AV454	R454	Conference Room
A455	PO455	AV455	R455	Office
A456	PO456	AV456	R456	Pantry
A551	PO551	AV551	R551	Corridor
A552	PO552	AV552	R552	WC Gents
A553	PO553	AV553	R553	Linen
A554	PO554	AV554	R554	Corridor
A555	PO555	AV555	R555	WC Ladies

A556	PO556	AV556	R556	Staircase
A557	PO557	AV557	R557	Corridor / Cabins
A652	PO652	AV652	R652	Cabins
A751	PO751	AV751	R751	Cabins
A851	PO851	AV851	R851	Information
A852	PO852	AV852	R852	Information Office
A853	PO853	AV853	R853	Staircase / Cabins
A951	PO951	AV951	R951	Hall / Luggage / Staircases
A1051	PO1051	AV1051	R1051	Cabins / Cleaning Room / Linen
A1151	PO1151	AV1151	R1151	Staircase
A1451	PO1451	AV1451	R1451	Staircase
A1452	PO1452	AV1452	R1452	Staircase

Table 30: Identification and location of air ventilations

A.1.8 Location and Identification of the Probes

The identification and location of the probes are presented in Table 31. The reference point of the coordinates can be found in Figure 237 and Figure 238.

Probe	Model scale [mm]		Full scale [mm]	
	X	Y	X	Y
RELM-1	153.77	130.00	3,075.40	2,600.00
RELM-2	164.37	332.50	3,287.40	6,650.00
RELM-3	175.00	472.50	3,500.00	9,450.00
RELM-4	175.00	926.12	3,500.00	18,522.40
RELM-5	907.50	618.50	18,150.00	12,370.00
RELM-6	907.50	332.50	18,150.00	6,650.00
RELM-7	907.50	130.00	18,150.00	2,600.00
RELM-8	1,145.00	926.12	22,900.00	18,522.40
RELM-9	1,145.00	332.50	22,900.00	6,650.00
RELM-10	1,555.00	200.00	31,100.00	4,000.00
RELM-11	1,877.75	1,099.00	37,555.00	21,980.00
RELM-12	2,037.50	215.70	40,750.00	4,314.00
RELM-13	2,117.50	622.96	42,350.00	12,459.20
RELM-14	2,037.50	997.49	40,750.00	19,949.80
RELM-15	2,715.00	215.00	54,300.00	4,300.00
RELM-16	2,715.00	995.00	54,300.00	19,900.00
RELM-17	3,747.50	215.00	74,950.00	4,300.00
RELM-18	3,747.50	995.00	74,950.00	19,900.00
RELM-19	5,462.50	425.00	109,250.00	8,500.00

RELM-20	5,462.50	790.00	109,250.00	15,800.00

Table 31: Identification and location of the water height probes

A.2 Caption Assignment

CFD caption	MARIN Test No
MARIN 1	40101015A
MARIN 2	40101018A
MARIN 3	40101022A
MARIN 4	40101025A
MARIN 5	40101028A
MARIN	Averaged over all five tests

Table 32: Assignment of captions used in figures

A.3 Geometrical Discrepancies

Opening / compartment	Marin Model Tests	PROTEUS3
O4001	ok	ok
O4002	ok	ok
O4107	ok	ok
O4108	ok	ok
O4109	ok	ok
O4110	? position (69 0 13.4 0.8)	ok
O4111	ok	ok
O4112	ok	ok
O4113	ok	ok
O4114	ok	ok
O4130	position and breadth (31.4 -7.8 13.4 0.8)	breadth (31.4 -7.8 13.4 0.8)
O4131	ok	ok
O4136	ok	ok
O4137	closed (37.55 7.2 13.4 0.8)	closed (37.55 7.2 13.4 0.8)
O4138	ok	closed (42.6 7.85 13.4 0.8)
O4139	ok	closed (42.6 0.25 13.4 0.8)

O4167	ok	closed (42.6 -7.75 13.4 0.8)
O4209	ok	ok
O4210	ok	ok
O4211	ok	ok
O4212	ok	ok
O4213	ok	ok
O4215	ok	ok
O4216	position (24.66 -6 13.4 0.6)	? position (24.66 -6 13.4 0.6)
O4217	ok	ok
O4218	ok	ok
O4219	ok	ok
O4220	position and breadth (23.4 -5.1 13.4 1.2)	ok
O4221	ok	ok
O4222	position and breadth (22.1 1.5 13.4 1.2)	ok
O4223	ok	ok
O4225	position (20.5 -6 13.4 0.6)	ok
O4226	position (15.8 -6 13.4 0.6)	ok
O4227	position (12.5 -6 13.4 0.6)	ok
O4228	position (9 -6 13.4 0.6)	ok
O4229	position (5.65 -6 13.4 0.6)	ok
O4230	ok	ok
O4233	ok	ok
O4234	ok	ok
O4235	ok	ok
O4237	ok	ok
O4238	ok	ok
O4248	ok	closed (95.4 -3.3 13.4 0.6)
O4249	ok	ok
PL1	ok	ok
PL2	ok	ok
R1051	ok	ok

R1151	ok	ok
R1451	ok	ok
R1452	ok	ok
R251	breadth, 0.9 m smaller	ok
R252	breadth, 0.9 m wider	ok
R253	ok	ok
R451	ok	ok
R452	ok	ok
R453	ok	ok
R454	breadth, 0.9m smaller	?
R455	ok	ok
R456	ok	ok
R551	breadth, 1 m smaller	ok
R552	breadth, 1 m wider	ok
R553	ok	ok
R554	larger volume due to change of room	ok
R555	ok	ok
R556	ok	ok
R557	ok	ok
R651	ok	ok
R652	ok	ok
R751	ok	ok
R851	ok	ok
R852	ok	ok
R853	ok	ok
R951	ok	ok
SL1	ok	ok
SL2	ok	ok

Table 33: Geometrical discrepancies between the used models

Appendix B

B.1 Mathematical Conventions

Where possible, vector quantities are displayed with a raised arrow (e.g., $\vec{a}$, $\vec{A}$). Boldfaced characters are reserved for vectors and matrices as they apply to linear algebra (e.g., the identity matrix, **I**).

The operator ∇, referred to as grad, nabla, or del, represents the partial derivative of a quantity with respect to all directions in the chosen coordinate system. In Cartesian coordinates, ∇ is defined to be

$$\frac{\partial}{\partial x}\vec{i}+\frac{\partial}{\partial y}\vec{j}+\frac{\partial}{\partial z}\vec{k}$$

∇ appears in several ways:

- The gradient of a scalar quantity is the vector whose components are the partial derivatives; for example,

$$\nabla p=\frac{\partial p}{\partial x}\vec{i}+\frac{\partial p}{\partial y}\vec{j}+\frac{\partial p}{\partial z}\vec{k}$$

- The gradient of a vector quantity is a second-order tensor; for example, in Cartesian coordinates,

$$\nabla(\vec{\upsilon})=\left(\frac{\partial}{\partial x}\vec{i}+\frac{\partial}{\partial y}\vec{j}+\frac{\partial}{\partial z}\vec{k}\right)\left(\upsilon_x\vec{i}+\upsilon_y\vec{j}+\upsilon_z\vec{k}\right)$$

This tensor is usually written as

$$\begin{pmatrix}\frac{\partial \upsilon_x}{\partial x} & \frac{\partial \upsilon_x}{\partial y} & \frac{\partial \upsilon_x}{\partial z}\\ \frac{\partial \upsilon_y}{\partial x} & \frac{\partial \upsilon_y}{\partial y} & \frac{\partial \upsilon_y}{\partial z}\\ \frac{\partial \upsilon_z}{\partial x} & \frac{\partial \upsilon_z}{\partial y} & \frac{\partial \upsilon_z}{\partial z}\end{pmatrix}$$

- The divergence of a vector quantity, which is the inner product between ∇ and a vector; for example,

$$\nabla \cdot \vec{\upsilon} = \frac{\partial \upsilon_x}{\partial x} + \frac{\partial \upsilon_y}{\partial y} + \frac{\partial \upsilon_z}{\partial z}$$

- The operator $\nabla \cdot \nabla$, which is usually written as ∇^2 and is known as the Laplacian; for example,

$$\nabla^2 T = \frac{\partial^2 T}{\partial x^2} + \frac{\partial^2 T}{\partial y^2} + \frac{\partial^2 T}{\partial z^2}$$

$\nabla^2 T$ is different from the expression $(\nabla T)^2$, which is defined as

$$(\nabla T)^2 = \left(\frac{\partial T}{\partial x}\right)^2 + \left(\frac{\partial T}{\partial y}\right)^2 + \left(\frac{\partial T}{\partial z}\right)^2$$

B.2 The Epanechnikov Kernel

In general, a kernel is a weighting function used in non-parametric estimation techniques. Kernels are used in kernel density estimation to estimate random variables' density functions, or in kernel regression to estimate the conditional expectation of a random variable.

A kernel is a non-negative real-valued integrable function K satisfying the following two requirements:

$$\int_{-\infty}^{+\infty} K(u)du = 1 \tag{B.2.1}$$

$$K(-u) = K(u) \tag{B.2.2}$$

The first requirement ensures that the method of kernel density estimation results in a probability density function. The second requirement ensures that the average of the corresponding distribution is equal to that of the sample used.

If K is a kernel, then the function K^* is defined by $K^*(u)=\lambda^{-1}K(\lambda^{-1}u)$, where $\lambda>0$. This can be used to select a scale that is appropriate for the data.

The Epanechnikov kernel has following notation (B.2.3) and can be seen in Figure 239:

$$K(u) = \frac{3}{4}\left(1-u^2\right)1_{(|u|\leq 1)} \tag{B.2.3}$$

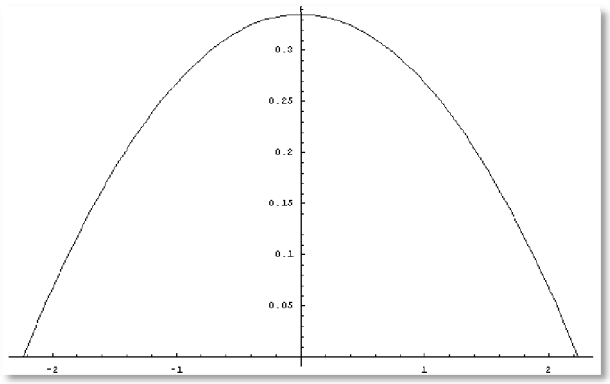

Figure 239: The Epanechnikov kernel

Appendix C

C.1 Governing Equations of Fluid Flow

C.1.1 General Remarks

The general equations of fluid flow represent mathematical statements of the conservation laws of physics, such as:

- Conservation of fluid mass
- The rate of change of momentum equals the sum of the forces on a fluid particle (Newton's second law)
- The rate of change of energy is equal to the sum of the rate of heat addition to and the rate of work done on a particle

The governing equations for an unsteady, three dimensional, compressible viscous flow are presented in the following paragraphs.

C.1.2 Continuity Equation

$$\frac{\partial \rho}{\partial t} + div\left(\rho u\right) = S_m \tag{C.1.1}$$

Equation (C.1.1) is the general form of the unsteady, three-dimensional mass conservation equation at a point in an incompressible as well as compressible fluid, see Figure 240. The first term on the left side is the rate of change in time of density, while the second term, called the convective term, describes the net flow of mass. The source S_m is the mass added to the continuous phase from the dispersed second phase (e.g., due to vaporization of liquid droplets) and any user-defined sources.

In many applications the fluid density for flows of liquid and for gases with a Mach number below 0.3 may be assumed as constant. Such flows are said to be incompressible. If the flow is also isothermal, the viscosity is also constant. If this is the case mass conservation equation reduces to:

$$div(\rho u) = 0 \tag{C.1.2}$$

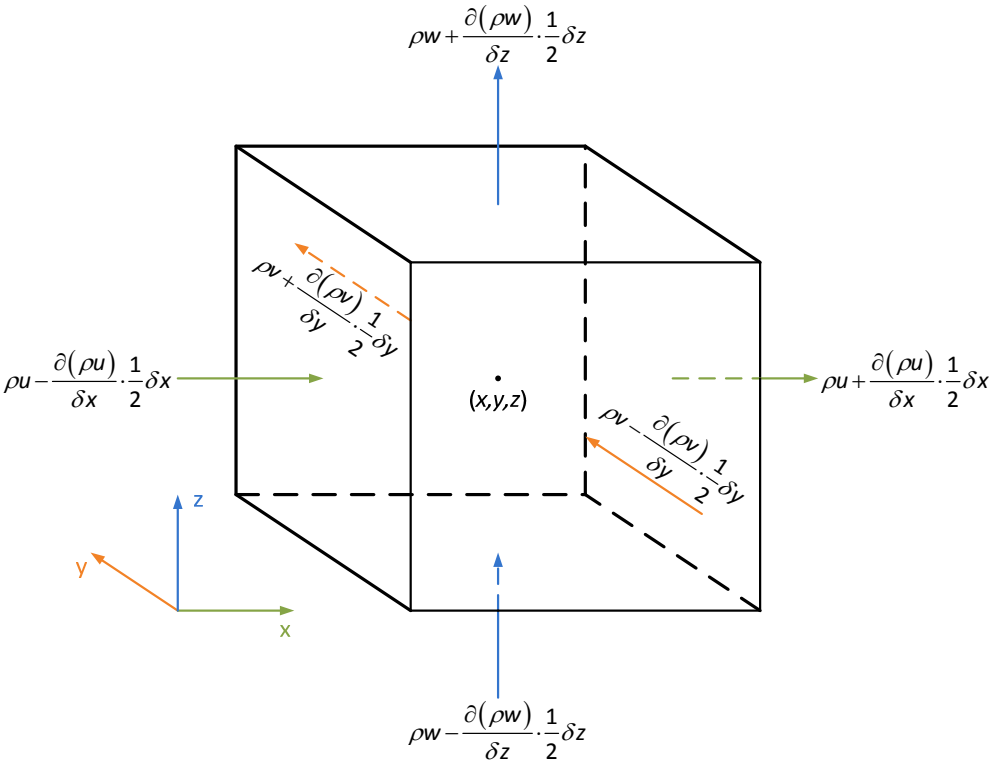

Figure 240: Mass flows in and out a fluid element

C.1.3 Momentum Equation

The term on the left hand side is the rate of increase of momentum of fluid particle which is equal to the term on the right hand side giving the sum of forces on fluid particle.

$$\frac{\partial}{\partial t}(\rho\vec{v}) + \nabla \cdot (\rho\vec{v}\vec{v}) = -\nabla p + \nabla \cdot \left(\bar{\bar{\tau}}\right) + \rho\vec{g} + \vec{F} \tag{C.1.3}$$

Where p is the static pressure, $\bar{\bar{\tau}}$ is the stress tensor, and $\rho\vec{g}$ and $\vec{F}$ are the gravitational body force and external body forces like centrifugal and Coriolis forces, electromagnetic forces, etc. $\vec{F}$ also contains other model-dependent source terms such as porous-media and user-defined sources.

For Newtonian fluids the stress tensor $\overline{\overline{\tau}}$, see Figure 241, which is the molecular rate of transport, is given by

$$\overline{\overline{\tau}} = \mu\left[\left(\nabla\vec{v} + \nabla\vec{v}^{T}\right) - \frac{2}{3}\nabla\cdot\vec{v}I\right] \tag{C.1.4}$$

where μ is the molecular viscosity, I is the unit tensor, and $\left(\nabla\vec{v} + \nabla\vec{v}^{T}\right)$ is the rate of strain (deformation) tensor.

The state of stress of a fluid element is defined in terms of the pressure and the nine viscous stress components. Viscous stresses are denoted by τ_{ij} where the suffices *i* and *j* indicate that the stress component acts in the *j*-direction on a surface normal to the *i*-direction.

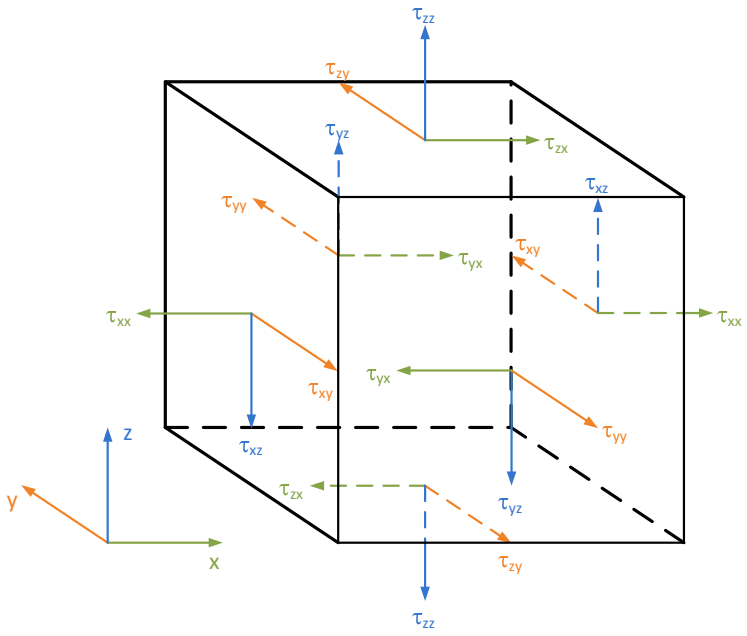

Figure 241: Stress components of fluid element

The magnitude of a force resulting from a surface stress is the product of stress and area, see Figure 242. The net force in the x-direction is the sum of the force components acting that direction on the fluid element.

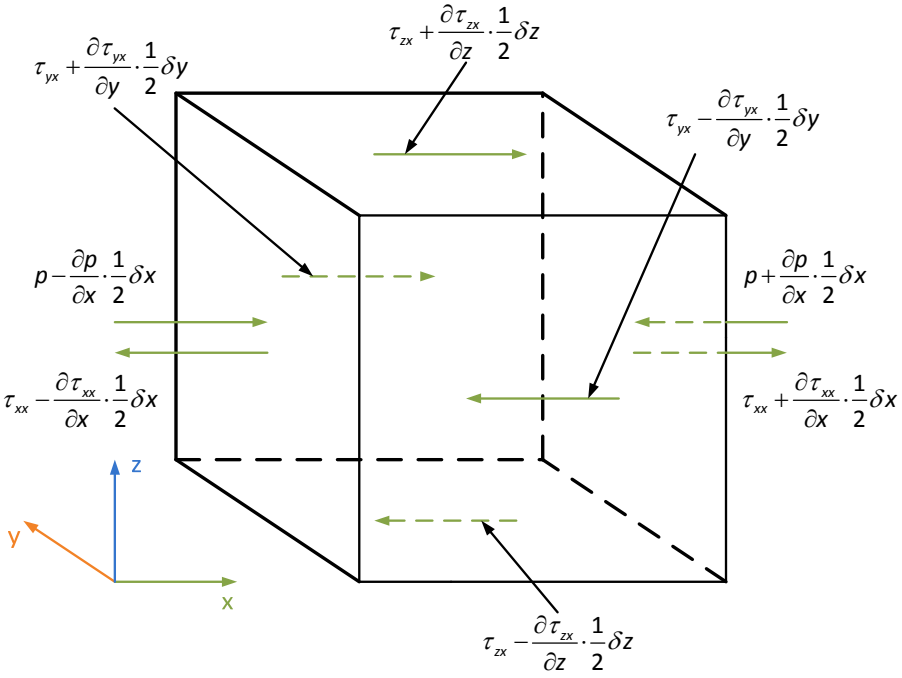

Figure 242: Stress components in x-direction

C.1.4 Energy Equation

The energy equation evolved from the first law of thermodynamics and denotes the increase in energy of a fluid particle is equal to the net rate of heat added to the fluid particle, plus the net rate of work done on the fluid particle. Equation (C.1.5) expresses the rate of increase of energy of a fluid particle per unit volume:

$$\rho\frac{DE}{Dt}=-div(pu)+\left[\begin{array}{l}\frac{\partial(u\tau_{xx})}{\partial x}+\frac{\partial(u\tau_{yx})}{\partial y}+\frac{\partial(u\tau_{zx})}{\partial z}+\frac{\partial(u\tau_{xy})}{\partial x}+\frac{\partial(u\tau_{yy})}{\partial y}+\frac{\partial(u\tau_{zy})}{\partial z}+\\ +\frac{\partial(u\tau_{xz})}{\partial x}+\frac{\partial(u\tau_{yz})}{\partial y}+\frac{\partial(u\tau_{zz})}{\partial z}\end{array}\right] \quad \text{(C.1.5)}$$

Equation (C.1.5) expresses the rate of work done on the fluid particle by a surface force is equal to the product of the force and velocity component in the direction of the force. S_E is a defined source of energy per unit volume per time.

The heat flux vector has three components q_x, q_y and q_z, see Figure 243. The net rate of heat transfer to the fluid particle due to heat flow in each direction is given

by the difference between the rate of heat input across the face *W* and the rate of heat loss across face *E*. Thus, the final equation describing the rate of heat addition to the fluid particle due to heat conduction can be written as:

$$-div\ q = div\left(k\ grad\ T\right) \tag{C.1.6}$$

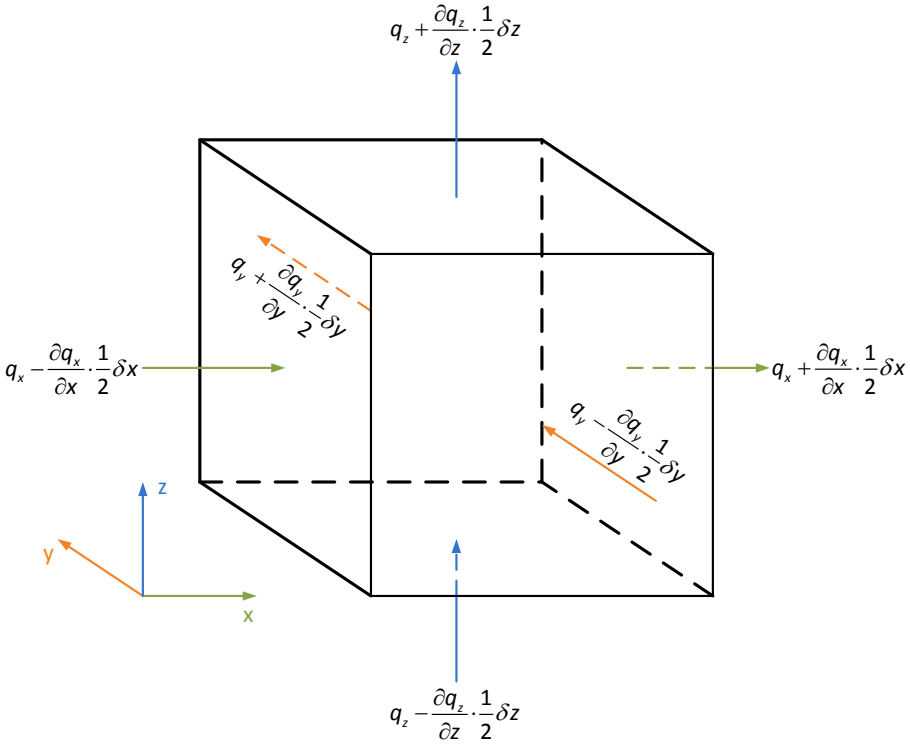

Figure 243: Components of the heat flux vector

There are two common views how the energy *E* of a fluid is defined. One is, that the energy of a fluid is defined as the sum of kinetic energy $\frac{1}{2}\left(u^2+v^2+w^2\right)$, gravitational potential energy and internal energy *i*. In contrary to this view where it is considered that the fluid element is storing gravitational potential energy, the gravitational force can also be regarded as a body force working on the fluid element while moving through the gravity field. Based on this latter view the equation (C.1.7) for the conservation of energy is defined by equating the rate of change of energy of a fluid particle (equation (C.1.5)) to the sum of the net rate of

work done on the fluid particle (right side of equation (C.1.5)) and the net rate of heat addition to the fluid (equation (C.1.6)) and the rate of increase of energy due to sources S_E.

$$\rho\frac{DE}{Dt}=-div(pu)+\left[\frac{\partial(u\tau_{xx})}{\partial x}+\frac{\partial(u\tau_{yx})}{\partial y}+\frac{\partial(u\tau_{zx})}{\partial z}+\frac{\partial(v\tau_{xy})}{\partial x}+\frac{\partial(v\tau_{yy})}{\partial y}+\frac{\partial(v\tau_{zy})}{\partial z}+\frac{\partial(w\tau_{xz})}{\partial x}+\frac{\partial(w\tau_{yz})}{\partial y}+\frac{\partial(w\tau_{zz})}{\partial z}\right]+div(k\ grad\ T)+S_E \tag{C.1.7}$$

C.1.5 Compressible Flow

Compressibility effects are encountered in gas flows at high velocity and/or in which there are large pressure variations. When the flow velocity approaches or exceeds the speed of sound of the gas or when the pressure change in the system ($\Delta p / p$) is large, the variation of the gas density with pressure has a significant impact on the flow velocity, pressure, and temperature.

Compressible flows are typically characterised by the total pressure p_0 and total temperature T_0 of the flow. For an ideal gas, these quantities can be related to the static pressure and temperature by the following:

$$\frac{p_0}{p}=\exp\left(\frac{\int_T^{T_0}\frac{C_p}{T}dT}{R}\right) \tag{C.1.8}$$

For constant C_p, Equation (C.1.8) reduces to:

$$\frac{p_0}{p}=\left(1+\frac{\gamma-1}{2}M^2\right)^{\frac{\gamma}{(\gamma-1)}} \tag{C.1.9}$$

$$\frac{T_0}{T}=1+\frac{\gamma-1}{2}M^2 \tag{C.1.10}$$

For compressible flows, the ideal gas law is written in the following form:

$$\rho = \frac{p_{op} + p}{\frac{R}{M_w} T} \tag{C.1.11}$$

These equations of state provide the linkage between the energy equation and the mass conservation and momentum equations due to density variations as a result of pressure and temperature variations in the flow field.

C.1.6 Navier-Stokes Equations

The Navier–Stokes equations, named after Claude-Louis Navier and George Gabriel Stokes, describe the motion of viscous fluid substances such as liquids and gases. These equations arise from applying Newton's second law to fluid motion, together with the assumption that the fluid stress is the sum of a diffusing viscous term (proportional to the gradient of velocity), plus a pressure term.

$$\rho \frac{Du}{Dt} = -\frac{\partial p}{\partial x} + div\left(\mu \; grad \; u\right) + S_{Mx} \tag{C.1.12}$$

$$\rho \frac{Dv}{Dt} = -\frac{\partial p}{\partial y} + div\left(\mu \; grad \; v\right) + S_{My} \tag{C.1.13}$$

$$\rho \frac{Dw}{Dt} = -\frac{\partial p}{\partial z} + div\left(\mu \; grad \; w\right) + S_{Mz} \tag{C.1.14}$$

The left side of the equation describes acceleration, and may be composed of time dependent or convective effects (also the effects of non-inertial coordinates if present). The right side of the equation is in effect a summation of body forces (such as gravity) and divergence of stress (pressure and stress).

When the Newtonian model is used in the internal energy equation following rearrangement has to be carried out:

$$\rho \frac{Di}{Dt} = -p \; div \; u + div\left(k \; grad \; T\right) + \Phi + S_i \tag{C.1.15}$$

where Φ is the dissipation function.

C.1.7 Summary of Governing Equations

The fluid flow of a compressible Newtonian fluid can be defined by following equations which represents a brief summary of the previous chapters, see Table 34.

Mass	$\frac{\partial p}{\partial t}\partial + div(\rho u) = S_m$	(C.1.16)
x-momentum	$\frac{\partial(\rho u)}{\partial t} + div(\rho u u) = -\frac{\partial p}{\partial x} + div(\mu\ grad\ u) + S_{Mx}$	(C.1.17)
y-momentum	$\frac{\partial(\rho v)}{\partial t} + div(\rho v u) = -\frac{\partial p}{\partial y} + div(\mu\ grad\ v) + S_{My}$	(C.1.18)
z-momentum	$\frac{\partial(\rho w)}{\partial t} + div(\rho w u) = -\frac{\partial p}{\partial z} + div(\mu\ grad\ w) + S_{Mz}$	(C.1.19)
Internal energy	$\frac{\partial(\rho i)}{\partial t} + div(\rho i u) = -p\ div\ u + div(k\ grad\ T) + \Phi + S_i$	(C.1.20)
Equations of state	$p = p(\rho, T)$ and $i = i(\rho, T)$	(C.1.21)
	e.g. perfect gas	
	$p = \rho R T$ and $i = C_v T$	(C.1.22)

Table 34: Summary of governing equation

Appendix D

D.1 Evaluation of the Discharge Coefficient

Ruponen (2006) evaluates the discharge coefficient based on the discharging time as follows. A tank with perpendicular walls that is discharging through an opening in the bottom of the tank is considered. The area of free surface in the tank is *S*. The initial water height is H_1 and the final water height is H_2, measured from the level of the opening. The area of the opening is *A* and the discharge coefficient C_d is unknown. Instead, the discharging time *T* is known. A schematic picture of the system is presented in Figure 244. It is assumed that C_d is independent on the Reynolds number so that it is constant during the whole discharging time.

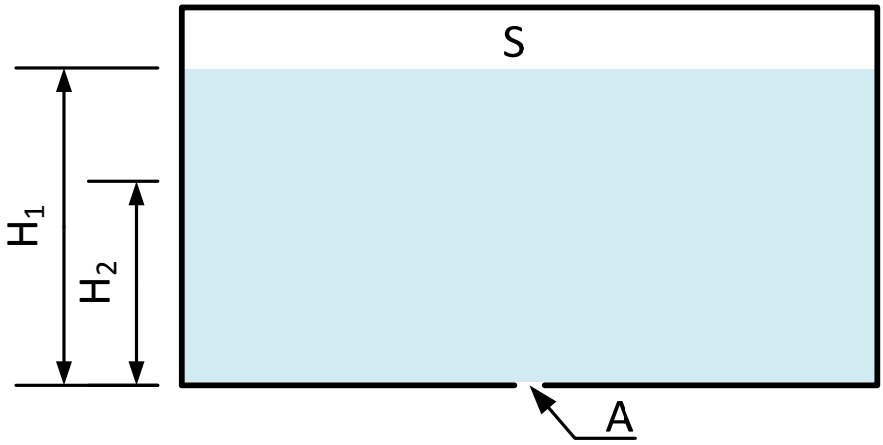

Figure 244: Draining tank (*Ruponen (2006)*)

Bernoulli's equation along a streamline between point 1 and point 2 is:

$$p_1 + \frac{1}{2}\rho u_1^2 + \rho g H(t) = p_2 + \frac{1}{2}\rho u_2^2 \tag{D.1.1}$$

where *p* is air pressure, ρ is density, *u* is flow velocity and *g* is the acceleration due to gravity. The point 2 is in the opening, and hence the water height *H* is present only on the left hand side.

In the case of fully vented system $p_1 = p_2$, and the air pressure has no effects on the discharge process. The velocity far from the opening can be taken as zero, i.e. u_1=0 . Hence the flow velocity through the opening, solved from equation (D.1.1), is:

$$u_2 = \sqrt{2gH(t)} \tag{D.1.2}$$

The instantaneous water height can be expressed as function of the volume of water since the area of free surface S is constant:

$$H(t) = \frac{V_w(t)}{S} \tag{D.1.3}$$

and the time derivative for the volume of water is the negation of the volumetric flow through the opening:

$$\frac{dV_w(t)}{dt} = -Q_w = -C_d A u_2 \tag{D.1.4}$$

Therefore, the discharge process is governed by the following differential equation:

$$\frac{dV_w(t)}{dt} = -C_d A\sqrt{2g\frac{V_w(t)}{S}} \tag{D.1.5}$$

and the initial condition is:

$$V_w(0) = H_1 S \tag{D.1.6}$$

and the volume of water in the tank is decreasing. This can be solved analytically:

$$V_w(t) = \frac{C_d^2 A^2 g}{2S}\cdot\left[t^2 - \frac{2\sqrt{2gH_1}S}{C_d A g}\cdot t + \frac{2H_1 S}{gC_d^2 A^2}\right] \tag{D.1.7}$$

When a time period T has elapsed, the water level has decreased to H_2, and therefore:

$$V_w(t) = H_2 S \tag{D.1.8}$$

When this is substituted into equation (D.1.7), the following equation is formed:

$$H_2 S = \frac{C_d^2 A^2 g}{2S} \cdot \left[T^2 - \frac{2\sqrt{2gH_1}S}{C_d A g} \cdot T + \frac{2H_1 S}{g C_d^2 A^2} \right] \tag{D.1.9}$$

This is a second order equation for the discharge coefficient and it can be rearranged, resulting in:

$$\frac{A^2 T^2 g}{2S} C_d^2 - \sqrt{2gH_1} TA \cdot C_d + H_1 S - H_2 S = 0 \tag{D.1.10}$$

The discharge coefficient can be solved:

$$C_d = \frac{AT\sqrt{2gH_0} \pm \sqrt{A^2 T^2 2gH_0 - 4 \cdot \frac{gA^2T^2}{2S} \cdot S(H_1 - H_2)}}{2 \cdot \frac{gA^2T^2}{2S}} = \frac{S\sqrt{2gH_1}}{ATg} \pm \frac{S\sqrt{2gH_2}}{ATg} \tag{D.1.11}$$

Therefore, the following equation for the discharge coefficient is obtained:

$$C_d = S \frac{\sqrt{2gH_1} - \sqrt{2gH_2}}{ATg} \tag{D.1.12}$$